Erbium-ytterbium-yttrium compounds for light emission at 1.54μm

by

Michiel Vanhoutte

M.Sc., B.Sc., Engineering Physics,
Ghent University, Belgium (2007)

Submitted to the Department of Materials Science and Engineering
in partial fulfillment of the requirements for the degree of

Doctor of Philosophy in Materials Science and Engineering

at the

MASSACHUSETTS INSTITUTE OF TECHNOLOGY

February 2013

Author .....
Department of Materials Science and Engineering
January 30, 2013

Certified by .....
Lionel C. Kimerling
Thomas Lord Professor of Materials Science and Engineering
Thesis Supervisor

Accepted by .....
Gerbrand Ceder
R. P. Simmons Professor of Materials Science and Engineering
Chair, Departmental Committee on Graduate Students

Erbium-ytterbium-yttrium compounds for light emission at 1.54μm

by

Michiel Vanhoutte

Submitted to the Department of Materials Science and Engineering
on January 30, 2013, in partial fulfillment of the
requirements for the degree of
Doctor of Philosophy in Materials Science and Engineering

Abstract

Silicon microphotonics has emerged as the leading technology to overcome the interconnect bottleneck that limits a further increase of computation power following Moore's law. Optical interconnects between different electronic microprocessors in an electronic-photonic integrated circuit (EPIC) can provide a fast, low-loss and high-bandwidth alternative to electrical interconnects, which suffer from issues such as resistive heating, RC delays and channel crosstalk at an increasing device density.

A crucial device in such an electronic-photonic integrated circuit is a compact, high-gain and low power optical amplifier to compensate for signal attenuation due to propagation losses and to recover signal strength after subsequent 3dB splits during fanout of the optical signal to different microprocessors. Erbium ions (Er^{3+}) are an excellent candidate to provide amplification around $\lambda = 1.54\mu m$ for optical telecommunications. Erbium-doped fiber amplifiers (EDFAs) have already enabled long-haul optical data transmission through silica optical fibers, but scaling down a fiber amplifier to an on-chip erbium-doped waveguide amplifier (EDWA) brings along significant materials and device design challenges.

In this thesis, erbium-ytterbium oxide ($Er_xYb_{2-x}O_3$) and erbium-ytterbium-yttrium silicate ($Er_xYb_yY_{2-x-y}Si_2O_7$) compounds are investigated as novel materials systems for the development of EDWAs. The high erbium and ytterbium solubility ($>10^{22}$ cm^{-3}) and refractive index ($1.71 < n < 1.92$) make these materials excellent candidates for compact, low-power optical amplifiers. $Er_xYb_{2-x}O_3$ and $Er_xYb_{2-x}Si_2O_7$ thin films were deposited on SiO_2 and analyzed structurally and optically. The role of ytterbium in these compounds is twofold. First, ytterbium can be used as an alternative to yttrium for dilution of the erbium concentration in order to mitigate parasitic concentration quenching effects. Second, ytterbium acts as a sensitizer for erbium during optical pumping at $\lambda = 980nm$. Comparison of the different oxide and silicate thin films reveals that the α-disilicate phase is the best candidate for an EDWA gain medium pumped at $\lambda = 980nm$.

By means of rate and propagation equations, the composition of an $Er_xYb_yY_{2-x-y}Si_2O_7$ gain medium was optimized for application as a 3dB EDWA. The optimal composition was found to be $Er_{0.025}Yb_{0.200}Y_{1.775}Si_2O_7$, which provides a 1.5dB/cm gain at only 3mW of pump power. In terms of the figure of merit 3dB gain/(device area · pump power), this material outperforms other EDWA materials reported in literature.

Thesis Supervisor: Lionel C. Kimerling
Title: Thomas Lord Professor of Materials Science and Engineering

Acknowledgments

Getting a PhD at MIT is a very humbling experience. Not only does it take you to the very limit of your capabilities, it makes you do this in an environment full of incredibly talented, intelligent and driven people. Getting to know the people whom I now consider to be my friends has been at least as valuable as the skills that I have learned from my research. Having only two pages to acknowledge everyone who taught me, mentored me, advised me, helped me out, supported me, welcomed me, became my friend and was there when I needed them, is almost as difficult a task as condensing more than five years of research into two hundred pages.

Prof. Lionel C. Kimerling has been an advisor in every sense of the word: as much as a supervisor for my research project, Kim has been a mentor and an example. Kim has a way of choosing the most interesting and relevant research projects, never loses the big picture out of sight and at the same time has a huge technical knowledge and intuition about materials science and engineering. Kim's confidence that no challenge is too big to overcome has been an inspiration and a motivation throughout my PhD. It has been an incredible privilege to work for Kim as a research and teaching assistant.

Dr. Jürgen Michel has served as my a PhD co-advisor. Jürgen's knowledge about erbium and photonics in general is limitless. Fortunately, his door was always open and he was always eager to help when I got stuck with research, did not know how to do a certain experiment or needed advice about my project. His help has been invaluable. I also want to thank my other committee members, Prof. Caroline Ross and Prof. Franz Kärtner, for their suggestions and recommendations while finishing up my work. Their comments have made this thesis a much better document.

Working with fellow students, postdocs, research scientists, faculty and staff at MIT has been a fantastic experience. I would like to mention in particular Anu Agarwal, Mindy Baughman, Sarah Bernardis, Jonathan Bessette, Lirong Broderick, Rodolfo Camacho, Jing Cheng, Juejun Hu, Jifeng Liu, Kevin McComber, Neil Patel, Vivek Raghunathan, Vivek Singh, Xiaochen Sun, Jianfei Wang and Tim Zens for their support and friendship. Brian Albert has helped me with oxide etching at MTL, Jaejin Kim has helped with the AFM analysis and Yan Cai with the micro-PL measurements. For them this may have seemed like a small amount of work, but it was enormously helpful to me. A special word of thanks goes out to Anat Eshed for all her help with setting up the sputtering system, getting my PhD project started and providing guidance and advice during the rest of my research. Anat has become a friend, and after all the chillers we fixed together, we can always start a plumbing business if all else fails.

Kurt Broderick at MTL and Dr. Scott Speakman at the CMSE XRD lab consistently go above and beyond their call of duty to help students with their work. Kurt was there to help me implement any crazy research ideas that I came up with. He truly makes the Exploratory Materials Laboratory (EML) worthy of its name. Scott

dedicated hours of his time to helping me with XRD analysis and never got tired when I asked him the same question over and over. His kindness and knowledgeability are nothing short of phenomenal.

Lisa Sinclair is officially EMAT's administrative assistant, but she is so much more than that. I know that for many people in our group she has been a huge source of encouragement when times got rough with the PhD. When the work is not going the way you want it to go and you feel like it is never going to work out, there is always Lisa to cheer you up and put things in perspective. Lisa is also an incredible artist and patissier. I will never forget the fantastic graduation cake she made. Lisa combines so many talents personally as well as professionally.

There are no words to describe how important my friends have been in the past 5 years. Without their support, this PhD would have been an impossible undertaking. Getting to know all of you is the greatest thing about coming to the US. In particular, I would like to thank Ana Carolina Areias, Salvador Barriga, Megan Baugh, Brian Beliveau, David Bradwell, Noémie Chocat, Machteld De Hertogh, Thomas Fellows, Kevin Huang, Ophelia Maertens, Roza Mahmoodian, Rahul Malik, Emily Miller, Robert Mitchell, Sophie Poizeau, Sahil Sahni, Matthew Smith, Andreas Wankerl and Lizzie Woods. Each of you have been an incredible support in your own way.

Lastly, I would like to thank my parents and my girlfriend Jo. They are the people who have supported me the most and who were there for me every second that I needed them. I cannot imagine how it must feel to have your son move to another continent to take the road less traveled. I cannot imagine what it must be like to see someone you love struggle all day and night to finish a PhD. Jo has been my rock in the past year and a half. Soon it will be my turn to be on the other side.

This work has been sponsored by the Flemish Foundation of Scientific Research (FWO) and the Si-laser MURI project funded by the Air Force Office of Scientific Research (AFOSR).

Contents

List of Figures

List of Tables

Chapter 1

Introduction

1.1 Motivation

1.1.1 Optical communications

The information revolution of the past decades has been driven by shrinkage of the size of a single transistor, which allowed to pack more and more transistors on a chip in order to increase its computation power. According to the *International Technology Roadmap for Semiconductors* (ITRS), further progress at current device densities ($> 10^7$ devices/chip) is now limited by the performance of interconnects between devices rather than a further reduction in transistor size [1].

The increasing electrical interconnect density causes problems such as resistive heating losses, crosstalk between channels and RC delays due to closer channel spacing. This problem is called the *interconnect bottleneck*. Figure 1-1 shows that even with the replacement of Al/SiO_2-technology by Cu and low-k dielectrics, interconnect delays start dominating transistor gate delays for gate lengths smaller than 180 nm [2].

Optical interconnections are currently the most promising solution to the RC problems of traditional metal interconnects [3, 4]. In contrast to electrons in metals, near-infrared (NIR) photons propagate through materials such as Si and SiO_2 with

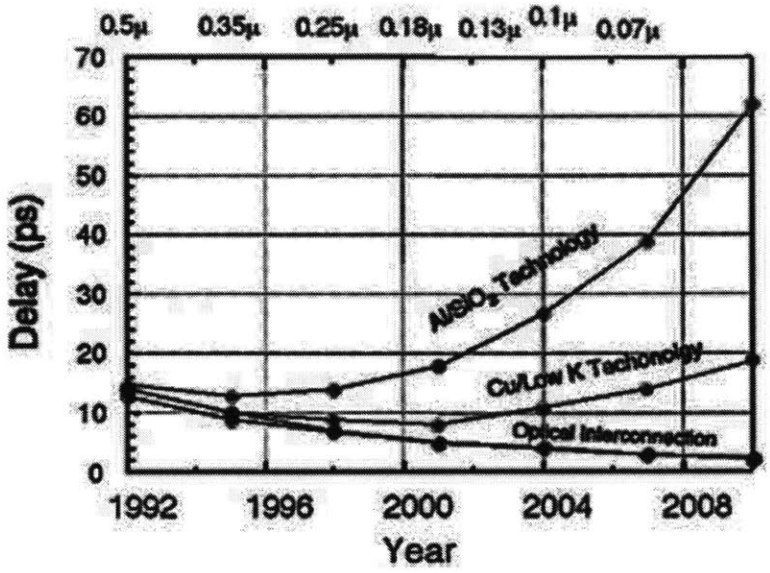

Figure 1-1: Signal transmission delay (over 1 cm) versus transistor technology generation for Al/SiO_2, Cu/low-k dielectric and optical interconnects. From [2].

negligible heat dissipation and crosstalk. In addition, the high frequency of the optical carrier wave ($\nu \sim 200$ THz) provides a very high data bandwidth for wavelength-division multiplexing (WDM).

The low loss and high information-carrying capacity of optical interconnects have already revolutionized the 'distance x data rate' performance metric for long haul telecommunications. Figure 1-2 shows that the transition from electrical to optical communications caused both a discontinuous increase in information capacity and in its rate of further growth. The success of long-haul optical communications was ultimately due to the combination of two key technologies that allow propagation of light at 1.5 μm over long distances:

1. silica optical fibers with ultra-low propagation loss ($\sim$0.2dB/km) at $\lambda = 1.5\mu m$
2. erbium-doped fiber amplifiers (EDFAs) which provide broad, all-optical amplification exactly in the SiO_2 transparency window around $\lambda = 1.5\mu m$

The overlap between the photoluminescence (PL) spectrum of the $^4I_{13/2} \rightarrow {}^4I_{15/2}$ transition in Er^{3+} in silica and the loss minimum around $\lambda = 1.5\mu m$ in silica optical fibers is shown in Figure 1-3.

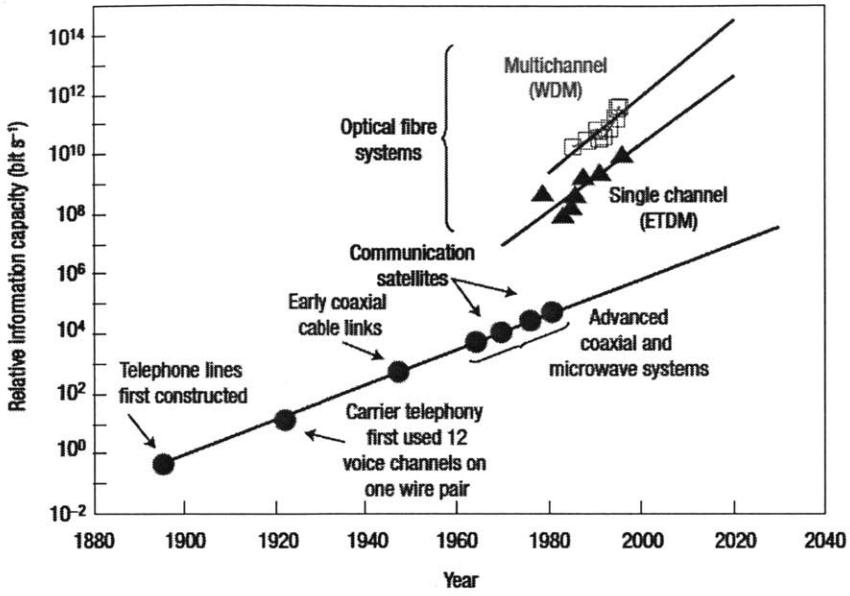

Figure 1-2: Trend in the information-carrying capacity of a single line (electrical or optical) with time and technology (WDM = wavelength-division multiplexing; ETDM = electronic time-division multiplexing). Figure adopted from [5].

1.1.2 Electronic-photonic integrated circuits

The long haul optical communications model described above can be adapted to an on-chip level thanks to the development of *silicon microphotonics*. Analogous to electronic integrated circuits (EICs) known from silicon microelectronics, electronic-photonic integrated circuits (EPICs) were developed in which all the microphotonic components are integrated on a single substrate. In such an electronic-photonic integrated circuit, the processing work is still done by electronic components, but the data transmission between different computation cores is performed optically, thereby combining the high computing power per area of electrical processors with the low-loss, high bandwidth data transmission of optical interconnects. In addition, silicon-based EPICS can benefit from the mature complementary metal-oxide-semiconductor (CMOS) technology already developed for silicon microelectronics processing, such as deposition, implantation, etching techniques et cetera.

An example of such an electronic-photonic integrated circuit is shown in Figure 1-4. The figure shows an EPIC for intra-chip optical clock signal distribution to the

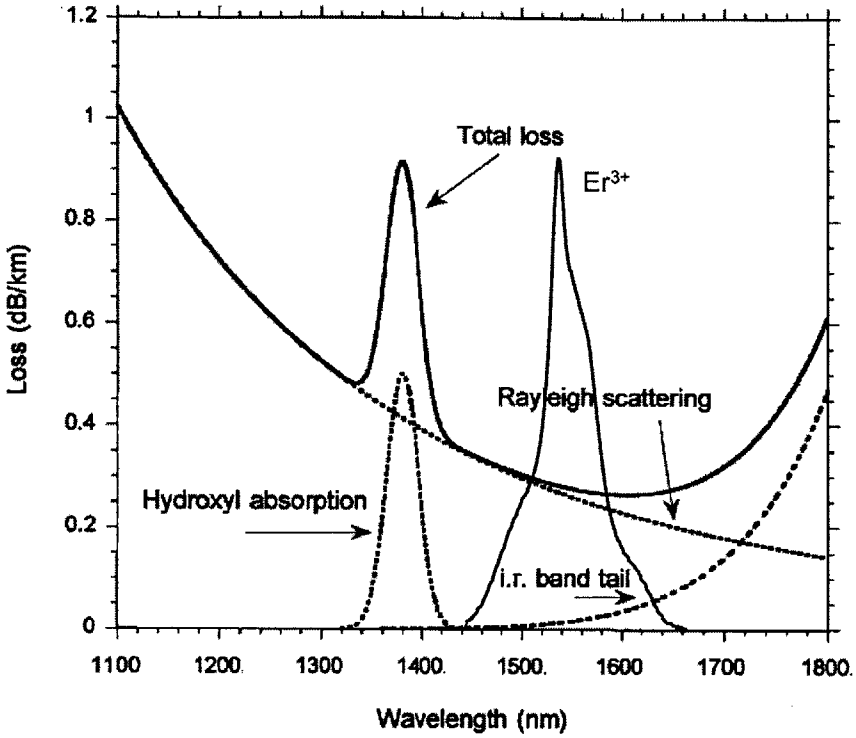

Figure 1-3: Photoluminescence spectrum of the $^4I_{13/2} \rightarrow {}^4I_{15/2}$ transition in Er^{3+} overlaid on the near-infrared loss spectrum of a silica optical fiber. Modified from [6].

electronic processing units, which is one of the most important functions of the interconnection. An *optical layer* that handles data transmission is overlaid on top of the *electrical layer* containing the electronic processing units. In between the two layers is a *transceiver interface* for the conversion between electrical and optical signals.

In conventional clocking, an electrical clocking signal is distributed through an electrically conducting wire, providig a timing reference for the movement of data within a system. Since clock signals operate at the highest speeds within the system, clocking is often the first application that suffers from problems related to electrical interconnects, such as prohibitive power consumption, crosstalk and RC delay, [4, 7]. Optical clock signal distribution would provide a solution to this problem.

The *H-tree* design shown in Figure 1-4 minimizes skew of the incoming clocking signal by ensuring an equal path length to the underlying electronic computation units [8]. It is clear that the major source of signal attenuation in the H-tree architecture is

the *fanout*, i.e. the subsequent Y-splits corresponding to a 50% = - 3dB loss in signal strength. A 3 dB optical amplifier is therefore required after each Y-split to compensate for these losses. A practical 3dB waveguide amplifier needs to be compatible with 1 Gb/s data transmission and would provide a 3dB gain at a 1mW pump power with a 1.75dB noise figure, within an areal footprint $< 2mm^2$ [4].

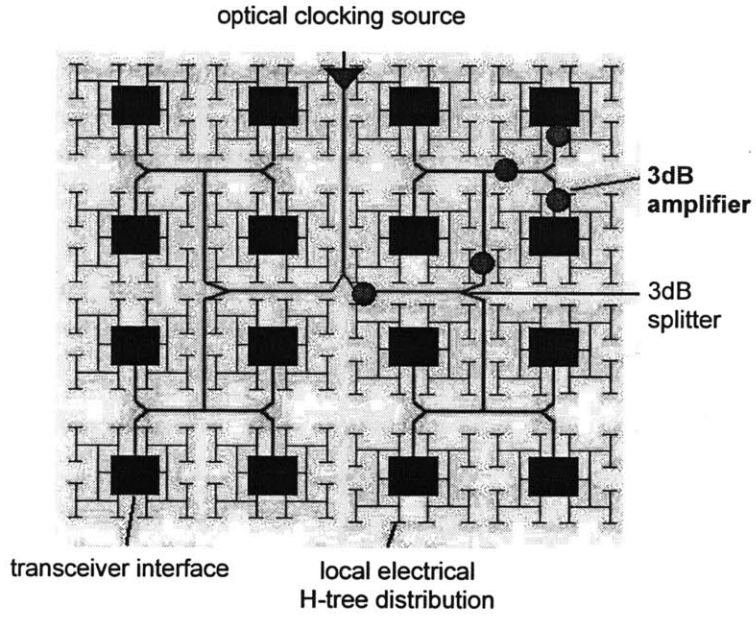

Figure 1-4: H -tree network for intra-chip optical clock signal distribution. Modified from [8] and [9].

1.1.3 Integrated optical amplifiers

Ultralow-loss (0.8dB/cm) Si/SiO_2 waveguides , optical filters, (de-)multiplexers, modulators, photodetectors and a Si-compatible Ge-laser have recently been demonstrated on a silicon platform [10–15]. However, a 3dB on-chip optical amplifier that fulfills the requirements described above remains a big challenge for the implementation of electronic-photonic integrated circuits.

Whereas III-V semiconductors such as InGaAsP are excellent light emitters that can provide a high gain around 1.5μm within a short distance, semiconductor optical amplifiers (SOAs) suffer from a number of issues that makes their use in a microphotonic

circuit problematic. Firstly, the short carrier lifetime in a SOA of about 100 ps to 1 ns, is of the order of the bit period in a 1 to 10Gb/s modulated signal. This leads the gain to be modulated by the bit pattern of the input signal and signals in other channels. This process, called cross-gain modulation (XGM) causes crosstalk in amplified WDM signals [16]. This limits the operation of a SOA to its linear regime, which in turn limits the output power. Due to the ms-lifetime in Er^{3+}, this problem does not occur in amplifiers based on erbium (so called *erbium-doped waveguide amplifiers* or EDWAs). Figure 1-5 shows that in EDWAs the gain modulation is negligible at frequencies larger than 10kHz, which makes WDM operation feasible at high powers.

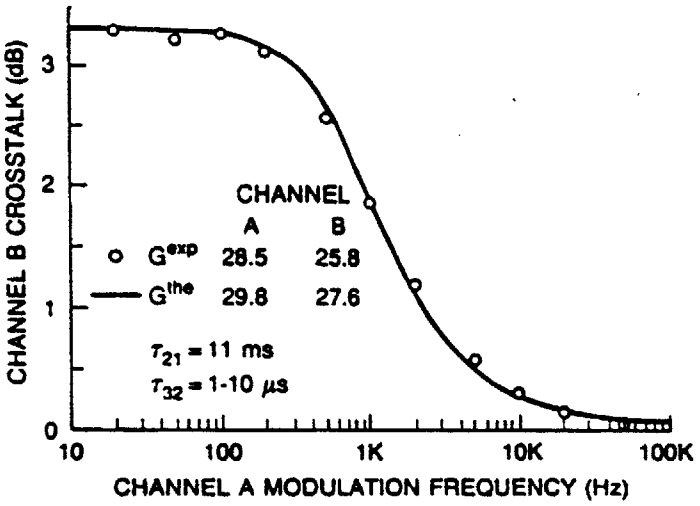

Figure 1-5: Peak-to-peak gain modulation (i.e. crosstalk) in a probe channel B as a function of the frequency of a saturated signal in channel A in an EDFA. The crosstalk disappears at frequencies higher than 10kHz. From [17,18].

Secondly, the short radiative lifetime in SOAs creates noise through amplified spontaneous emission. The rate of spontaneous emission is inversely proportional to the radiative lifetime, and this spontaneous emission is amplified just like the signal. The noise figure in EDWAs can therefore be several dB lower than in SOAs [19,20].

In this thesis, we investigate novel materials for the development of a compact high-gain, low-threshold, erbium-based integrated optical amplifier for intra-chip or inter-chip optical communications.

1.2 Thesis outline

Chapter 2 introduces the background and theory used in Chapters 4 through 7, explaining the source of 1.54μm luminescence in Er^{3+} and the interactions between Er^{3+} and Yb^{3+} ions. An overview is given of the material properties required for EDWAs. The chapter ends with a review of the literature on traditional hosts for erbium in EDWAs.

Chapter 3 gives an overview of the experimental methods used in this thesis, including RF magnetron sputter deposition, X-ray diffractometry and photoluminescence measurements.

The structural and luminescence properties of erbium-ytterbium oxides ($Er_xYb_{2-x}O_3$) and erbium-ytterbium disilicates ($Er_xYb_{2-x}Si_2O_7$) are studied in Chapter 4 and Chapter 5, respectively.

Chapter 6 discusses the possibility of energy transfer from silicon to ytterbium as a pathway to electrical excitation of erbium.

In Chapter 7, we engineer an erbium-ytterbium-yttrium silicate gain medium for optimal gain, using a rate equation model with the parameters obtained in Chapters 4 and 5.

Chapter 2

Background and Theory

2.1 Rare earths

This thesis investigates light emission at $\lambda = 1.54$ μm from oxides and silicates of the rare earth elements erbium (Er), ytterbium (Yb) and yttrium (Y). The term *rare earths* refers to the 15 lanthanide elements - lanthanum (La) through lutetium (Lu) in the periodic table - plus the transition metals yttrium and scandium (Sc), which are often grouped together because of their chemical similarity. In fact, because of this chemical similarity, pure rare earth minerals do not occur in nature but are always found containing a mixture of different rare earth ions.

The chemical similarities of the rare earth (RE) elements are due to the fact that their ions are found in the same oxidation states and have similar ionic radii. The normal valence of rare earth ions is 3^+, although 2^+ and 4^+ ions are also known [21]. The lanthanide ionic radius for sixfold coordination decreases gradually from 1.06Å for La^{3+} to 0.88Å for Lu^{3+}. This effect, known as the *lanthanide contraction*, is due to poor shielding by the $4f$ electrons of the nuclear charge.

Table 2.1 shows the ionic radii for sixfold coordination for Y^{3+}, Er^{3+} and Yb^{3+} and the melting point and refractive index of their oxides RE_2O_3 and silicates RE_2SiO_5 and $RE_2Si_2O_7$. The refractive index n_p for the silicates is the index along the principal

optical axis; the silicates are birefringent with Δn between 0.010 and 0.030. It is clear that the chemical properties of the compounds with different rare earths are very similar. In this work, we have fabricated and investigated erbium-ytterbium oxides and silicates and we have modeled erbium-ytterbium-yttrium silicates.

Table 2.1: Ionic radii (IR) for Y^{3+}, Er^{3+} and Yb^{3+} with sixfold coordination [22] and melting point T_m and refractive index of their compounds. Z = atomic number, n_{1550} = RE_2O_3 index at λ = 1550nm, n_p = index along the principal optical axis for silicates. RE_2SiO_5 and $RE_2Si_2O_7$ data from [23], † from [24], ‡ from [25].

RE	Z	IR(Å)	RE_2O_3		RE_2SiO_5		$RE_2Si_2O_7$	
			T_m(°C)	n_{1550}	T_m(°C)	n_p	T_m(°C)	n_p
Y^{3+}	39	0.900	2425	1.893†	1980	1.807	1775	1.737
Er^{3+}	68	0.890	2344	1.923‡	1980	1.807	1800	1.740
Yb^{3+}	70	0.868	2355	1.910‡	1950	1.807	1850	1.740

Despite their chemical similarities, the light emission properties of the different rare earth ions can be very different. This is due to electronic transitions between the $4f$ orbitals in the lanthanide elements, which happen to lie in the UV, visible and infrared wavelength range. Since the $4f$ electrons are shielded from their environment by the $5s^2$ and $5p^6$ electrons, they do not contribute significantly to chemical bonds and the electronic transitions between them are largely independent of their host [26].

The electron configurations of Er, Yb and Y and their 3^+ ions are

$$\begin{aligned} \mathrm{Er} = [\mathrm{Xe}]4f^{12}6s^2 &\Rightarrow \mathrm{Er}^{3+} = [\mathrm{Xe}]4f^{11} \\ \mathrm{Yb} = [\mathrm{Xe}]4f^{14}6s^2 &\Rightarrow \mathrm{Yb}^{3+} = [\mathrm{Xe}]4f^{13} \\ \mathrm{Y} = [\mathrm{Kr}]4d^{1}5s^2 &\Rightarrow \mathrm{Y}^{3+} = [\mathrm{Kr}] \end{aligned} \tag{2.1}$$

The $4f$ electronic transitions in erbium and ytterbium will be discussed in the following sections. Yttrium, on the other hand, has no $4f$ electrons and therefore no corresponding electronic transitions. This makes yttrium a very interesting rare earth metal, since it can chemically substitute Er and Yb but it has no energy levels in the visible or infrared wavelength range. In other words, it is a pure dilutant.

2.2 Rare earth oxide and silicate phases

The erbium-ytterbium oxide ($Er_xYb_{2-x}O_3$) alloy system is the first compound that will be investigated in this research. The oxides have the cubic crystal structure known from yttria (Y_2O_3), which has been studied extensively as a laser medium doped with Yb^{3+} for lasers emitting around 1μm. The $Er_xYb_{2-x}O_3$ alloy system will be discussed in Chapter 4.

Co-deposition of rare earth oxides with SiO_2 gives rare earth silicates. Figure 2-1 shows the phase diagram of Yb_2O_3 and SiO_2. Three different compounds are distinguished: monosilicates $RE_2O_3 \cdot SiO_2$, disilicates $RE_2O_3 \cdot 2SiO_2$ and oxyapatites with intermediate composition $7RE_2O_3 \cdot 9SiO_2$.

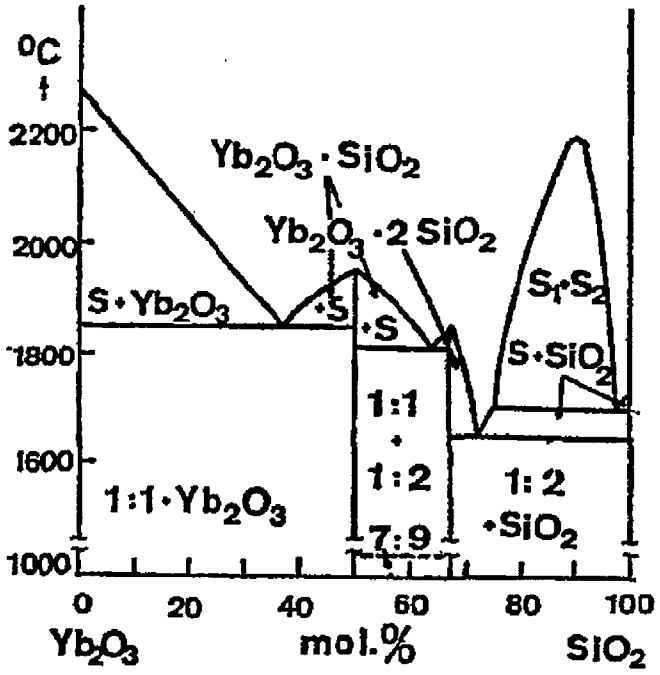

Figure 2-1: Phase diagram of Yb_2O_3 and SiO_2, adopted from [27].

The silicates are highly polymorphic. In his 1973 review *The Crystal Chemistry of the Rare-Earth Silicates* [21], J. Felsche describes two RE_2SiO_5 polymorphs, called A- or X1-type (monoclinic symmetry, space group $P2_1/c$) and B or X2-type (monoclinic symmetry, space group B2/b). According to Felsche, only the X2-type monosilicate

is stable for the smaller rare earth ions including Er, Yb and Y. However, more recently the stability of the X1-phase has been demonstrated as a low-temperature (T < 1050°C) phase for all rare earths including Er, Yb and Y [28].

As for the disilicates, Felsche describes seven $RE_2Si_2O_7$ polymorphs, four of which (the α, β, γ and δ-phases) are stable in the Yb^{3+}-Er^{3+}-Y^{3+} ionic radius range [21]. The transition temperatures between the different phases for $Y_2Si_2O_7$ are [29]

$$\alpha\text{-}Y_2Si_2O_7 \xrightarrow{1225\ ^\circ C} \beta\text{-}Y_2Si_2O_7 \xrightarrow{1445\ ^\circ C} \gamma\text{-}Y_2Si_2O_7 \xrightarrow{1535\ ^\circ C} \delta\text{-}Y_2Si_2O_7 \qquad (2.2)$$

Because of the smaller ionic radii of Yb and Er, the $\alpha \rightarrow \beta$ transition temperature is expected to be lower and the $\beta \rightarrow \gamma$ and $\gamma \rightarrow \delta$ transition temperatures to be higher than for Y. In other words, at least for bulk disilicates, only the α and β disilicates are stable in the temperature range studied in this thesis (T < 1200°C).

Additionally, one more low-temperature y-$Y_2Si_2O_7$ phase is known (not to be confused with γ-$Y_2Si_2O_7$), which has the same temperature stability range as the α-phase but slower crystallization kinetics [30]- [32]. More recent research on $Y_2Si_2O_7$ has revealed further disilicate polymorphs, such as ζ-$Y_2Si_2O_7$ [33] and η-$Y_2Si_2O_7$ [34].

The relevant silicate phases will be discussed in Chapters 4 and 5.

2.3 Luminescence from erbium

The luminescence from rare earth ions is a result of electronic transitions between their incompletely filled $4f$ energy levels [35]. Figure 2-2 shows the Er^{3+} energy levels, as determined by the subsequent effect of spin-orbit coupling of the $4f$ electrons and of the Stark effect in the external crystal field. Photon emission at 1.54 µm comes from the transition between the first excited state $^4I_{13/2}$ and the ground level $^4I_{15/2}$.

In a free ion, the intra-$4f$ transitions in erbium are partly forbidden by parity selection rules. However, in a low symmetry crystal site the degeneracy of the atomic levels is

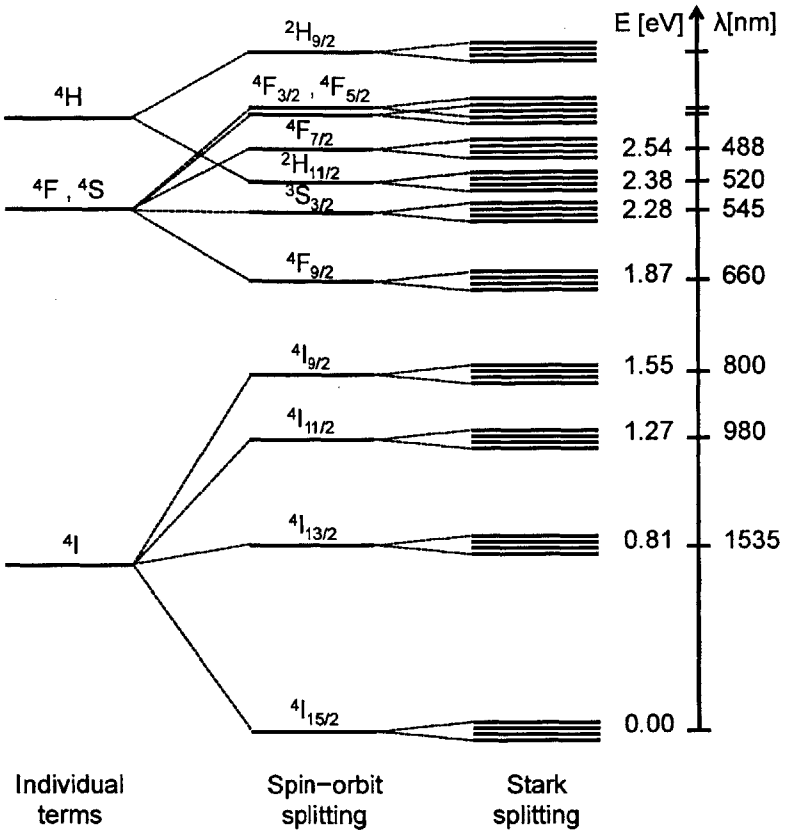

Figure 2-2: Er^{3+} energy level diagram after subsequent spin-orbit and Stark splitting. The energy levels are shown with their Russell-Saunders notation $^{2S+1}L_J$, where S is the total spin of the ion, L is the total orbital angular momentum and J is the total angular momentum. The letters F, H and I stand for $L = 3$, 5 and 6, respectively. After [26].

lifted due to Stark splitting in the crystal field of the host material. In the case of cubic symmetry, the $^4I_{15/2}$ ground state is split into five different levels, whereas in lower symmetry environments the ground state is split into eight sublevels [26]. The Stark effect mixes odd- and even-parity wavefunctions and relaxes the parity selection rules. The $^4I_{13/2} \rightarrow {}^4I_{15/2}$ transition then becomes partly allowed, albeit with very low absorption and emission cross sections (see Table 2.2).

Because of the shielding of the $4f$ orbitals from their environment by the larger $5s$ and $5p$ orbitals, the Stark splitting due to the external crystal field is much weaker than the spin-orbit coupling. It generates a series of energy levels close to the original spin-orbit level, causing a broad room temperature luminescence spectrum around

$\lambda = 1.54$ µm which is relatively independent of the ion's host material. Table 2.2 shows indeed that both the peak emission wavelength λ_{peak} and the absorption and emission cross sections for Er^{3+} around $\lambda = 1.54$µm are very similar in a wide variety of materials.

Table 2.2: Er^{3+} absorption and emission cross sections around $\lambda = 1.54$µm, adopted from [36].

Host material	structure	λ_{peak} (nm)	σ_{abs} (10^{-21}cm^2)	σ_{em} (10^{-21}cm^2)	ref.
Al-P co-doped silica	amorphous	1531	6.60	5.70	[37]
Silicate (L22) glass	amorphous	1536	5.80	7.27	[37]
Fluorophosphate glass	amorphous	1533	6.99	7.16	[37]
Germanosilicate glass	amorphous	1530	7.9 ± 0.3	6.7 ± 0.3	[38]
Aluminosilicate glass	amorphous	1530	7.9 ± 0.3	7.9 ± 0.3	[38]
Phosphate glass	amorphous	1535	5.4		[39]
Al_2O_3	amorphous	1532	5.7 ± 0.7	5.7	[40]
Y_2O_3	polycrystalline	1536	5.5	5.5	[41]
$LiNbO_3$	monocrystalline	1534.6	24.4	24.4	[42]
Y_2O_3	monocrystalline	1535.5	18	18	[43]

2.4 Material requirements for EDWAs

A practical optical amplifier needs to provide a high gain at a low pump power and within a small areal footprint. Additionally, the amplifier should have a low noise figure (NF), which is defined as the degradation of signal-to-noise ratio (SNR) due to amplified spontaneous emission (ASE) in the amplifier:

$$\mathrm{NF} = 10 \log \left(\frac{\mathrm{SNR}_i}{\mathrm{SNR}_o} \right) = \mathrm{SNR}_{\mathrm{i,dB}} - \mathrm{SNR}_{\mathrm{o,dB}} \tag{2.3}$$

We can now define an amplifier figure of merit

$$\mathrm{FOM} = \frac{\text{gain efficiency}}{\text{device footprint} \cdot \text{noise figure}} = \frac{\gamma_{\mathrm{eff}}\ [\mathrm{dB/mW}]}{A\ [\mathrm{cm^2}] \cdot \mathrm{NF}\ [\mathrm{dB}]} \tag{2.4}$$

An optimization of this figure of merit requires the following material properties:

1. high Er^{3+} concentration without erbium precipitation
2. low upconversion and energy migration
3. high Er^{3+} excitation cross section (through sensitization)
4. long lifetime of Er^{3+} first excited state
5. high maximum phonon energy
6. high refractive index

These different material requirements are discussed in sections 2.4.1 through 2.4.6 below.

2.4.1 High Er^{3+} concentration without precipitation

In materials such as Si, SiO_2 or Si_3N_4, where Er^{3+} is a dopant, limited erbium solubility leads to precipitation of erbium clusters at high erbium concentrations. These clustered erbium ions are not optically active and cannot contribute to luminescence or gain.

Figure 2-3 shows the photoluminescence (PL) intensity and lifetime for Er-implanted SiO_2 as a function of annealing temperature. For annealing temperatures up to 700°C the PL lifetime and intensity increase together, consistent with repair of irradiation damage [44]. The concurrent increase in PL intensity and lifetime is consistent with an increase in quantum efficiency $\eta = \tau/\tau_{\text{rad}}$, since the PL intensity is given by

$$I_{\text{PL}} \propto [\text{Er}_{\text{act}}]\frac{\tau}{\tau_{\text{rad}}} \tag{2.5}$$

where τ is the total (measured) erbium lifetime and τ_{rad} is the radiative lifetime.

At temperatures higher than 1050°C however, erbium clustering due to Ostwald ripening causes a drop in PL intensity while the PL lifetime stays constant [45]. This is

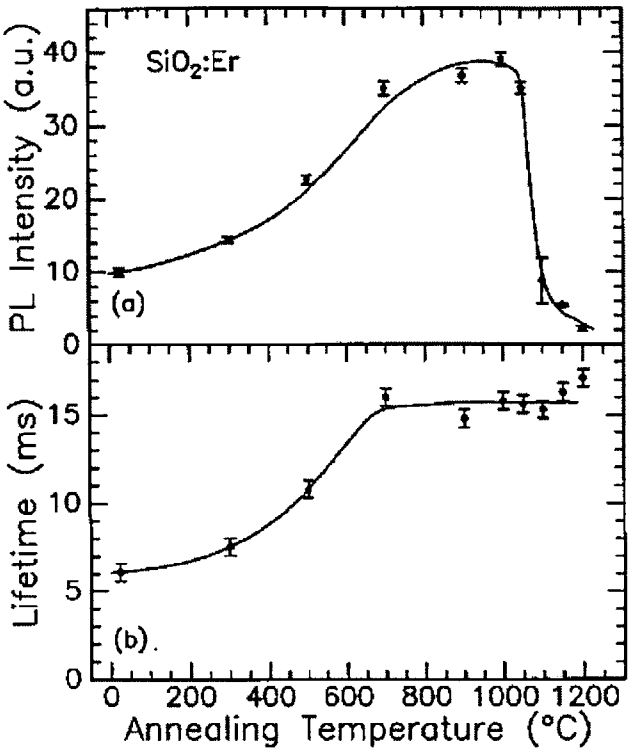

Figure 2-3: Decrease of optically active erbium concentration due to precipitation at annealing T > 1050°C in Er-implanted SiO_2 causes the PL intensity to drop dramatically while the lifetime stays constant. Implanted [Er] = 0.1 at.%, corresponding to $\sim 8 \times 10^{19}$ cm^{-3}. Figure from [44].

consistent with a decrease in optically active erbium concentration in Equation 2.5. The lifetime is not affected since it comes from the optically active erbium only.

2.4.2 Concentration quenching in erbium compounds

In erbium oxides and silicates, clustering of Er^{3+} ions is prevented due to their rigid position in the crystal lattice [46]. But even without clustering, different concentration quenching effects limit the maximum erbium concentration. The two major processes, cooperative upconversion and energy migration, are depicted in Figure 2-4.

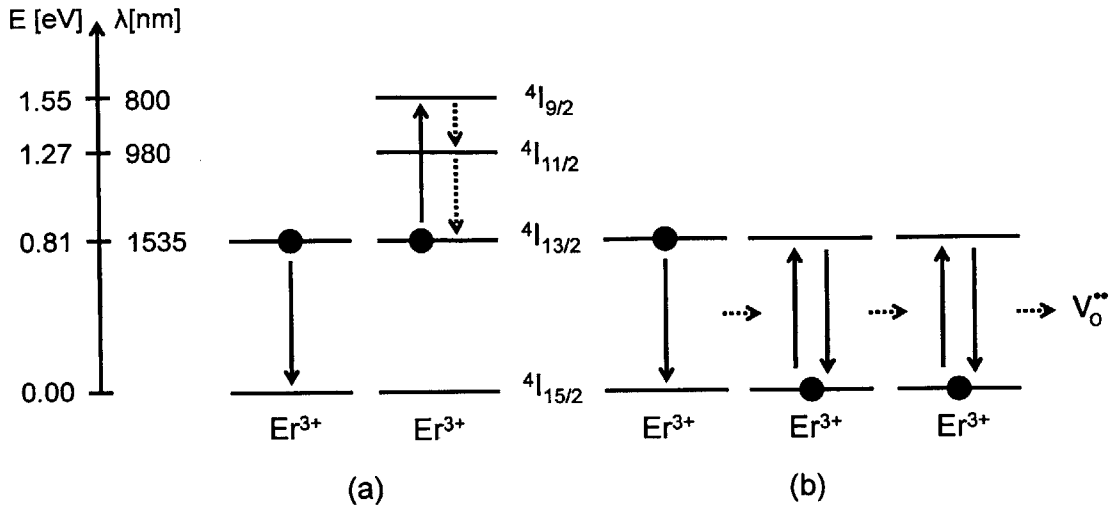

Figure 2-4: Two concentration quenching effects at high erbium concentrations: (a) cooperative upconversion, (b) energy migration (to an oxygen vacancy).

Energy migration

In the process of *energy migration*, energy migrates between Er^{3+} ions whereby one excited ion transfers its energy to another ion in the ground state. This energy transfer by itself does not alter the populations of the erbium levels, since the net loss of excitation is zero. However, when the excitation migrates to a quenching center, the excitation is lost. Common quenching centers are hydroxyl (OH^-) groups (the second harmonic of the OH^--stretch mode is resonant with the 1.5μm transition), oxygen vacancies or grain boundary sites [47].

The rate W_{em} for energy migration is proportional to the concentration N_q of quenching centers and the concentration of Er^{3+} ions in the ground state [48]. We get

$$W_{\text{em}} = 8\pi C_{\text{em}} N_{\text{Er}} N_q = C'_{\text{em}} N_{\text{Er}} \tag{2.6}$$

with the energy migration coefficients C_{em} in $\text{cm}^6.\text{s}^{-1}$ and C'_{em} in $\text{cm}^3.\text{s}^{-1}$. In the rate equation for the first excited state, this becomes

$$\left.\frac{dN_1}{dt}\right|_{\text{em}} = -C'_{\text{em}} N_{\text{Er}} N_1 \tag{2.7}$$

which leads to a single exponential decay since there this term is directly proportional to the population of the first excited state N_1.

Cooperative upconversion

During *cooperative upconversion*, two Er ions in the first excited state $^4I_{13/2}$ combine their excitation energy instead of both emitting a photon at 1.54µm. One ion transfers its energy to the other one and excites it to the $^4I_{9/2}$ level:

$$2\ {}^4I_{13/2} \rightarrow {}^4I_{9/2} + {}^4I_{15/2} \tag{2.8}$$

The Er ion in the $^4I_{9/2}$ state is likely to decay back non-radiatively to the $^4I_{13/2}$ level via the $^4I_{11/2}$ level, since the rates for both decays are very fast ($> 10^5 s^{-1}$, [49])

$${}^4I_{9/2} \rightsquigarrow {}^4I_{11/2} \rightsquigarrow {}^4I_{13/2} \tag{2.9}$$

Alternatively, the decay to the ground state can happen radiatively by emission of a 800nm photon. In either case, the net effect is the loss of one excitation.

In the rate equation for the first excited state $^4I_{13/2}$, the net loss of one excitation due to upconversion adds a term equal to $-C_{up}N_1^2$, where C_{up} is the upconversion coefficient (in $cm^3.s^{-1}$)

$$\left.\frac{dN_1}{dt}\right|_{up} = -C_{up}N_1^2 \tag{2.10}$$

Because the rate of upconversion is proportional to the square of the population N_1, upconversion will cause a PL decay that is not a single exponential function.

Upconversion coefficient

Since the energy transfer between erbium ions involved in upconversion and energy migration is a dipole-dipole interaction and the interaction strength of dipole-dipole interactions scales as $1/d^6$ with the distance d between ions, both the upconversion

coefficient C_{up} and the energy migration coefficients C_{em} and C'_{em} depend strongly on erbium concentration.

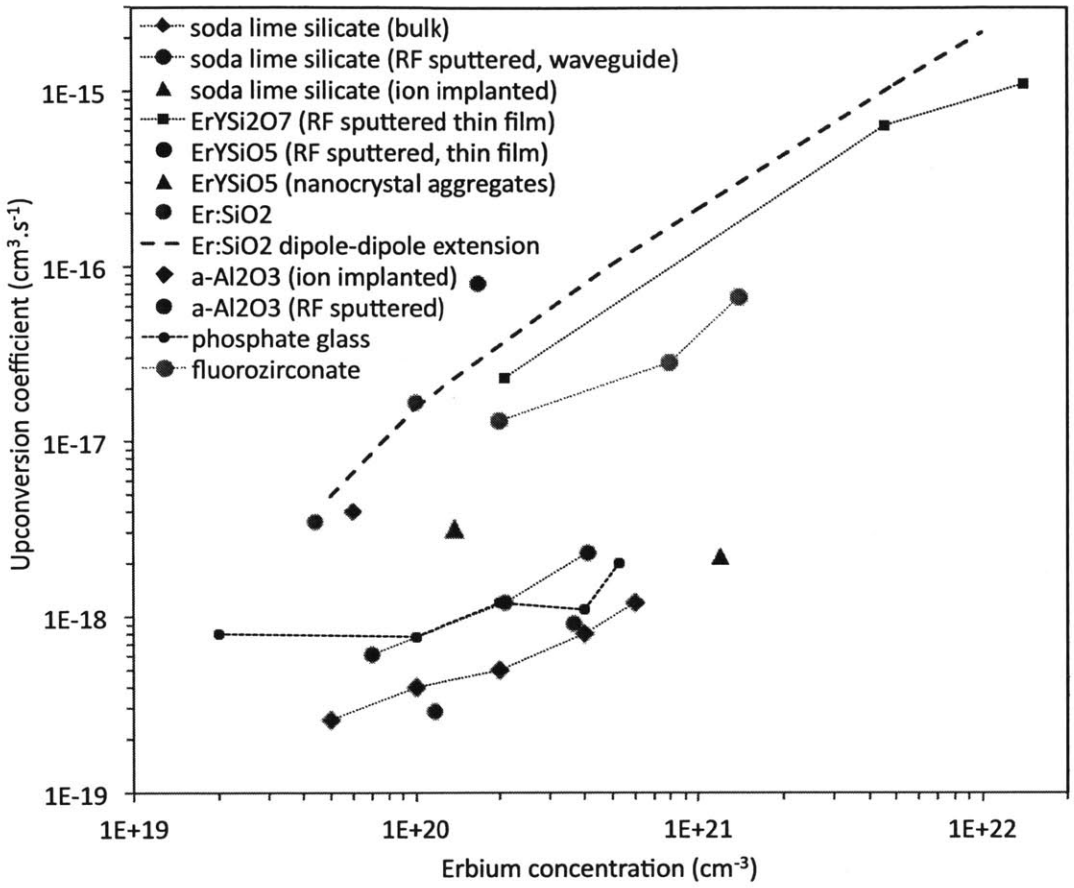

Figure 2-5: Upconversion coefficient as a function of erbium concentration for different host materials and fabrication technologies. Data from [50, 51] (soda lime silicate), [52–54] ($Er_xY_{2-x}SiO_5$ and $Er_xY_{2-x}Si_2O_7$), [55–58] ($Er:SiO_2$ + extension), [59,60] ($a\text{-}Al_2O_3$), [39,61–63] (phosphate glass), [64] (fluorozirconate)

Figure 2-5 shows the upconversion coefficient C_{up} as a function of erbium concentration in different host materials. As expected, for a given materials system and method of fabrication, the upconversion coefficient increases monotonically with erbium concentration. Two other aspects of this figure are striking:

(i) for a given erbium concentration, the upconversion coefficient can differ by several orders of magnitude between different materials systems. The best properties are found for phosphate and soda-lime silicate glass. Indeed, Table 2.6 shows that for

these materials a very large gain per unit length has been demonstrated. This variation of upconversion coefficient among different materials systems is due to a variation in the nearest-neighbor Er^{3+} spacing, the oscillator strengths and the spectral overlap of the transitions involved [36].

(ii) even within a certain materials system, the upconversion coefficient is strongly dependent on the fabrication technology. The large variation of the upconversion coefficient within the same material but for different fabrication methods can be explained by the homogeneity of the Er^{3+} distribution in the host, which can depend on the fabrication process.

For example, RF-sputtered soda-lime silicate thin films exhibit an upconversion coefficient that is 2.4 times higher than in bulk soda-lime silicate glasses. The upconversion coefficient of Er^{3+}-implanted soda-lime silicate is yet another 3 times larger, indicating a higher level of clustering and a less homogeneous distribution of Er^{3+} in ion-implanted thin films than in RF sputtered films. The same effect is seen when comparing ion-implanted and RF sputtered Er:Al_2O_3.

Lastly, it is interesting to note the close correspondence between upconversion coefficients measured for erbium-yttrium disilicates $Er_xY_{2-x}Si_2O_7$ [52] and an extension of Er:SiO_2 data calculated by assuming a dipole-dipole interaction model for upconversion. According to Federighi and Di Pasquale [55,57], the upconversion coefficient can then be expressed as a linear function of erbium concentration

$$C_{\text{up}} = \frac{4\pi}{3}\frac{d_0^6}{d_{\text{Er-Er}}^3\tau} \propto N_{\text{Er}} \tag{2.11}$$

where d_0 is a critical distance and τ is the lifetime of the Er^{3+} first excited state.

Using this linear extension of the Er:SiO_2 data reported by Federighi [55], we see a close match to the $Er_xY_{2-x}Si_2O_7$ data. In other words, in terms of upconversion, erbium-yttrium silicates can be regarded as Er:SiO_2 where clustering is prevented and the upconversion coefficient increases linearly with erbium concentration according to the well-understood dipole-dipole model.

PL saturation at high pump flux Φ

Now that we understand the dynamics of upconversion and energy migration, the relationship of PL intensity vs. excitation pump flux Φ can easily be derived using a simple two-level model for erbium where we only consider the ground level $^4I_{15/2}$ and the first excited level $^4I_{13/2}$ at 1550nm. In the rate equation for the first excited state we consider 3 processes:

1. **Pump absorption:** the rate of absorption of pump photons is $\sigma\Phi$, where σ is the absorption cross section (in cm^2) and Φ is the pump photon flux (in $cm^{-2}.s^{-1}$).

2. **Single exponential decay** with rate $1/\tau$. For the sake of simplicity of notation we can lump all the different processes that cause a single exponential decay in one single term with an overall lifetime τ. These processes include spontaneous radiative emission, non-radiative decay through phonon emission and energy migration.

3. **Upconversion** as discussed above, the rate of upconversion equals $-C_{up}N_1^2$.

With $N_1 = N_{Er} - N_0$, the rate equation for the first excited level then becomes

$$\frac{dN_1}{dt} = \sigma\Phi\left(N_{Er} - N_1\right) - \frac{N_1}{\tau_0} - C'_{em}N_{Er}N_1 - C_{up}N_1^2 \tag{2.12}$$

with $1/\tau = 1/\tau_0 + C'_{em}N_{Er}$, we can rewrite this as

$$\frac{dN_1}{dt} = \sigma\Phi\left(N_{Er} - N_1\right) - \frac{N_1}{\tau} - C_{up}N_1^2 \tag{2.13}$$

In steady state ($dN_1/dt = 0$), solving the quadratic equation on the right hand side gives

$$N_1 = \frac{-1 - \sigma\Phi\tau + \sqrt{1 + 2\sigma\Phi\tau + 4C_{up}\tau^2\sigma\Phi N_{Er} + \sigma^2\Phi^2\tau^2}}{2C_{up}\tau} \tag{2.14}$$

Linear regime at low Φ: At low flux densities, the above expression for N_1 can be simplified using the taylor expansion $\sqrt{1+a\Phi} \approx 1 + a\Phi/2 + \mathcal{O}(\Phi^2)$

$$N_1 = \frac{-1 - \sigma\Phi\tau + 1 + \sigma\Phi\tau + 2C_{\text{up}}\tau^2\sigma\Phi N_{\text{Er}}}{2C_{\text{up}}\tau} = \sigma\Phi\tau N_{\text{Er}} \tag{2.15}$$

We see that at low pump flux Φ there is a *linear regime* where the PL intensity varies linearly with pump flux. At higher fluxes, the signal will saturate due to upconversion. The PL intensity is now proportional to the population of the first excited state N_1 and we can write

$$I_{\text{PL}}(\Phi) = \frac{N_1}{\tau_{\text{rad}}} \propto \sigma\Phi\tau N_{\text{Er}} \tag{2.16}$$

assuming τ_{rad} is constant. Given that τ_{rad} is proportional to the square of the refractive index [65] and that the refractive index is constant throughout the entire concentration range of erbium-ytterbium oxides and silicates (see Table 2.1), this is a safe assumption.

2.4.3 Erbium and ytterbium

Just like yttrium, ytterbium can play the role of dilutant and substitute erbium ions in the lattice. However, ytterbium can also increase the effective excitation cross-section for erbium at 980nm optical excitation. As shown in Table 2.3, the optical absorption cross section of Yb^{3+} at 980nm is about an order of magnitude higher than that for Er^{3+} ions. Furthermore, the $^2F_{5/2} \rightarrow {}^2F_{7/2}$ transition in Yb^{3+} is resonant with the $^4I_{11/2} \rightarrow {}^4I_{15/2}$ transition in Er^{3+}. Therefore, upon 980nm pumping, Yb^{3+} can act as a sensitizer for Er^{3+}. This process is shown in Figure 2-6.

The rate of energy transfer W_{tr} between Yb^{3+} and Er^{3+} can be described by an expression similar to expression 2.6 for the energy transfer to a quenching center

$$W_{\text{tr}} = 8\pi C_{\text{tr}} N_{\text{Yb}} N_{\text{Er}} = C'_{\text{tr}} N_{\text{Er}} \tag{2.17}$$

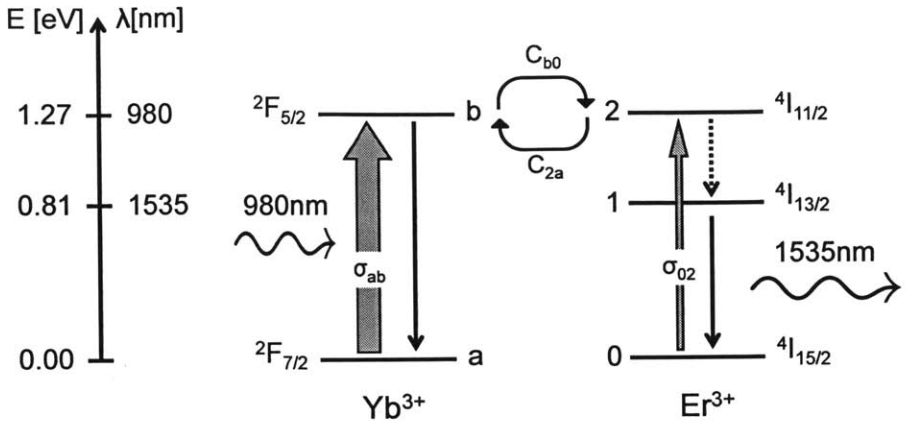

Figure 2-6: Atomic energy levels of Er^{3+} and Yb^{3+} in the Russells-Saunders notation. The $^2F_{5/2} \rightarrow {}^2F_{7/2}$ transition in Yb^{3+} is resonant with the $^4I_{11/2} \rightarrow {}^4I_{15/2}$ transition in Er^{3+}. After [40].

Table 2.3: Er^{3+} and Yb^{3+} absorption and emission cross sections at $\lambda = 980$nm.

Host	Ion	λ (nm)	σ_{abs} (10^{-21}cm^2)	σ_{em} (10^{-21}cm^2)	ref.
Al_2O_3	Er^{3+}	980.5	1.7 ± 0.7		[40]
Al_2O_3	Yb^{3+}	974.5	11.7 ± 0.7	11.6	[40]
phosphate glass	Er^{3+}	977	1.9		[66]
phosphate glass	Yb^{3+}	974	12.8 ± 2.6	12.7 ± 2.6	[66]
phosphate glass	Yb^{3+}	977	10.4	11.9	[66]
phosphate glass	Er^{3+}	980	2.2		[39]

In the rate equation this becomes

$$\left.\frac{dN_b}{dt}\right|_{\text{tr}} = -C'_{\text{tr}} N_{\text{Er}} N_b \tag{2.18}$$

Analogously, backtransfer from Er^{3+} to Yb^{3+} can be described as

$$\left.\frac{dN_2}{dt}\right|_{\text{btr}} = -C'_{\text{btr}} N_{\text{Yb}} N_2 \tag{2.19}$$

However, backtransfer can typically be neglected because of the fast transition from the $^4I_{11/2}$ to the $^4I_{13/2}$ energy levels in erbium, which causes the population of the $^4I_{11/2}$ level to be very small [67].

In the absence of backtransfer, the rate equations for the levels N_b and N_2 are

$$\frac{dN_b}{dt} = \sigma_{ab}\Phi_p N_{\mathrm{Yb}} - C_T N_b N_{\mathrm{Er}} - W_b N_b \tag{2.20}$$

$$\frac{dN_2}{dt} = \sigma_{02}\Phi_p N_{\mathrm{Er}} + C_T N_b N_{\mathrm{Er}} - W_2 N_2 \tag{2.21}$$

In steady state ($dN_b/dt = 0$) it follows from equation 2.20 that

$$N_b = \frac{\sigma_{ab}\Phi_p N_{\mathrm{Yb}}}{W_b + C_T N_{\mathrm{Er}}} \tag{2.22}$$

And therefore

$$\frac{dN_2}{dt} = \left(\sigma_{02} + \frac{C_T N_{\mathrm{Yb}}}{W_b + C_T N_{\mathrm{Er}}}\sigma_{ab}\right)\Phi_p N_{\mathrm{Er}} \tag{2.23}$$

It follows that because of energy transfer from Yb^{3+} to Er^{3+} the effective excitation cross-section of erbium at 980nm will become

$$\sigma'_{02} = \sigma_{02} + \frac{C_T N_{\mathrm{Yb}}}{W_b + C_T N_{\mathrm{Er}}}\sigma_{ab} \tag{2.24}$$

2.4.4 Long lifetime of the Er^{3+} first excited state $^4I_{13/2}$

A long lifetime of the Er^{3+} first excited state $^4I_{13/2}$ has two beneficial effects on amplifier performance. First, a longer first excited state lifetime increases the population of the first excited state and therefore the gain coefficient $\gamma = \sigma(N_1 - N_0)$ for a given pump power. Second, spontaneous emission from Er^{3+} around $\lambda = 1.5\mu m$ is amplified just like the signal, creating a noise background around $\lambda = 1.5\mu m$ at the EDWA output. A longer radiative lifetime is equivalent to a lower rate of spontaneous emission and therefore a better EDWA noise figure.

Table 2.4 shows the radiative lifetime of the Er^{3+} first excited state $^4I_{13/2}$ in different materials. The lifetime of 14.7ms in silicate glasses is seen to be the longest of all the common erbium hosts, and is twice as long as in rare earth oxides (7.2ms).

Table 2.4: $^4I_{13/2}$ lifetimes in different host materials, data from [49,68–70]

Host material	$^4I_{13/2}$ lifetime (ms)
Phosphate glass	10.7
Silicate glass	14.7
a-Al_2O_3	7.8
Tellurite glass	4.0
Fluoride glass	10.3
Y_2O_3	7.2

2.4.5 High phonon energy

While a long radiative lifetime is desired for the first Er^{3+} excited state, the lifetime of the higher lying levels should be as short as possible, since any build-up of population of these levels will be at the expense of the population of the first excited state. Therefore, it is important that these higher lying states decay to the first excited state as fast as possible. In the case of pumping at 980nm into the second Er^{3+} excited state, and especially when using Yb^{3+} as a sensitizer, a fast $^4I_{11/2} \rightarrow {}^4I_{13/2}$ transition rate W_{21} is of utmost importance. Indeed, the $^4I_{11/2} \rightarrow {}^4I_{13/2}$ transition competes with backtransfer from Er^{3+} to Yb^{3+} and with excited state absorption.

The decay from high lying levels in Er^{3+} to the first excited state happens non-radiatively through the emission by multiple phonons. P.C. Becker [49] showed that the transition rate for multiphonon decay decreases exponentially with the number of phonons needed for the transition. In other words, the decay rate increases exponentially with the phonon energy, since less phonons are required to bridge a certain energy difference. The maximum phonon energy in different hosts for Er^{3+} and the corresponding multiphonon decay rates for different energy gaps are shown in Figure 2-7. Silicate glasses have a large maximum phonon energy of 1100cm^{-1}, corresponding to a $^4I_{11/2} \rightarrow {}^4I_{13/2}$ ($\Delta E \sim 3500$ cm^{-1}) transition rate of $\sim 10^5$ s^{-1}. However, in rare earths oxides such as Y_2O_3, with a maximum phonon energy of ~400 cm^{-1}, the 980nm emission lifetime is as high as 2.5ms [69,70]. This suggests that rare earth

silicates are much better suited for pumping at 980nm and sensitization by Yb^{3+} than rare earth oxides.

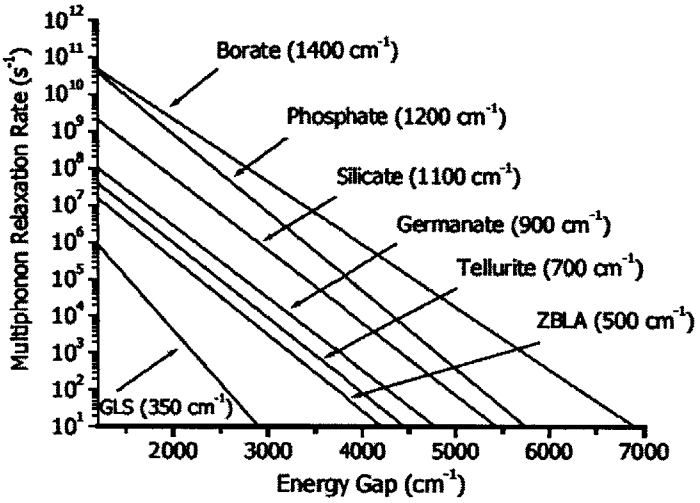

Figure 2-7: Non-radiative (multiphonon) decay of Er^{3+} levels in various hosts. The decay rate of the $^4I_{11/2}$ level at 980nm in silicate hosts is around $10^5 s^{-1}$. From [68]

2.4.6 High refractive index

A high refractive index contrast Δn between the waveguide core and its SiO_2 cladding reduces the waveguide cross section and thereby increases the photon flux at a given pump power. This, in turn, leads to a lower inversion threshold and a higher gain at a given pump power. Furthermore, it is expected that because of size constraints on an integrated chip, EDWAs will have to be arranged into a coil or serpentine structure rather than as a straight waveguide (see Figure 2-8). A high refractive index contrast reduces the radiative bending losses in waveguide bends, allowing sharper turn radii for a given propagation loss constraint and therefore enabling smaller device footprints.

The effect of the refractive index contrast Δn between amplifier core and cladding on the amplifier figure of merit defined in Equation 2.4 was quantified by Saini et al. [71]. The authors found that the gain efficiency γ_{eff} increases as $\Delta n^{1.2}$ in the

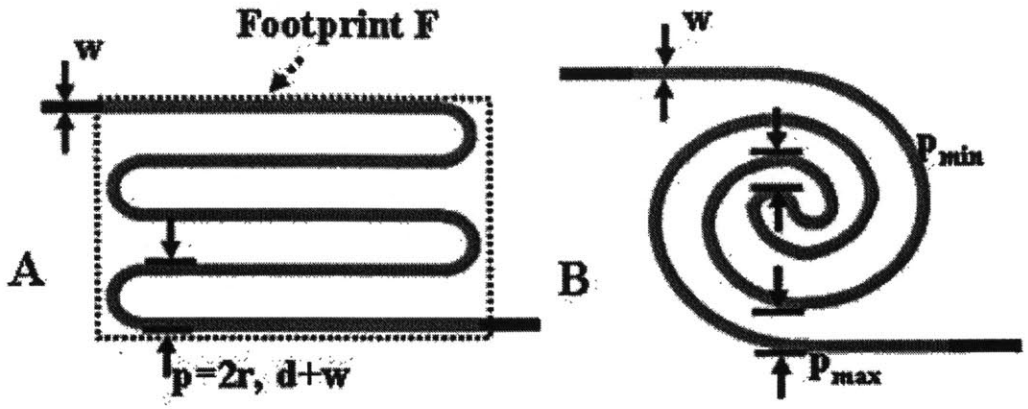

Figure 2-8: EDWA arranged in a (A) serpentine structure, minimizing areal extent with straight-line waveguide segments and a (B) coil structure, optimally packing a planar area with curved waveguides. From [71].

absence of upconversion and as $\Delta n^{0.93}$ with upconversion (see Figure 2-9). The device footprint is proportional to $1/\Delta n^{1.4}$, due to a reduction of waveguide width and turning radius for a fixed turning loss per unit length. The output signal-to-noise (SNR) is independent of Δn. As a result, we get FOM $\propto \Delta n^{2.6}$ in the absence of upconversion and FOM $\propto \Delta n^{2.33}$ with upconversion.

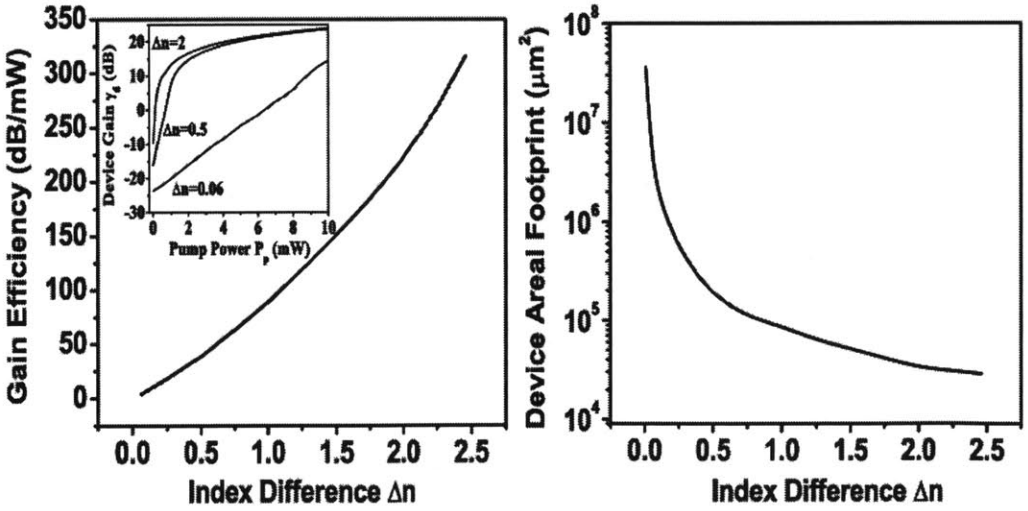

Figure 2-9: Effect of refractive index contrast Δn between amplifier core and cladding on gain efficiency (left) and device areal footprint for a serpentine EDWA design with total length of 1cm (right). From [71].

Table 2.5 shows the refractive index of several common EDWA materials found in literature and the indices for rare earth oxides and silicates measured by spectroscopic ellipsometry. It is clear that while phosphate glass and soda-lime silicate glass have excellent upconversion properties and can consequently provide a high gain per unit length, their very low refractive index is prohibitive in the creation of an actual EDWA. The rare earth oxides and silicates have a large index contrast between $0.26 \leq \Delta n \leq 0.47$.

Table 2.5: Refractive indices for common host materials for erbium. † indicates own measurement by spectroscopic ellipsometry.

Host material	Refractive index n	Refractive index difference Δn	Ref.
Phosphosilicate	1.46	0.01	[72]
Er/Yb silica	1.51	0.06	[73]
Soda-lime silicate glass	1.52	0.07	[74]
Phosphate glass	1.55	0.10	[39]
Aluminosilicate glass	1.61	0.16	[75]
Al_2O_3	1.65	0.20	[76]
$Er_xYb_{2-x}Si_2O_7$	1.71	0.26	†
$Er_xYb_{2-x}SiO_5$	1.80	0.35	†
$Er_xYb_{2-x}O_3$	1.92	0.47	†
Si_3N_4	1.98	0.53	[77]
Bi_2O_3	2.03	0.58	[78]
TeO_2	2.04	0.69	[79]
Si	3.47	2.02	[24]

2.5 Erbium-doped waveguide amplifiers

Since the invention of the erbium-doped fiber amplifier in 1987 by Desurvire et al. and Mears et al. [80,81] and its success in long-haul telecommunications, significant effort has gone into developing an efficient on-chip erbium-doped waveguide amplifier [36,47]. However, scaling down EDFAs from erbium-doped silica fibers that are meters long and contain very small amounts of Er^{3+} to microphotonic amplifiers that are over two orders of magnitude smaller brings about significant material and device design

challenges. Simply increasing the erbium concentration to get more gain per length is not an option, since parasitic effects such as erbium precipitation, upconversion and energy migration limit the gain at high erbium concentrations. It is clear that novel materials solutions need to be found to develop a useful EDWA.

2.5.1 Traditional erbium-doped materials

Maximizing Er^{3+} concentration and refractive index

Because of its low Er^{3+} solubility, silica itself is not a very good material for EDWAs. Precipitation of erbium at concentrations larger than 0.1 at.% limits the gain coefficient (see section 2.4.1). Furthermore, the refractive index difference between an Er:SiO_2 waveguide core and the SiO_2 cladding is so small that eventual EDWAs would be prohibitively large.

Erbium-doped silicon is an obvious candidate and has been extensively investigated in the 1990s [26, 82, 83]. Silicon has excellent optical properties: it is transparent at 1.54µm and it has a very high refractive index $n = 3.5$, which allows very compact devices operating at low pump powers (see section 2.4.6). Additionally, as a semiconductor, Si has the benefit that Er^{3+} ions can be excited electrically via energy transfer from electron-hole pairs. However, Er:Si suffers from strong temperature quenching of the luminescence at room temperature due to energy backtransfer from the excited Er^{3+} ions to the carriers in the silicon.

Several glasses have turned out to be excellent hosts for erbium. Soda-lime silicate (SiO_2-Na_2O-CaO) and phosphate (P_2O_5) glass are particularly succesful because of their high erbium solubility and low upconversion coefficients. For example, soda-lime silicate glass can accommodate up to 2 at.% erbium without precipitation while maintaining an upconversion coefficient as low as 2×10^{-18} $cm^3 \cdot s^{-1}$, compared to the 0.1% limit in silica. It is therefore not surprising that record gain coefficients were reported for soda-lime silicate [50, 51] and phosphate [39, 61–63] EDWAs (see Table 2.6).

Another useful host for erbium is Al_2O_3 [59, 67, 84–86], since it combines a high refractive index ($n = 1.65$) with a high Er^{3+} solubility due to the valence matching between Al^{3+} and Er^{3+}. This has enabled a gain coefficient of 0.58dB/cm for a 4-cm long spiral Er:Al_2O_3 waveguide at a pump power of only 9mW [87].

Increasing Er^{3+} excitation cross section through sensitization

Until now, we have compared different materials with respect to erbium solubility and refractive index. This approach relies on exciting Er^{3+} through optical pumping at a wavelength resonant with on one of the Er^{3+} ionic energy levels. An alternative strategy is to increase the *effective* excitation cross section of erbium ions through energy transfer from an intermediate (a so-called *sensitizer*) which has a large cross section for the absorption of pump photons and subsequently transfers the absorbed pump energy to Er^{3+} [88, 89].

An efficient sensitization mechanism at room temperature was achieved by doping nanocrystalline Si (nc-Si) with rare earth ions, thanks to the enlarged bandgap of silicon as a result of quantum confinement. Kenyon et al. and Fujii et al. [90]-[92] demonstrated room temperature PL around 1.54μm in erbium-doped nc-Si and Fujii et al. and Zhao et al. [93, 94] reported room temperature PL around 1.0μm in ytterbium-doped nc-Si. In both cases, the excitation occurs through recombination of photogenerated carriers spatially confined in nc-Si and the subsequent energy transfer to the rare earth ions. Recently, Yerci et al. showed electroluminescence in erbium-doped silicon-rich silicon nitride (Er:SiN_x) [95].

Silicon nanocrystals turn out to be excellent sensitizers for erbium luminescence. With a broad absorption spectrum in the visible wavelength range, they can increase the erbium excitation cross section by orders of magnitude [96]. However, just like other erbium-doped materials, the silicon nanocrystals suffer from a low rare earth solubility. The high excitation cross section may result in a very low-inversion-threshold and thus an energy efficient device, but the gain coefficient will still be limited by the total

erbium concentration. As a result, amplifiers would still have to be prohibitively long. Furthermore, free carriers in the silicon nanocrystals cause free carrier absorption of signal light, which introduces significant losses.

2.5.2 Erbium and erbium-yttrium compounds

Pure erbium oxides and silicates

A novel approach to overcoming the problem of low erbium solubility is to work with compounds where erbium is a constituent of the material rather than a dopant, such as erbium oxide (Er_2O_3) or erbium silicates (Er_2SiO_5 and $Er_2Si_2O_7$). Due to the fixed position of Er^{3+} ions in the (poly)crystalline lattice, these materials can accomodate over 1×10^{22} cm^{-3} optically active Er^{3+} ions without clustering [46,97].

The earliest reports on erbium compounds focused on Er_2O_3 [98,99], which can easily be deposited on Si or SiO_2 substrates by reactive sputtering of Er metal in an Ar/O_2 plasma [100] or by direct RF-sputtering of Er_2O_3 in Ar [101]. With a maximum erbium concentration of 40 at.% or 2.72×10^{22} cm^{-3}, Er_2O_3 could theoretically provide a gain coefficient of ~150dB/cm. In addition, erbium oxide has a very high refractive index of $n = 1.92$ (see Table 2.1), which allows the design of compact, low-pump energy devices. Broad (FWHW $\sim$ 45nm) room temperature photoluminescence (PL) was reported around 1535nm, and it was found that post-deposition annealing at 1200°C increases the luminescence intensity by almost two orders of magnitude compared to the as deposited films [102]. However, erbium oxides are known to suffer from film deterioration due to chemical reactions with the Si and SiO_2 substrates, resulting in erbium silicide or silicate formation [103].

More recently, research focus has shifted from erbium oxides to erbium silicates. Not only do the silicates exhibit lower chemical reactivity with the substrate, they also have a larger maximum phonon energy ($\sim$ 1200 cm^{-1}). High phonon energies cause fast non-radiative decay from higher excited Er^{3+} states to the first excited state, which increases the level of population inversion $N_1 - N_0$. As explained in section

2.4.5, high phonon energies are especially important for pumping at λ = 980nm, where a fast decay from the level at 980nm to the first excited state at 1.54μm is essential.

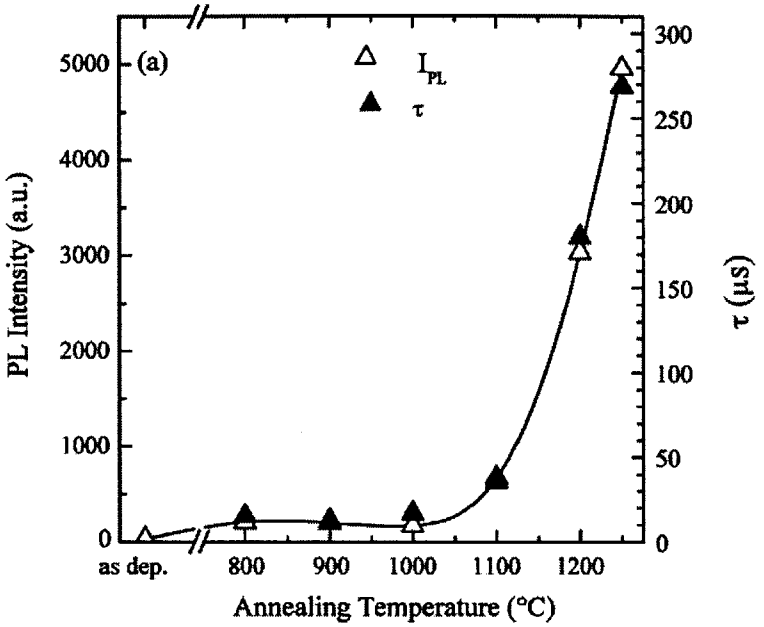

Figure 2-10: PL intensity (left-hand scale) and lifetime (right-hand scale) at 1535 nm as a function of the annealing temperature in the range 800-1250°C for erbium silicate films. Adopted from [104].

Er_2SiO_5 and $Er_2Si_2O_7$ thin films have since been fabricated by a variety of techniques, including sol-gel processing [105–107], metalorganic molecular beam epitaxy (MOMBE) [108–110], pulsed laser deposition (PLD) [111] and RF magnetron co-sputtering of Er_2O_3 and SiO_2 [104, 112, 113]. Just like the case of erbium oxide, the silicate photoluminescence intensity and lifetime were found to increase dramatically with annealing temperature. Figure 2-10 shows that PL intensity and lifetime follow the same trend, indicating that the increase in PL intensity is due to a reduction of the non-radiative decay rate. A comparison of the photoluminescence properties of Er_2SiO_5, $Er_2Si_2O_7$ and a mixture of both revealed that the α-$Er_2Si_2O_7$ phase provides the highest optical efficiency for Er^{3+} ions [114].

However, even though erbium precipitation can be prevented in pure erbium oxides and silicates, concentration quenching effects such as upconversion and energy mi-

gration limit practical applications. For example, the longest room temperature PL lifetime measured in the erbium oxide was 63µs, compared to a radiative lifetime in the order of milliseconds. This indicates a very large amount of non-radiative decay through concentration quenching and therefore a very low luminescence quantum efficiency (see section 2.4.2).

Erbium-yttrium oxides and silicates

The concentration quenching effects in pure erbium oxides and silicates can be diminished by diluting the erbium concentration through alloying with other rare earth compounds. Because of their nearly identical ionic radii and valence states (see Table 2.1), different rare earth ions readily substitute for each other in a crystal lattice. In fact, yttria (Y_2O_3) and YAG ($Y_3Al_5O_{12}$) are already very well known hosts for e.g. Nd^{3+} and Er^{3+} in solid-state lasers [115].

Lo Savio et al. investigated the PL properties as a function of erbium concentration in the erbia-yttria ($Er_xY_{2-x}O_3$) alloy system [116]. Figure 2-11 shows the PL intensity and lifetime at 1.54µm as a function of x in $Er_xY_{2-x}O_3$. The lifetime increases monotonically with decreasing erbium concentration, from 31µs at x = 0.72 to 5.6 ms at x = 0.01. This can be explained as a pure increase in PL quantum efficiency due to concentration quenching effects. The PL intensity, on the other hand, reaches a maximum at x = 0.17. This is in line with expectations, since the PL intensity is the product of erbium concentration and PL quantum efficiency.

In 2008, Suh et al. were the first to report on the optical properties of erbium-yttrium monosilicates $Er_xY_{2-x}SiO_5$ [53]. $Er_xY_{2-x}SiO_5$ nanocrystals were fabricated by spin coating an ethanol solution containing $YCl_3 \cdot 6H_2O$ and $ErCl_3 \cdot 6H_2O$ onto a two-dimensional array of Si nanowires, in order to form a so-called *nano-bush* of $Er_xY_{2-x}SiO_5$ nanocrystals. This technique allows to grow very high quality crystallites with a very narrow PL spectrum (FWHM<5nm, due to the absence of inhomogeneous broadening) and a very low upconversion coefficient of $(2.2 \pm 1.1) \times 10^{-18} cm^3.s^{-1}$ at

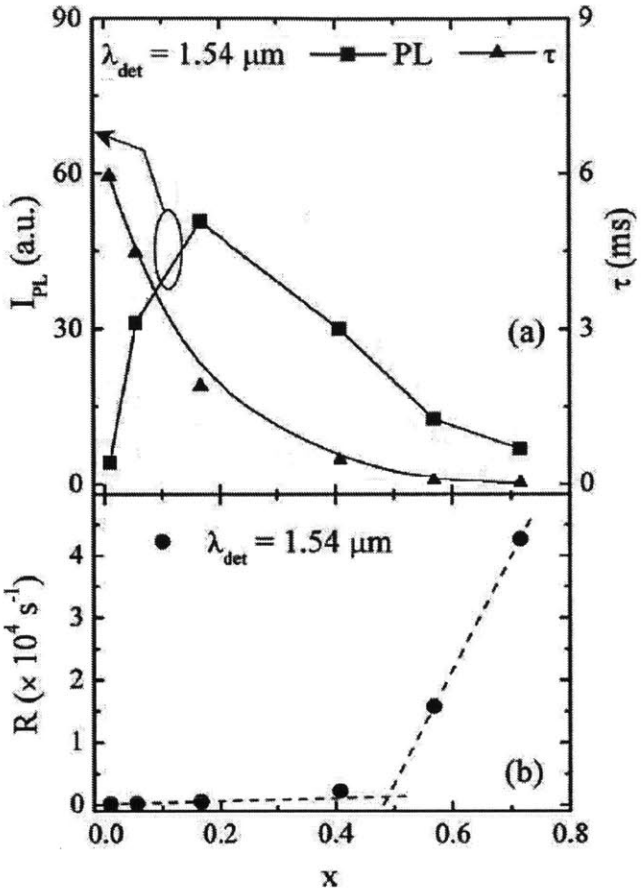

Figure 2-11: Integrated 1.5μm PL intensity and lifetime τ (top) and PL decay rate $1/\tau$ (bottom) as a function of x in $Er_xY_{2-x}O_3$ thin films on Si. The PL is pumped at $\lambda = 488$nm and is collected at room temperature. Adapted from [116].

an Er concentration of $1.2 \times 10^{21}\text{cm}^{-3}$. However, the same authors also reported ion-beam sputter-deposited $Er_xY_{2-x}SiO_5$ thin films, where they measured an upconversion coefficient of $(8\pm3)\times10^{17}\text{cm}^3.\text{s}^{-1}$ at an Er concentration of $1.7\times10^{20}\text{cm}^{-3}$ [54]. This suggests that the low upconversion coefficient measured for the nanocrystallites is not an inherent silicate quality but rather a consequence of the deposition technique.

2.5.3 Erbium-ytterbium compounds

In this thesis, we investigate the properties of erbium-ytterbium oxides ($Er_xYb_{2-x}O_3$) and erbium-ytterbium silicates ($Er_xYb_{2-x}SiO_5$ and $Er_xYb_{2-x}Si_2O_7$) as novel materials systems for an EDWA waveguide core. Just like yttrium ions, ytterbium ions (Yb^{3+}) have an ionic radius that is very close to the ionic radius of Er^{3+} and they can be used as an alternative dilutant.

Additionally, whereas Y^{3+} is optically inactive due to the lack of $4f$ electrons, Yb^{3+} has an energy level at 980nm which is resonant with the Er^{3+} energy level at 980nm. The excitation cross section of Yb^{3+} at 980nm is about an order of magnitude larger than the one for Er^{3+} (see section 2.4.3). As a result, ytterbium can absorb 980nm pump light very efficiently and then transfer the absorbed energy to erbium, thereby increasing the *effective* Er^{3+} excitation cross section and decreasing the pump energy required to achieve population inversion. Furthermore, as opposed to silicon nanocrystals, Yb^{3+} does not cause free carrier absorption and does not limit the solubility of Er^{3+}.

In other words, the role of Yb^{3+} in erbium-ytterbium compounds is expected to be *twofold*: (i) as a *dilutant* it will diminish concentration quenching effects and increase PL quantum efficiency and (ii) as a *sensitizer* it will increase the effective excitation cross section of Er^{3+} at 980nm, allowing a more energy-efficient amplifier.

2.6 The state of the art

Before starting our study on erbium-ytterbium compounds, it is useful to give an overview of the gain reported in 'competing' materials systems. This can serve as a benchmark for our study.

When comparing the gain coefficients reported in literature for different materials, it is important to clarify the nomenclature used to describe signal gain in an EDWA:

Signal enhancement refers to a reduction in absorption by Er^{3+} ions when these are pumped from the ground state to the first excited state. This results in a decrease in waveguide transmission losses when the pump is turned on.

Relative gain, or simply **gain**, occurs when the stimulated emission becomes larger than the absorption caused by the Er^{3+}-ions. The *gain coefficient* γ in cm^{-1} or $dB.cm^{-1}$ is given by

$$\gamma = \sigma_{em} N_1 - \sigma_{abs} N_0 \approx \sigma(N_1 - N_0) \tag{2.25}$$

where we used $\sigma_{em} \approx \sigma_{abs}$ (see Table 2.3) and N_0 and N_1 are the populations of the ground and first excited state in Er^{3+}, respectively [117]. Gain occurs when $\gamma > 0$. The equation shows that this happens when $N_1 > N_0$. This condition is called *population inversion.*

Net gain occurs when the gain coefficient γ is large enough to overcome the sum α of all waveguide propagation losses not related to Er^{3+}, such as scattering loss, bending loss and absorption by e.g. hydroxyl groups. In other words, net gain occurs when $\gamma > \alpha$.

Values for gain and net gain reported in literature are usually **internal (net) gain** figures. This is the gain excluding any coupling losses to fibers or waveguides that deliver the pump and input signal to the EDWA and collect the amplified signal at the output. Of course, coupling losses determine the performance of an actual 3dB amplifier, but since they depend on the eventual device design, internal (net) gain figures are the best way to compare different EDWA materials.

Table 2.6 on page 58 shows the record *internal net gain* figures reported in literature for EDWAs made out of different erbium-doped host materials. The results are ranked from highest gain coefficient in dB/cm to lowest. The highest gain coefficients were obtained in phosphate and soda-lime silicate glasses. This is due to a combination of their high erbium solubility and low upconversion coefficients.

Reports of internal gain in $Er_xY_{2-x}SiO_5$ and $Er_xYb_{2-x}SiO_5$

The first internal gain in erbium-*yttrium* silicates was reported in 2010 by Suh et al. [54]. The authors fabricated a 9.3mm long 175nm × 2μm strip-loaded SiO_2 waveguide on top of a 275nm thick blanket $Er_xY_{2-x}SiO_5$ film. They achieved an internal gain of 0.40dB at 60mW of bidirectional pumping at 1480nm. However, no *net* gain was achieved, since the gain of 0.43dB/cm was much smaller than the background loss of 3.4 ± 0.6 dB/cm. The large background loss compared to the values reported in Table 2.6 is explained by scattering at grain boundaries in this polycrystalline material.

A similar strip-loaded SiO_2 waveguide on erbium-*ytterbium* silicate ($Er_{0.1}Yb_{1.9}SiO_5$) was reported by Guo et al. [135]. The authors reported a signal enhancement of 7.05dB/cm by pumping with 372mW of 1480nm light, but were not able to achieve population inversion. Again, the structure suffers from a very large propagation loss of 8.1dB/cm. The same authors also reported a 1.7 dB signal enhancement for a 6 mm-long c-Si/$Er_{0.17}Yb_{1.83}SiO_5$/a-Si slot waveguide, but again no population inversion was achieved and the propagation loss amounted to 14.7dB/cm [136].

Wang et al. [137] were able to reduce the background loss to 3.2 ± 0.3 dB/cm by using a 250nm x 2.4μm Si_3N_4 strip waveguide on thermal SiO_2 with a $Er_{0.2}Yb_{1.8}SiO_5$ overcladding. They achieved a 3.1dB signal enhancement for 5.9mm long waveguide (5.25dB/cm) under 1476nm pumping at 372mW. Very recently, the authors also demonstrated 1.25dB/cm internal gain (but no net gain), for a similar hybrid Si_3N_4-$Er_{0.02}Yb_{0.005}Y_{1.955}SiO_5$ and with the same pumping conditions [138].

It is interesting to note that in the papers by Guo et al. and Wang et al., the erbium-ytterbium waveguides are pumped at 1480nm instead of 980nm, which defeats the purpose of using ytterbium. Indeed, Yb^{3+} has no sensitization effect at 1480nm and can only cause a parasitic decay path through energy transfer from Er^{3+} to Yb^{3+}. In this case, it is better to use erbium-*yttrium* silicate instead.

Table 2.6: Record internal gain figures reported in literature.

Host material	Er conc. $\times 10^{20}$ cm^{-3} or as indicated	Yb conc. $\times 10^{20}$ cm^{-3} or as indicated	Sample length (cm)	Background loss (dB/cm)	Pump wavelength (nm)	Pump power (mW)	Peak internal net gain (dB/cm)	Ref.
Phosphate glass	7.5 (8 wt% Er)	11 (12 wt% Yb)	0.3	0.5	980	150	13.7	[118]
	2.3 wt% Er_2O_3	3.6 wt% Yb_2O_3	3.1	0.4	975	460	5.3	[119]
	5.33 (0.75 at%)	-	3.1	0.9	980	21	4.1	[39]
Soda-lime silicate glass	4.3	-	2.4	1	980	120	4.2	[120, 121]
	14600 ppm	-	4.5	1	980	280	3.3	[122]
Bismuthate glass	0.63 wt% Er	-	8.7	0.2	980	1050	2.3	[78]
Borosilicate glass	3 wt% Er_2O_3	5 wt% Yb_2O_3	3.9	0.15	980	130	2.3	[123]
Al_2O_3	2.12	-	2.1	0.14	977	80	2.0	[76]
	2.7	-	4.0	0.35	1480	9	0.58	[87]
Ti:$LiNbO_3$	not reported	-	5.7	0.1	1484	170	2.0	[124]
Aluminosilicate glass	not reported	-	5	0.2	980	130	1.9	[75]
Oxyfluoride silicate glass	1 wt% Er_2O_3	2 wt% Yb_2O_3	1	0.34	980+1480	342	1.9	[125]
Y_2O_3	1.3	-	4.3	0.9	1480	10	1.3	[126]
Fluoride glass	not reported	-	1.9	0.6	1480	340	1.3	[127]
Aluminophopho-silicate	0.25 mol% Er_2O_3	0.25 mol% Yb_2O_3	5	< 0.2	980	175	1.1	[128]
Polymer	0.357 (1 wt%)	-	1.6	< 1	980	70	0.84	[129]
Phosphosilicate	0.48 wt%	-	7.5	0.17	980	420	0.67	[130]
Phosphotellurite	0.7	-	2.5	1.35	980	220	0.5	[131]
Er-doped silica	3800 ppm	-	23	0.90	980	99	0.41	[132, 133]
ZrO_2	0.88	-	6.5	0.45	980	36	0.005	[134]

Chapter 3

Experimental Methods

This chapter discusses the methods for film deposition and for structural and optical analysis used in this thesis. In the first section, we explain how erbium-ytterbium oxide and silicate thin films are deposited by means of RF magnetron sputtering. The composition of the oxide and silicate alloys is controlled by varying the RF power applied to Er_2O_3, Yb_2O_3 and SiO_2 sputtering targets. Secondly, we review the X-ray diffraction (XRD) analysis performed for structural characterization. Finally, we discuss the photoluminescence and lifetime measurements used to study the light emission properties of the deposited films. We explain how to measure the beam radius of the pump lasers in order to calculate the photon flux corresponding to a certain pump power. Additionally, we discuss the non-linearities of the measurement setup in order to be able to correctly measure PL saturation curves.

3.1 Deposition

3.1.1 RF magnetron sputtering

Erbium-ytterbium oxides and silicates were deposited by means of RF magnetron co-sputtering of Er_2O_3, Yb_2O_3 and SiO_2. RF magnetron sputtering is a CMOS com-

patible deposition technique that allows for accurate and reproducible stoichiometry control of the deposited films. A schematic of the sputtering system used in this thesis is shown in Fig. 3-1. The system consists of a main chamber connected to a cryogenic pump that pumps the chamber down to a base pressure of 10^{-8} Torr $< p < 10^{-7}$ Torr. A load lock pumped by a separate turbo pump allows to load substrates without venting the entire processing chamber.

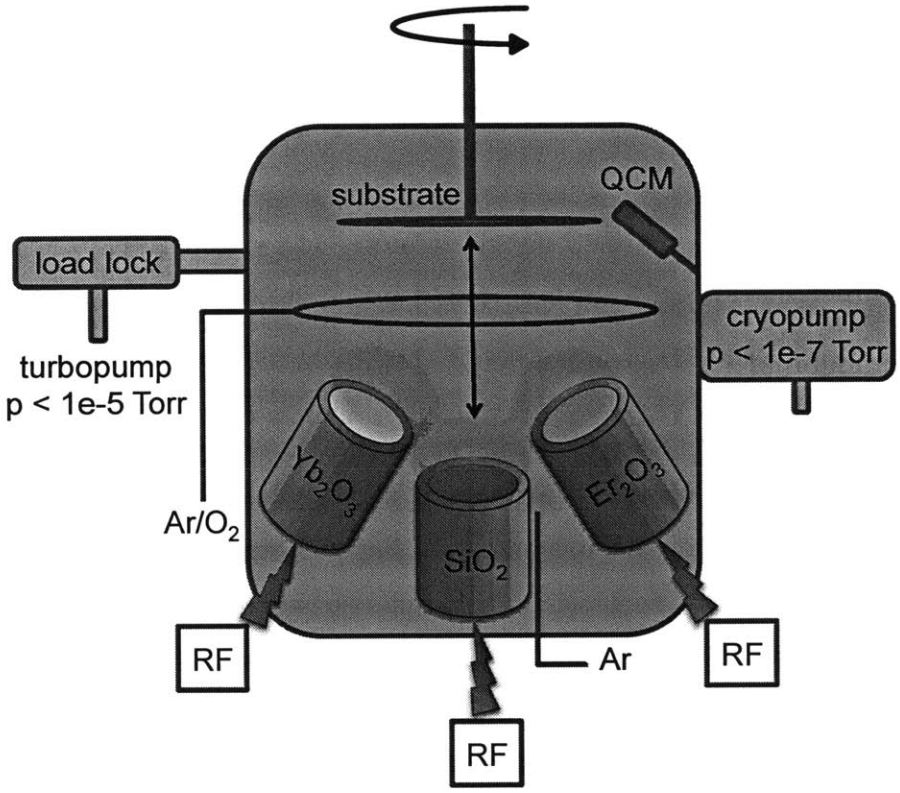

Figure 3-1: Schematic of Kurt J. Lesker RF magnetron sputter system used for thin film deposition.

The sputtering system supports three 3″ targets that can be sputtered simultaneously (so-called *co-sputtering*). All sputtering targets were purchases from the Kurt J. Lesker Company, which is also the manufacturer of the sputtering system. The sputtering targets consists of either 0.125″ thick SiO_2 glass or 0.125″ thick pressed rare oxide powder bonded onto a 0.125″ thick copper backing plate with an indium bonding. The three sputtering guns are directed confocally towards the center of the substrate, at a working distance of 30cm. During deposition the substrate is rotated

at 60rpm to achieve radial uniformity of the sputtered films.

Three gas lines deliver Ar gas directly below each target for sputtering with an inert Ar plasma. As discussed in section 3.1.2, the use of Er_2O_3, Yb_2O_3 and SiO_2 targets allows for easy stoichiometry control of the deposited erbium-ytterbium oxide and silicate alloys. However, whereas metals and semiconductors can be sputtered using a DC power supply, dielectric insulators such as oxides suffer from charge build-up due to collisions with Ar^+ ions during sputtering. As a consequence, RF power supplies and corresponding impedance matching networks need to be used for each sputtering target. The RF power supplies change the sign of the electric bias applied to the sputtering targets at a rate of 13.56 MHz, hence preventing charge build-up.

The argon pressure during sputtering was set at 3mTorr. It was found early on that higher Ar pressures can cause thin film blistering during annealing (see Figure 3-2). This effect disappears at lower Ar pressures, suggesting it may be due to Ar being trapped in the films during deposition. Inclusion of Ar in the sputtered films was also confirmed by RBS measurements (see Table 3.2 in section 3.1.3).

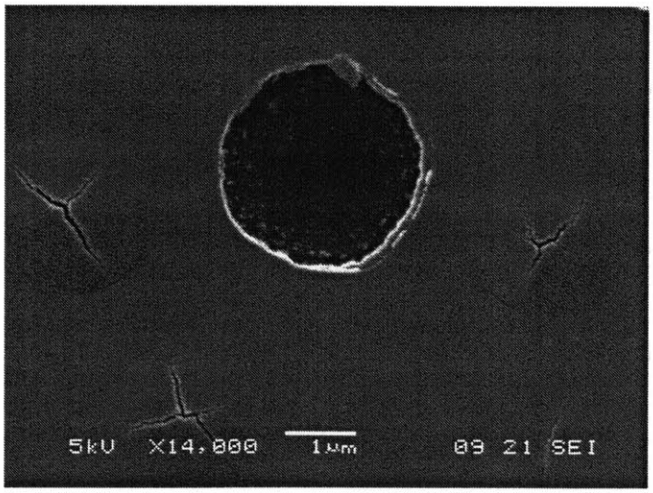

Figure 3-2: SEM picture of blistering of Er_2O_3 film on Si sputtered at p(Ar) = 20mTorr after 800°C anneal.

The substrate was not heated or temperature controlled during deposition, but estimated thermocouple measurements suggest substrate temperatures in the range of 200-250°C by the end of a typical 1 h deposition [9].

3.1.2 Deposition rates

The deposition of erbium-ytterbium oxides and silicates can be done by directly sputtering oxide targets in a non-reactive Ar plasma. Alternatively, reactive sputtering of Er and Yb metal and Si using a reactive Ar/O_2 gas mixture can also be used. As mentioned above, sputtering of oxides requires the use of expensive RF power supplies and impedance matching networks, but also allows for easy stoichiometry control of the complicated ternary ($Er_xYb_{2-x}O_3$) or quaternary ($Er_xYb_{2-x}SiO_5$ and $Er_xYb_{2-x}Si_2O_7$) compounds deposited in this research.

Once the deposition rate of each target can be controlled individually, erbium-ytterbium oxides ($Er_xYb_{2-x}O_3$), monosilicates ($Er_xYb_{2-x}SiO_5$) and disilicates ($Er_xYb_{2-x}Si_2O_7$) can be deposited from Er_2O_3, Yb_2O_3 and SiO_2 sputtering targets by simply combining the deposition rates according to the following chemical equations

$$x\ Er_2O_3 + (2-x)\ Yb_2O_3 \rightarrow 2\,Er_xYb_{2-x}O_3 \tag{3.1}$$

$$x\ Er_2O_3 + (2-x)\ Yb_2O_3 + 2\,SiO_2 \rightarrow 2\,Er_xYb_{2-x}SiO_5 \tag{3.2}$$

$$x\ Er_2O_3 + (2-x)\ Yb_2O_3 + 4\,SiO_2 \rightarrow 2\,Er_xYb_{2-x}Si_2O_7 \tag{3.3}$$

Figure 3-3 below shows the deposition rates of the rare earth oxides Er_2O_3, Yb_2O_3 and Y_2O_3 as a function of the applied RF power. The yttrium oxide target (Y_2O_3) is included for the deposition of ytterbium-yttrium silicates in Chapter 6. Figure 3-4 shows the deposition rates of Si and SiO_2. The Si target was used for the deposition of oxide/Si or silicate/Si multilayers in Chapter 6. The deposition rates are monitored by means of a quartz crystal monitor (QCM) during sputtering and film thicknesses are measured with a KLA Tencor P-16+ profilometer.

The concentration of a particular compound (in units/cm^3) in a sputtering target (for example Er_2O_3) can be calculated with the expression

$$[Er_2O_3] = \frac{N_A \cdot \rho(Er_2O_3)}{M(Er_2O_3)} \tag{3.4}$$

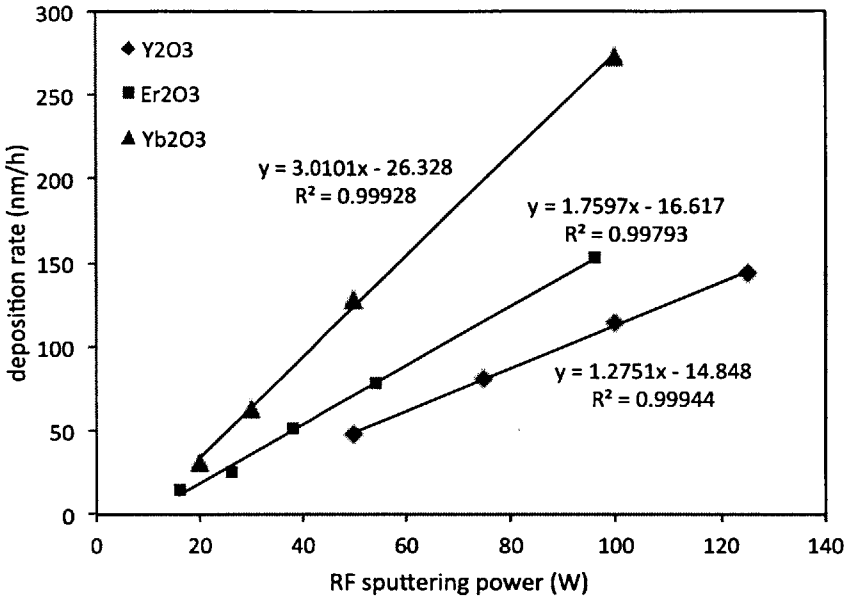

Figure 3-3: Deposition rate vs. RF power applied to rare earth oxide sputtering targets.

where ρ is the density in g/cm^3, M is the molar mass in g/mol and $N_A = 6.022 \times 10^{23}$ mol^{-1} is the Avogadro number. The results are shown in Table 3.1.

Table 3.1: Density, molar mass and concentration for each of the sputtering targets.

compound	density (g/cm^3)	molar mass (g/mol)	concentration (#/cm^3)
Er_2O_3	8.64	382.56	1.36×10^{22}
Yb_2O_3	9.17	394.08	1.40×10^{22}
Y_2O_3	5.01	225.81	1.34×10^{22}
SiO_2	2.65	60.08	2.65×10^{22}
Si	2.33	28.09	4.99×10^{22}

In order to deposit a specific stoichiometry, the deposition rates need to be matched to the composition. To convert between deposition rates measured in nm/h to deposition rates in atoms/h, the concentrations in Table 3.1 are used.

For example, to sputter a particular erbia-ytterbia alloy $Er_xYb_{2-x}O_3$, the relative

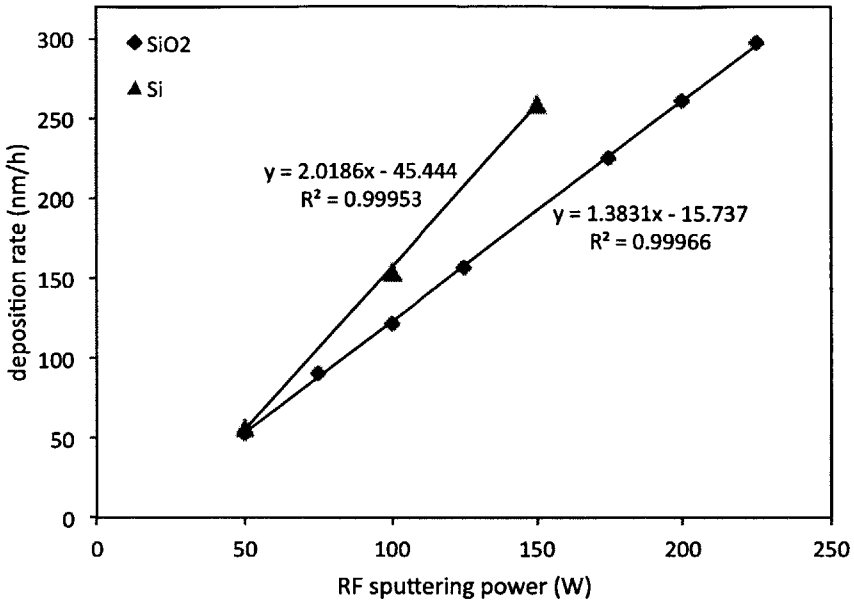

Figure 3-4: Deposition rate vs. RF power applied to Si and SiO_2 sputtering targets.

deposition rates of erbia and ytterbia are

$$\frac{[Er_2O_3]}{[Yb_2O_3]} = \frac{x}{2-x} \Leftrightarrow \frac{rEr_2O_3}{rYb_2O_3} = \frac{1.40 \times 10^{22}}{1.36 \times 10^{22}} \cdot \frac{x}{2-x} = 1.03 \cdot \frac{x}{2-x} \tag{3.5}$$

Similarly, to deposit the silicates Yb_2SiO_5 and $Yb_2Si_2O_7$, the relative rates of rare earth oxide and silicon oxide are found by the following calculations

$$Yb_2SiO_5 \rightarrow \frac{[Yb_2O_3]}{[SiO_2]} = 1 \Leftrightarrow \frac{rYb_2O_3}{rSiO_2} = \frac{2.65 \times 10^{22}}{1.40 \times 10^{22}} = 1.8941 \tag{3.6}$$

$$Yb_2Si_2O_7 \rightarrow \frac{[Yb_2O_3]}{[SiO_2]} = \frac{1}{2} \Leftrightarrow \frac{rYb_2O_3}{rSiO_2} = \frac{1}{2} \cdot \frac{2.65 \times 10^{22}}{1.40 \times 10^{22}} = 0.9471 \tag{3.7}$$

3.1.3 Concentration analysis

RBS and PIXE

To confirm that the linear combination of deposition rates described above results in the targeted composition, a film with nominal concentration $Er_{0.5}Yb_{1.5}SiO_5$ was

sent out to Evans Analytical Group (EAG) for a concentration measurement. RBS (Rutherford Backscattering Spectroscopy) was used to determine the concentrations of Si and O and the total concentration of rare earths (Er+Yb). Since the masses of Er and Yb are too similar to resolve by means of RBS, the PIXE (Particle-Induced X-ray Emission) spectrum was used to distinguish between Er and Yb. The RBS and PIXE spectra are shown in Figure 3-5(a) and Figure 3-5(b). The concentrations can be determined from the area underneath the respective peaks. The results are shown in Table 3.2.

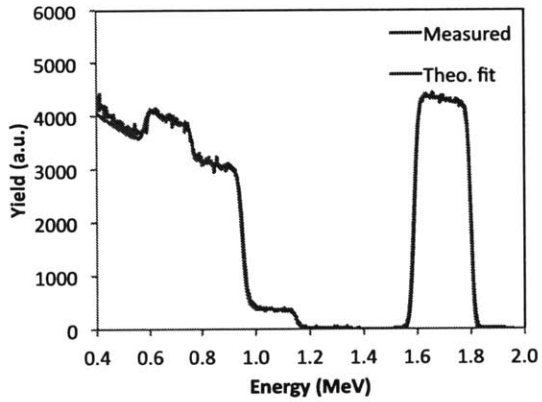

(a) RBS

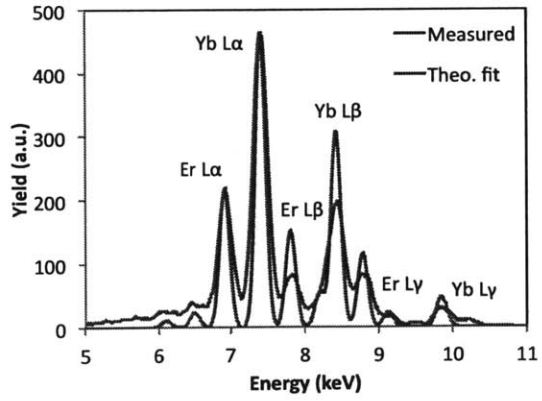

(b) PIXE

Figure 3-5: RBS and PIXE spectra of $Er_{0.5}Yb_{1.5}SiO_5$

Table 3.2: RBS-PIXE results of $Er_{0.5}Yb_{1.5}SiO_5$

element	target at. %	measured at. %
Er	6.25	5.4 ± 1.5
Yb	18.75	15.4 ± 2.5
Si	12.5	12.5 ± 1.0
O	62.5	66.2 ± 4.0
Ar	0.0	0.5 ± 0.2

SIMS

In addition to the RBS and PIXE measurements discussed above, the erbium-ytterbium ratio in three different silicate samples was determined using Secondary Ion Mass Spectrometry (SIMS). During SIMS, the film is sputtered with an oxygen ion beam and the sputtered atoms are identified using mass spectroscopy. To account for different etching rates of Er and Yb and for different natural abundances of different Er and Yb isotopes, the PIXE result discussed previously was used as a standard to calibrate the Er and Yb rates. The results are shown in Table 3.3.

Table 3.3: SIMS results of $Er_xYb_{2-x}SiO_5$

nominal x(Er)	measured x(Er)	$\Delta\,(x^{meas} - x^{nom})$
0.20	0.17 ± 0.01	-15%
0.50	0.52 ± 0.03	+4%
1.00	1.00 ± 0.03	0%

A good correspondence is found between target (nominal) Er and Yb concentrations and the SIMS results. Only the low Er concentration is 15% lower than targeted. This can be explained as follows: during the deposition rate measurement of Er_2O_3 at low powers, the mean free path between the Er_2O_3 sputtering target and the substrate is longer than during sputtering at higher powers or during co-sputtering with Yb_2O_3 and SiO_2. In the latter case, the mean free path decreases due to the presence of additional particles in the vacuum and the deposition rate will be lower than what was measured during the deposition rate measurement. This problem is less important for Yb_2O_3 and SiO_2 sputtering, since the deposition rates are always

higher than for Er_2O_3. As seen in the chapter on erbium-ytterbium silicates, the erbium concentration is indeed lower than what was nominally expected.

3.2 X-Ray Diffractometry

3.2.1 Phase identification

X-ray diffractograms were collected at room temperature using a PANalytical X'Pert PRO diffractometer set up in the Bragg-Brentano geometry. A copper anode operating at 45kV and 40mA was used as X-ray source emitting a $K\alpha_1$ spectral line at $\lambda = 1.540598$Å and a $K\alpha_2$ line at $\lambda = 1.544426$Å. A 20µm nickel filter was used to filter out the Cu $K\beta$ lines.

An automatic programmable divergence slit in the incident beam path keeps the irradiated length on the sample constant at 6mm during the scan by increasing its aperture from 0.12° to 0.75° for 2θ going from 10° to 65°. 6mm corresponds to the average sample size; a larger beam length gives more intensity but less angular resolution (broader peaks) and more background noise. The diffracted beam anti-scatter slit is matched to the incident beam automatic programmable divergence slit (i.e. 6mm irradiated length). An incident beam fixed 2° anti-scatter slit is used to limit incident beam divergence.

Phase identification is achieved by comparing the collected X-ray diffraction patterns with the Powder Diffraction File (PDF) database by the International Centre for Diffraction Data (ICDD). Database files in this thesis are referenced by their PDF number.

3.2.2 Rietveld refinement for phase quantification

Rietveld refinement was used to determine the mole fraction of different phases in multiphase XRD patterns. Using the position, height and width of the measured

peaks, this technique matches a theoretical profile to the data by means of the least squares method. The position of the peaks is used for phase identification when the peaks are matched to a database file. If certain crystal orientations are preferred (so-called *texture*), the peaks corresponding to these orientations will be stronger than in a powder with random orientation. By comparing the relative intensities of the peaks corresponding to a particular phase with a powder diffraction file, the texture of the film can be determined [139].

3.2.3 Estimating grain size and microstrain

The grain size and microstrain in a certain phase can be determined from an XRD spectrum by analysis of the broadening of the XRD peaks associated to that particular phase in the X-ray diffractogram. For a perfect single crystal, the XRD peaks would be infinitely narrow. However, the finite crystallite size in nano- or polycrystalline materials and microstrain (i.e. line and plane defects in the lattice, such as dislocations) cause broadening of the peaks.

Crystallite size broadening depends on the crystallite size L as

$$B(2\theta) = \frac{K\lambda}{L\cos\theta} \tag{3.8}$$

where $\lambda = 1.540598\text{Å}$ and $K \approx 1$ is the Scherrer constant [140].

Broadening due to a microstrain $\epsilon[\%] = \Delta d/d$ is given by the term [141]

$$B(2\theta) = 4|\epsilon|\frac{\sin\theta}{\cos\theta} \tag{3.9}$$

Adding the expressions for broadening due to crystallite size and microstrain, we derive the expression for total broadening

$$B(2\theta) = \frac{K\lambda}{L\cos\theta} + 4|\epsilon|\frac{\sin\theta}{\cos\theta} \tag{3.10}$$

and therefore

$$\text{Breadth} \times \cos\theta = \frac{K\lambda}{\text{Crystallite size}} + 4 \times \text{Microstrain} \times \sin\theta \qquad (3.11)$$

In other words, by plotting $B \times \cos\theta$ versus $\sin\theta$ for the different XRD peaks corresponding to a certain phase and by fitting the data with a linear regression, we can derive the crystallite size and the microstrain from the y-intercept and the slope of the linear regression, respectively. Such a plot is called a *Williamson-Hall plot.* Note that smaller grains cause a larger y-intercept and infinitely large grains would cause a regression through the origin.

Any peak broadening introduced by the X-ray diffractometer itself is deconvoluted from specimen broadening before the analysis. However, even after this deconvolution, the maximum grain size (i.e. narrowest peaks) that can be resolved remains limited by the peak broadening introduced by the diffractometer. In our case, the maximum crystallite size that can be resolved is $\sim$ 1000 Å.

3.3 Photoluminescence measurements

3.3.1 Measurement setup

The erbium photoluminescence spectrum, intensity and lifetime around 1.5µm were analyzed using a SPEX monochromator and a Hamamatsu liquid-nitrogen cooled photomultiplier tube connected to a lock-in amplifier and an oscilloscope. The PL is excited by either an Ar-ion pump laser (λ_p = 488nm) for direct excitation of erbium or by a diode laser with λ_p = 980nm for mediated excitation through ytterbium. Two lenses collect the PL emitted from the sample and subsequently focus it into the monochromator. A long wavelength pass filter is used at the input slit of the monochromator to filter out any scattered pump laser light that may otherwise be collected and cause artifacts in the PL spectrum. A schematic of the PL measurement

setup is shown in Figure 3-6.

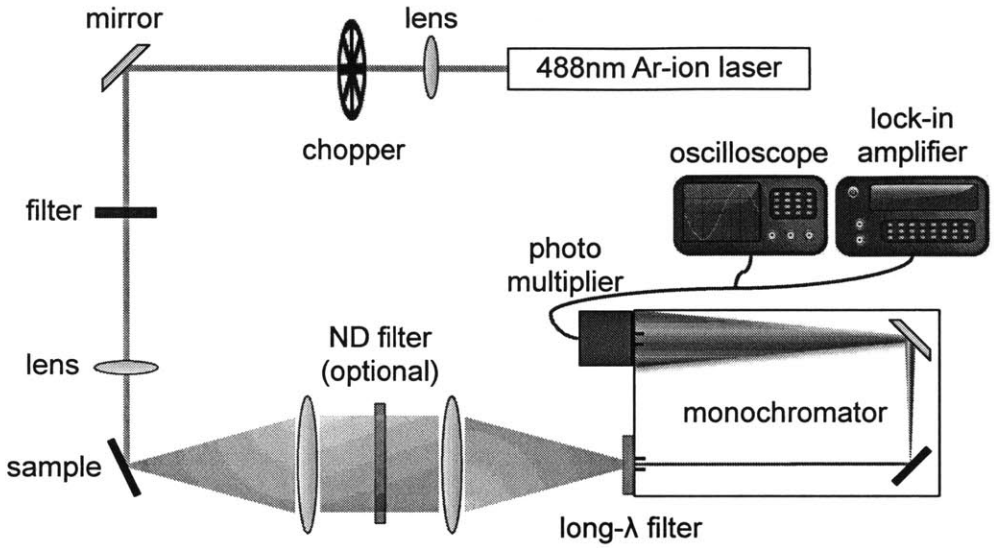

Figure 3-6: Schematic of the PL setup using the Ar-ion pump laser at 488 nm. The laser beam reflected off the sample is directed away from the collection optics and is not shown.

The Ar-ion laser operates continuously and is modulated by an external chopper generating a square-wave pump pattern, whereas the laser at 980nm is driven electrically and can be modulated directly. The modulation frequency is chosen so that $f^{-1} > 10\tau$, where τ is the decay lifetime of the PL signal. If f is too high, the PL signal will not rise and decay completely during one half modulation period and the lock-in amplifier will underestimate the PL intensity. At $f^{-1} = 10\tau$, the PL intensity reaches $1 - e^{-5} = 99.3\%$ of its maximum/minimum value within one half modulation period.

Filters were used to scale down the pump intensity to the linear PL regime. This gives us a range of powers as low as 349μW and as high as 417mW for 488nm pumping and between 41μW and 271mW for 980nm pumping.

3.3.2 Pump beam profile and spot size

In order to calculate the photon flux Φ (in photons/cm^2.s) corresponding to a certain pump power, the spot size of the pump laser beam at the sample needs to be determined. This can be done by measuring the fraction of the total beam transmitted as the beam is partially blocked by a sharp edge. In this case, a razor blade mounted on a micro translation stage was moved across the laser beam in one direction and the transmitted power was measured with a Si detector. Assuming that the laser beam has a Gaussian shape and is radially symmetric, the beam profile can be described by means of the expression

$$\Phi(x,y) = \frac{2}{\pi w^2} \exp\left(-2\frac{x^2+y^2}{w^2}\right) \tag{3.12}$$

where w is the *beam radius* defined as the distance from the beam axis where the electric field strength drops to $1/e$ and the optical intensity drops to $1/e^2 \approx 13.5\%$ of its maximum value [142]. The power $P(x)$ measured by the Si detector as the razor blade is moved across the beam in the x-direction will then be

$$P(x) = \int_{-\infty}^{x}\int_{-\infty}^{+\infty} \Phi(\chi,y)dyd\chi = \frac{1}{2} + \frac{1}{2}\mathrm{erf}\left(\frac{\sqrt{2}x}{w}\right) \tag{3.13}$$

The beam radius w can now be determined by taking the derivative of $P(x)$ and by fitting a Gaussian function to the result

$$\frac{d}{dx}P(x) = \frac{\sqrt{2}}{\sqrt{\pi}w} \exp\left(-\frac{2x^2}{w^2}\right) \tag{3.14}$$

The measured cross-section of the 488nm and the 980nm laser beams is shown on Figure 3-7. The red data (right y-axis) on the plots show the normalized measured laser power $P(x)$ and the black data (left y-axis) show its derivative. The blue line is a Gaussian fit to $dP(x)/dx$ according to Eq. 3.14. The proportionality constant A accounts for the arbitrary units.

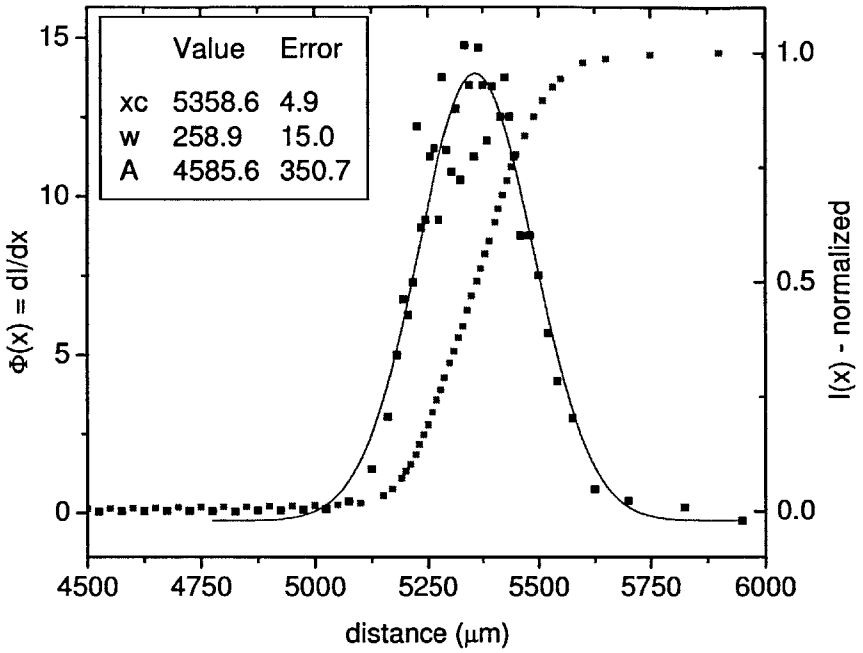

(a) 488nm laser beam.

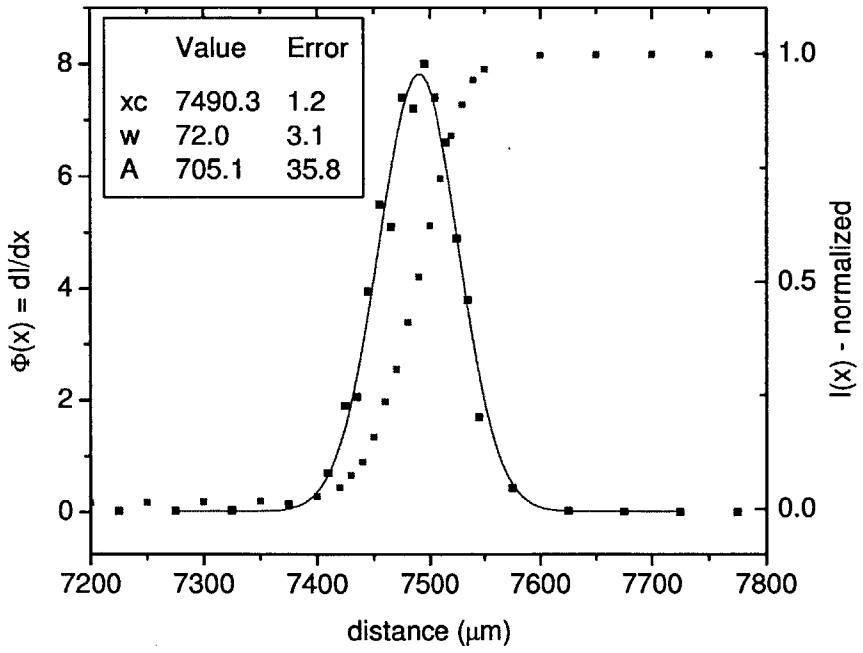

(b) 980nm laser beam.

Figure 3-7: Beam profiles of 488nm and 980nm laser beam. Red data (right axis) shows the (normalized) laser intensity measured with the razor blade method. Black data (left axis) is the derivative of the laser intensity, with a Gaussian fit (blue line).

The 488nm beam radius at the sample is found to be $w_{488} = 258.9 \pm 15.0$ µm and the 980nm beam radius is $w_{980} = 72.0 \pm 3.1$ µm.

With λ expressed in µm, the pump power P in W and beam radius w in cm, the photon flux Φ can now be calculated as

$$\Phi \left[\frac{\text{photons}}{\text{cm}^2.\text{s}}\right] = \frac{\lambda}{1.24 \cdot 1.602 \times 10^{-19}} \left[\frac{\text{photons}}{\text{J}}\right] \times \frac{P}{\pi w^2} \cdot \cos(58°) \left[\frac{\text{J}}{\text{cm}^2 \cdot \text{s}}\right] \quad (3.15)$$

where the factor cos(58°) is included to account for the incidence angle of 58°.

3.3.3 Measuring PL saturation

As explained in Chapter 5, it is crucial to measure the upconversion coefficient accurately. Upconversion causes the photoluminescence intensity to saturate at high pump powers, whereas it increases linearly with pump power at low pump powers. The upconversion coefficient can therefore be determined by measuring the saturation of PL intensity at high pump powers.

In order to accurately measure the PL saturation, any potential non-linearities that may be introduced by either the pump lasers, mirrors, lenses, the spectrometer or the detector need to be accounted for. First, the linearity will be examined of all the components on the *excitation side* of the setup, meaning the lasers, filters, mirrors and lenses in the optical path before the sample. Secondly, the *collection side* will be examined, consisting of the collection optics, the monochromator, photomultiplier and lock-in amplifier.

Excitation side

Figure 3-8 shows the incident power at the sample (green data) measured by a Si detector for both the 488nm laser and the 980nm laser as a function of the laser power setting and the laser drive voltage respectively, which are used to control the laser output power for each laser. It is seen that the output powers for both lasers

are linear with the control setting. Both figures also show the power measured at the sample when different filters are used to scale down the pump flux (blue and red data). Again, the filters used for both the 488nm and 980nm light are linear.

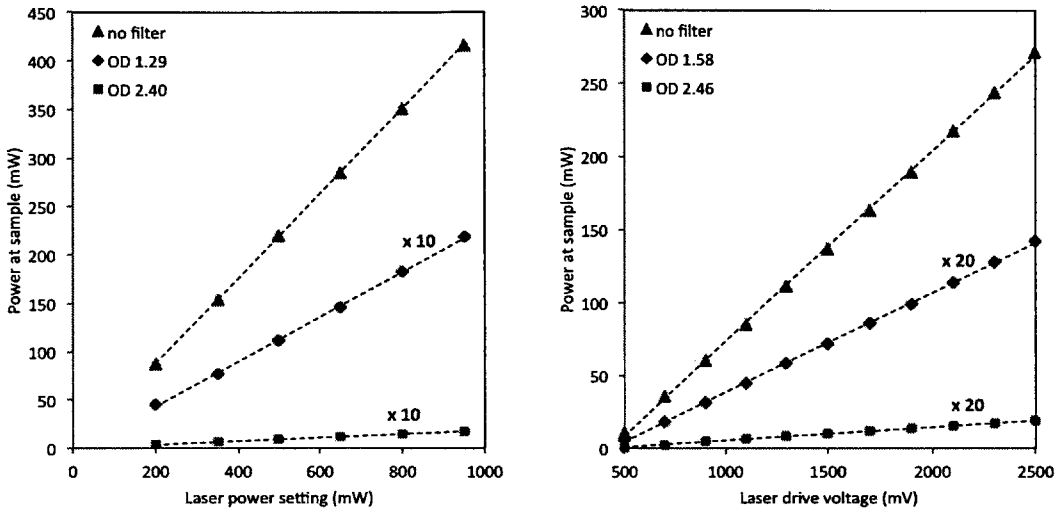

(a) 488nm excitation

(b) 980nm excitation

Figure 3-8: Linearity of excitation side. For the sake of visibility, the powers measured with the different filters are scaled by a factor 10 for λ =488nm and by a factor 20 for λ =980nm.

Collection side

Saturation of the collection side is determined by comparing the PL saturation of different samples with and without a filter positioned between the sample and the detector. A neutral density (ND) filter with transmission $T = 10.25\%$ is placed in the middle of the two lenses of the collection optics in Figure 3-6. By comparing the lock-in amplifier reading with and without the ND filter, the saturation introduced by the spectrometer, detector and lock-in amplifier can be measured.

Figure 3-9 shows the PL saturation (i.e. lock-in amplifier reading) with and without the ND filter. The data with filter were scaled by a factor $T^{-1} = 9.7553$. At low pump powers, the PL in both cases increases linearly with pump power. At higher pump powers however, it is seen that the PL saturates more without the filter than

with the filter.

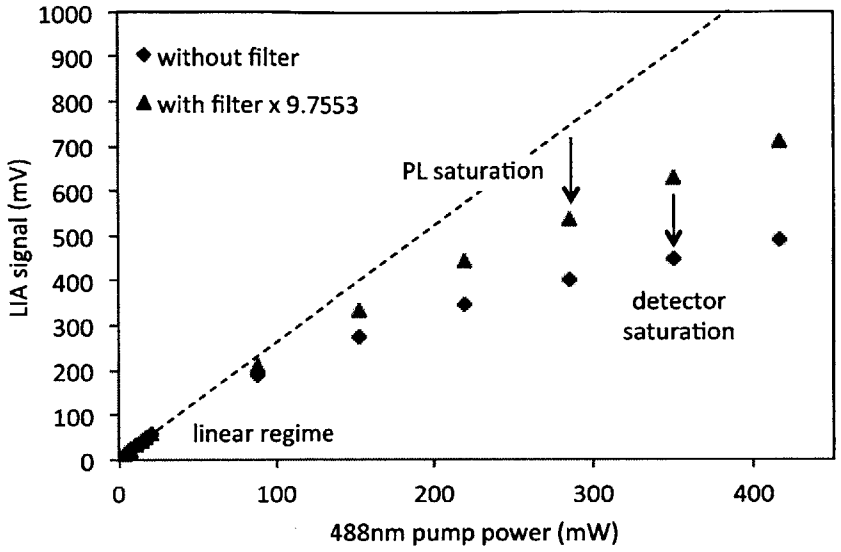

Figure 3-9: PL saturation measured with (green data, scaled x9.7553) and without (blue data) ND filter. The straight line shows an extrapolation of the linear regime.

Figure 3-10 shows the PL without filter plotted versus the PL with filter. If the saturation were the same, these data would follow the straight line (dashed) on the figure. This measurement was done for three different samples with different Er compositions. As the figure shows, the saturation is the same for all three samples.

3.3.4 Measuring PL lifetime

For the PL decay time measurements, Er was pumped directly using the 488nm laser to avoid possible effects of Yb-Er energy transfer rates on the measured lifetime. Two characteristic times limit the shortest PL decay time that can be resolved. First of all, the response time of the photomultiplier tube (PMT) is limited by its RC constant. Decreasing the PMT resistance will decrease the RC constant, but will also decrease sensitivity. We found that the 100kΩ setting was the lowest resistance with acceptable signal-to-noise ratios. Secondly, the finite time taken by the mechanical chopper to completely cut through the laser beam will also limit the shortest lifetime that can

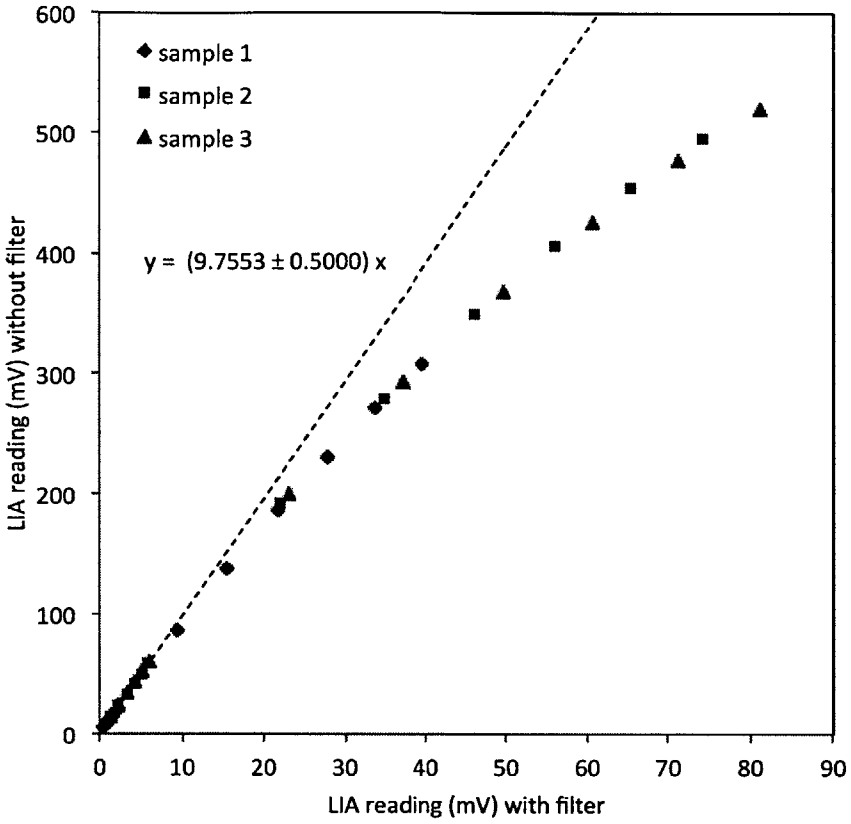

Figure 3-10: Detector saturation for three different samples.

be measured. However, when measuring very short decay times, this chopping time can be made arbitrarily short by increasing the modulation frequency f and thus the speed of the chopping blade. As shown in Figure 3-11, already at $f = 46$Hz the response time of the PMT becomes the dominant effect.

To determine the PMT response time, scattered 488nm argon laser light was directly collected from different scattering sources. Any long-λ pass filters normally used in front of the monochromator to filter out laser light were removed first. 488nm lies outside the operating range (800nm $< \lambda <$ 1700nm) of the grating in the monochromator, however, any diffraction angle θ_m that fulfills the Bragg condition $2d \sin\theta_m = m\lambda$ for a certain wavelength λ will also fulfill it for $\lambda/2$ with diffraction order $2m$. Therefore, the monochromator was set at 976nm to measure the 488nm laser light.

Figure 3-11 shows the decay curves for scattered laser light modulated at 46Hz (blue

curve) and 92Hz (red curve). The decay is the same, indicating that it is due to the PMT response rather than the finite chopping time. The figure shows a 90%-10% response time of 65µs. Since for a PL signal with exponential decay $\exp(-t/\tau)$

$$t_{10} - t_{90} = -\ln(0.1)\tau + \ln(0.9)\tau = 2.2\tau \tag{3.16}$$

this means that photoluminescence decay lifetimes close to or shorter than $\tau = 30\mu s$ cannot be resolved.

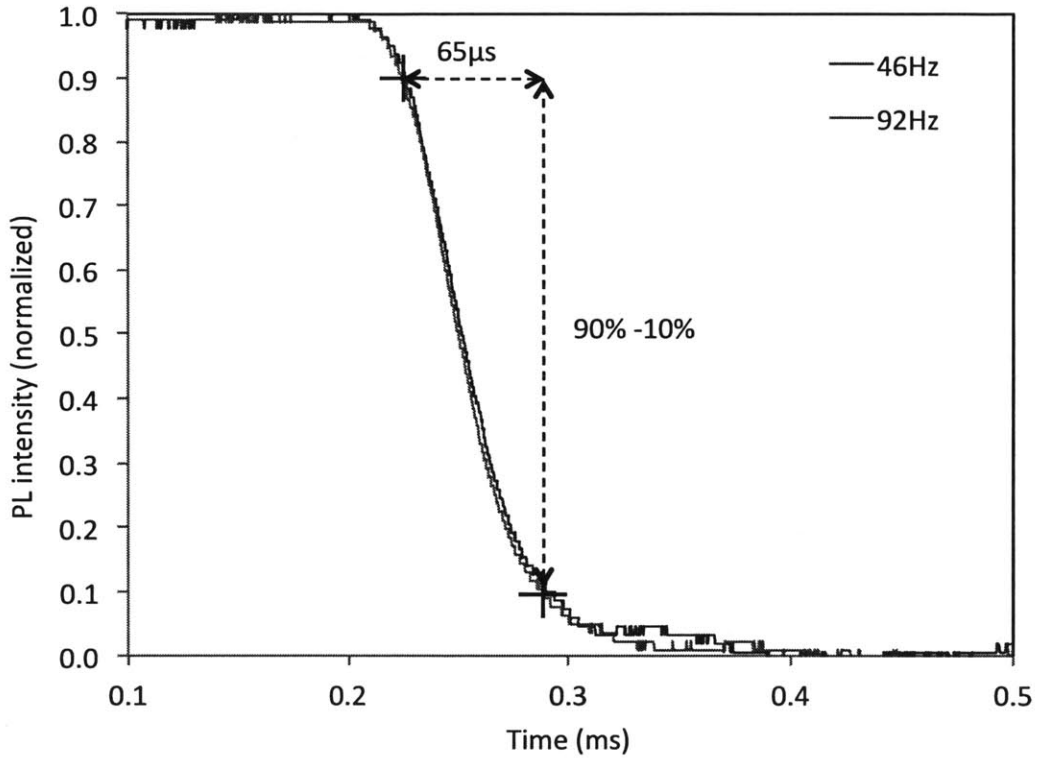

Figure 3-11: Response time of the Hamamatsu PMT at the 100kΩ setting

Chapter 4

Erbium-Ytterbium Oxides

In this chapter, we study the erbium-ytterbium oxide ($Er_xYb_{2-x}O_3$) alloy system. With a maximum erbium concentration of 40 at.% or $N_{Er} = 2.72 \times 10^{22}$ cm^{-3}, erbium-ytterbium oxide is the compound with the highest achievable erbium concentration studied in this thesis.

By means of XRD analysis, we investigate the structural properties of $Er_xYb_{2-x}O_3$ thin films deposited on SiO_2. Studying the XRD peak shifts as a function of erbium concentration (i.e. x in $Er_xYb_{2-x}O_3$) allows us to demonstrate full alloying across the entire erbium concentration range. Moreover, we found that at annealing temperatures above 1000°C, interaction of the oxide films with the SiO_2 substrate can lead to crystallization of erbium-ytterbium silicates.

Secondly, we discuss the photoluminescence properties as a function of erbium concentration and annealing temperature. We show a successful increase of PL quantum efficiency with increasing annealing temperature and decreasing erbium concentration. The latter is explained by a reduction of parasitic *energy migration* through dilution of erbium with ytterbium, consistent with yttrium dilution known from literature. Moreover, we provide direct evidence for ytterbium to erbium energy transfer in $Er_xYb_{2-x}O_3$ by studying the effective erbium excitation cross section at 980nm and its dependence of ytterbium concentration.

4.1 Deposition

The $Er_xYb_{2-x}O_3$ thin films were deposited by means of RF magnetron co-sputtering of Er_2O_3 and Yb_2O_3. Seven different alloy concentrations with different erbium-ytterbium ratio (i.e. x in $Er_xYb_{2-x}O_3$) were deposited by controlling the RF power applied to the two sputtering targets, using the method described in Chapter 3. The different alloy concentrations are shown in Table 4.1. The table shows the nominal erbium concentration (x-values as well as concentration in cm^{-3}), the RF power applied to the Er_2O_3 and Yb_2O_3 sputtering targets, deposition time and film thickness measured by profilometry. The targeted thickness for each film was 200nm. The concentrations in cm^{-3} are calculated from the densities of Er_2O_3 and Yb_2O_3 found in the ICDD database (resp. pdf references 00-008-0050 and 00-041-1106).

Table 4.1: Parameters for sputter deposition of $Er_xYb_{2-x}O_3$

x(Er)	[Er] (cm^{-3})	P(Er_2O_3) (W)	P(Yb_2O_3) (W)	Time (min)	Thickness (nm)
0.07	9.80×10^{20}	16	113	42	207 ± 4
0.19	2.66×10^{21}	26	108	42	211 ± 3
0.30	4.19×10^{21}	38	103	42	207 ± 5
0.50	6.96×10^{21}	54	88	42	180 ± 3
1.00	1.38×10^{22}	96	58	42	191 ± 3
1.41	1.93×10^{22}	96	29	60	194 ± 3
2.00	2.72×10^{22}	96	0	86	182 ± 4

As shown in the table, deposition of a 200nm $Er_xYb_{2-x}O_3$ film on SiO_2 takes 42min for compositions where $0.07 \leq x \leq 1.00$. Because of the slower deposition rate of Er_2O_3 compared to Yb_2O_3 (see Figure 3-3), the depositions of $Er_{1.41}Yb_{0.59}O_3$ and pure Er_2O_3 are slower and take 60 min and 86 min, respectively.

The films were deposited on 4″ Si substrates coated with 3μm of thermal silicon oxide. Because of its low refractive index of $n = 1.45$ compared to rare earth oxides ($n \sim 1.92$) and silicates ($1.74 < n < 1.81$), SiO_2 is the substrate of choice to achieve strong optical confinement in the gain media studied in this thesis.

4.2 Structural properties

4.2.1 Crystallinity as a function of annealing temperature

Figure 4-1 shows the XRD spectra of the $Er_{0.30}Yb_{1.70}O_3$ film deposited on SiO_2, measured after deposition and after annealing for 30min in O_2 at different temperatures. For the sake of visibility of the smaller peaks, particularly in the pattern for the film annealed at 1200°C, a logarithmic scale was used and the spectra were offset for clarity.

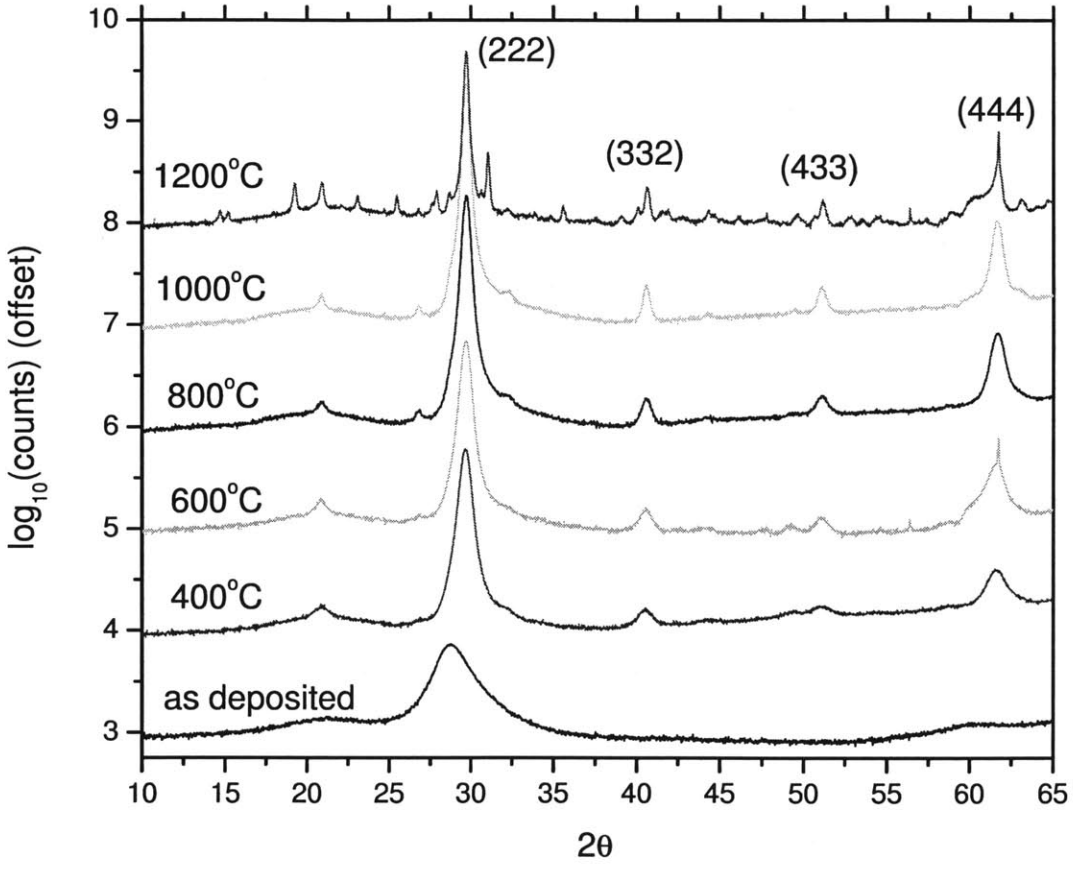

Figure 4-1: XRD patterns (logarithmic scale) of $Er_{0.30}Yb_{1.70}O_3$ on SiO_2 for different annealing temperatures. The spectra are offset for clarity. The (hkl) peaks corresponding to the cubic Yb_2O_3 phase (pdf 00-041-1106) are indictated.

After deposition, the film already shows onset of the crystalline peaks that appear after annealing. Note that the substrate was not heated during deposition, but the

substrate temperature reaches up to 250°C after 1h of deposition [9]. The peaks in the XRD patterns for the annealed films can be matched to the crystal structure of cubic Yb_2O_3 (see section 4.2.2). The (hkl) numbers corresponding to the strongest peaks are indicated in the plot. The prominence of the (222) and (444) peaks compared to their intensities in the pdf database entry for Yb_2O_3 powder indicate that the film exhibits a preferred orientation (i.e. *texture*) in the (111) direction upon crystallization.

Grain size and microstrain

Figure 4-1 also shows that increasing the annealing temperature causes the XRD peaks to become sharper, which is in line with increasing grain sizes and decreasing microstrain at higher annealing temperatures. Figure 4-2 shows the Williamson-Hall plot (see section 3.2.3) for the $Er_{0.30}Yb_{1.70}O_3$ thin film on SiO_2 annealed at different temperatures. The crystallite size and microstrain calculated from the slope and the intercept of the linear regressions are summarized in Table 4.2.

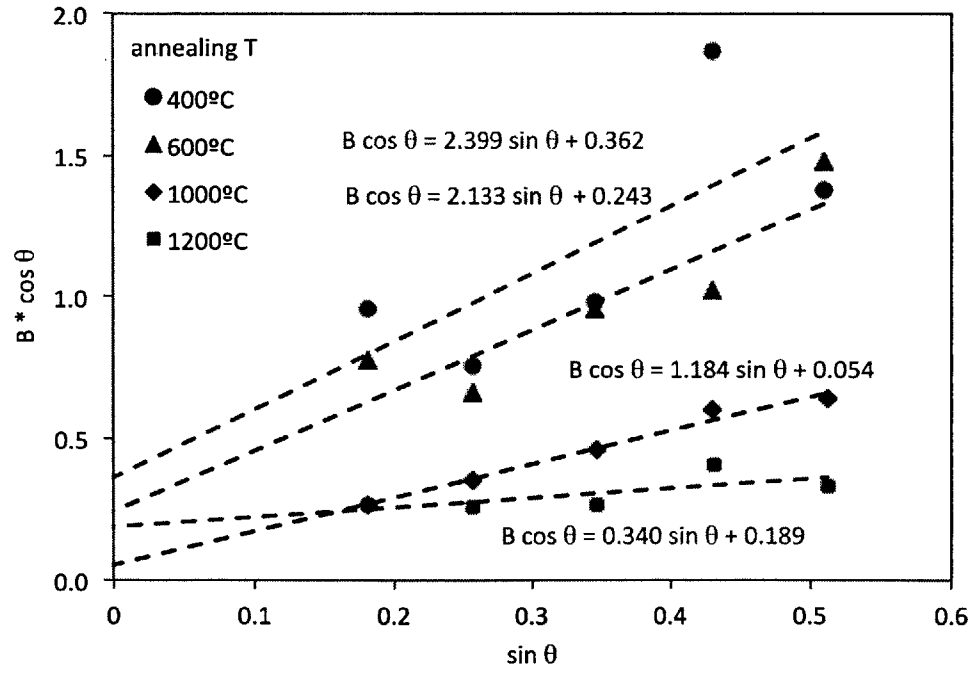

Figure 4-2: Williamson-Hall plot for the cubic oxide phase crystallized at different annealing temperatures in the $Er_{0.30}Yb_{1.70}O_3$ thin film on SiO_2.

Table 4.2 shows that the microstrain decreases monotonically with annealing temperature, which indicates that annealing reduces lattice defects. This is confirmed by the observation in section 4.3 that the PL lifetime increases monotonically with annealing temperature as well, due to a reduction of the rate of non-radiative decay to lattice defects.

Table 4.2: Crystallite size and microstrain in $Er_{0.30}Yb_{1.70}O_3$ thin films on SiO_2 annealed at different temperatures, derived from the Williamson-Hall plots.

annealing T (°C)	crystallite size (Å)	microstrain (%)
400	242 ± 151	1 ± 1
600	364 ± 193	0.9 ± 0.3
800	545 ± 383	0.7 ± 0.5
1000	≥1000	0.52 ± 0.05
1100	454 ± 194	0.3 ± 0.2
1200	468 ± 150	0.1 ± 0.1

The oxide grain size in Table 4.2 increases with annealing temperature up to T = 1000°C, when grain size broadening becomes smaller than the instrument broadening introduced by the X-ray diffractometer. As a result, we conclude that the grain size for the film annealed at 1000°C is larger than our detection limit of 1000Å. The increase of grain size with annealing temperature in this regime is consistent with thermally activated grain growth.

These results are fully consistent with literature reports on the structural properties of Er_2O_3 thin films deposited on Si and SiO_2. Mikhelashvili et al. [143] deposited 100nm Er_2O_3 thin films on (100) Si by e-beam evaporation and subsequent annealing in O_2 for 1h at 750°C. The films crystallized into the cubic phase with a <111> texture and with grain sizes between 20 and 50 nm. Singh et al. [144] deposited Er_2O_3 thin films on (100) Si by metalorganic chemical vapor deposition (MOCVD), followed by a post-deposition anneal at temperatures up to 700°C in O_2. The grain sizes after annealing are in the range 18-35nm.

However, at temperatures above 1000°C, the oxide grain size *decreases* with a further increase of annealing temperature. T = 1000°C corresponds to the crystallization

temperature of rare earth silicates, which can be formed due to chemical reactions of the oxide thin films with the SiO_2 substrate. Indeed, Figure 4-1 shows that at T > 1000°C, XRD peaks corresponding to rare earth silicate phases appear. The reduction in oxide grain size at these temperatures can be explained by the formation of silicate phases at the expense of the oxide phase, leading to a reduction in oxide grain size. The formation of silicates due to interaction of the rare earth oxide films with the SiO_2 substrate is discussed in more detail in section 4.2.4

4.2.2 $Er_xYb_{2-x}O_3$ crystal structure

Figure 4-3 shows the unit cell of the crystal structure of Yb_2O_3 (pdf 00-041-1106) that was matched to the XRD patterns in Figure 4-1. The phase has a body centered cubic (bcc) lattice with symmetry group Ia-3 and a lattice parameter a = 10.4347Å. The same phase is also known for Er_2O_3 (pdf 00-008-0050), with a lattice parameter a = 10.5480Å that is only 1% different from the Yb_2O_3 lattice parameter. This allows for good alloying of the two oxides, as discussed in section 4.2.3.

The cubic rare oxide phase is well-known from research on yttrium oxide (Y_2O_3). The unit cell contains 32 rare earth ions in 2 non-equivalent crystal sites, indicated by Yb1 (magenta spheres) and Yb2 (yellow spheres) in Figure 4-3. The ratio of Yb2:Yb1 sites equals 3:1, meaning that per unit cell there are 24 rare earth ions in site 2 and 8 rare earth ions in site 1. Both the Yb1 and the Yb2 crystal sites have sixfold coordination with oxygen ions, but the Yb1 sites is an inversion center, which makes electric dipole transitions in Yb1 forbidden. The erbium luminescence in $Er_xYb_{2-x}O_3$ therefore mainly originates from ions in site 2.

4.2.3 Er_2O_3-Yb_2O_3 alloying

Figure 4-4 shows the (222) peak for the $Er_xYb_{2-x}O_3$ films annealed at 1000°C. The data show a clear shift of the (222) peak towards lower angles, i.e. larger *d*-spacing, for increasing Er concentration. Since Er is the larger ion compared to Yb, this agrees

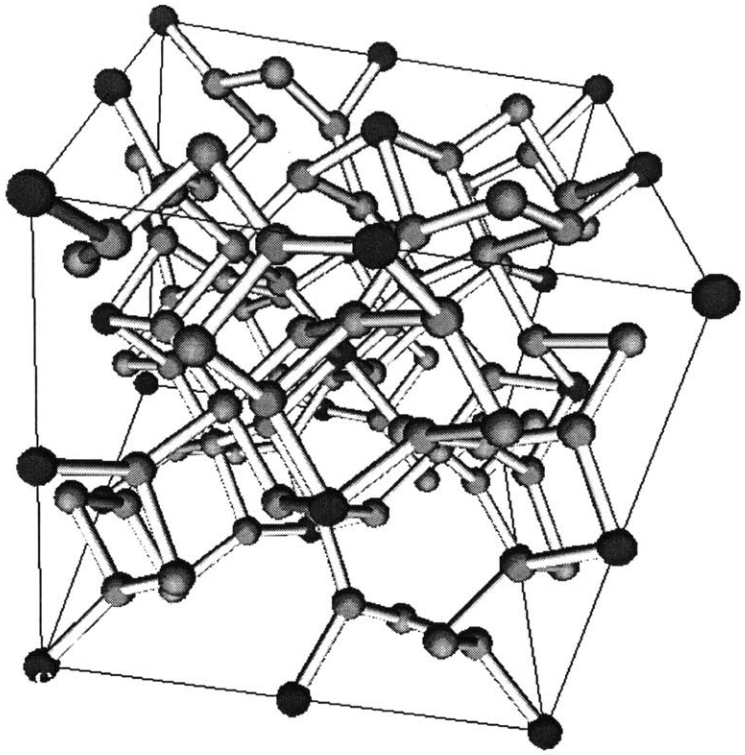

Figure 4-3: Unit cell of cubic Yb_2O_3 crystal structure, space group Ia-3 (pdf 00-041-1106). Magenta spheres = Yb1, yellow spheres = Yb2, cyan spheres = O.

with an expected increase in unit cell as the Er:Yb ratio increases. The observation of one shifting XRD peak rather than two separate peaks with varying intensities indicates alloying of Er_2O_3 and Yb_2O_3 rather than phase separation.

The exact peak position was determined by means of the peak profile fitting function in the XRD analysis software Highscore Plus, which fits a combination of a Gaussian and Lorentzian peak to the XRD data. The results are shown in Figure 4-5. From the 2θ-position we can now calculate the corresponding d-spacing between the (222) lattice planes using Bragg's law

$$2d \sin\theta = n\lambda \tag{4.1}$$

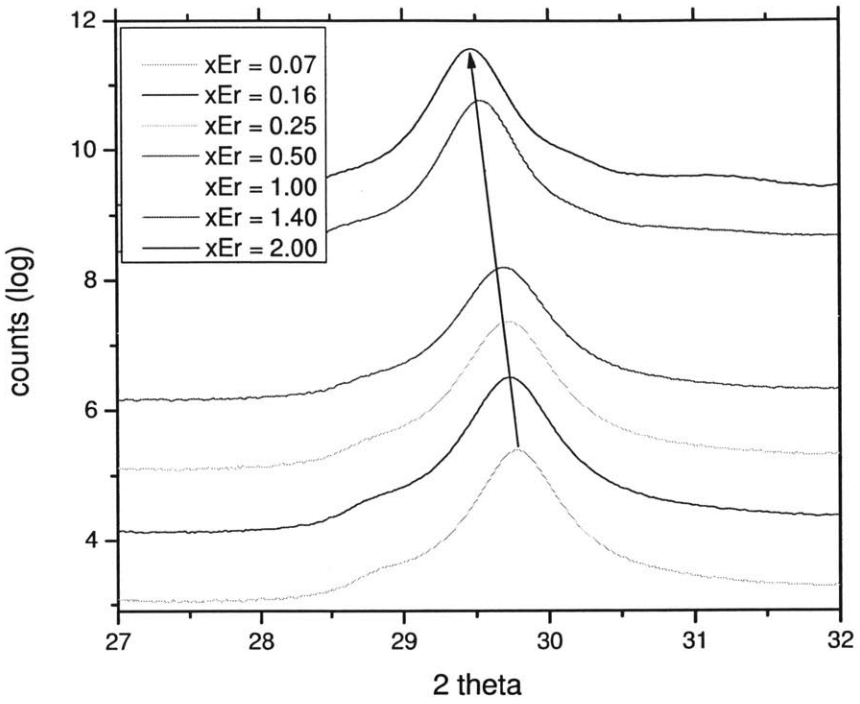

Figure 4-4: Shift of (222) peak with x in $Er_xYb_{2-x}O_3$. Note that the y-axis shows the logarithm of the XRD data, offset per data set for clarity.

Given that the spacing between (hkl) planes in a cubic crystal is given by

$$d_{hkl} = \frac{a}{\sqrt{h^2 + k^2 + l^2}} \tag{4.2}$$

the lattice parameter a can now be calculated as

$$a = 2\sqrt{3}\, d = \frac{\sqrt{3}\lambda}{\sin\theta} \tag{4.3}$$

With $\lambda = 1.540598$Å, we calculate the blue data set on Figure 4-5. A linear regression fit to the data shows almost the exact slope that would be obtained from the bulk Er_2O_3 and Yb_2O_3 entries in the pdf database, shown as the green line in the plot. The overall lattice parameter in the thin films, however, is smaller by about 0.38% than the bulk data from the database entries. This may be due to compressive strain as a consequence of processing.

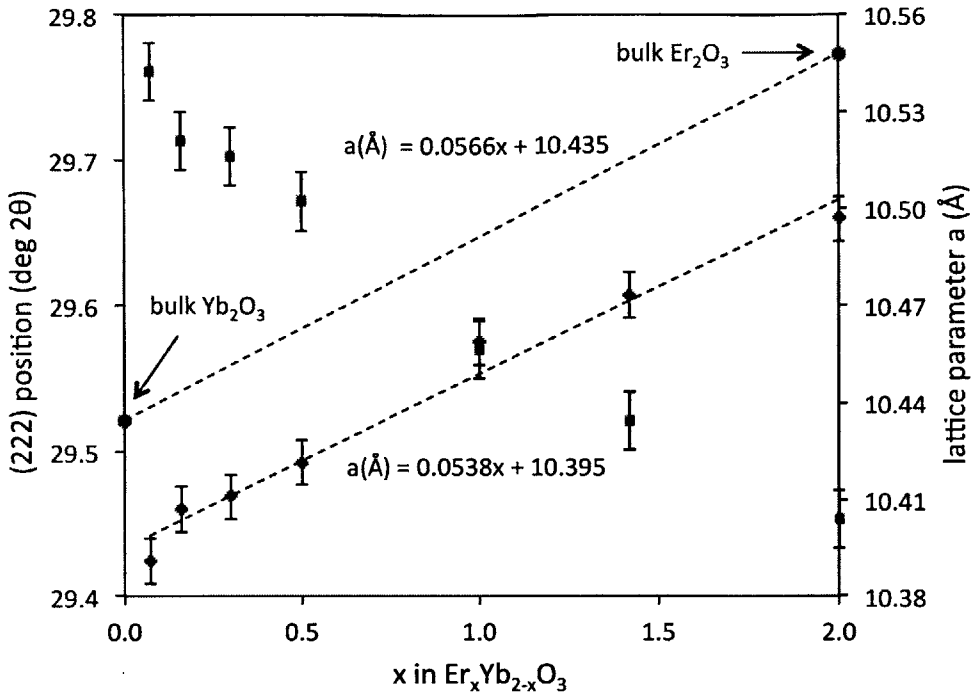

Figure 4-5: 2θ shift of (222) peak (red data set, left y-axis) and lattice parameter a (blue data set, right y-axis) as a function of x(Er). The green lines correspond to the database entries for bulk Yb_2O_3 and Er_2O_3.

4.2.4 Rare earth silicate formation at annealing T > 1000°C

As discussed above, silicate peaks appear in the XRD patterns of the oxide films annealed at temperatures above 1000°C. This is due to an interfacial reaction of the sputtered rare earth oxide film with the SiO_2 substrate. The silicate peaks in the XRD patterns are identified as B-monosilicate and β-disilicate phases. Using Rietveld refinement to fit the measured XRD profile to the database entries for the different phases identified, the amount of each phase in the film can be quantified.

Rietveld refinement was performed on the XRD pattern of $Er_{0.30}Yb_{1.70}O_3$ annealed at 1200°C. Figure 4-6 shows a part ($13° < 2\theta < 33°$) of the XRD data (black dotted line) with the theoretical fit obtained by Rietveld analysis (grey line). A square-root scaled y-axis ($y = \sqrt{counts}$) is used to resolve the smaller peaks; on a linear y-axis the small peaks would be obscured by the very intense peak Yb_2O_3 (222)-peak around

30°. The blue, red and green peaks correspond to ytterbium oxide, B-monosilicate and β-disilicate phases in the pdf database, respectively. Phase quantification shows that the film consists of 35.9% Yb_2O_3, 40.8% B-type Yb_2SiO_5 and 23.3% β-type $Yb_2Si_2O_7$, with an error in the mole fractions of 1%.

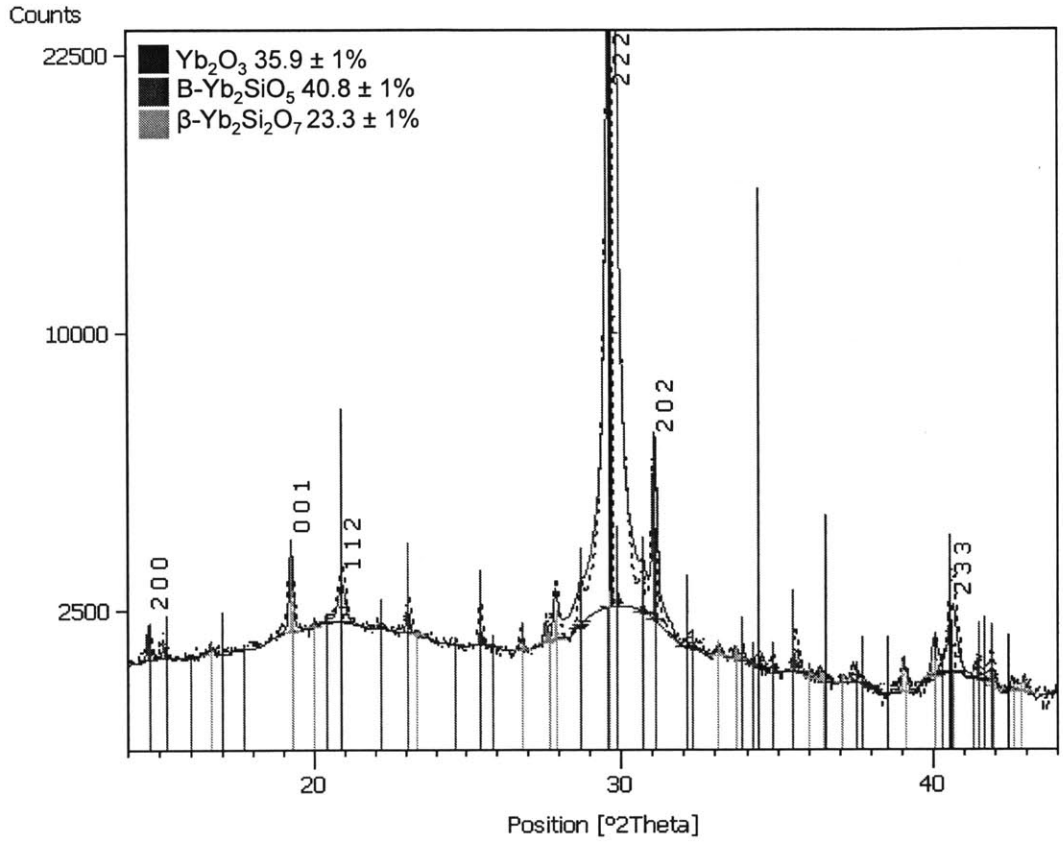

Figure 4-6: XRD pattern of $Er_{0.30}Yb_{1.70}O_3$ sputtered on SiO_2 after a 30min post-deposition anneal at 1200°C in O_2. A square-root y-axis ($y = \sqrt{counts}$) is used to make the smaller peaks visible. Black dotted line = XRD data, grey line = Rietveld fit. Blue, red and green peaks are peaks from the database.

Grain size and microstrain revisited

We saw in section 4.2.1 that the oxide grain size decreases beyond T > 1000°C, which corresponds to the crystallization temperature of rare earth silicates. We can

now analyze the silicate grain growth at these temperatures. Figure 4-7 compares the Williamson-Hall plots corresponding to the three different phases identified in the Rietveld section. The crystallite size and microstrain numbers derived from this figure are summarized in Table 4.3.

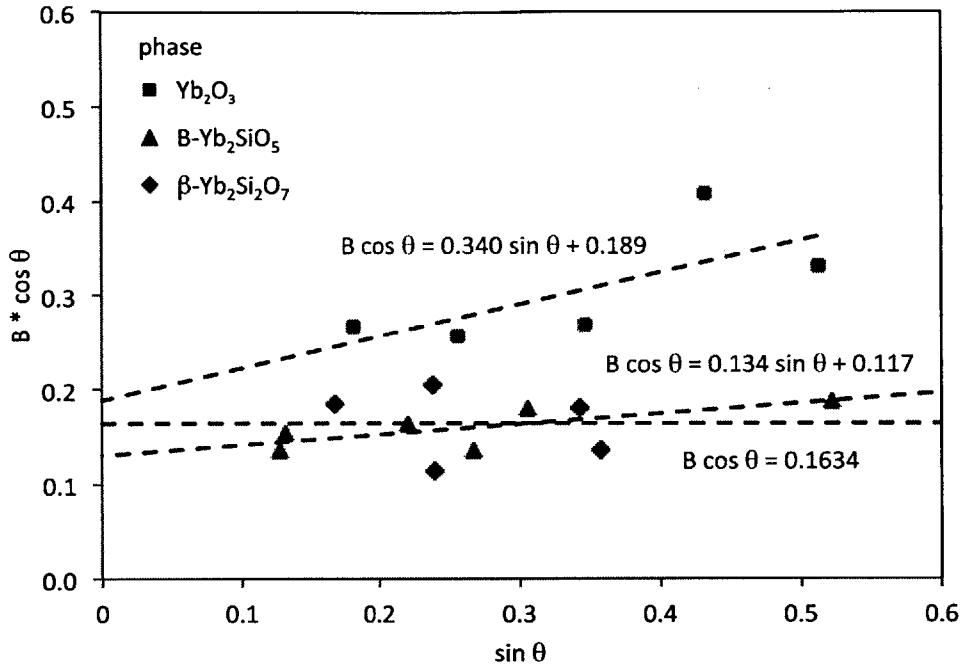

Figure 4-7: Williamson-Hall plot corresponding to the three different phases (oxide, B-monosilicate and β-disilicate) crystallized in the $Er_{0.30}Yb_{1.70}O_3$ thin film annealed at 1200°C.

Table 4.3: Crystallite size and microstrain derived from the Williamson-Hall plot for different phases crystallized in $Er_{0.30}Yb_{1.70}O_3$ thin film annealed at 1200°C.

phase	crystallite size (Å)	microstrain (%)
Yb_2O_3	468 ± 150	0.1 ± 0.1
B-Yb_2SiO_5	678 ± 80	0.05 ± 0.03
β-$Yb_2Si_2O_7$	539 ± 56	-

It is seen that all three phases exhibit negligible microstrain. In fact, the best fit for the β-$Yb_2Si_2O_7$ was obtained by assuming crystallite size broadening only (i.e. no microstrain, or a linear regression with slope zero). This observation is consistent with the explanation that annealing reduces lattice defects. The grain sizes of the

silicates phases are 53.9nm and 67.8nm, slightly larger than the oxide grain size of 46.8nm and comparable to the disilicate grain size at 1100 and 1200°C measured in Chapter 5. These observations are consistent with the reduction in oxide grain size due to formation of silicates at the expense of the oxide.

4.3 Photoluminescence properties

4.3.1 PL dependence on annealing temperature

Figure 4-8 shows the PL spectrum of the $Er_{0.30}Yb_{1.70}O_3$ film annealed at different temperatures. The spectra are offset by 0.1 per increasing annealing temperature for clarity. Two trends are noteworthy. First of all, it is clear that the photoluminescence increases dramatically with annealing temperature. Note that for the sake of visibility, the spectra at lower annealing temperatures are multiplied by factors of 20, 20 and 5, respectively. As shown in Figure 4-9, the increase in PL intensity goes along with an increase in PL lifetime, indicating that it is due to an increasing PL quantum efficiency because of reduction of non-radiative decay paths.

Secondly, the spectral shape of the PL spectrum can clearly be related to the phases present. At annealing temperatures below the crystallization temperature for silicates ($T \sim 1000°C$), the films crystallize as rare earth oxides. The spectra of the films annealed at 600°C, 800°C and 900°C (not shown) differ in intensity, but the spectral shape remains the same. As soon as the annealing temperature exceeds 1000°C, silicate phases crystallize and a change in spectral shape is noticed.

Figure 4-9 shows the integrated PL intensity and measured decay lifetimes for the spectra measured above. It is seen that the lifetime and PL intensity increase together. The only outlier is the sample annealed at 1000°C, where the PL intensity is lower than expected from the lifetime measurement. This film suffers from upconversion that suppressed the measured PL intensity. The lifetime shown in Figure 4-9 is the lifetime fit to the single exponential tail after the initial fast decay due to upconversion.

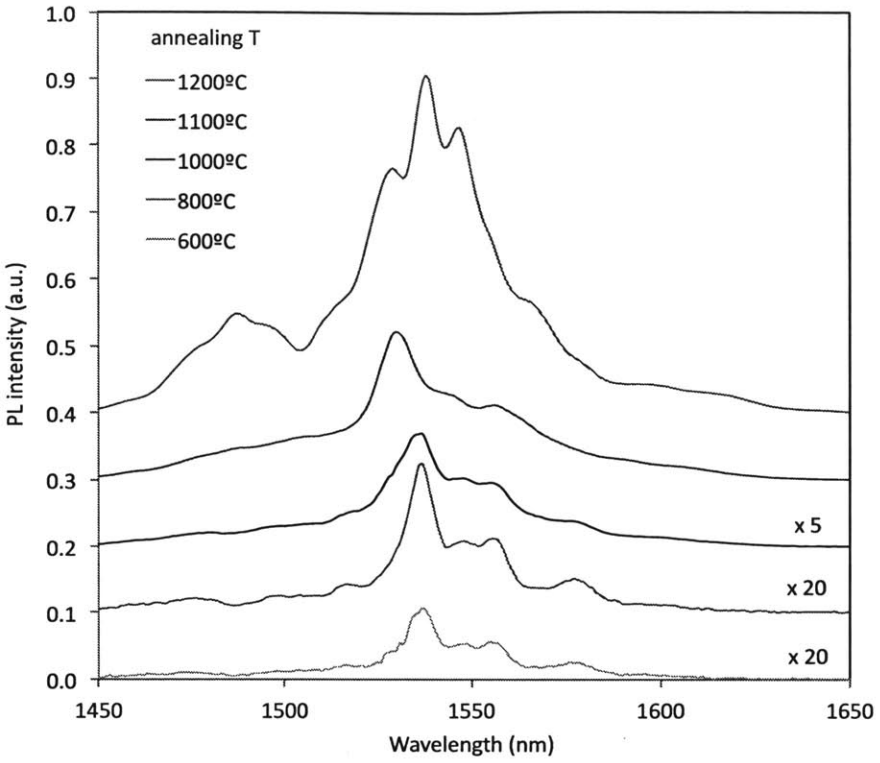

Figure 4-8: $Er_{0.30}Yb_{1.70}O_3$ PL (λ_{ex} = 488nm) for different annealing temperatures. For the sake of clarity, the spectra are offset by 0.1 a.u. for each measurement at higher annealing temperature and the spectra at low annealing temperatures are scaled for visibility. The scaling factors are indicated in the figure.

The observed concurrent increase in PL intensity and lifetime indicates that the excitation cross section at λ =488 nm is not significantly different for rare earth oxides and silicates, as the PL intensity is given by the expression

$$I_{\mathrm{PL}}(\Phi) = \frac{N_1}{\tau_{\mathrm{rad}}} \propto \sigma \Phi \tau N_{\mathrm{Er}} \tag{4.4}$$

Since the photoluminescence is significantly more intense for the samples annealed at 1200°C than for other annealing temperatures, these films are the easiest and most interesting to investigate further. We will look more closely into these films and compare the dependence of their optical properties on erbium concentration.

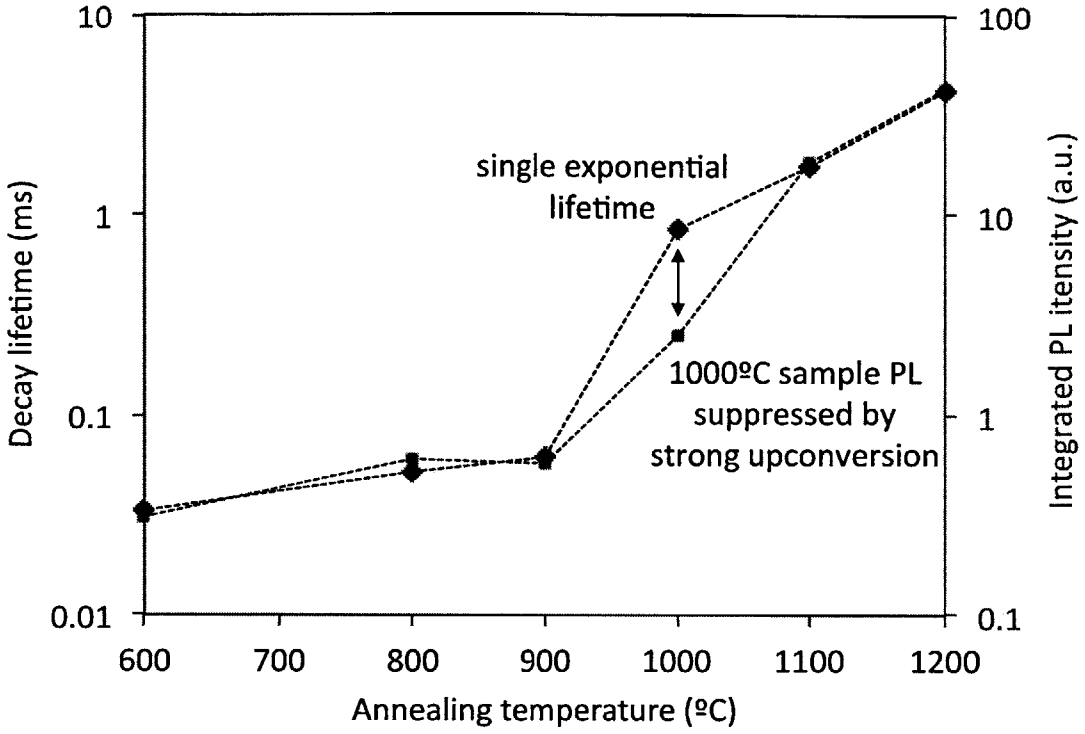

Figure 4-9: $Er_{0.30}Yb_{1.70}O_3$ decay time and integrated PL intensity (λ_{ex} = 488nm) as a function of annealing temperature. The integrated PL intensity and lifetime follow the same trend, except for the sample annealed at 1000°C (see text).

4.3.2 PL spectra for $Er_xYb_{2-x}O_3$ films annealed at 1200°C

Figure 4-10 shows the spectra of the different $Er_xYb_{2-x}O_3$ films on SiO_2 annealed at 1200°C. The spectra have been normalized and offset to allow for comparison of their spectral shapes. As the figure shows, three different PL spectra can be distinguished: the three films with lowest erbium concentration have the same spectrum, as do the three films with the highest erbium concentration. The film with x(Er) = 0.50 has a spectrum that is a mixture of the other two PL spectra.

The spectral shape can be related to the phases present in the film. As explained in the Rietveld analysis section, the films with low erbium concentration consist of a mixture of rare earth oxide, monosilicate and disilicate due to interaction with the SiO_2 substrate. No quantitative analysis was performed on the films with higher er-

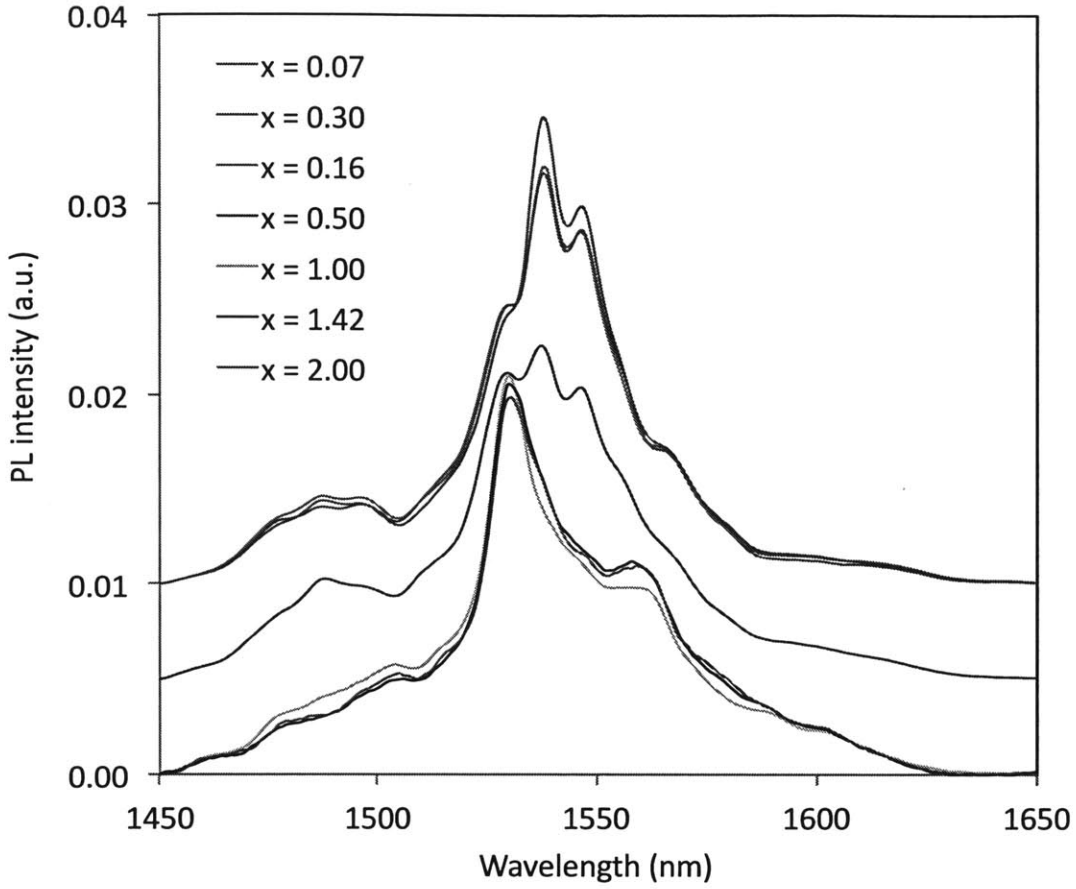

Figure 4-10: Room temperature PL spectra of $Er_xYb_{2-x}O_3$ films annealed at 1200°C.

bium concentration, but the A-monosilicate phase was identified in the XRD pattern. The PL spectra at high and low erbium concentrations can thus be related to the A-monosilicate phase for high x(Er) and the B-monosilicate and β-disilicate phase for low x(Er), respectively.

4.3.3 PL intensity as a function of erbium concentration

Figure 4-11 shows the integrated PL intensity between 1450nm and 1650nm as a function of pump power, in the low-power, linear regime described in Chapter 2,

where the PL intensity is given by the expression

$$I_{\mathrm{PL}}(\Phi) \propto \sigma \Phi N_{\mathrm{Er}} \frac{\tau}{\tau_{\mathrm{rad}}} = \sigma \Phi N_{\mathrm{Er}} \eta \tag{4.5}$$

where $\eta = \tau/\tau_{\mathrm{rad}}$ is the PL quantum efficiency.

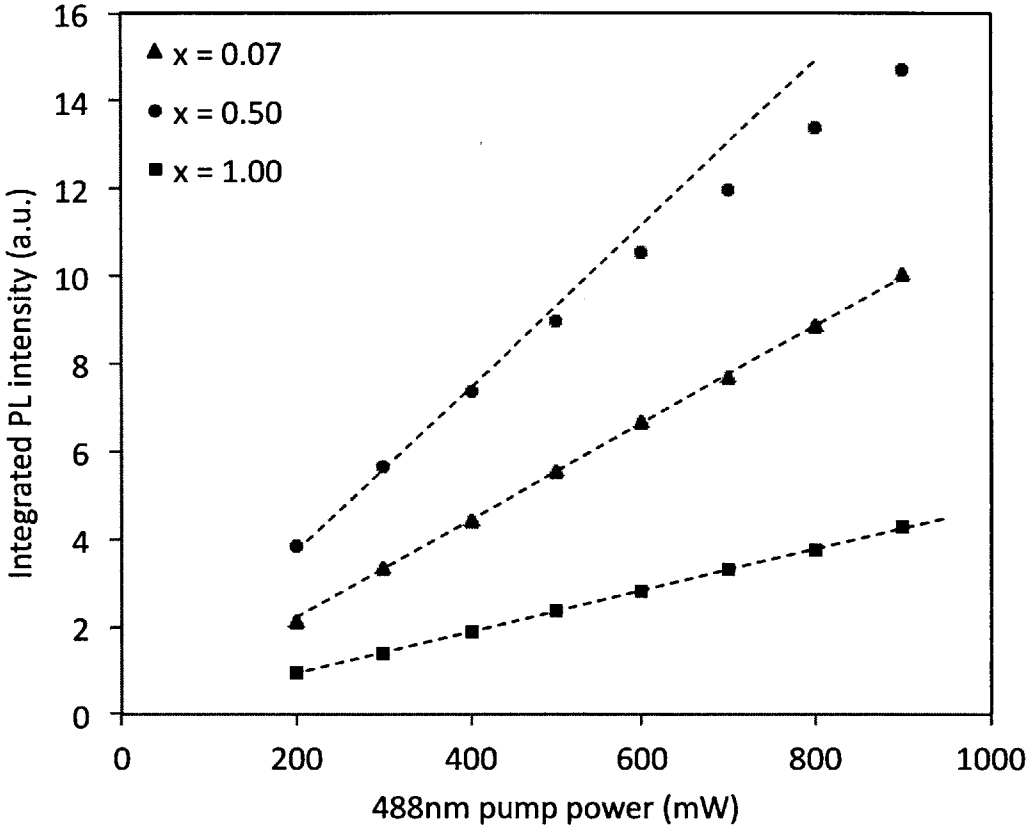

Figure 4-11: Integrated room temperature PL spectra of $Er_xYb_{2-x}O_3$ films annealed at 1200°Cin the linear regime excited at $\lambda = 488$nm pumping.

Apart from experimentally demonstrating the linear dependence between PL intensity and photon flux at low pump powers, Figure 4-11 also shows that different erbium concentrations result in different PL intensities. Between the three erbium concentrations shown in Figure 4-11, the film with intermediate concentration x(Er) = 0.50 has a higher PL intensity than the films at lower (x(Er) = 0.07) and higher (x(Er) = 1.00) erbium concentrations.

Figure 4-12 shows the slopes of the integrated PL intensity in the linear regime as a function of erbium fraction x excited at λ =488 nm (blue data, right y-axis) and λ =980 nm (red data, left y-axis). Both data sets are normalized so that the integrated PL intensity for pure Er_2O_3 (x=2.0) equals 1. Note that the y-scale for the 980nm data is 6 times larger than the scale for the 488nm data.

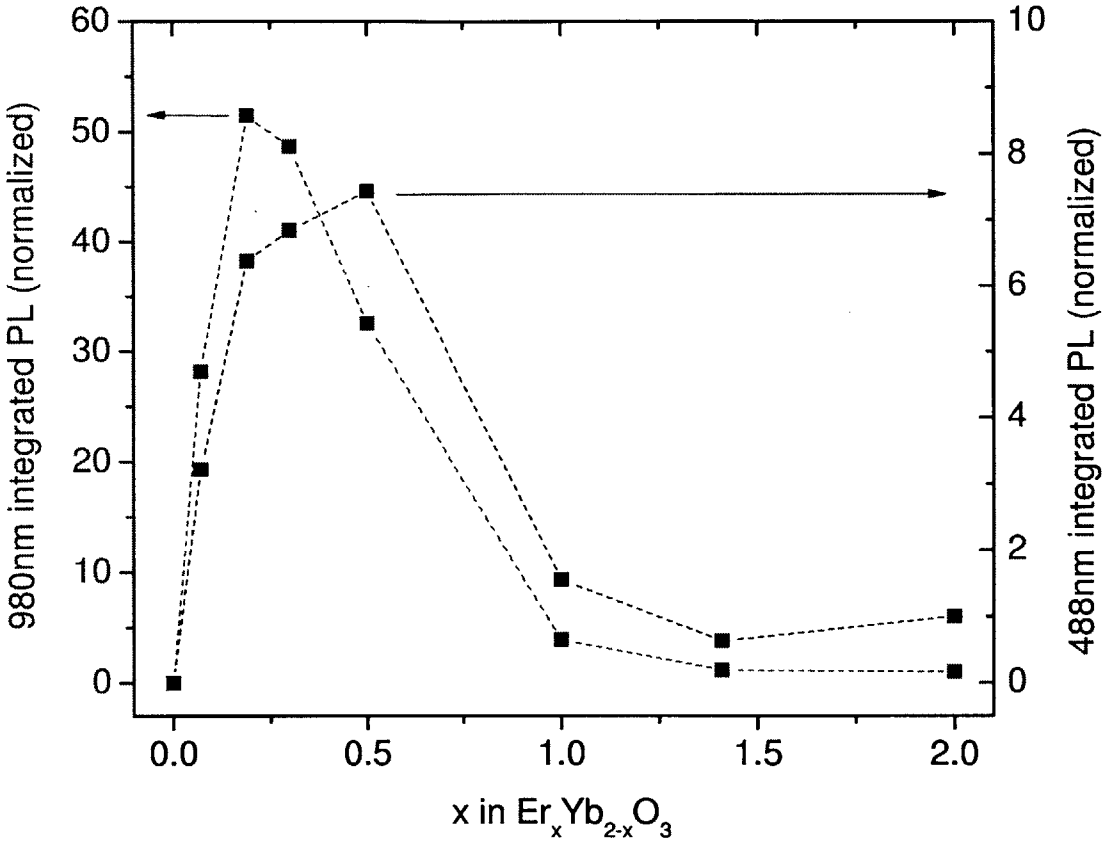

Figure 4-12: Integrated PL intensity between 1450nm and 1650nm excited at 488nm and 980nm light, respectively. Both data sets are normalized to PL(Er_2O_3) = 1.

Three different trends are noteworthy in the data in Figure 4-12. First of all, the data are a good demonstration of the effect of energy migration at high erbium concentrations. In the absence of concentration quenching effects, the PL intensity would increase monotonically with the concentration of erbium luminescence centers. However, after an initial increase of PL intensity with erbium concentration, it is seen that the PL intensity reaches a maximum and subsequently decreases with erbium

concentration. This indicates a decrease in PL quantum efficiency (see Equation 4.5) due to energy migration. This will be discussed in more detail in section 4.4.

Secondly, the erbium concentration at which the PL reaches a maximum is different for 488nm excitation and 980nm excitation. In the case of 980nm excitation, the PL intensity peaks at lower x (i.e. lower Er and higher Yb concentration in $Er_xYb_{2-x}O_3$) than in the case of 488nm excitation. Thirdly, the peak intensity for 980nm excitation is a factor 52 stronger than the intensity at x = 2.0 (normalized to 1), whereas the peak intensity for 488nm excitation is onlyr 7.5 times stronger than the intensity at x = 2.0. The second and third observation clearly indicate that ytterbium plays an important role as a *sensitizer* for erbium at 980nm, increasing its effective excitation cross section. This effect is absent in the case of direct excitation of Er^{3+} at 488nm, since Yb^{3+} has no energy levels at 488nm and Er^{3+} is thus excited directly (see section 2.4.3). The role of Yb^{3+} as a sensitizer is investigated in more detail in section 4.5.

4.4 Quantum efficiency enhancement through dilution of Er^{3+}

Figure 4-13 shows the PL decay curves in the linear regime (low pump flux) for the three oxide films also shown earlier in Figure 4-11 (x=0.07, 0.50 and 1.00). Two aspects of the decay curves are noteworthy. First of all, the decay for all three concentrations follows a single exponential decay in the linear regime, as illustrated by the straight lines in the semilog plot. Secondly, the decay lifetime decreases sharply with increasing erbium concentration.

The strong dependence of decay rate with erbium concentration can be attributed to the concentration quenching effects discussed in section 2.4.2. Since upconversion in negligible in the linear pump regime (moreover, upconversion causes a decay that is not a single exponential), the variation of decay rates with erbium concentration

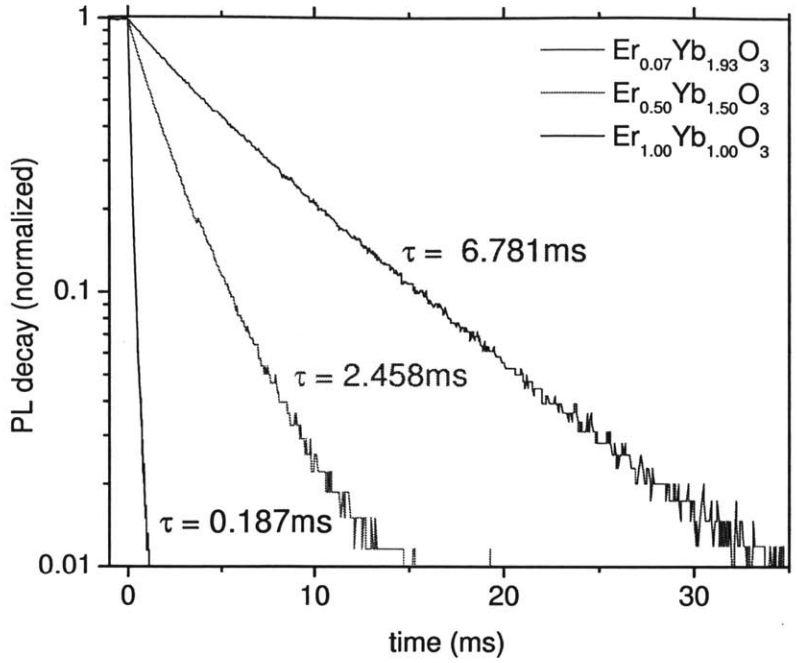

Figure 4-13: Decay curves of $Er_xYb_{2-x}O_3$ annealed at 1200°C for different x, showing single exponential decay with different decay rate as a result of energy migration.

can be attributed to energy migration: at increasing erbium concentration, dipole-dipole interactions between the different Er^{3+} ions can cause their excitation energy to migrate to quenching centers. At high erbium concentrations, the rate for this non-radiative decay mechanism can completely dominate the radiative decay rate, thereby decreasing the luminescence quantum efficiency dramatically. In terms of radiative and non-radiative decay rates, we arrive at

$$\eta = \frac{\tau}{\tau_{\text{rad}}} = \frac{W_{\text{rad}}}{W_{\text{rad}} + W_{\text{n-rad}}} \ll 1 \quad \text{if} \quad W_{\text{rad}} \ll W_{\text{n-rad}} \tag{4.6}$$

The decay times in the linear flux regime for all $Er_xYb_{2-x}O_3$ films annealed at 1200°C were fit by a single exponential decay curve. The lifetimes obtained from the fits are shown in Table 4.4. According to Equation 4.6, the increase in lifetime from $\tau = 40\mu s$ at x = 2.0 to $\tau = 6.781ms$ at x = 0.07 corresponds to a 170× increase in quantum efficiency due to dilution.

The decay rate $W = 1/\tau$ calculated from the lifetime values in Table 4.4 is shown in

Table 4.4: Lifetimes of $Er_xYb_{2-x}O_3$

x(Er)	[Er] (cm^{-3})	lifetime (ms)
0.07	9.80×10^{20}	6.781
0.19	2.66×10^{21}	5.461
0.30	4.19×10^{21}	4.551
0.50	6.96×10^{21}	2.458
1.00	1.38×10^{22}	0.187
1.41	1.93×10^{22}	0.080
2.00	2.72×10^{22}	0.040

Figure 4-14 as a function of erbium concentration. Two regimes are apparent: one regime at low erbium concentration and another regime at high erbium concentration. The rates in the low concentration regime can be fit by a linear regression function according to the expression

$$W = W_{\text{rad}} + W_{\text{n-rad}} = \frac{1}{\tau_0} + C'_{\text{em}} N_{\text{Er}} \tag{4.7}$$

The intercept with the y-axis now determines the radiative decay rate $W_{\text{rad}} = 1/\tau_0$ in the absence of energy migration. We find a value of $\tau_0 = 8.0$ms, which is consistent with literature on erbium-yttrium oxides [116]. The slope of the linear fit is determined by the energy migration coefficient C'_{em} discussed in section 2.4.2. From the slope of 0.3139, we find $C'_{\text{em}} = 2.31 \times 10^{-23}$ $s^{-1}.cm^3$ for low x. Note that the coefficient C'_{em} is not a fundamental material property, but depends on the concentration of quenching centers N_q as shown in Equation 2.6.

In conclusion, we have shown that ytterbium can act as a dilutant of erbium, yielding similar results as erbium dilution by yttrium. A 170× increase in luminescence quantum efficiency η is achieved through reduction of the non-radiative decay rate related to energy migration.

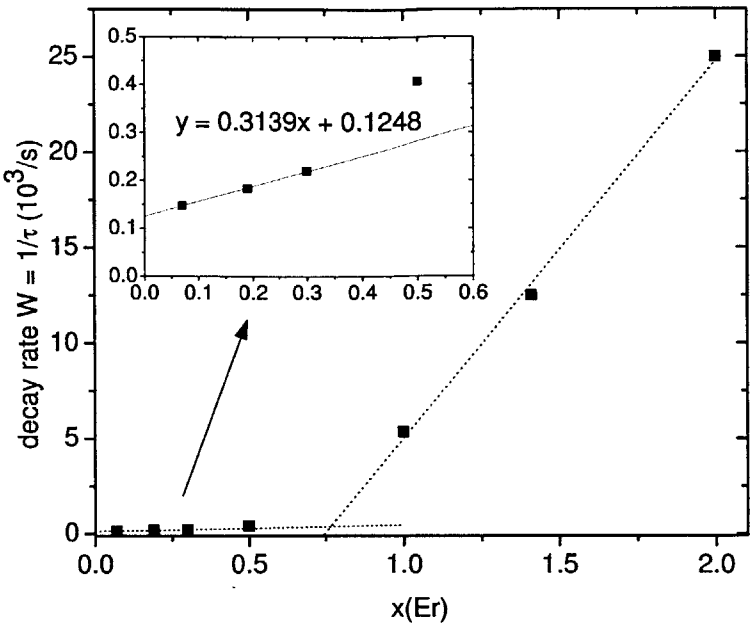

Figure 4-14: Decay rate of $Er_xYb_{2-x}O_3$ annealed at 1200°C as a function of xEr.

4.5 Sensitization of Er^{3+} by Yb^{3+}

A clear picture about the role of ytterbium other than as a dilutant is obtained by studying ratio of the PL intensities of $Er_xYb_{2-x}O_3$ excited at 980nm and 488nm. The dependence of PL intensity on erbium concentration for the two excitation wavelengths was already discussed in section 4.3.3 and displayed in Figure 4-12. According to Equation 4.5, the ratio between the two curves on Figure 4-12 should equal

$$\frac{I^{980}}{I^{488}} \propto \frac{\sigma^{980}}{\sigma^{488}} \tag{4.8}$$

The ratio of excitation cross sections $\sigma^{980}/\sigma^{488}$ in Equation 4.8 is shown in Figure 4-15 as a function of erbium concentration. The blue data points are calculated as the ratio of the integrated PL intensities I^{980}/I^{488} from Figure 4-12, normalized so that the ratio at x = 2.00 (pure Er_2O_3) equals 1. The blue line serves as a guide to the eye. A clear monotonic increase of $\sigma^{980}/\sigma^{488}$ with decreasing x (i.e. *decreasing* Er and *increasing* Yb concentrations in $Er_xYb_{2-x}O_3$) is observed. Since the excitation

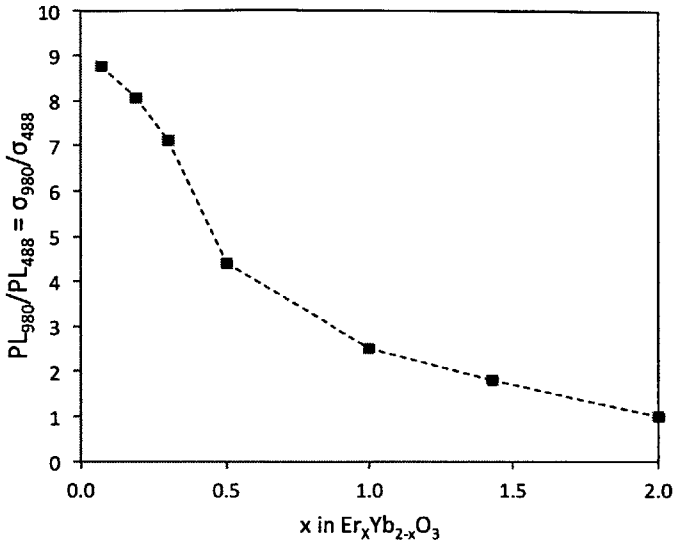

Figure 4-15: Ratio of excitation cross section $\sigma(\lambda = 980)/\sigma(\lambda = 488)$, normalized so that the ratio for pure Er_2O_3 equals 1. The dotted line serves as a guide to the eye.

cross section σ^{488} for direct excitation of erbium at $\lambda = 488$nm does not depend on the erbium or ytterbium concentration, this means that the excitation cross section σ^{980} at $\lambda = 980$nm increases monotonically with increasing ytterbium concentration. In other words, ytterbium increases the *effective* erbium excitation cross-section at $\lambda = 980$nm.

As an additional argument, rather than looking at the ratio of the excitation cross sections $\sigma^{980}/\sigma^{488}$, we can calculate the excitation cross sections directly from Equation 4.5 as

$$\sigma = K \cdot \frac{I_{\mathrm{PL}}(\Phi)}{N_{\mathrm{Er}} \cdot \tau} \tag{4.9}$$

where K is a proportionality constant related to the PL collection efficiency of the measurement system and the radiative lifetime τ_{rad}. Since both the collection efficiency and the radiative lifetime are independent of erbium concentration, we can plot the trend of the excitation cross sections σ^{980} and σ^{488} as a function of erbium concentration using the right hand side of Equation 4.9. The results are shown in Figure 4-16.

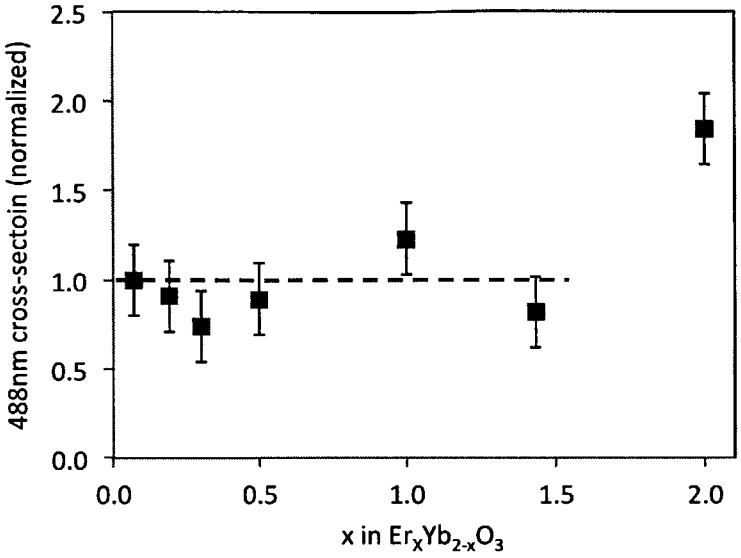

(a) Excitation cross section at 488nm, normalized so that $\sigma' = 1$ for $Er_{0.07}Yb_{1.93}O_3$.

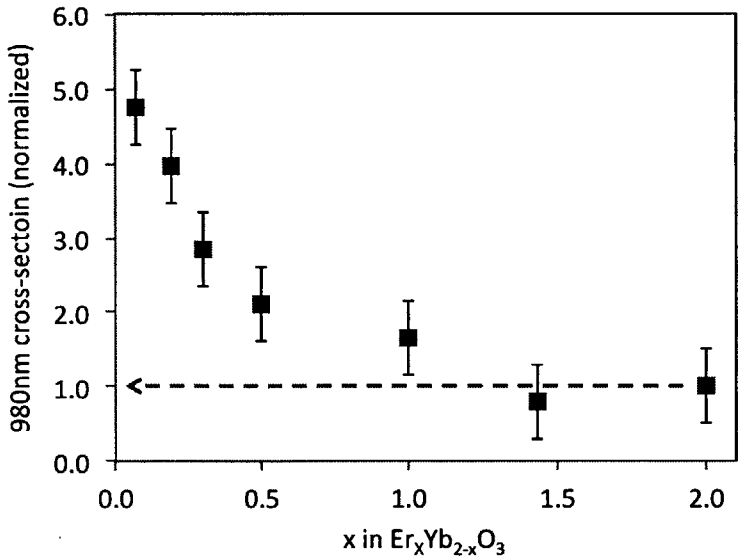

(b) *Effective* excitation cross section at 980nm, normalized so that $\sigma' = 1$ for Er_2O_3.

Figure 4-16: Erbium excitation cross sections at 488nm (direct excitation) and 980nm (excitation mediated by Yb) in $Er_xYb_{2-x}O_3$ films annealed at 1200°C.

It is clear that the excitation cross section σ^{488} for direct erbium excitation at $\lambda =$ 488nm is indeed independent of erbium concentration. Only for pure Er_2O_3 we see that the excitation cross section is about twice the cross section observed at lower erbium concentations. This can be explained by a phenomenon called *photon cutting*, where one 488nm photon excites two single erbium ions. This is an effect known to occur at very high erbium concentrations [52] and is unrelated to the presence of ytterbium. On the other hand, the excitation cross section σ^{980} at $\lambda = 980$nm increases monotonically with increasing ytterbium concentration. An 4.8× increase in effective erbium excitation cross section is obtained in the $Er_{0.07}Yb_{1.93}O_3$ film compared to the pure Er_2O_3 film.

4.6 Conclusion

In this chapter we studied the erbium-ytterbium oxide alloy system $Er_xYb_{2-x}O_3$. We demonstrated that because of their nearly identical ionic radii, Er^{3+} and Yb^{3+} ions can substitute each other in the $Er_xYb_{2-x}O_3$ crystal lattice, allowing solid solutions across the entire concentration spectrum between pure erbium oxide and pure ytterbium oxide. PL intensity and lifetime increase with annealing temperature, consistent with an increase in $Er_xYb_{2-x}O_3$ grain size and PL quantum efficiency. At annealing temperatures above 1000°C, rare earth silicates crystallize due to interfacial reactions between the sputtered $Er_xYb_{2-x}O_3$ films and the SiO_2 substrate. However, we found that the PL emission cross section for the rare earth silicates does not differ significantly from the emission cross section for rare earth oxides.

Intense photoluminescence around $\lambda = 1.54\mu$m was measured for the films annealed at 1200°C. Comparison of the PL intensity as a function of erbium concentration (x in $Er_xYb_{2-x}O_3$) for the excitation wavelengths $\lambda = 488$nm and $\lambda = 980$nm showed that the role of ytterbium is twofold.

First of all, dilution of erbium by substitution with ytterbium increases the PL quantum efficiency through a decrease of concentration quenching. This dilution effect is

consistent with the results for yttrium dilution described in literature. We demonstrated an increase in PL lifetime from $\tau = 40\mu s$ in pure Er_2O_3 to $\tau = 6.781ms$ in $Er_{0.07}Yb_{1.93}O_3$ due to a reduction of the non-radiative decay rate, corresponding to a $170\times$ increase in PL quantum efficiency.

Secondly, it was shown that the effective excitation cross section of Er^{3+} at $\lambda = 980nm$ increases monotonically with Yb^{3+} concentration, indicating sensitization of Er^{3+} by Yb^{3+} through resonant energy transfer at 980nm. An increase in excitation cross section in $Er_{0.07}Yb_{1.93}O_3$ by a factor 4.8 was observed compared to pure Er_2O_3.

Chapter 5

Erbium-Ytterbium Silicates

In this chapter, we investigate erbium-ytterbium silicates. As already discussed in section 2.2 and as illustrated in the Yb_2O_3-SiO_2 phase diagram in Figure 2-1, there are three different rare earth silicate compounds: rare earth monosilicates (RE_2SiO_5), rare earth disilicates ($RE_2Si_2O_7$) and rare earth oxyapatites with intermediate stoichiometry $7RE_2O_3 \cdot 9SiO_2$, corresponding to the chemical formula $RE_{9.33}Si_6O_{26}$. The monosilicate and the disilicate each have different polymorphic phases, i.e. different crystal structures with the same stoichiometry.

We will focus on the erbium-ytterbium disilicates ($Er_xYb_{2-x}Si_2O_7$) for two reasons. Firstly, the fact that the disilicates are the compound with the highest SiO_2 content of all the silicates should limit any interfacial reactions with the SiO_2 substrate, as was the case for the rare earth oxides discussed in Chapter 4. Secondly, literature comparing the luminescence properties of the pure erbium silicates Er_2SiO_5, y-$Er_2Si_2O_7$ and α-$Er_2Si_2O_7$ (i.e. not diluted with Yb or Y) concluded that the highest optical efficiency was found in the α-$Er_2Si_2O_7$ phase [114].

As in Chapter 4, we begin this chapter with a study of the structural properties of the $Er_xYb_{2-x}Si_2O_7$ thin films by means of XRD analysis. We identify and discuss the different silicate polymorphs that crystallize at different erbium-ytterbium compositions and at different annealing temperatures. Secondly, we discuss the photoluminescence

properties and relate the PL spectra to the silicate phases identified by XRD. We also measure the upconversion coefficient, which is a crucial parameter for modeling and optimizing a gain medium in Chapter 7.

5.1 Deposition

$Er_xYb_{2-x}Si_2O_7$ thin films were deposited on Si substrates coated with 3μm thermal SiO_2 by RF magnetron co-sputtering of Er_2O_3, Yb_2O_3 and SiO_2. The same seven erbium-ytterbium concentrations (i.e. x in $Er_xYb_{2-x}Si_2O_7$) were deposited as for the rare earth oxides studied in Chapter 4. In fact, the RF power applied to the Er_2O_3 and Yb_2O_3 sputtering targets and the deposition times are the same as for the rare earth oxides. The RF power applied to the SiO_2 sputtering target in order to deposit stoichiometric disilicate is determined by Equation 3.7 for the deposition rates:

$$Er_xYb_{2-x}Si_2O_7 \rightarrow \frac{[Er_xYb_{2-x}O_3]}{[SiO_2]} = \frac{1}{2} \Leftrightarrow \frac{r(Er_xYb_{2-x}O_3)}{r(SiO_2)} = 0.9471 \qquad (5.1)$$

This means that the deposition rate for SiO_2 should be 1.0559 (=1/0.9471) times larger than the $Er_xYb_{2-x}O_3$ deposition rate. Given that the rare earth oxide films were 200nm thick, the total film thickness for the sputtered disilicates is therefore expected to be 411nm.

A summary of the deposition parameters for the different $Er_xYb_{2-x}Si_2O_7$ films is shown in Table 5.1. It is seen that the film thicknesses measured by profilometry are thinner by about 30% than the expected thickness of 411nm. It is also seen that the two films with the highest Er concentrations and longest deposition times (i.e. lowest deposition rates) are thicker than the films with lower Er concentrations by about 13% and 18%, respectively. This is in line with the observation made in Chapter 3 that co-sputtering at high deposition rates decreases the overall deposition rate due to a decrease of the mean free path between the sputtering targets and the substrate.

Table 5.1: Parameters for sputter deposition of $Er_xYb_{2-x}Si_2O_7$. Film thicknesses are measured by profilometry.

x(Er) (nominal)	[Er] (cm^{-3}) (nominal)	P(Er_2O_3) (W)	P(Yb_2O_3) (W)	P(SiO_2) (W)	Time (min)	Thickness (nm)
0.07	4.90×10^{20}	16	113	224	42	302 ± 11
0.19	1.33×10^{21}	26	108	224	42	273 ± 7
0.30	2.10×10^{21}	38	103	224	42	307 ± 6
0.50	3.50×10^{21}	54	88	224	42	321 ± 4
1.00	7.00×10^{22}	96	58	224	42	292 ± 7
1.41	9.80×10^{22}	96	29	158	60	339 ± 3
2.00	1.40×10^{22}	96	0	114	86	354 ± 5

After deposition, the $Er_xYb_{2-x}Si_2O_7$ thin films were annealed for 30min in O_2 at different temperatures. The effect of anncaling on the structural and luminescence properties of the films are discussed in the following sections.

5.2 Structural properties

The X-ray diffraction patterns were analyzed of the $Er_xYb_{2-x}Si_2O_7$ thin films annealed at 1000°C, 1100°C and 1200°C. All the films annealed at temperatures below 1000°C are amorphous. The XRD patterns for the films annealed at 1000°C, 1100°C and 1200°C are discussed in sections 5.2.1, 5.2.2 and 5.2.3, respectively. A summary of the phases identified in each film is shown in Table 5.2.

Table 5.2: Phases crystallized for $Er_xYb_{2-x}Si_2O_7$ thin films on SiO_2 for different compositions and at different annealing temperatures.

x(Er)	T < 1000°C	T = 1000°C	T = 1100°C	T = 1200°C
0.07	amorphous	amorphous	α-$RE_2Si_2O_7$	β-$RE_2Si_2O_7$
0.19	amorphous	amorphous	α-$RE_2Si_2O_7$	β-$RE_2Si_2O_7$
0.30	amorphous	amorphous	α-$RE_2Si_2O_7$	β-$RE_2Si_2O_7$
0.50	amorphous	amorphous	α-$RE_2Si_2O_7$	β + α-$RE_2Si_2O_7$
1.00	amorphous	amorphous	α-$RE_2Si_2O_7$	α-$RE_2Si_2O_7$
1.41	amorphous	α-$RE_2Si_2O_7$	α-$RE_2Si_2O_7$	α-$RE_2Si_2O_7$
2.00	amorphous	amorphous	$RE_{9.33}Si_6O_{26}$	$RE_{9.33}Si_6O_{26}$

5.2.1 $Er_xYb_{2-x}Si_2O_7$ thin films annealed at 1000°C

Figure 5-1 shows the X-ray diffraction patterns of the $Er_xYb_{2-x}Si_2O_7$ thin films annealed at 1000°C. All films are still amorphous, except for the film with composition $Er_{1.41}Yb_{0.59}Si_2O_7$, which crystallizes into the α-disilicate phase, a triclinic phase with space group $P\bar{1}$ (pdf 00-030-1439). As shown in the next section, the α-disilicate is the phase that crystallizes for all the films annealed at 1100°C, except for the pure erbium disilicate film. The α-phase remains the dominant phase in the films with high erbium concentration ($x \geq 1.00$ in $Er_xYb_{2-x}Si_2O_7$) after annealing at T = 1200°C. The α-disilicate phase is discussed in detail in section 5.2.5.

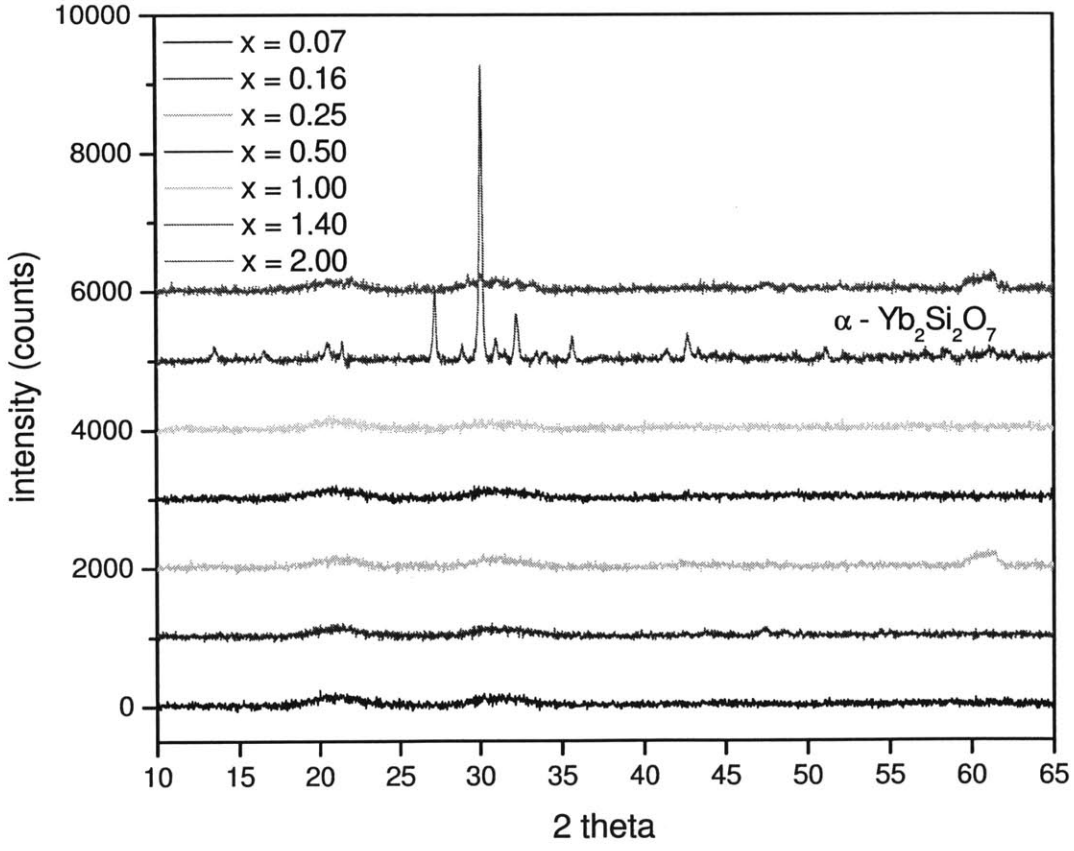

Figure 5-1: XRD patterns of $Er_xYb_{2-x}Si_2O_7$ on SiO_2 annealed at 1000°C. The patterns are offset by 1000 counts for each film with increasing erbium concentration.

5.2.2 $Er_xYb_{2-x}Si_2O_7$ thin films annealed at 1100°C

Figure 5-2 shows the X-ray diffraction patterns of the $Er_xYb_{2-x}Si_2O_7$ thin films annealed at 1100°C. All the films except for pure $Er_2Si_2O_7$ crystallize in the α-disilicate phase. The XRD pattern for the $Er_2Si_2O_7$ film can be matched to the hexagonal erbium oxyapatite ($RE_{9.33}Si_6O_{26}$) phase with space group $P6_3/m$ (pdf 04-007-9171). The extraordinarily sharp (210)-peak at $2\theta = 29.2°$ (the entire peak is not shown in the figure but is 120000 counts high) and the intense (420)-peak at $2\theta = 60.6°$ indicate a film with very strong texture (i.e. preferred grain growth) in the [210]-direction.

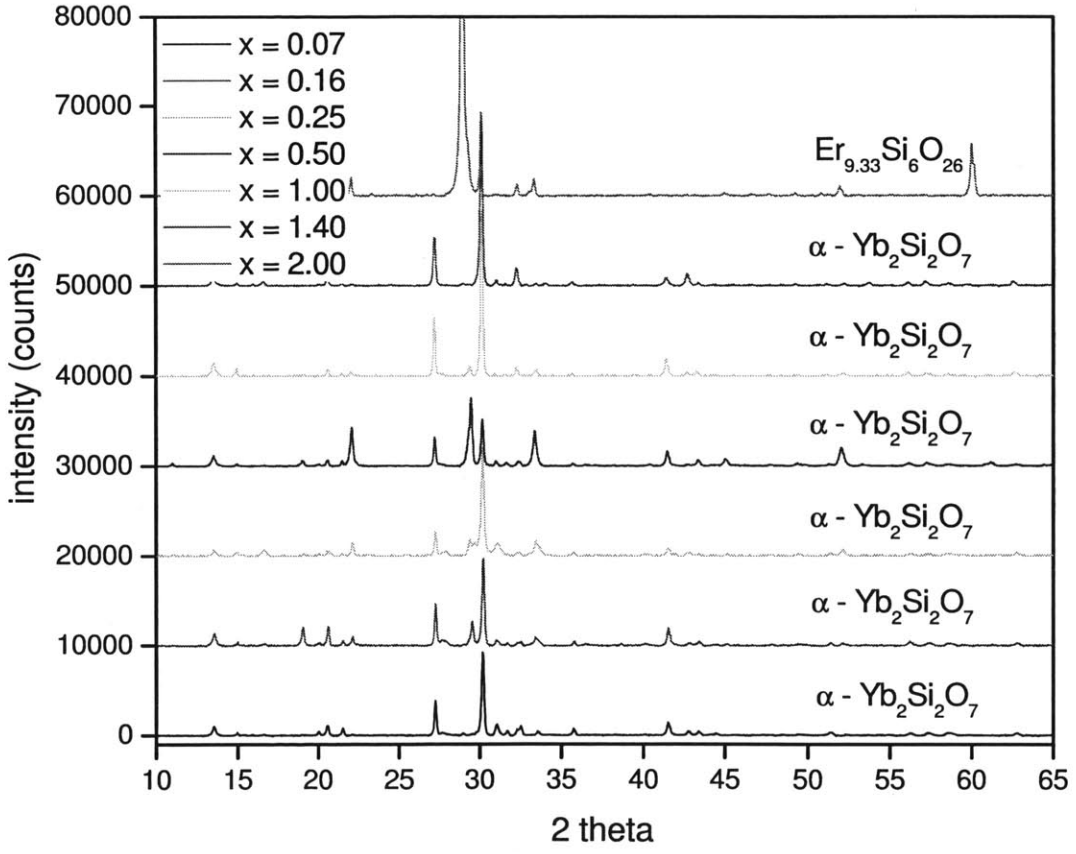

Figure 5-2: XRD patterns of $Er_xYb_{2-x}Si_2O_7$ on SiO_2 annealed at 1100°C. The patterns are offset by 10000 counts for each film with increasing erbium concentration.

5.2.3 $Er_xYb_{2-x}Si_2O_7$ thin films annealed at 1200°C

Figure 5-3 shows the X-ray diffraction patterns of $Er_xYb_{2-x}Si_2O_7$ on SiO_2 ($x \geq 0.50$) annealed at 1200°C. The film with composition $Er_2Si_2O_7$ crystallizes in the same hexagonal erbium oxyapatite phase as at 1100°C. The films with compositions x(Er) = 1.00 and x(Er) = 1.41 also crystallize to the same phase as the samples annealed at 1100°C, i.e. α-disilicate. The film with composition $Er_{0.50}Yb_{1.50}Si_2O_7$ crystallizes into a mixture of the α-disilicate phase identified at higher Er concentrations and the β-disilicate. As discussed below, the β-disilicate phase is the phase stable at lower Er concentrations.

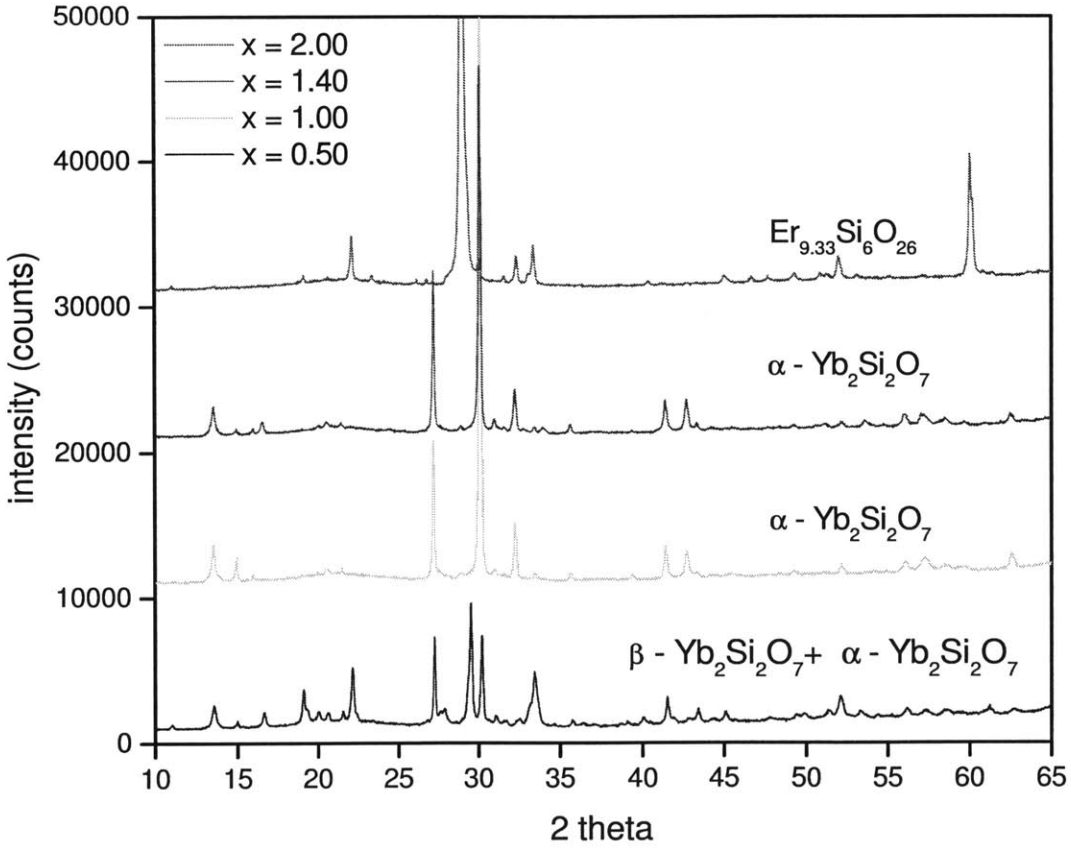

Figure 5-3: XRD patterns of $Er_xYb_{2-x}Si_2O_7$ on SiO_2 ($x \geq 0.50$) annealed at 1200°C. The patterns are offset by 10000 counts for each film with increasing erbium concentration.

Figure 5-4 shows the X-ray diffraction patterns of $Er_xYb_{2-x}Si_2O_7$ on SiO_2 ($x \leq 0.50$) annealed at 1200°C. The phase crystallized at low erbium concentration is the β-disilicate, a monoclinic phase with space group C2/m (pdf 04-007-8967). The film with intermediate composition $Er_{0.50}Yb_{1.50}Si_2O_7$, which was already discussed above and crystallizes into a mixture of the α- and β-disilicate phase, is reprinted in this figure as a reference to compare the XRD spectra with the films with lower erbium concentration. The β-disilicate phase is discussed in detail in section 5.2.6.

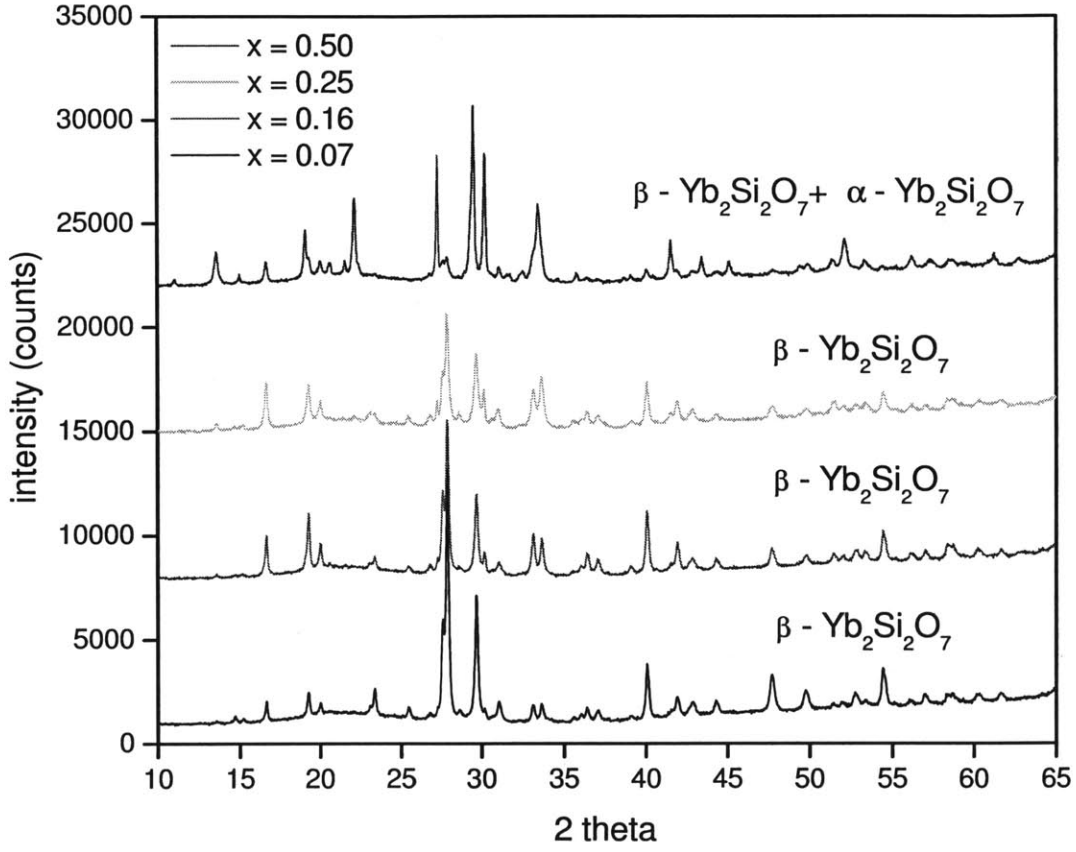

Figure 5-4: XRD patterns of $Er_xYb_{2-x}Si_2O_7$ on SiO_2 ($x \leq 0.50$) annealed at 1200°C. The patterns are offset by 7000 counts for each film with increasing erbium concentration.

5.2.4 Polymorphic disilicate compounds

Figure 5-5 shows the seven different rare-earth disilicate polymorphs as a function of temperature and rare earth ionic radius, as identified by J. Felsche in *The Crystal Chemistry of the Rare-Earth Silicates* [21]. Yttrium (Y) is not included in the graph, but with an ionic radius of 0.90Å it would be close to holmium (Ho) on the horizontal axis. According to the plot, types B and C would be stable for the temperatures (T < 1200°C) and ionic radii (0.86Å < r < 0.90Å) studied in this research. These types correspond to the α-disilicate and β-disilicate discussed in the XRD sections. Type B (aka α-disilicate) should be favored at high Er (low Yb) concentrations and lower annealing temperatures, whereas type C (aka β-disilicate) should be stable at low Er (high Yb) concentrations and high annealing temperatures.

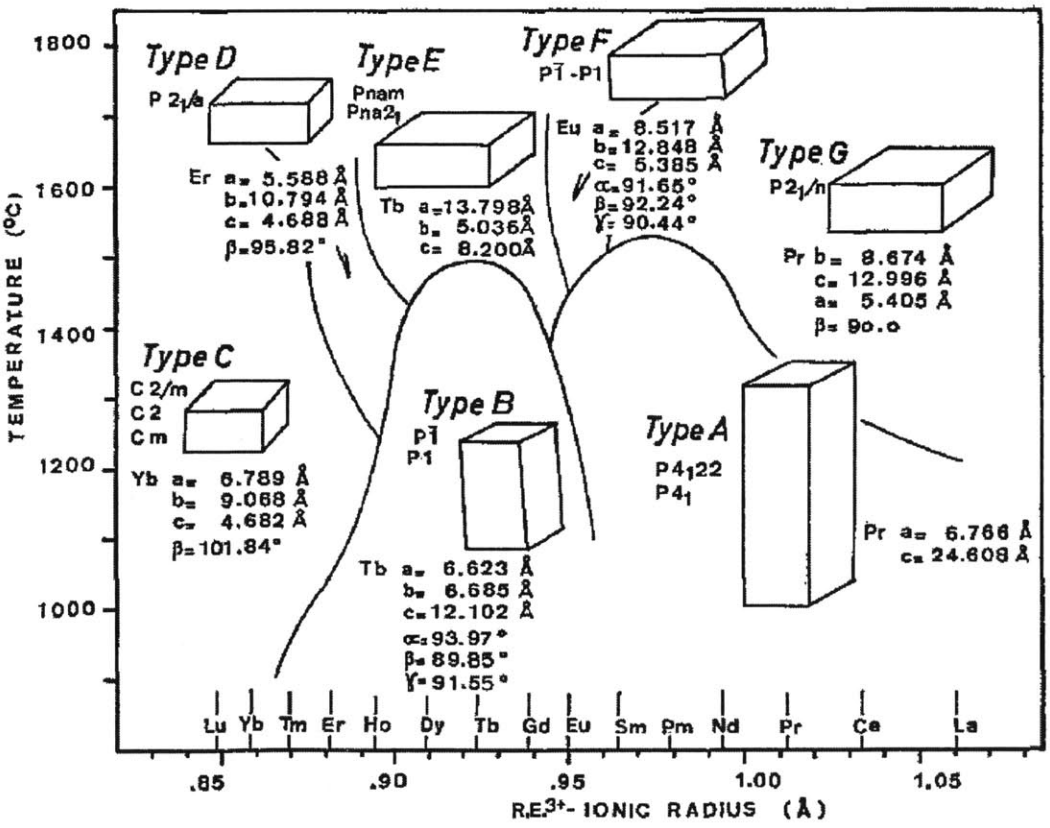

Figure 5-5: Polymorphic disilicate compounds, adopted from [145]. Type B, C and D are also known as α, β and γ-disilicate, respectively.

This is indeed what is observed in the XRD patterns discussed in sections 5.2.2 and 5.2.3: for the alloys with low x(Er), we observe crystallization of the α phase at 1100°C and crystallization of the β phase at 1200°C. For the intermediate concentration of x(Er) = 0.50, we observe both α and β phases at 1200°C. For high x(Er), we obtain the α phase at both 1100°C and 1200°C.

Table 5.3 shows an overview of the unit cell parameters for the different phases identified above. Each phase is discussed in detail in the sections below.

Table 5.3: Unit cell dimensions for α and β - $Er_2Yb_{2-x}Si_2O_7$ and the oxyapatite phase $Er_{9.33}Si_6O_{26}$. Z = formula units per unit cell, V = unit cell volume, from [21].

	α-$Er_2Si_2O_7$	β-$Yb_2Si_2O_7$	$Er_{9.33}Si_6O_{26}$
crystal system	triclinic	monoclinic	hexagonal
space group	$P\bar{1}$	C2/m	$P6_3/m$
a (Å)	6.583	6.789	9.324
b (Å)	6.609	9.067	9.324
c (Å)	12.000	4.681	6.686
α (°)	94.50	90	90
β (°)	90.57	101.86	90
γ (°)	91.79	90	120
V(Å^3)	520.3	282.1	503.4
Z	4	2	1
ρ (g/cm^3)	6.28	6.01	7.08

5.2.5 α - $RE_2Si_2O_7$ (Type B)

The unit cell for α - $Y_2Si_2O_7$ (pdf 04-016-5897) is depicted in Figure 5-6. It contains 8 rare earth ions, which are evenly distributed over 4 non-equivalent lattice sites RE1, RE2, RE3 and RE4. These different sites are shown in the figure as yellow, cyan, red and magenta spheres, respectively.

Determining the coordination of the different RE sites by oxygen ions is not trivial. There are no pdf database entries for α-$Yb_2Si_2O_7$ or α-$Er_2Si_2O_7$ containing structural information that allows to calculate bond lengths. However, coordination numbers and RE-O bond lengths were calculated for α-$Y_2Si_2O_7$ (pdf 01-078-2543) and α-

$Tm_2Si_2O_7$ (pdf 04-011-2465). Considering only RE-O distances shorter than 3.00Å, we find that all four Tm sites in α-$Tm_2Si_2O_7$ are eightfold coordinated by oxygen, whereas in α-$Y_2Si_2O_7$, the sites the Y1, Y2 and Y4 are eightfold coordinated and site Y3 is sixfold coordinated by oxygen. Table 5.4 also shows that the minimum, maximum and average bond distances vary significantly for the four different RE sites.

Table 5.4: RE coordination number (CN) and maximum, minimum and average RE-O bond lengths (d_{RE-O}) calculated for α-$Y_2Si_2O_7$ (pdf 01-078-2543) and α-$Tm_2Si_2O_7$ (pdf 04-011-2465), only considering $d_{RE-O} < 3.00$Å.

	Y_1	Y_2	Y_3	Y_4	Tm_1	Tm_2	Tm_3	Tm_4
CN	8	8	6	8	8	8	8	8
avg d_{RE-O} (Å)	2.42	2.42	2.31	2.43	2.39	2.39	2.47	2.40
min d_{RE-O} (Å)	2.22	2.23	2.12	2.29	2.22	2.20	2.17	2.26
max d_{RE-O} (Å)	2.81	2.72	2.45	2.71	2.87	2.74	2.36	2.71

The shape of the ($RE-O_8$) polyhedra varies between a highly distorted cube and a distorted type of dodecahedron. As seen in Figure 5-7, these rare earth-oxygen polyhedra form chains in the [101] direction by edge sharing [21].

Another interesting feature is the presence of Si_3O_{10} groups consisting of three neighboring SiO_4 tetrahedra, as well as isolated SiO_4 tetrahedra. All other rare earth disilicate phases feature Si_2O_7 double-tetrahedra groups. Just like the rare earth-oxygen polyhedra, the (Si_3O_{10})-chains line up along the [101] direction, as shown clearly in Figure 5-7. The SiO_4-tetrahedra also exhibit a high degree of distortion, with the largest Si-O bond length variation found in all silicate structures (0.14Å) [21].

In conclusion, the triclinic α - $RE_2Si_2O_7$ phase is a very low symmetry phase with 4 different rare earth sites, each having a large variation in bond distances with the surrounding oxygen ions. As discussed in section 5.3, this strongly non-uniform environment for the rare earth ions can be related to a broad and intense photoluminescence spectrum around 1.54μm.

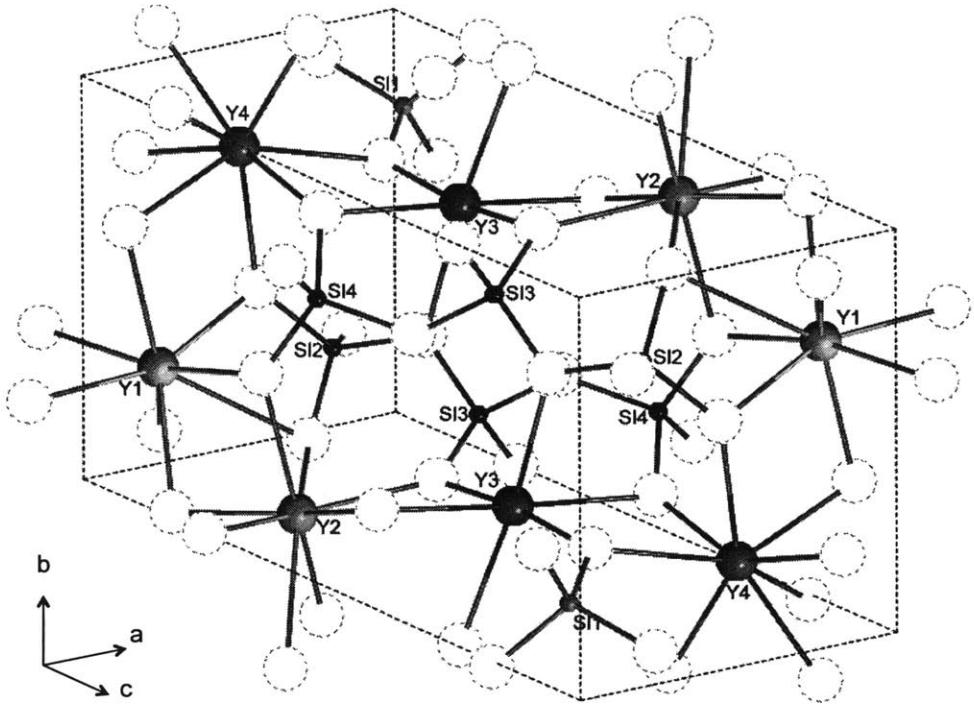

Figure 5-6: The α - $Y_2Si_2O_7$ unit cell (pdf 04-016-5897). Eight rare earth ions per unit cell are distributed evenly over four non-equivalent lattice sites (yellow, cyan, red and magenta spheres). Blue and green spheres = Si, white spheres = O.

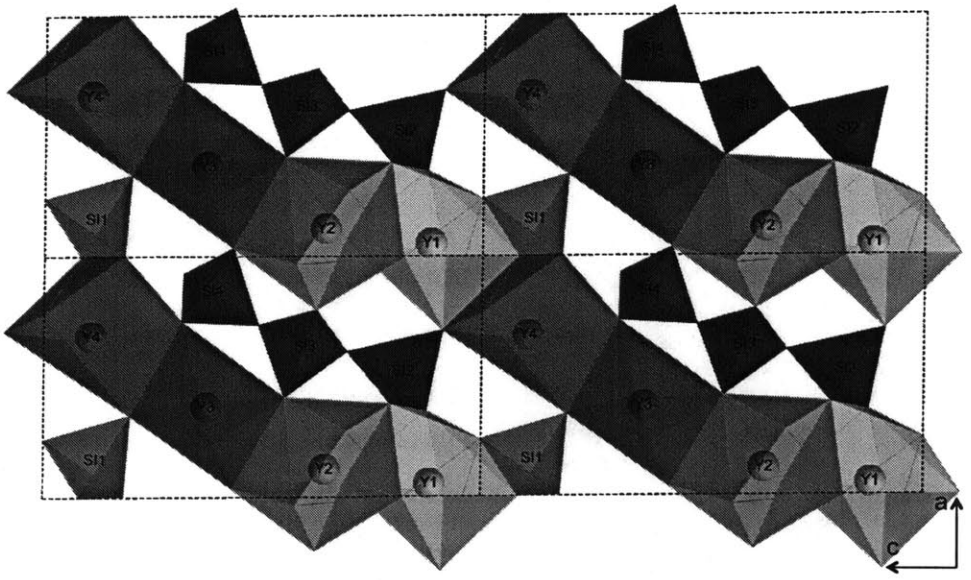

Figure 5-7: 4 neighboring α - $Y_2Si_2O_7$ unit cells seen along the [010] direction clearly show the Si_3O_{10}-chains and the (RE-O_8)-chains along the [101] direction.

5.2.6 β - $RE_2Si_2O_7$ (Type C)

The unit cell for β - $Yb_2Si_2O_7$ is shown in Figure 5-8. As opposed to the very low-symmetry triclinic α-phase discussed above, the β-phase is monoclinic with space group C2/m. The unit cell contains 4 (YbO_6)-octahedra and 4 (SiO_4)-tetrahedra. As opposed to the α-phase, all the rare earth sites and all silicon sites are equivalent. Additionally, the Yb-O and Si-O bonds exhibit a very low degree of distortion, with an average Si-O bond length of 1.63 $\pm$ 0.01Å and an average Yb-O bond length of 2.24 $\pm$ 0.04Å [21].

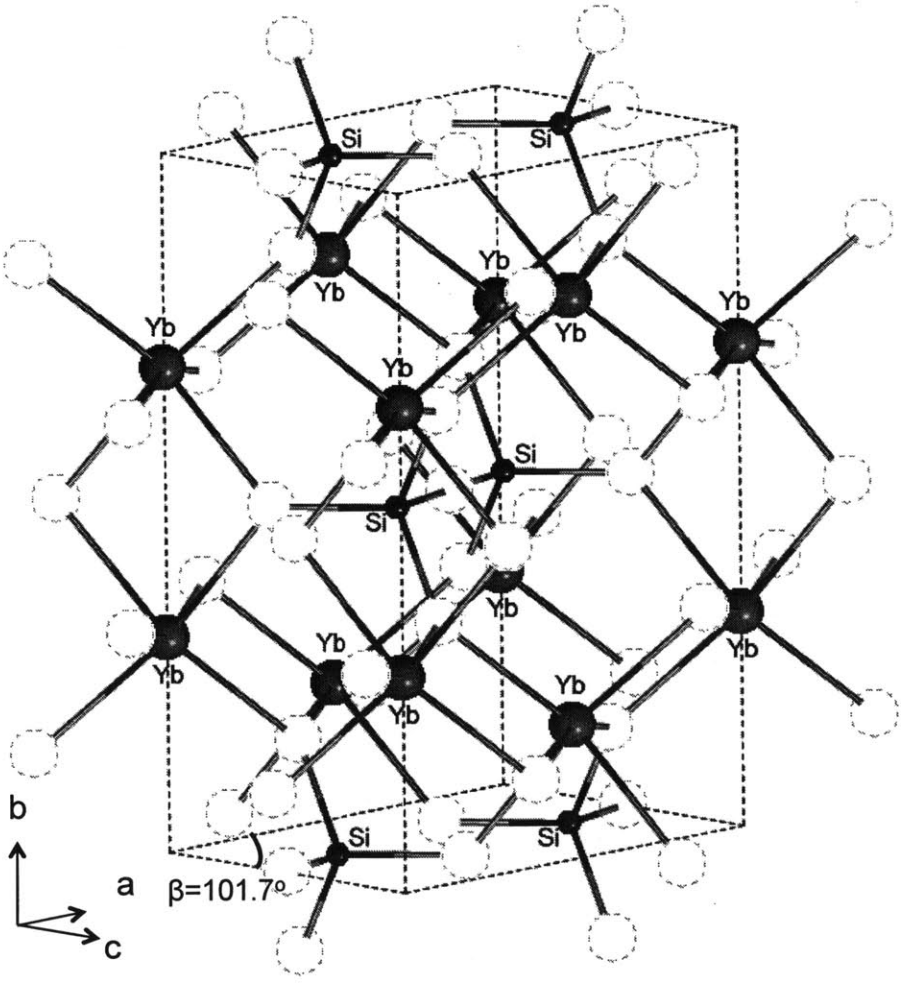

Figure 5-8: β - $Yb_2Si_2O_7$ unit cell (pdf 04-007-8967).

5.2.7 Oxyapatite - $RE_{9.33}Si_6O_{26}$

As discussed in sections 5.2.2 and 5.2.3, the film consisting of pure $Er_2Si_2O_7$ crystallizes into the oxyapatite phase $Er_{9.33}Si_6O_{26}$. This phase has a composition intermediate between the monosilicate and disilicate, corresponding to

$$7\ RE_2O_3 + 9\ SiO_2 \rightarrow 1.5\ RE_{9.33}\square_{0.67}(SiO_4)_6O_2 \tag{5.2}$$

where Felsche's notation $Er_{9.33}\square_{0.67}(SiO_4)_6O_2$ was used, indicating the presence of rare earth vacancies represented by "□" (see below) [21].

The $Er_{9.33}Si_6O_{26}$ oxyapatite has a hexagonal unit cell with space group $P6_3/m$, shown in Figure 5-9. It contains erbium ions in two non-equivalent lattice sites: Er1 and Er2. There are six Er1 sites (yellow) per unit cell: two near the center and 4 on the (100) and (010) planes shared with the neighboring unit cells. The Er1 ions are 7-fold coordinated by 6 oxygen ions that are part of SiO_4 tetrahedra and one isolated O^{2-} ion (grey spheres in Figure 5-9). Additionally, there are four Er2 ions (cyan) per unit cell, two close to the center and 2 on the (001) lattice planes. The Er2 ions are ninefold coordinated by oxygen ions that are all part of SiO_4 tetrahedra.

Note that the total number of Er *sites* per unit cell equals 10 (= 6Er1 + 4Er2), whereas according to the formula unit there are only 9.33 Er *ions* per unit cell. In other words, per unit cell there are 0.67 erbium vacancies (i.e. there are two vacancies per three unit cells). According to Felsche [21], these erbium vacancies are on the Er2 sites.

The oxyapatite silicates are known for all rare earth ions ranging from La to Lu. In fact, this is the only rare earth silicate structure to include all the rare earths. However, the oxyapatite phase is only metastable for the smaller rare earths and decomposes into B-type monosilicate and $\beta+\gamma$ disilicate [21]. Since Er^{3+} is slightly larger than Yb^{3+}, this may explain why in our case the oxyapatite phase only crystallizes for pure Er silicate $Er_2Si_2O_7$.

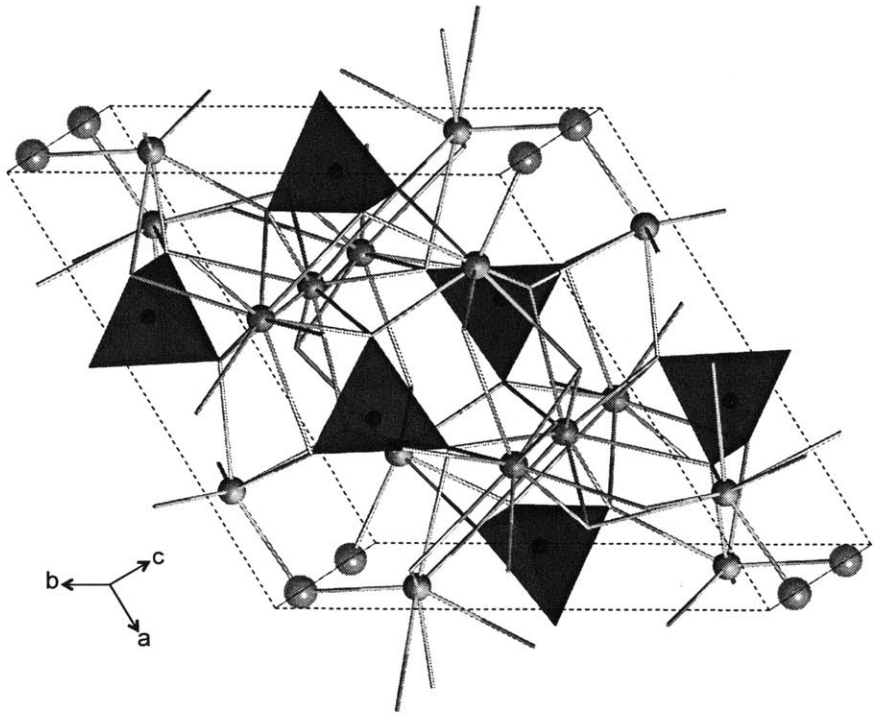

Figure 5-9: Oxyapatite $Er_{9.33}Si_6O_{26}$ (pdf 04-007-9171). Er1 = yellow, Er2 = cyan, SiO_4 = blue tetrahedra, isolated O^{2-} ions = grey.

5.2.8 Grain size and microstrain

Figure 5-10 shows the Williamson-Hall plot for the α-disilicate phase crystallized in the $Er_{1.0}Yb_{1.0}Si_2O_7$ thin film annealed at 1100°C and 1200°C. A linear regression assuming 0% microstrain[1] results in grain sizes of 479 ± 96Å and 554 ± 103Å for the films annealed at 1100°C and 1200°C. Note that these values are consistent with the 0% microstrain and the grain size of 539 ± 56Å determined for the β-disilicate phase in the $Er_{0.30}Yb_{1.70}O_3$ film annealed at 1200°C (see Table 4.3).

[1] a linear regression including microstrain gives a small negative slope, which is unphysical. This situation indicates 0% microstrain, where the small negative slope in the regression is due to the error bar on the data.

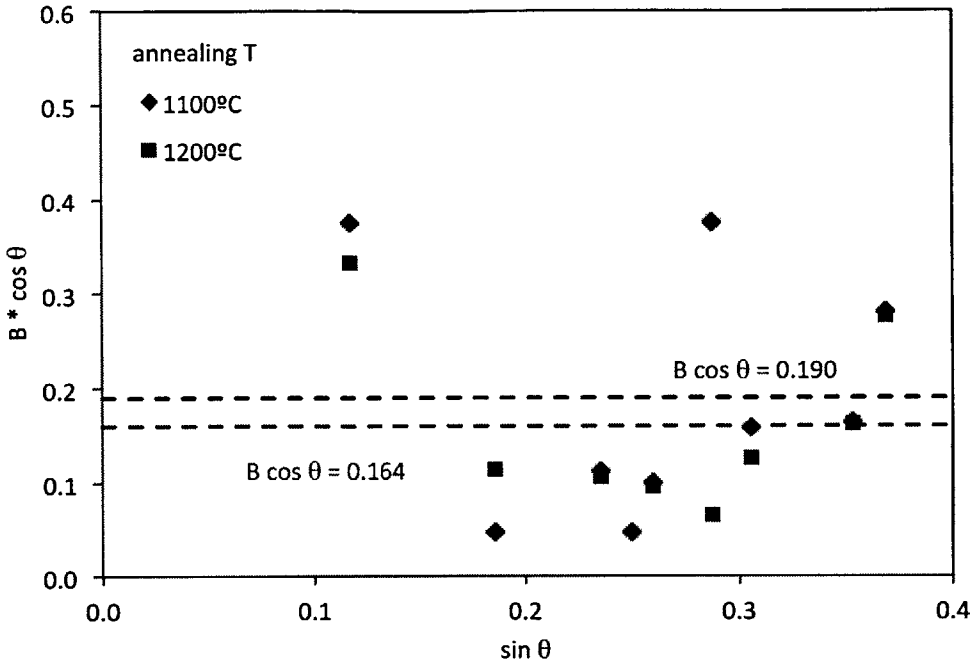

Figure 5-10: Williamson-Hall plot for the α-disilicate phase crystallized in the $Er_{1.0}Yb_{1.0}Si_2O_7$ thin film annealed at 1100°C and 1200°C.

5.3 Photoluminescence properties

5.3.1 PL spectra for crystalline silicates

The photoluminescence spectra measured at room temperature for the $Er_xYb_{2-x}Si_2O_7$ films annealed at 1200°C are shown in Figure 5-11. All spectra are normalized to make the integrated PL intensity between 1450nm and 1650nm equal to 1, so that the spectral shapes can be compared. The figure shows four different spectra, each corresponding to a particular range of erbium concentrations. All samples with the same spectrum are grouped together in the figure and each group is offset for clarity.

The first group of spectra (offset by 0.015 on Fig. 5-11) corresponds to the three $Er_xYb_{2-x}Si_2O_7$ films with the lowest erbium concentrations (x = 0.07, x = 0.16 and x = 0.30). Even though homogeneous broadening increases the spectral linewidths for

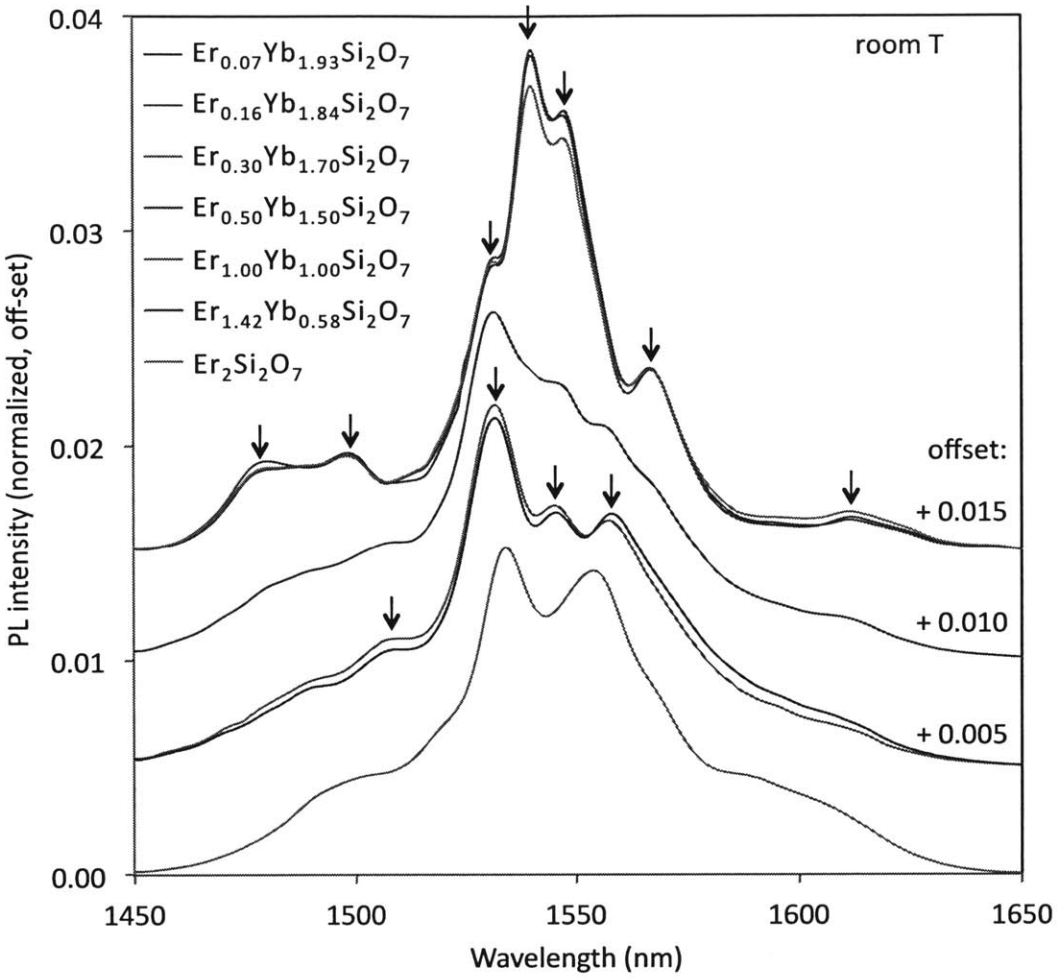

Figure 5-11: Room temperature PL spectra of $Er_xYb_{2-x}Si_2O_7$ annealed at 1200°C. The spectra are grouped into four sets of samples that have the same spectrum, each set is offset differently for clarity.

the transitions between the different Stark-split energy levels, seven clear peaks can be distinguished in the PL spectrum, even at room temperature (at 1480nm, 1498nm, 1532nm, 1540nm, 1547nm, 1567nm and 1611nm). The full width at half maximum (FWHM) is 28nm. As discussed in section 5.2 on the structural analysis of these films, the dominant phase crystallized at 1200°C for these compositions was identified as β-$Yb_2Si_2O_7$, suggesting that this PL spectrum is characteristic for the β-$Yb_2Si_2O_7$ phase.

Secondly, the figure shows that the silicates with intermediate erbium concentrations

(x = 1.00 and x = 1.50, offset by 0.005 in Fig. 5-11) also share the same PL spectrum. At room temperature, this spectrum has 4 peaks (at 1507nm, 1532nm, 1546nm and 1558nm) and a FWHM = 47nm, which is 68% broader than the PL spectrum discussed previously. The phase crystallized for these compositions was identified as α-$Yb_2Si_2O_7$, suggesting that this PL spectrum is characteristic for the α-$Yb_2Si_2O_7$ phase.

Thirdly, the crystal structure for the film with composition x = 2.00 (pure $Er_2Si_2O_7$) was identified in section 5.2 as the oxyapatite $Er_{9.33}Si_6O_{26}$. The PL spectrum related to this phase shows two peaks at 1534nm and 1554nm and a FWHM = 48nm, comparable to the α-$Yb_2Si_2O_7$.

Lastly, the PL spectrum for the film with composition x = 0.50 looks like a combination of the spectrum at low Er concentrations and the spectrum at intermediate concentrations. In fact, in section 5.2 we concluded that this film was a mixture of the α- and β- disilicate phases. This is now confirmed by the PL spectrum.

Figure 5-12 shows the spectral shape at x = 0.50 decomposed into a linear combination of the α- and β-disilicate PL spectra. The best fit is obtained with a 86.52% - 13.48% contribution of the α- and β-spectra, respectively. However, since the α-phase turns out to be a stronger emitter than the β-phase (see further), these values cannot be translated into quantitative information about the amount α- and β-disilicate in the $Er_{0.50}Yb_{1.50}Si_2O_7$ film. Rietveld analysis was used to quantify the amounts of α- and β-disilicate, but due to strong texture in the film we could not obtain accurate information with the available XRD data.

5.3.2 PL spectra for amorphous silicates

Figure 5-13 shows the room temperature PL spectra of the $Er_xYb_{2-x}Si_2O_7$ films annealed at 1000°C. As discussed in section 5.2, all these films are still amorphous, except for the film with concentration $Er_{1.41}Yb_{0.59}Si_2O_7$, which crystallizes as α-disilicate. As a consequence of inhomogeneous broadening, the PL spectra corresponding to

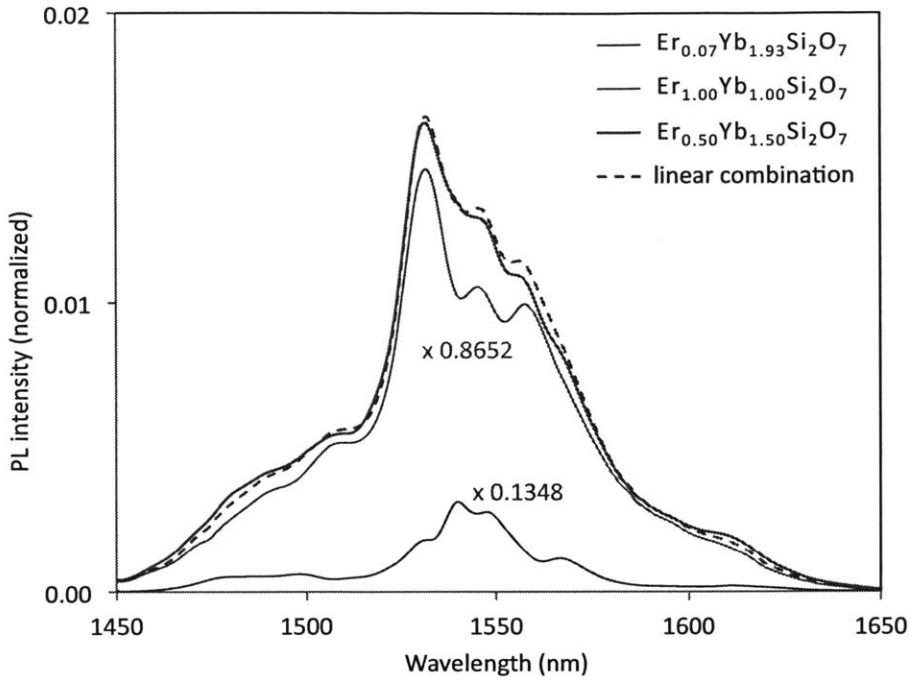

Figure 5-12: PL spectrum of $Er_{0.50}Yb_{1.50}Si_2O_7$ as a linear combination of the PL spectra of $Er_{0.07}Yb_{1.93}Si_2O_7$ and $Er_{1.00}Yb_{1.00}Si_2O_7$, corresponding to the β-disilicate the α-disilicate phase, respectively.

the amorphous films are broad (FWHM = 45nm) and show no individual peaks. The spectrum for the $Er_{1.41}Yb_{0.59}Si_2O_7$ film corresponds to the α-disilicate spectrum identified in section 5.3.2.

5.3.3 PL lifetime for amorphous and crystalline silicates

Figure 5-14 shows the decay rates of $Er_xYb_{2-x}Si_2O_7$ vs x(Er) annealed at 1000°C (blue data) and 1200°C (red data). The inset shows a magnification of the low x(Er) decay rates. We notice two trends: firstly, the lifetime at 1000°C is always shorter than at 1200°C, consistent with lower non-radiative decay to defects at higher annealing temperatures. Secondly, the lifetime decreases with increasing erbium concentration, consistent with the increase in concentration quenching effects (see section 4.4).

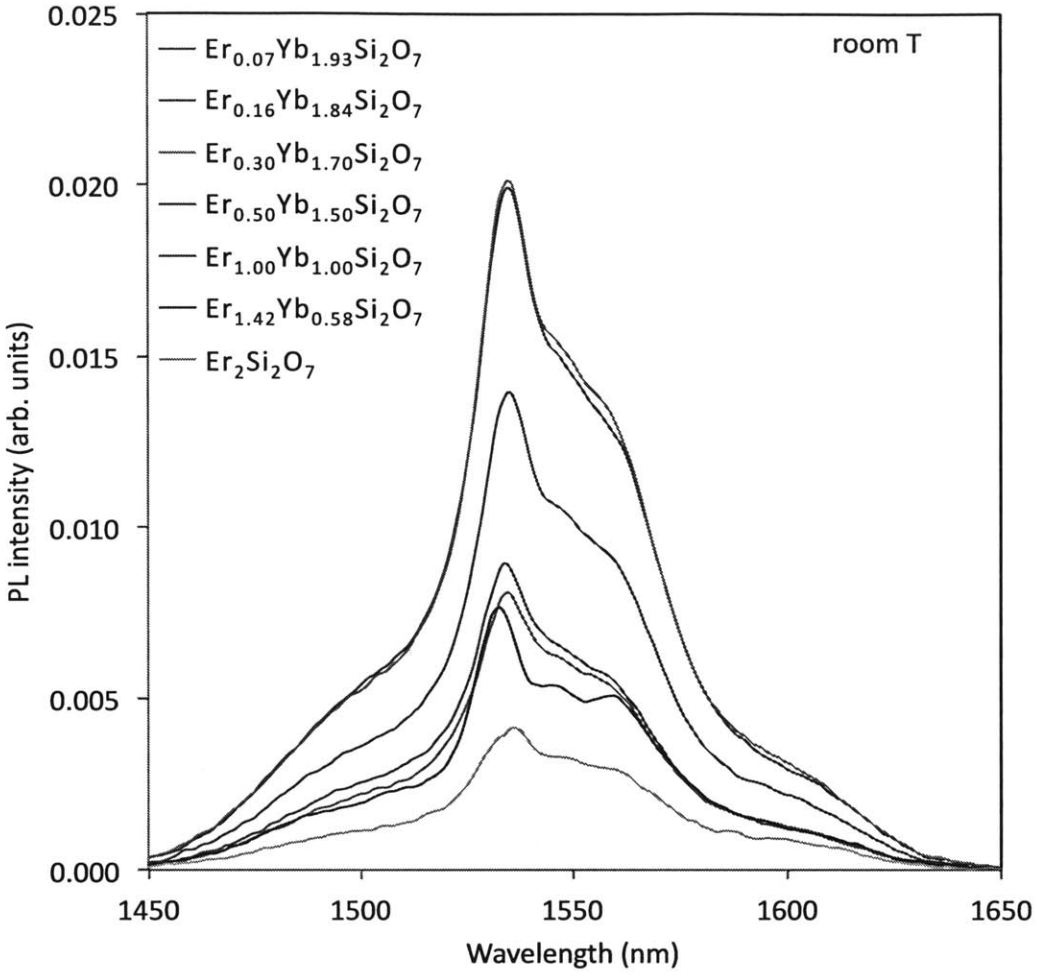

Figure 5-13: PL spectra (at room T) of $Er_xYb_{2-x}Si_2O_7$ annealed at 1000°C.

5.3.4 PL as a function of annealing temperature

Figure 5-15 shows the PL spectra of the film with composition $Er_{0.16}Yb_{1.84}Si_2O_7$, annealed at different temperatures for 30min in O_2.

The figure shows that the sample annealed at 1100°C has a spectrum corresponding to the ytterbium α-disilicate phase. This corresponds to the α-disilicate phase being present in all the 1100°C samples in the XRD spectrum. The film annealed at 1200°C has a disilicate phase. The samples annealed at 900°C and 1000°C are amorphous. In other words, the peaks in the PL spectra are due to crystallization, and their precise

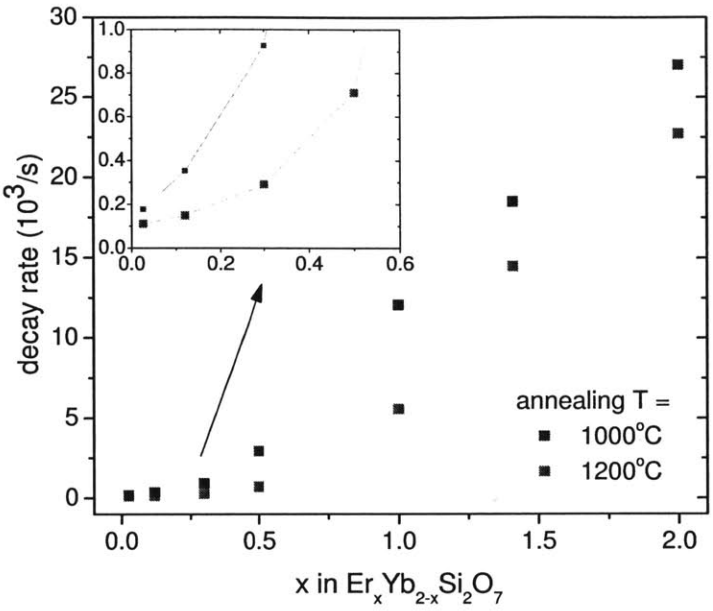

Figure 5-14: Decay rate of $Er_xYb_{2-x}Si_2O_7$ vs x annealed at 1000°C (blue data) and 1200°C(red data). The dotted lines serve as guides to the eye.

location is related to which phase exactly is crystallized.

It is also apparent from the picture that the PL decreases for the annealing temperature of 1200°C, while the lifetime keeps increasing. The β-phase clearly has a lower emission cross-section than the α-phase. The increase of lifetime in this case is not only due to a decrease in non-radiative decay rate due to the reduction of defects, but also due to a decrease in radiative decay rate because of a reduction in emission cross section. The relation between cross section σ and radiative lifetime τ_{rad} is given by the relation

$$\sigma(\nu) = \frac{\lambda^2}{8\pi\tau_{\text{rad}}} g(\nu) \tag{5.3}$$

where $g(\nu)$ is the lineshape function which determines the frequency dependence of the cross section.

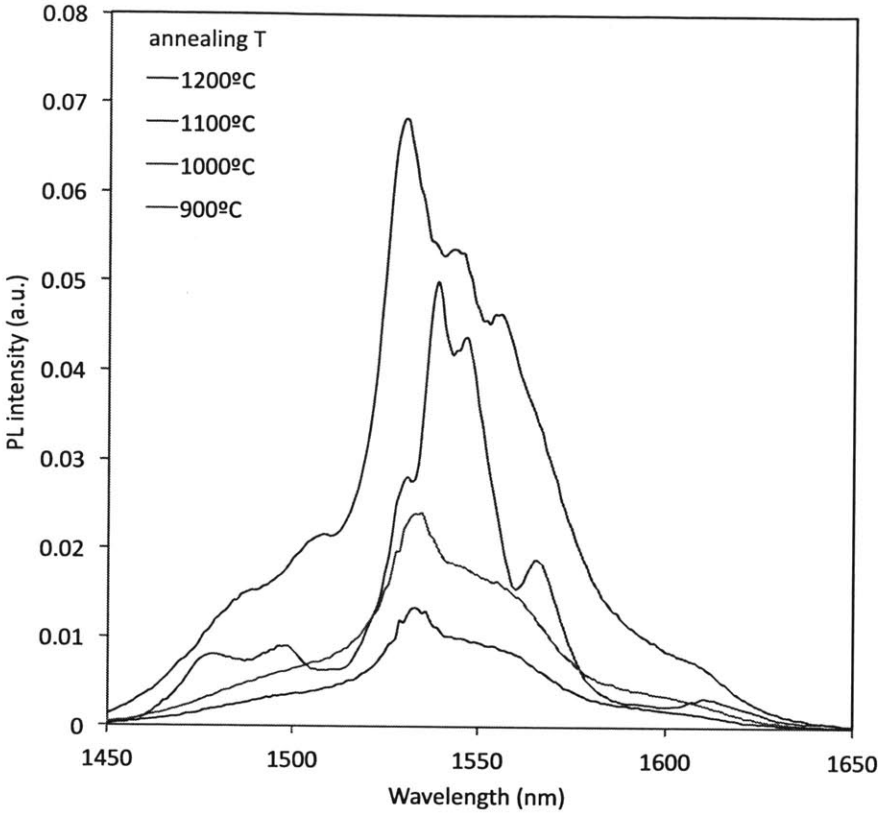

Figure 5-15: PL spectra of $Er_{0.16}Yb_{1.84}Si_2O_7$ for annealing temperatures.

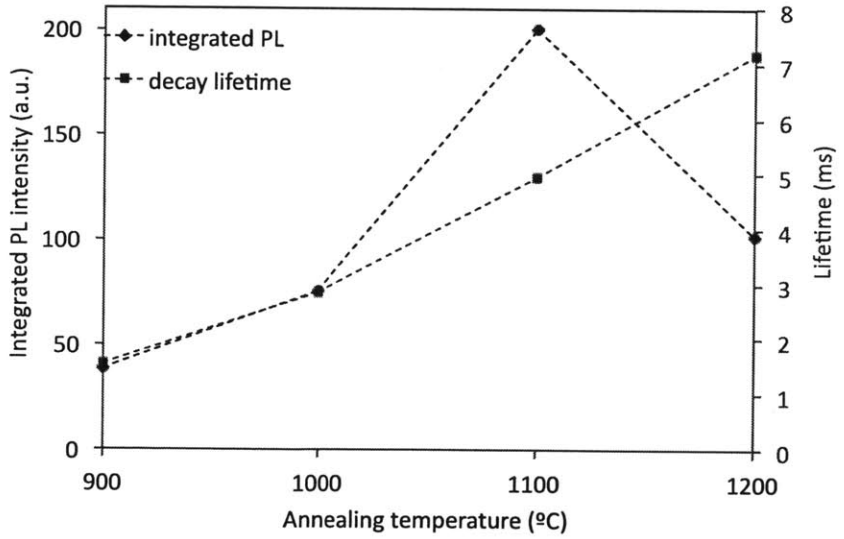

Figure 5-16: Integrated PL intensity (blue data, left y-axis) and decay lifetime (red data, right y-axis) of $Er_xYb_{2-x}Si_2O_7$ vs annealing temperature. The dashed lines are shown to guide the eye.

5.4 Upconversion coefficient

As discussed in section 2.4.2, the photoluminescence intensity as a function of pump flux Φ is given by Equation 2.14 (reproduced here)

$$I_{\mathrm{PL}} \propto \frac{-1-\sigma\Phi\tau+\sqrt{1+2\sigma\Phi\tau+4C_{\mathrm{up}}\tau^2\sigma\Phi N_{\mathrm{Er}}+\sigma^2\Phi^2\tau^2}}{2C_{\mathrm{up}}\tau} \tag{5.4}$$

By fitting the PL saturation curve with Equation 5.4, we can derive the upconversion coefficient C_{up}. Figure 5-17 shows the PL saturation curve (blue data) measured for the film with concentration $Er_{0.16}Yb_{1.84}Si_2O_7$ annealed at 1200°C, fit (green line) by Equation 5.4. An upconversion coefficient $C_{\mathrm{up}} = 1.50 \times 10^{-16}$ cm^3s^{-1} is obtained.

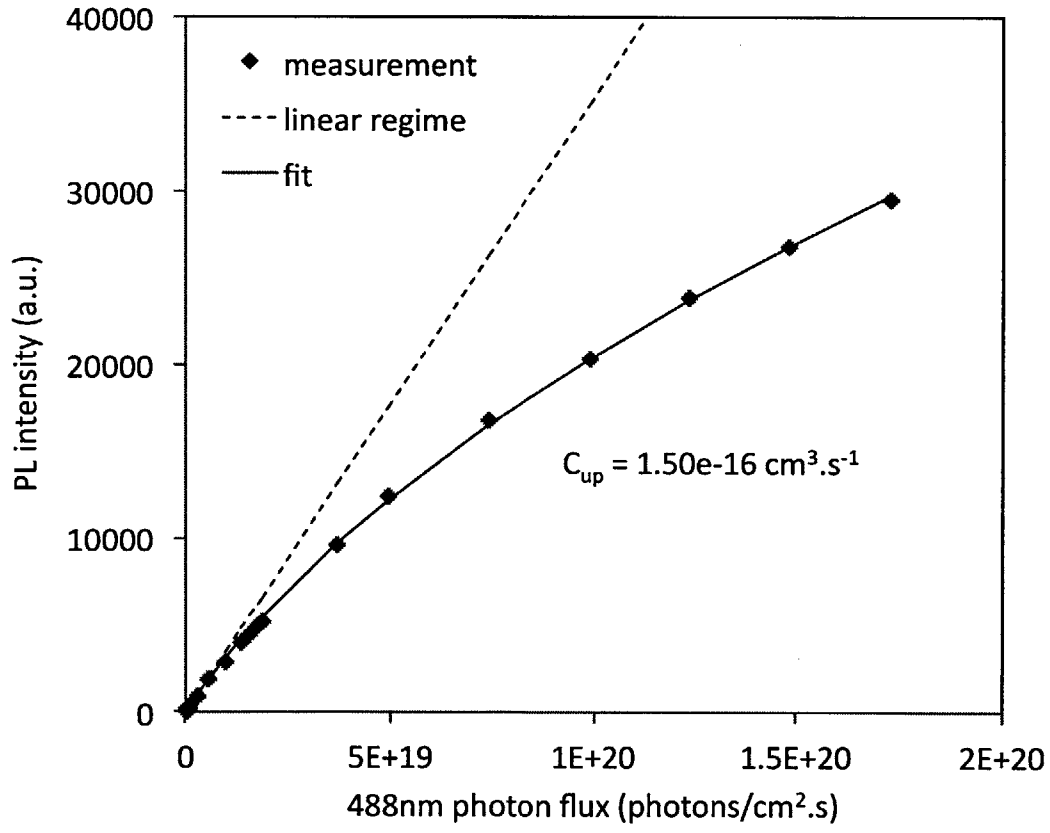

Figure 5-17: PL saturation curve for $Er_{0.16}Yb_{1.84}Si_2O_7$ (blue data) fit with Equation 5.4 (green line). The red dotted line shows a fit to the linear regime.

Figure 5-18 shows the upconversion coefficient measured for the $Er_xYb_{2-x}Si_2O_7$ films as a function of Er concentration (blue data, the dotted line serves as a guide to the eye). The figure also includes literature values measured for erbium-yttrium disilicates $Er_xY_{2-x}Si_2O_7$ [52] and the extension of the Er-doped SiO_2 data by the dipole-dipole model (see Eq. 2.11, [55–58]) discussed in section 2.4.2. The figure also includes the upconversion coefficient for the $Er_{0.16}Yb_{1.84}Si_2O_7$ annealed at different temperatures. We see that the upconversion coefficient decreases with increasing annealing temperature.

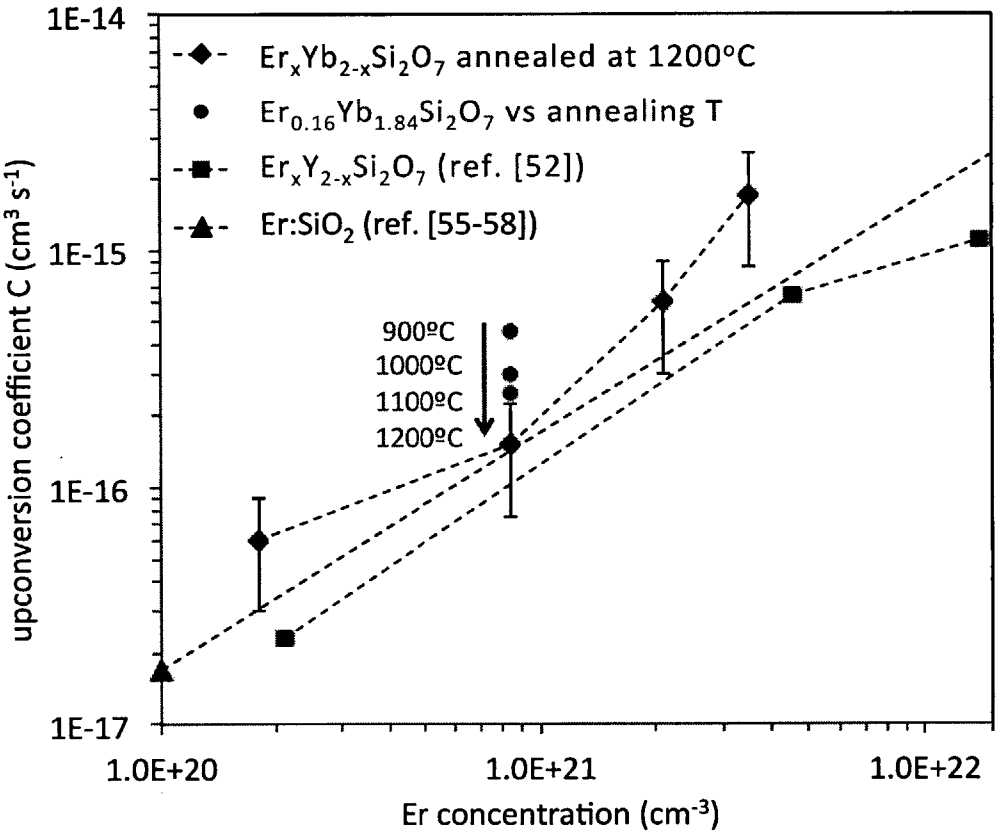

Figure 5-18: Upconversion coefficient determined for $Er_xYb_{2-x}Si_2O_7$ films annealed at 1200°C (blue data) as a function of Er concentration and for the $Er_{0.16}Yb_{1.84}Si_2O_7$ film as a function of annealing temperature (red data). The green data are literature values for erbium-yttrium α-disilicate [52]. The dotted lines serve as guides to the eye.

We see that both the magnitude of the upconversion coefficient measured in the $Er_xYb_{2-x}Si_2O_7$ films and the increase with erbium concentration are consistent with

the upconversion coefficients predicted by the Er:SiO_2 dipole-dipole model and the literature values measured for $Er_xY_{2-x}Si_2O_7$. The slightly larger values may be due to an overestimation of the upconversion coefficient in our measurement due to possible energy transfer from Er^{3+} to Yb^{3+} at 980nm. In the PL saturation model developed in section 2.4.2, it was assumed that all ions upconverted to the level $^4I_{9/2}$ decay immediately to the $^4I_{11/2}$ level at 980nm and then back to the first excited state, leading to a net loss of *one* excitation during the process of upconversion. If a fraction of the upconverted ions that end up in the $^4I_{11/2}$ level transfer their energy to the $^2F_{5/2}$ level in Yb^{3+} instead of decaying back to the first excited state in Er^{3+}, this would lead to a net loss of *more than one* excitations. Since we did not account for this process in our model, this would appear as a larger upconversion coefficient.

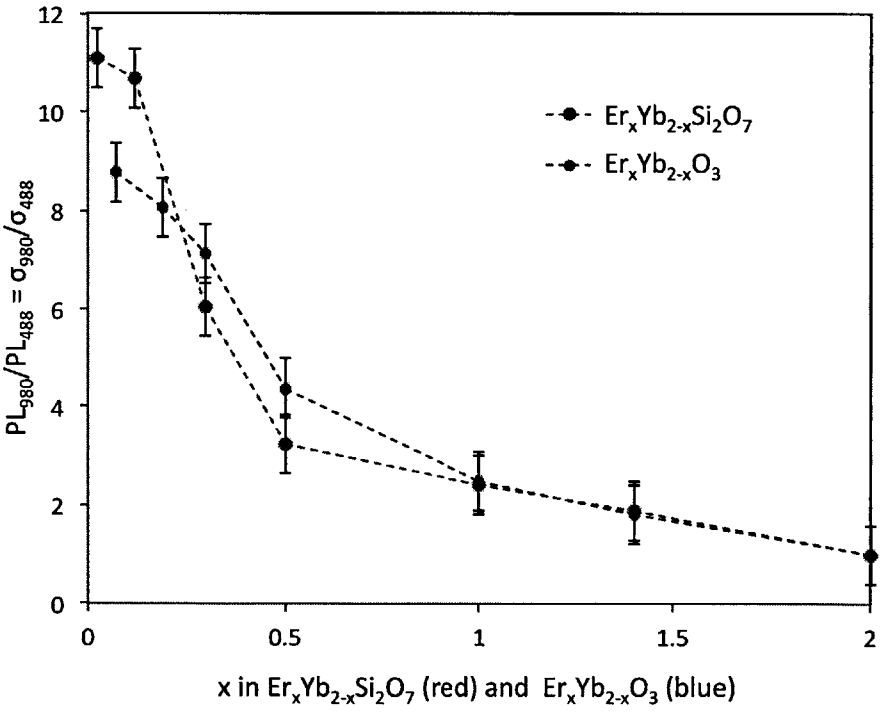

Figure 5-19: Ratio of excitation cross section $\sigma(\lambda = 980)/\sigma(\lambda = 488)$ for $Er_xYb_{2-x}Si_2O_7$ (red data), compared to the data for $Er_xYb_{2-x}O_3$ (blue data) as discussed in section 4.5. The ratios are normalized so that the ratio for pure Er_2O_3 equals 1. The dotted lines serve as a guide to the eye.

5.5 Sensitization

In order to investigate sensitization of Er^{3+} by Yb^{3+} in $Er_xYb_{2-x}Si_2O_7$, we use the apply the same technique as discussed for the erbium-ytterbium oxides in section 4.5 and Figure 4-15. The result for the silicates is shown in Figure 5-19.

Again, we observe a monotonic increase of the ratio of excitation cross sections with increasing ytterbium concentration, showing sensitization of Er^{3+} by Yb^{3+}. The effect is seems about 25% larger here than for the oxides.

5.6 Conclusion

This chapter investigates the structural and optical properties of $Er_xYb_{2-x}Si_2O_7$ thin films deposited on thermal SiO_2. We found that the crystallization temperature of the silicate thin films lies between 1000°C and 1100°C and we identified the different silicate phases that crystallize for different erbium-ytterbium concentrations and at different annealing temperatures. Pure $Er_2Si_2O_7$ was found to crystallize into the oxyapatite phase $Er_{9.33}Si_6O_{26}$. For the other compositions, we distinguish a low and a high erbium concentration regime. At low erbium concentrations, the α-disilicate phase crystallizes at 1100°C and the β-disilicate phase crystallizes at 1200°C. At high erbium concentrations, the α-disilicate crystallizes at both temperatures. These findings are consistent with the literature on bulk rare earth silicates.

We were able to correlate the photoluminescence spectra of the different films to the phases identified during XRD. The β-disilicate corresponds to a narrow PL spectrum (FWHW = 28nm) with several peaks apparent even at room temperature. The α-disilicate and the oxyapatite, like the amorphous silicates, have a broad spectrum (FWHW $\approx$ 45nm). This difference can be explained by the fact that there are several non-equivalent rare earth sites in the α-disilicate and the oxyapatite, whereas the β-disilicate has only one type of rare earth site. The rare earth ions in different sites each cause a different spectrum, giving rise to a bandwidth similar to the one for

amorphous materials.

Concerning the role of ytterbium in $Er_xYb_{2-x}Si_2O_7$, we demonstrated the same twofold role as in the $Er_xYb_{2-x}O_3$ films studied in Chapter 4. Dilution of erbium by ytterbium decreases concentration quenching effects and ytterbium increases the effective erbium excitation cross section at $\lambda = 980$nm. The sensitization effect is of similar magnitude as the effect observed in Chapter 4.

The upconversion coefficient C_{up} of $Er_xYb_{2-x}Si_2O_7$ was determined by fitting the PL saturation curves as a function of photon flux. C_{up} increases from 6.00×10^{-17} cm^3s^{-1} at $N_{Er} = 1.54 \times 10^{20}cm^{-3}$ to 1.70×10^{-15} cm^3s^{-1} at $N_{Er} = 3.50 \times 10^{21}cm^{-3}$, consistent with the upconversion coefficients predicted by the Er:SiO_2 dipole-dipole model and the literature values measured for $Er_xY_{2-x}Si_2O_7$.

Chapter 6

Pathways to electrical pumping

In the previous chapters we have studied energy transfer from Yb^{3+} to Er^{3+}, where the rare earth ions were excited optically at $\lambda = 488$nm or 980nm. Optical excitation of erbium is the current pumping mechanism in erbium-doped fiber and waveguide amplifiers, but it requires an additional light source to generate the pump light. An efficient electrical excitation mechanism could skip this step. In this chapter, we investigate a potential role of ytterbium in the electrical excitation of erbium by examining possible energy transfer mechanisms between silicon and ytterbium. In that case, ytterbium could serve as an intermediate for energy transfer from silicon to erbium.

Electrical excitation of rare earth ions has been investigated since the first report of 1.54 μm photoluminescence at T = 77K in Er-implanted silicon by Ennen et al. [146]. Two years after the demonstration of PL, Ennen et al. achieved electroluminescence (EL) at 77K through carrier injection in an Er-doped Si light-emitting diode (LED) [147]. Around the same time, Haydl et al. demonstrated ytterbium electroluminescence around 1.0 μm in Yb-doped InP [148]. In both cases, the bandgap of the semiconductor at 77K is slightly larger than the energy difference between the rare earth ground state and first excited state (1.18eV for Si vs. 0.81eV in Er^{3+} and 1.38eV for InP vs. 1.27eV in Yb^{3+}), allowing for energy transfer from exciton recombination

in the semiconductor to the rare earth ions. However, in both cases the luminescence suffers from strong thermal quenching due to Auger recombination and energy back flow from the excited rare earth ions to carriers in the semiconductors, resulting in very weak luminescence at room temperature.

As explained in section 2.5, an efficient electrical excitation mechanism for rare earth ions at room temperature was achieved by doping the ions in nanocrystalline Si (nc-Si). Due to the enlarged bandgap of silicon as a result of quantum confinement, the energy transfer from nc-Si to the rare earth ions is very effective. However, the silicon nanocrystals still suffer from a low rare earth solubility and cause free carrier absorption of signal light, which introduces significant propagation losses.

6.1 Proposed energy transfer mechanism

In this chapter, we wish to explore possible energy transfer from single or polycrystalline Si to Yb^{3+} ions across a $Si/Er_xYb_{2-x}Si_2O_7$ or $Si/Er_xYb_{2-x}O_3$ interface. The bandgap of crystalline silicon at room temperature (1.12eV) is close to the 1.27eV energy gap between the ground and first excited state in Yb^{3+}. This energy difference of 160meV corresponds to the phonon energy ($1100cm^{-1} \approx 136meV$) of a Si-O bond, plus kT at room temperature (26meV), and could therefore be bridged by the absorption of one single phonon. A schematic of this energy transfer mechanism is shown in Figure 6-1,

An eventual device design for electrical excitation using energy transfer from Si to Yb^{3+} across an interface could look like the multilayer structure shown in Figure 6-2. The structure consists of a series of alternating $Er_xYb_{2-x}Si_2O_7$ and Si layers deposited on SiO_2, with two electrodes and a p- and n- region implanted vertically by means of ion implantation. This design was originally developed by Krzyzanowska et al. [149] for electrical excitation of $Er:SiO_2$. The multilayer stack avoids the problem of free carrier absorption in silicon, since it acts as a horizontal multislot structure that confines the light into the lower-index silicate layers, away from the free carriers in

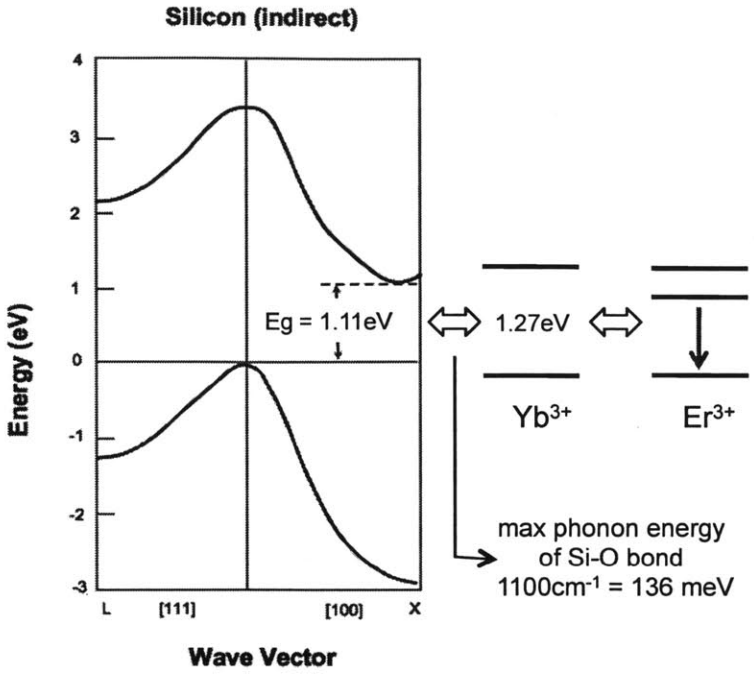

Figure 6-1: Schematic of hypothetical energy transfer from Si to Yb.

Si [150]. As opposed to rare earth ions doped directly in silicon, this structure also benefits from the high erbium concentration in $Er_xYb_{2-x}Si_2O_7$. Furthermore, in the case of electrical excitation, the lateral p-i-n structure allows easy carrier injection into the Si layers compared to a vertical structure, i.e. with the electrodes on the top and bottom of the multilayer stack, where the current density would be limited by the high resistivity of the silicate layers.

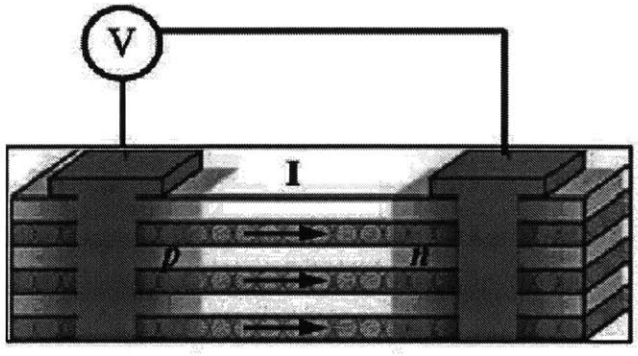

Figure 6-2: Proposed $Er_xYb_{2-x}Si_2O_7$/Si multilayer structure with a lateral p-i-n configuration, originally from [149].

To test our hypothesis of energy transfer from Si to Yb^{3+} across an interface, we have studied the photoluminescence around 980nm of Si/Yb_2O_3 and $Si/Yb_2Si_2O_7$ multilayers pumped at $\lambda = 532$nm. This wavelength is non-resonant with any absorption bands in Yb^{3+}, but is readily absorbed by polycrystalline Si. Any Yb^{3+}-related PL observed around 980nm should therefore be the result of energy transferred from Si to Yb^{3+}.

6.2 Yb_2O_3/Si and Yb−Si−O/Si multilayers

We deposited Si/Yb_2O_3 and Si/Yb−Si−O multilayer stacks with the same total amount of Si and Yb_2O_3 or Yb−Si−O, but in pairs of varying layer thickness. Comparison of the PL of the different structures allows to investigate energy transfer across the interfaces. For this analysis we fabricated

1. four different Yb_2O_3/Si multilayer stacks, each containing a total of 150nm Si and 150nm of Yb_2O_3: 20 pairs of 7.5nm thick layers, 10 pairs of 15nm thick layers, 6 pairs of 25nm thick layers and finally 3 pairs of 50nm thick layers.

2. four different Yb−Si−O/Si multilayer stacks, each containing a total of 150nm Si and 150nm of Yb−Si−O: 30 pairs of 5nm thick layers, 10 pairs of 15nm thick layers, 6 pairs of 25nm thick layers, 3 pairs of 50nm thick layers.

6.2.1 Structural properties

Yb_2O_3/Si multilayers

Figure 6-3 shows the XRD patterns of Yb_2O_3/Si multilayers deposited on quartz and annealed at 1000°C for 1h in Ar. Each spectrum is offset by an additional 30000 counts. Even though 1000°C is below the crystallization temperature of silicate thin films (see Chapter 5), the XRD spectra for the 15nm and 7.5nm thick layers exhibit clear silicate peaks. In contrast, the thicker layers crystallize into the cubic Yb_2O_3

oxide phase discussed in Chapter 4. This behavior incidates that crystallization is facilitated by nucleation sites at the Yb_2O_3/Si interfaces.

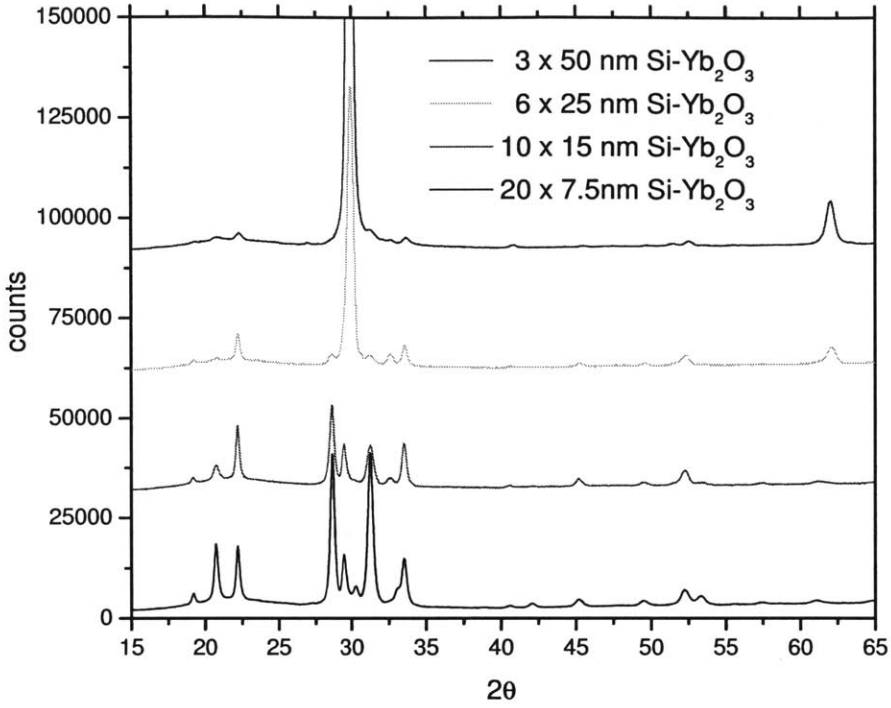

Figure 6-3: XRD patterns Yb_2O_3/Si multilayers on quartz, annealed at 1000°C for 1h in Ar.

The interaction between the different Yb_2O_3/Si layers resulting in silicate formation, especially in the case of very thin layers, is problematic if we want to fabricate a multilayer structure. Therefore, we choose to work with Yb−Si−O/Si multilayers instead, since chemical reactions between the Si and silicate layers should be less detrimental than in the case of oxide layers.

Yb−Si−O/Si multilayers

Figure 6-4 shows the XRD patterns of Yb−Si−O/Si multilayers annealed for 1h in Ar at 1000°C. As a reference, the XRD patterns of a blanket 150nm thick Yb-Si-O film and of 150nm sputtered silicon annealed in the same conditions are also shown.

Again, comparing the multilayer films with the blanket Yb−Si−O-film annealed under

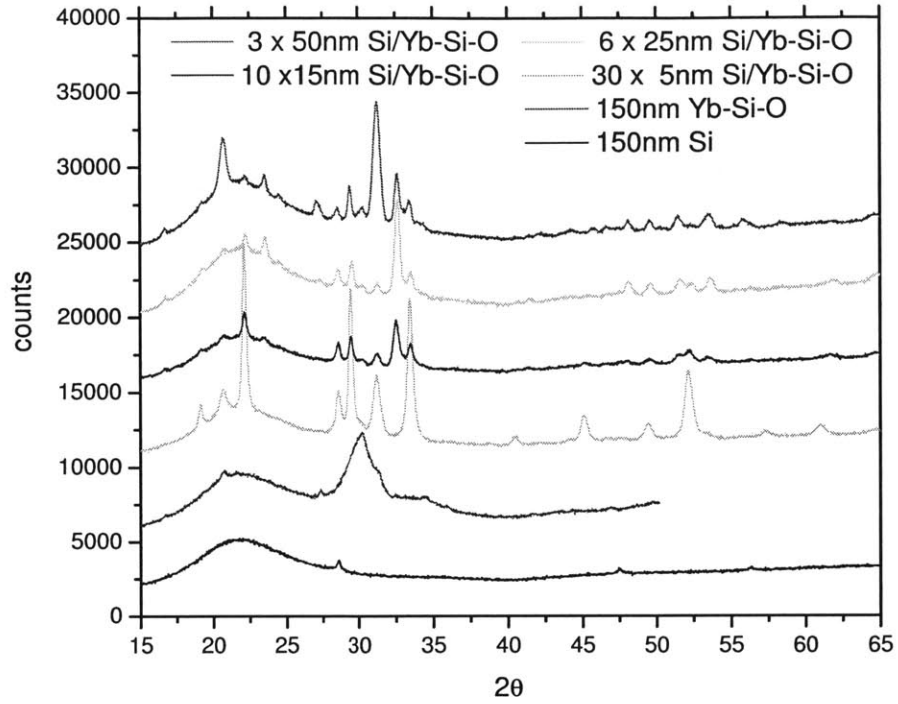

Figure 6-4: XRD patterns Yb−Si−O/Si multilayers on quartz, annealed at 1000°C for 1h in Ar.

the same conditions, it is seen that Yb−Si−O/Si interfaces can act as nucleation sites for crystallization. It is clear that the strongest crystallization occurs for the multilayer with 5nm thick layers. The XRD peaks can be matched to the oxyapatite phase discussed in Chapter 5.

6.2.2 Photoluminescence excited at $\lambda = 532$nm

Figure 6-5 shows Yb−Si−O/Si multilayer PL around 980nm pumped at 532nm. It is clear that no Yb^{3+} photoluminescence is observed.

The failure to observe any PL may be due to ytterbium concentration quenching. Indeed, the ytterbium concentration in both the Yb_2O_3/Si and Yb−Si−O/Si multilayers is of the order of $10^{21}cm^{-3}$. A second experiment to investigate the possibility of silicon to ytterbium energy transfer is discussed in section 6.3.

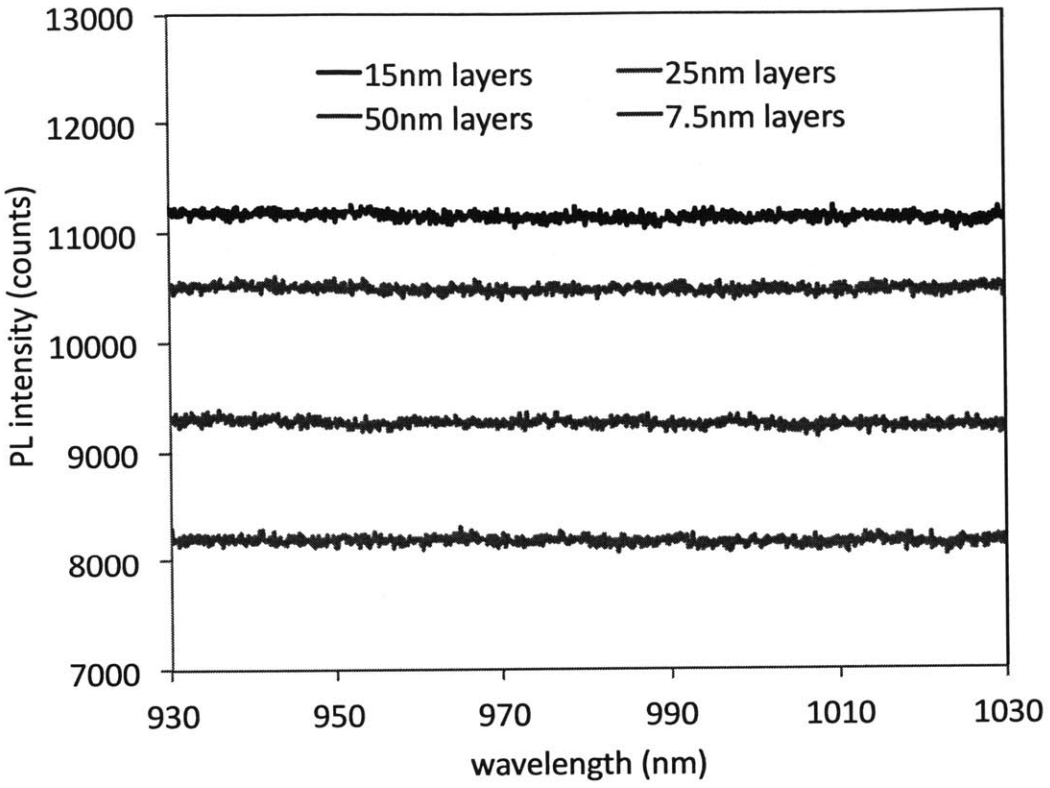

Figure 6-5: Multilayer PL around 980nm. The spectra are offset for clarity.

6.3 $Yb_yY_{2-y}Si_2O_7$ thin films

Since we were not able to demonstrate silicon to ytterbium energy transfer with PL measurements on the Yb_2O_3/Si and Yb−Si−O/Si multilayers, a second experiment was designed. To solve the problem of ytterbium concentration quenching due to high ytterbium concentrations, ytterbium was diluted by co-sputtering ytterbium oxide with yttrium oxide Y_2O_3. In order to miminize interfacial interactions between the sputtered film and the Si or SiO_2 substrates, we deposited the disilicate $Yb_yY_{2-y}Si_2O_7$. Since there is no stable compound with higher Si concentration than the disilicate, surface interactions with the Si or SiO_2 substrates are limited.

The $Yb_yY_{2-y}Si_2O_7$ films were deposited simultaneously on three different substrates

1. crystalline Si treated with buffered oxide etch (BOE) before sputtering to remove native oxide. The deposition on the Si substrate was done within 1h of the BOE treatment, to prevent regrowth of the native oxide.

2. Si coated with 3μm of thermal SiO_2

3. quartz

Upon excitation with $\lambda = 532$nm laser light, comparison between the PL around 1μm should teach us the following. The film on the quartz substrate should exhibit no photoluminescence, since ytterbium is not able to absorb $\lambda = 532$nm laser light and there are no other known excitation mechanisms. Comparison of the PL of the film deposited on Si and the film deposited on thermal SiO_2 should tell us whether there is energy transfer between silicon and ytterbium and whether this is a short range interaction (at the interface) or a long range interaction (for example due to photon emission from Si and subsequent absorption by Yb).

6.3.1 Structural properties

Figure 6-6 shows the XRD spectra for the $Yb_yY_{2-y}Si_2O_7$ thin films on the three different substrates, annealed for 30min at 1200°C in O_2. The broad peak centered at $2\theta = 22°$ is due to amorphous SiO_2 from either the thermal or quartz substrate. As expected, the amorphous peak is completely absent in the case of the Si substrate, and it is larger for the quartz substrate than for the substrate with 3 μm thermal SiO_2.

The XRD peaks of the film on quartz can all be matched to the anorthic α-$Y_2Si_2O_7$ phase (pdf 04-016-5897). For the films deposited on Si and thermal SiO_2, a mixture between α-$Y_2Si_2O_7$, β-$Y_2Si_2O_7$ (pdf 04-012-4410) and oxyapatite is found. It is unclear why the phase structure of the two films on quartz and thermal SiO_2 is different.

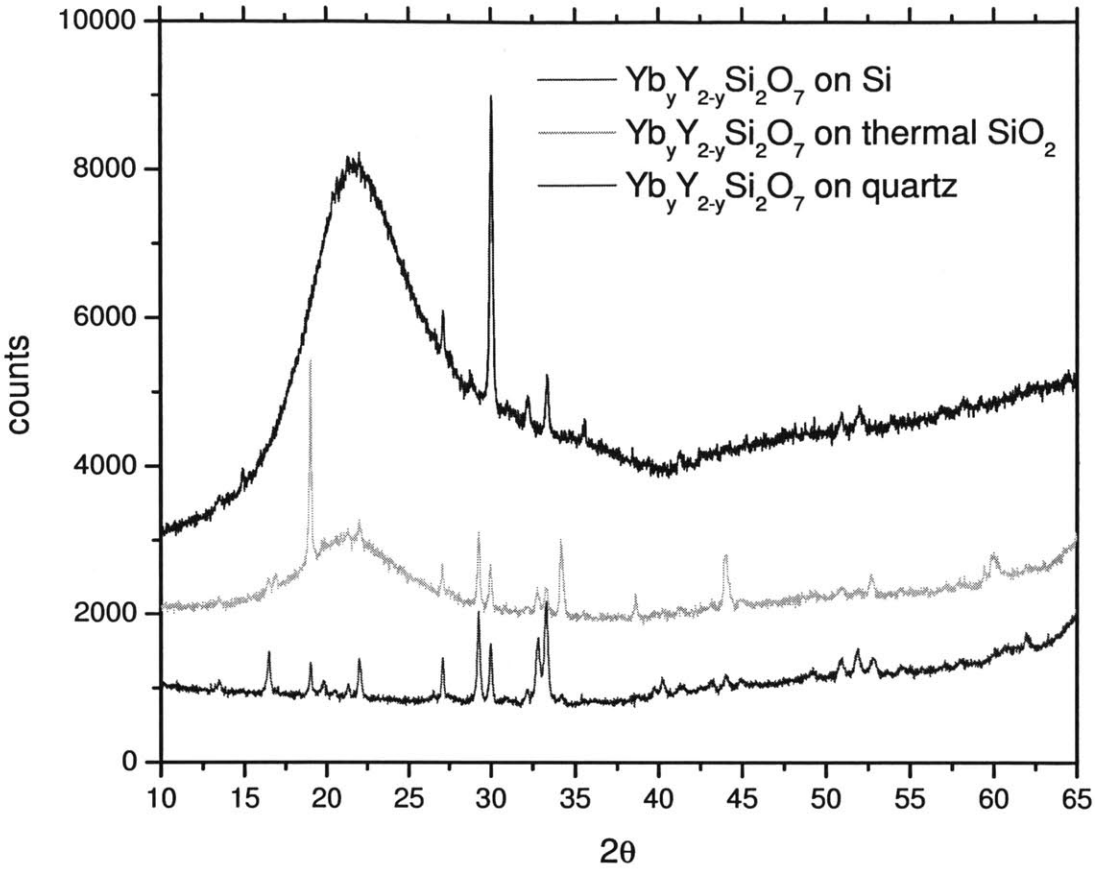

Figure 6-6: The XRD spectrum from $Yb_yY_{2-y}Si_2O_7$ on quartz annealed for 30min at 1200°C in O_2 matches with α-$Y_2Si_2O_7$ (pdf 04-011-2465). The films deposited on Si and SiO_2 show peaks matching β-$Y_2Si_2O_7$ (pdf 04-012-4410).

6.3.2 Photoluminescence excited at $\lambda = 532$nm

Two different PL spectra are present in the films annealed at 1200°C. In the films on Si and SiO_2, both spectra appear, whereas on the film on quartz, only one spectrum is present. This can be correlated to the existence of only one phase (the α disilicate) in the film deposited on quartz, whereas multiple phases are present in the films deposited on Si and SiO_2.

Figure 6-7 shows three different PL spectra. First of all, we notice a difference in background between the Si and SiO_2 substrates and quartz. The onset around 900nm is due to silicon bandgap PL from the substrate. The decrease beyond $\lambda = 1000$nm is

due to detector sensitivity of the silicon CCD detector. The same spectra are present on the thermal SiO_2 substrate. Spectrum 1 is very narrow peak around 973.4nm (FWHM = 1.6nm) with a smaller shoulder around 977.3nm. Spectrum 2 shows two broader peaks at 962.9nm and 974.6nm.

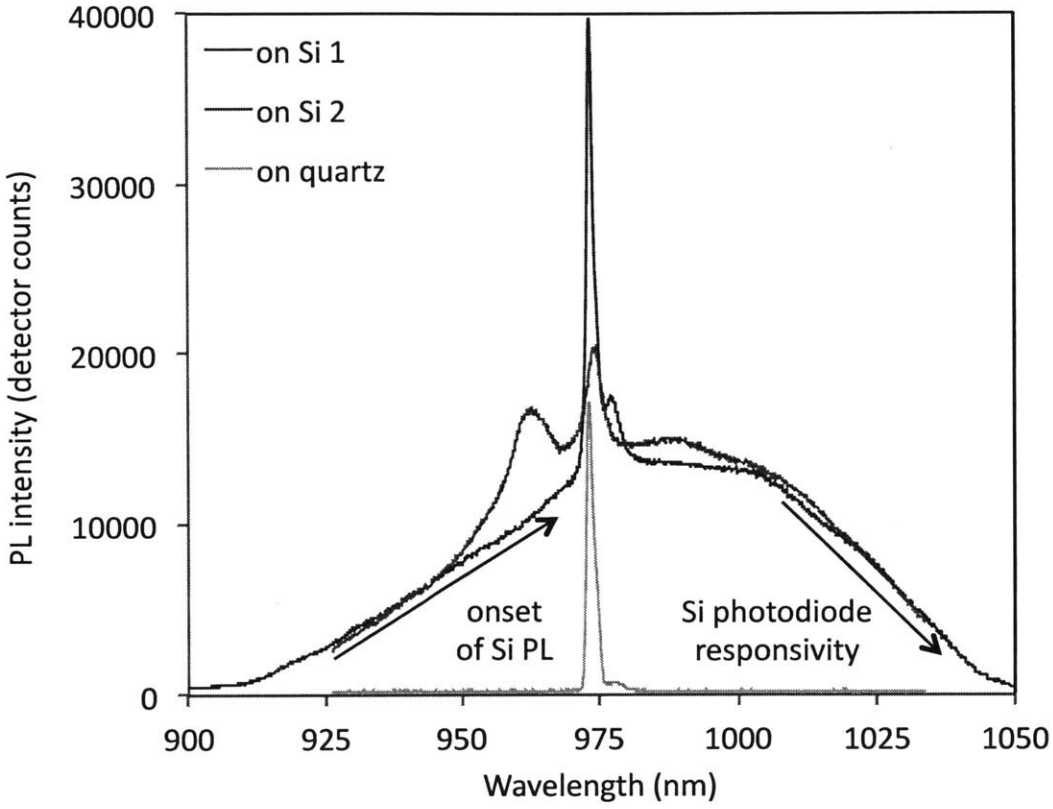

Figure 6-7: Room temperature PL excited at $\lambda = 532$nm from $Yb_yY_{2-y}Si_2O_7$ thin films deposited on silicon and quartz substrates.

Secondly, the fact that there is PL at all for the film deposited on quartz is remarkable since there is no known excitation mechanism for ytterbium at this wavelength. The photoluminescence around 1μm of the $Yb_yY_{2-y}Si_2O_7$ thin films deposited on quartz must occur through indirect excitation of Yb^{3+} at $\lambda = 532$nm through a currently unidentified mechanism. Similar PL intensities are measured for the $Yb_yY_{2-y}Si_2O_7$ thin films deposited on silicon and deposited on quartz, indicating no additional energy transfer from crystalline silicon to the $Yb_yY_{2-y}Si_2O_7$ thin film across the interface.

6.4 Conclusion

Two different experiments were performed to investigate the possibility of energy transfer from silicon to ytterbium across an interface. First of all, Yb_2O_3/Si and Yb−Si−O/Si multilayers were deposited with varying layer thicknesses, to investigate the influence of the interface between Si and ytterbium compounds. It was found that the interfaces drive crystallization by increasing nucleation sites, but no PL was observed.

Secondly, $Yb_yY_{2-y}Si_2O_7$ thin films were deposited on quartz, silicon and thermal SiO_2 in order to compare the influence of possible energy transfer from the crystalline silicon substrate. Similar PL intensities were observed for the $Yb_yY_{2-y}Si_2O_7$ thin films deposited on silicon and deposited on quartz, indicating photoluminescence of ytterbium excited by an unidentified mechanism, but showing no additional energy transfer from crystalline silicon to the $Yb_yY_{2-y}Si_2O_7$ thin film across the interface.

Chapter 7

Engineering gain in erbium-ytterbium-yttrium disilicates

In Chapters 4 and 5, we demonstrated the twofold role of Yb^{3+} in erbium-ytterbium oxides and silicates. Firstly, dilution of erbium by ytterbium reduces concentration quenching effects such as energy migration and upconversion, thereby increasing luminescence quantum efficiency. Secondly, because of its large absorption cross section and its resonance with erbium at $\lambda = 980$nm, Yb^{3+} increases the effective excitation cross section of Er^{3+} for optical pumping at $\lambda = 980$nm. From the perspective of an amplifier, an increased luminescence quantum efficiency will increase the *level of population inversion* and therefore the magnitude of the *gain coefficient* γ at a given pump power. An increased excitation cross section will decrease the *inversion threshold*, i.e. the pump power where the population of the Er^{3+} first excited state exceeds the population of the ground level. This twofold effect makes erbium-ytterbium oxides and disilicates excellent candidates for an on-chip amplifier.

In this chapter, we apply our knowledge about the role of ytterbium to engineer a waveguide amplifier. Using the rate equations and propagation equations discussed in sections 7.1 and 7.3, we model a single-mode waveguide with a co-propagating pump at λ =980nm and signal at λ =1540nm, as depicted in Figure 7-1. For the gain

medium we use $Er_xYb_yY_{2-x-y}Si_2O_7$, in other words, we include yttrium (Y^{3+}) as a third rare earth element besides erbium (Er^{3+}) and ytterbium (Yb^{3+}). As discussed in Chapter 2, yttrium has no $4f$ electrons and therefore has no energy levels in the visible or infrared. As opposed to ytterbium, it acts as a pure dilutant and does not absorb or transfer 980nm photons. Adding yttrium allows to vary the Er^{3+} and Yb^{3+} concentrations independently.

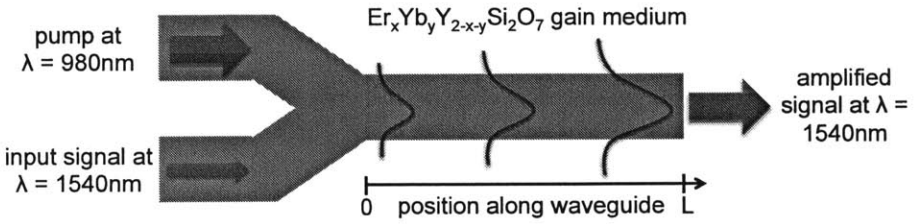

Figure 7-1: $Er_xYb_yY_{2-x-y}Si_2O_7$ waveguide amplifier with co-propagating pump and signal.

7.1 Rate equation model

Figure 7-2 shows the energy levels of Er^{3+} and Yb^{3+} and their interactions.

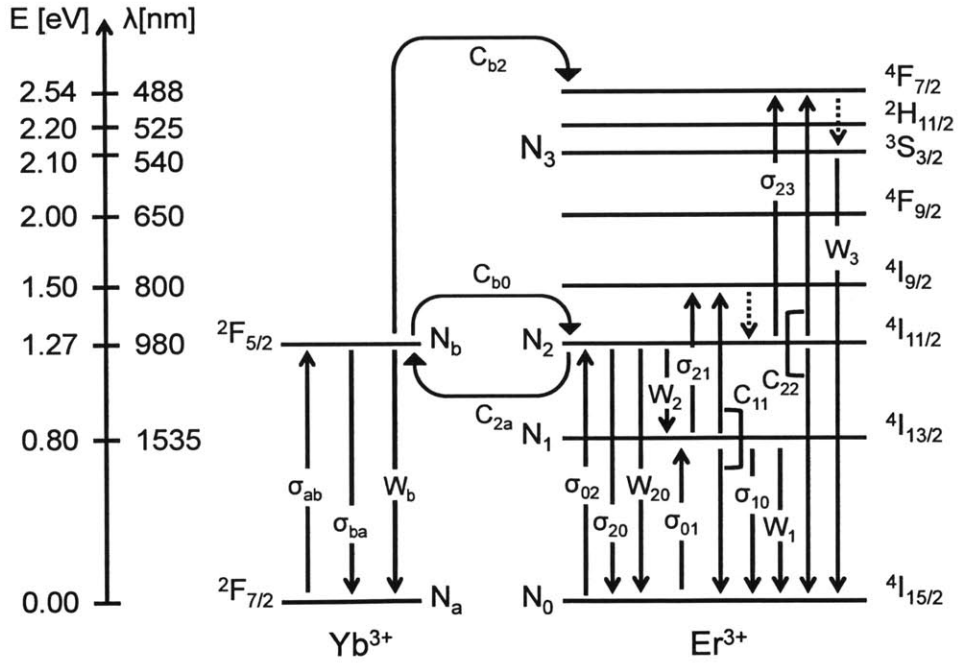

Figure 7-2: Energy level diagram of Er^{3+} and Yb^{3+} used in the rate equation model.

Ytterbium has only two energy levels in the energy range of interest: the ground level and the first excited level at 980nm. We write the populations as N_a and N_b respectively. In erbium, we only consider the ground state (population N_0) and the levels at 1550nm, 980nm and 488nm (populations N_1, N_2 and N_3, respectively). The other levels decay very quickly (rates $> 10^5$ s^{-1}) through either radiative or non-radiative relaxation and are not relevant for our model [49].

The **decay rate** of a particular level $|i\rangle$ is given by W_i. This rate includes decay by spontaneous emission and non-radiative transitions by phonon decay. Given its single exponential decay, we can also include decay by **energy migration** in W_i.

Energy transfer between ytterbium and erbium was described in detail in section 2.4.3. The energy transfer rates are of the type $C_{tr}N_gN_r$, where C_{tr} is the energy transfer coefficient in $cm^3.s^{-1}$, N_g is the population of the level giving its energy away and N_r is the population of the level receiving the energy. For example, the rate for the resonant energy transfer from Yb^{3+} to Er^{3+} at 980nm is given by $-dN_b/dt = dN_2/dt = C_{b0}N_bN_0$, where C_{b0} is the transfer coefficient. Analogously, the rate of backtransfer is $dN_b/dt = -dN_2/dt = C_{2a}N_2N_a$. Ytterbium can also transfer its energy to the $^4I_{11/2}$ level of erbium exciting it to the $^4F_{7/2}$ level at 488nm. The rate of this transfer process would then be $C_{b2}N_bN_2$.

Upconversion can be modeled by a similar term as energy transfer. After all, upconversion is an energy transfer process between to erbium ions in the same state $|i\rangle$. The rate of upconversion is $dN_i/dt = -2C_{ii}N_i^2$, where C_{ii} is the upconversion coefficient in $cm^3.s^{-1}$. In the upconversion process, two Er ions in state $|i\rangle$ will combine their energy, exciting one Er^{3+} ion to state $|k\rangle$ (where $|k\rangle$ has twice the energy of $|i\rangle$) and one Er^{3+} ion to the ground state. This causes a term $+C_{11}N_1^2$ in the rate equations for level $|k\rangle$ and for the ground state.

Absorption and stimulated emission: the transition rate from an initial state $|i\rangle$ to a final state $|k\rangle$ by absorption of a photon of wavelength λ is given by $\sigma_{ik}\Phi_\lambda N_i$, where σ_{ik} is the absorption cross section in cm^{-2}. The rate of the reverse process, stimulated emission, is given by $\sigma_{ki}\Phi_\lambda N_k$, where σ_{ki} is the emission cross section.

The population of each level in Er^{3+} and Yb^{3+} at given photon fluxes at 980nm and 1550nm can now be calculated by means of the rate equations

$$\frac{dN_b}{dt} = (\sigma_{ab}N_a - \sigma_{ba}N_b)\,\Phi_{980} - W_bN_b - C_{b0}N_bN_0 + C_{2a}N_aN_2 - C_{b2}N_bN_2 \quad (7.1)$$

$$\frac{dN_1}{dt} = (\sigma_{01}N_0 - \sigma_{10}N_1)\,\Phi_{1550} - \sigma_{12}\Phi_{1550}N_1 + W_{21}N_2 - W_1N_1 - 2C_{11}N_1^2 \quad (7.2)$$

$$\begin{aligned}\frac{dN_2}{dt} &= \sigma_{02}\Phi_{980}N_0 - \sigma_{20}\Phi_{980}N_2 + \sigma_{12}\Phi_{1550}N_1 - \sigma_{23}\Phi_{980}N_2 - W_{20}N_2 \\ &\quad + C_{11}N_1^2 - 2C_{22}N_2^2 \qquad \text{(upconversion)} \\ &\quad + C_{b0}N_bN_0 - C_{2a}N_aN_2 - C_{b2}N_bN_2 \qquad (\text{transfer } Yb^{3+} \leftrightarrow Er^{3+})\end{aligned} \quad (7.3)$$

$$\frac{dN_3}{dt} = \sigma_{23}\Phi_{980}N_2 - W_3N_3 + C_{22}N_2^2 + C_{b2}N_bN_2 \quad (7.4)$$

$$N_{\mathrm{Yb}} = N_a + N_b \quad (7.5)$$

$$N_{\mathrm{Er}} = N_0 + N_1 + N_2 + N_3 \quad (7.6)$$

where Φ_{980} and Φ_{1550} are the flux densities (in photons/cm^2.s) at 980nm and 1550nm, respectively, which include both pump, signal and amplified spontaneous emission from Er and Yb.

The choice of parameters is discussed in the next section.

Numerical Solution After substitution of Eq.7.5 and 7.6 into Eq.7.1-7.4, we obtain a system of 4 ordinary differential equations which can be solved numerically using the Runge-Kutta method. We found that the standard Matlab Runge-Kutta solver `ode45` is rather slow since the system is stiff, i.e. the step size needs to be chosen very small lest the numerical solution become unstable. Therefore we used Matlab function `ode15s`, which is the solver for a stiff system of equations. We found that `ode15s` can solve the system of rate equations up to 2.5 times faster than `ode45`, while maintaining good accuracy.

7.2 Choice of parameters for the model

Decay rates W_i

W_1 has three different contributions: radiative decay through spontaneous emission of a photon at $\lambda = 1.5\mu m$, non-radiative decay through the emission of one or more phonons, and energy migration to quenching centers. Measurement of the decay rate W_1 including all these effects was discussed in section 5.3.3. We use the data reported in Figure 5-14.

As discussed in Chapter 2, the decay (with rate W_{21}) from the 980nm level in Er^{3+} to the first excited state occurs through the emission by multiple phonons. For the $^4I_{11/2} \rightarrow {}^4I_{13/2}$ transition in silicates we saw that $W_{21} \approx 10^5\ s^{-1}$. Given the very fast multiphonon decay to the first excited state, we can safely assume that the branching ratio is 100% in favor of the transition to the $^4I_{13/2}$ level ($W_2 = W_{21}$).

In the absence of concentration quenching, different values for the Yb^{3+} decay rate W_b have been reported in literature [151], [152]. We choose a lifetime of 1.5ms. For the concentration quenching contribution, there are no values available in literature. However, we can approximate the concentration quenching distribution for Yb^{3+} by the contribution for Er^{3+} at the equivalent concentration.

According to Figure 2-7, W_3 is about $10^6\ s^{-1}$. The branching ratio to the ground state is not known accurately for silicates, but since population N_3 will generally be low, knowledge of the exact rate and branching ratio is not crucial for our model.

Energy transfer coefficients C_{b0}, C_{2a} and C_{b2}

As discussed in section 2.4.3, energy transfer from Yb^{3+} to Er^{3+} can be modeled with a similar expression as energy migration to a quenching center. In this analogy, Er^{3+} ions can be regarded as quenching centers for the excitations in Yb^{3+}. According to Equation 2.17, the energy transfer rate C_{b0} (in $cm^3.s^{-1}$) is therefore proportional to

the ytterbium concentration N_{Yb}

$$\frac{dN_b}{dt} = -C_{b0}N_bN_{\mathrm{Er}} = -(C'_{b0}N_{\mathrm{Yb}})N_bN_{\mathrm{Er}} \tag{7.7}$$

The proportionality constant was recently determined to be $C'_{b0} = 3.0 \times 10^{-39}\mathrm{cm}^6.\mathrm{s}^{-1}$ [153]. We assume that the rate constant $C_{b2} = C_{b0}$.

The rate for backtransfer C'_{2a} can now be determined using the known rate for forward transfer and the measured increase in effective excitation cross section shown in Figure 5-19. The result is shown in Figure 7-3. We find that the backtransfer coefficient can also be written as $C_{2a} = (C'_{2a}N_{\mathrm{Er}})$, where $C'_{2a} = 8.89 \times 10^{-38}\mathrm{cm}^6.\mathrm{s}^{-1}$.

Upconversion coefficients C_{11} and C_{22}

The upconversion coefficient C_{11} was determined in section 5.4. Since the interaction between the $^4\mathrm{I}_{11/2}$ levels in two neighboring Er^{3+} ions is of the same dipole-dipole type as the interactions between two $^4\mathrm{I}_{13/2}$ levels, we can assume $C_{22} = C_{11}$.

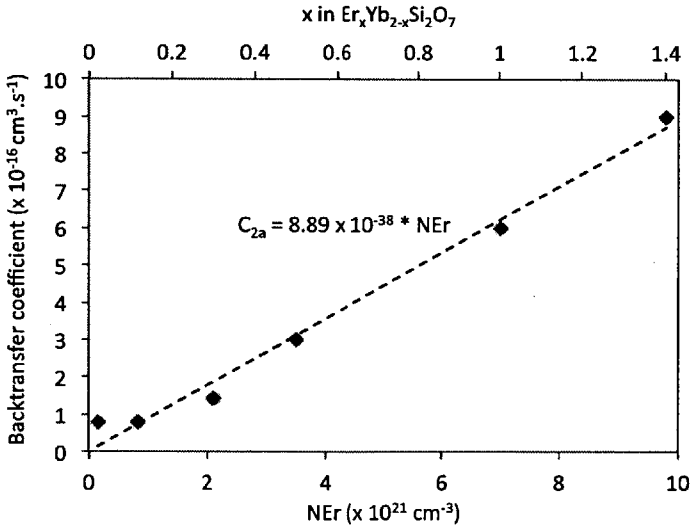

Figure 7-3: Backtransfer coefficient for $\mathrm{Er}_x\mathrm{Yb}_{2-x}\mathrm{Si}_2\mathrm{O}_7$.

Amplified spontaneous emission linewidth $\Delta\nu$ at 980nm and at 1550nm

Since we found in Chapter 5 that the α-disilicate phase has the best light emission properties, we choose the linewidths measured for this phase in our model. For the spontaneous emission linewidth at $\lambda = 1550$nm, we found in section 5.3.1 that $\Delta\lambda_{1550}$ = 47nm and for the linewidth at λ =980nm we found in secion 6.3.2 that $\Delta\lambda_{980}$ = 1.6nm. The linewidth $\Delta\nu$ in Hz can now be calculated as

$$\Delta\nu = \frac{c}{\lambda^2}\Delta\lambda \tag{7.8}$$

We find $\Delta\nu_{1550} = 5.868 \times 10^{12}$ Hz and $\Delta\nu_{980} = 0.500 \times 10^{12}$ Hz.

Absorption and emission cross sections σ_{ik} and σ_{ki}

There are many different values for the absorption and emission cross sections of Er^{3+} and Yb^{3+}, but these are relatively independent of the host material. We choose the values used by Strohhöfer et al. for Er^{3+}-Yb^{3+} co-doped Al_2O_3 [67]. The different values are shown in Table 7.3.

Table 7.1: Parameters for $Er_xYb_yY_{2-x-y}Si_2O_7$ rate equation model

Parameter	Symbol	Value
Total rare earth concentration $N_{Er} + N_{Yb} + N_Y$	N_{RE}	1.40×10^{22} cm^{-3}
Decay rate of Er^{3+} level $^4I_{13/2}$	W_1	see Figure 5-14
Decay rate of Er^{3+} level $^2I_{11/2}$	W_2	10^5 s^{-1}
Decay rate of Er^{3+} level $^4S_{3/2}$	W_3	10^6 s^{-1}
Decay rate of Yb^{3+} level $^2F_{5/2}$	W_b	see text, p.147
Transition rate of Er^{3+} $^4I_{11/2} \rightarrow {}^4I_{13/2}$	W_{21}	10^5 s^{-1}
Signal absorption cross section	σ_{01}	5.7×10^{-21} cm^2
Signal emission cross section	σ_{10}	5.7×10^{-21} cm^2
Yb^{3+} absorption cross section at 980nm	σ_{ab}	1.2×10^{-20} cm^2
Yb^{3+} emission cross section at 980nm	σ_{ba}	1.2×10^{-20} cm^2
Er^{3+} absorption cross section at 980nm	σ_{02}	1.7×10^{-21} cm^2
Er^{3+} emission cross section at 980nm	σ_{20}	1.7×10^{-21} cm^2
Er^{3+} ESA absorption cross section at 1550nm	σ_{12}	1×10^{-21} cm^2
Er^{3+} ESA absorption cross section at 980nm	σ_{23}	0×10^{-21} cm^2
Energy transfer coefficient $Yb^{3+} \rightarrow Er^{3+}$ $^2F_{5/2}+{}^4I_{15/2} \rightarrow {}^2F_{7/2}+{}^4I_{11/2}$	C_{b0}	see text, p.147
Energy transfer coefficient $Er^{3+} \rightarrow Yb^{3+}$ $^2F_{7/2}+{}^4I_{11/2} \rightarrow {}^2F_{5/2}+{}^4I_{15/2}$	C_{2a}	see text, p.147
Energy transfer coefficient $Yb^{3+} \rightarrow Er^{3+}$ $^2F_{5/2}+{}^4I_{11/2} \rightarrow {}^2F_{7/2}+{}^4F_{7/2}$	C_{b2}	see text, p.147
Cooperative upconversion coefficient $^4I_{13/2}+{}^4I_{13/2} \rightarrow {}^4I_{15/2}+{}^4I_{9/2}$	C_{11}	see Figure 5-18
Cooperative upconversion coefficient $^4I_{11/2}+{}^4I_{11/2} \rightarrow {}^4I_{15/2}+{}^4F_{7/2}$	C_{22}	see Figure 5-18
Waveguide loss coefficient at $\lambda_s = 1550$nm	α_{1550}	0 cm^{-1}
Waveguide loss coefficient at $\lambda_p = 980$nm	α_{980}	0 cm^{-1}
Spontaneous emission width at 980nm	$\Delta\nu_{980}$	0.500×10^{12} Hz
Spontaneous emission width at 1550nm	$\Delta\nu_{1550}$	5.868×10^{12} Hz

7.3 Propagation equations

Propagation of pump and signal in the waveguide are described by

$$\frac{dP_p}{dz} = \gamma_p(z)P_p(z) - \alpha_p P_p(z) \tag{7.9}$$

$$\frac{dP_s}{dz} = \gamma_s(z)P_s(z) - \alpha_s P_s(z) \tag{7.10}$$

$$\frac{dP_{se}^{\pm}}{dz} = \pm\gamma_{se}(z)P_{se}^{\pm}(z) \pm 2h\nu\Delta\nu\gamma_{se}(z) \mp \alpha_{se}P_{se}^{\pm}(z) \tag{7.11}$$

where the *gain coefficient* γ is defined as

$$\gamma_p(z) = \iint_A \psi_p\big(\sigma_{ba}N_b - \sigma_{ab}N_a + \sigma_{20}N_2 - \sigma_{02}N_0\big)dxdy \tag{7.12}$$

$$\gamma_s(z) = \iint_A \psi_s\big(\sigma_{10}N_1 - \sigma_{01}N_0\big)dxdy \tag{7.13}$$

In the above equations, $\psi_p(x,y)$ and $\psi_s(x,y)$ are the normalized pump and signal intensities respectively, which can be calculated with a mode solver such as FIMMWAVE (see section 7.5). All level populations N_i are functions of (x,y,z) and the integrals are evaluated across the $Er_xYb_yY_{2\text{-}x\text{-}y}Si_2O_7$ waveguide core. The form of the noise term $2h\nu\Delta\nu$ associated with spontaneous emission in Equation 7.11 is discussed in section 7.4.

Waveguide losses such as scattering are incorporated in the loss coefficient α, which depends on the specific design and fabrication conditions and is constant along the length of the waveguide. *Net gain* is achieved when

$$G = \int_0^L \gamma(z)dz > \alpha L \tag{7.14}$$

However, the exact value of α does not affect the results of this model. Therefore we will choose $\alpha_s = \alpha_p = 0$ cm^{-1}. The coefficients γ_{se} and α_{se} in the propagation equation for amplified spontaneous emission can be chosen equal to the coefficients γ and α at their respective wavelengths (1550nm or 980nm).

Implementation

The propagation equations can be discretized by applying the Taylor expansion

$$P(z \pm dz) = P(z) \pm \frac{dP}{dz}(z)dz + \mathcal{O}(dz^2) \tag{7.15}$$

Substitution of dP/dz by equations 7.9-7.11 gives us

$$P(z + dz) = P(z) + dz\big(\gamma(z)P(z) - \alpha P(z)\big) + \mathcal{O}(dz^2) \tag{7.16}$$

or in terms of indices in an array

$$P(k + 1) = P(k) + dz\big(\gamma(k)P(k) - \alpha P(k)\big) \tag{7.17}$$

Note that the error due to discretization is of the order of dz^2 and can be made arbitrarily small by reducing the step size dz.

The solution is obtained iteratively by moving back and forth throughout the waveguide until a stable solution is reached. We use the boundary conditions $P_{se}^{+}(0) = 0$, $P_{se}^{-}(L) = 0$, $P_p(0) = P_{p0}$ and $P_s(0) = P_{s0}$.

The forward and backward propagation equations for amplified spontaneous emission (ASE) become

$$P^{\pm}(k \pm 1) = P^{\pm}(k) \pm dz\big(\pm \gamma_{se}(k)P^{\pm}(k) \pm 2h\nu\Delta\nu\gamma_{se}(k) \mp \alpha_{se}P^{\pm}(k)\big) \tag{7.18}$$

Overlap Integral Approximation

To evaluate the integrals in expressions 7.12 and 7.13, we need to know the mode intensities $\psi_s(x, y)$ and $\psi_p(x, y)$ at each point across the waveguide core, as well as the populations $N_i(x, y)$ at each position, which in turn depend on the mode intensities through the rate equations. In other words, at each point z along the waveguide length, we need to solve the rate equations $n_x \times n_y$ times, where n_x and n_y are the

number of discretization steps in the x and y directions. For a step size of 50nm in a $500\times500\text{nm}^2$ waveguide, this would be 100 times. This can be a very time-consuming calculation.

Fortunately, the problem is significantly simplified if we assume that the populations N_i are uniform across the waveguide core. Then, the integrals become

$$\gamma_p(z) = \left(\sigma_{ba}N_b - \sigma_{ab}N_a + \sigma_{20}N_2 - \sigma_{02}N_0\right)\Gamma_p \tag{7.19}$$

$$\gamma_s(z) = \left(\sigma_{10}N_1 - \sigma_{01}N_0\right)\Gamma_s \tag{7.20}$$

$$\gamma_{se}(z) = \sigma_{10}N_1\Gamma_{se} \tag{7.21}$$

where $\Gamma_{p,s,se}$ is the so-called *overlap integral* or *confinement factor.*

$$\Gamma_{p,s,se} = \iint_A \psi_{p,s,se}(x,y)dxdy \tag{7.22}$$

The pump and signal fluxes can now be calculated as

$$\Phi_{980} = \frac{\Gamma_p\left(P_p + P^+_{se,980} + P^-_{se,980}\right)}{A_{\text{core}}} \tag{7.23}$$

$$\Phi_{1550} = \frac{\Gamma_p\left(P_s + P^+_{se,1550} + P^-_{se,1550}\right)}{A_{\text{core}}} \tag{7.24}$$

It has been shown that this so-called *overlap integral approximation* is accurate for erbium-doped fiber amplifiers if the integration is done across the region containing erbium [49].

Using the symmetric square waveguide design described in section 7.5, we can approximate the modes in a cylindrical fiber amplifier and use the overlap integral approximation accurately. The benefit of using the approximation is obvious: the most time-consuming part of the calculation is the solution of the rate equations. The number of these calculations can typically be decreased by two orders of magnitude.

7.4 Amplified spontaneous emission

Spontaneous emission from erbium ions in a waveguide amplifier can be coupled into the guided modes and will be amplifed just like the signal. The spontaneous emission will be coupled into both forward and backward propagating modes and amplified in both directions.

Amplified spontaneous emission (ASE) must be considered in waveguide amplifiers as it has two detrimental effects. Since spontaneous emission is not part of the signal, but occupies the same wavelength range, forward ASE will be a significant source of noise at the amplifier output. In addition, ASE will depopulate the erbium first excited level $^4I_{13/2}$ through stimulated emission, hence decreasing population inversion and thus amplifier gain. Backward propagating ASE diminishes gain to an even greater extent. It is strongest at the input of the waveguide, where the pump is also strongest and therefore most of the gain occurs.

In a typical erbium-doped waveguide amplifier, ASE will only occur at the signal wavelength $\lambda_s = 1.5\mu m$. In materials containing ytterbium, the ytterbium excited state $^2F_{5/2}$ can emit 980nm photons, which can then be amplified by stimulated emission between the ytterbium $^2F_{5/2}$ and $^2F_{7/2}$ levels. ASE at the waveguide output would not affect the noise figure since it is outside of the signal wavelength range, but it can depopulate the ytterbium $^2F_{5/2}$ level and thus make pumping more inefficient. Amplified spontaneous emission at 980nm can therefore not *a priori* be disregarded. In the model we use, we will compare amplifier gain with and without 980nm ASE.

Equivalent noise power

In order to include ASE in our model, we need to find an expression for the power corresponding to the spontaneous emission, called the *equivalent noise power*. P.C. Becker et al. [49] derive the expression from the following simple consideration: according to the quantum electrodynamical description of photon emission from an

excited state, the rate of spontaneous emission into a given mode is equal to the rate of stimulated emission into that mode with one single photon already present in the mode.

Assuming a mode with length L, the power associated with a photon propagating in this mode will be equal to $h\nu c/L$. Multiplying this power with the number of modes $2L\Delta\nu/c$ within a certain bandwidth $\Delta\nu$, we get for the total noise power in one direction

$$P_{ASE} = h\nu\Delta\nu \tag{7.25}$$

In the case of a fiber or a square waveguide with symmetric cladding, there will be two degenerate TE/TM modes and we have to mulitply the power in Equation 7.25 with a factor 2.

In our model, we will consider only one frequency slot $\Delta\nu$ equal to the FWHM of our photoluminescence spectrum. A more accurate noise figure at a certain wavelength can be obtained by using a set of smaller frequency slots.

7.5 Waveguide design

As a waveguide design, we choose a square, single-mode $Er_xYb_yYb_{2-x-y}Si_2O_7$ waveguide core with a symmetric cladding of SiO_2. As discussed before, this design allows us to use the overlap integral approximation. Furthermore, since the optimum erbium-ytterbium-yttrium concentration is independent of the exact waveguide design, the results in this chapter will remain valid for more complicated waveguide geometries. A waveguide cross section is shown in Figure 7-4(a), with the modes at $\lambda = 980$nm and $\lambda = 1550$nm calculated using the mode-solver FIMMWAVE.

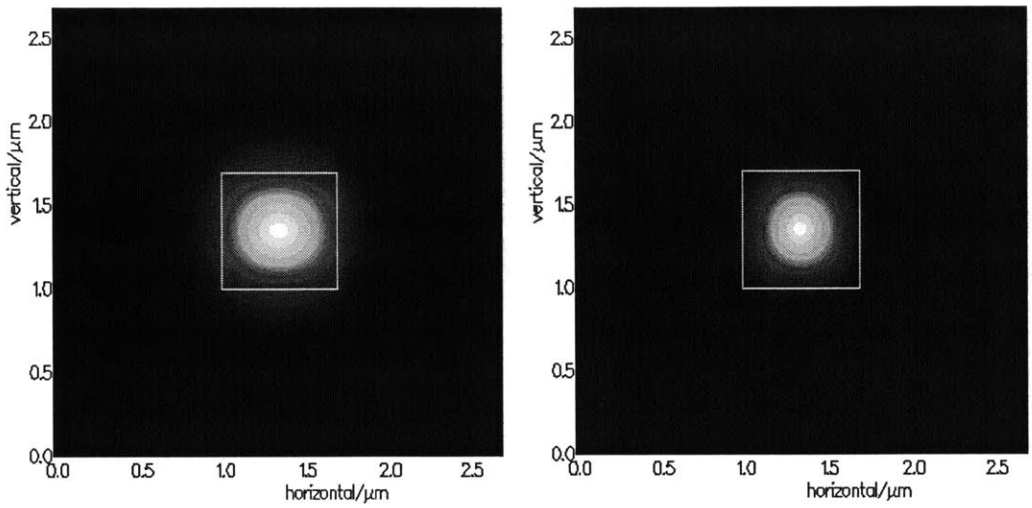

(a) λ = 1550nm. Γ = 47.69% and n_{eff} = 1.5019. (b) λ = 980nm. Γ = 83.11% and n_{eff} = 1.5892.

Figure 7-4: 700×700nm^2 square waveguide with $Er_xYb_yY_{2-x-y}Si_2O_7$ ($n = 1.73$) core and SiO_2 ($n = 1.45$) cladding. The waveguide is single mode for both 1550nm and 980nm, with degenerate TE/TM modes. The confinement factor Γ, effective index n_{eff} and effective mode area A_{eff} for each wavelength are in the captions of the individual figures.

Waveguide dimensions

When choosing the dimensions of the square waveguide, we need to optimize both the signal confinement factor Γ_s and the pump flux Φ_p for a given pump power. The pump flux will be proportional to the confinement factor divided by the area of the core. Since the confinement factor will decrease with a decreasing core area, it is not immediately clear which dimension will be optimal. For optimal amplifier performance, we should therefore maximize the figure of merit

$$\text{FOM} = \Phi_p \Gamma_s = \frac{\Gamma_p \Gamma_s}{A} \tag{7.26}$$

This figure of merit is shown in Figure 7-5. For dimensions larger than 700 x 700 nm^2, the waveguide becomes multimode at λ = 980nm. It is clear that the figure of merit in Equation 7.26 is maximized for waveguide dimensions of 700x700nm^2.

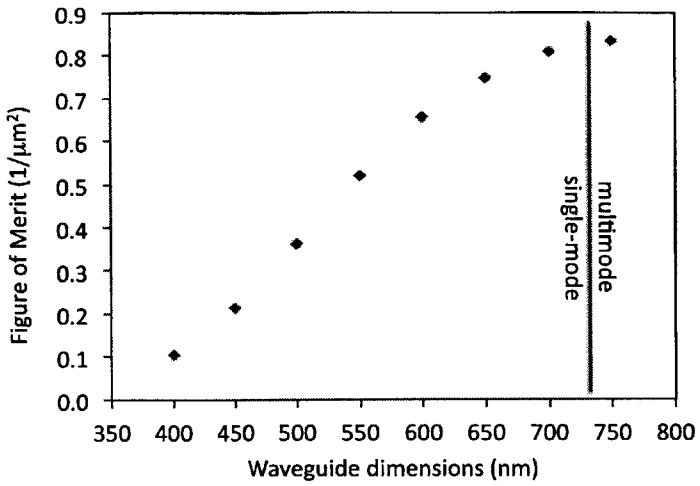

Figure 7-5: Waveguide design figure of merit (Eq. 7.26). For dimensions larger than 700 x 700 nm^2, the waveguide becomes multimode at $\lambda = 980nm$.

7.6 Results and Discussion

In Chapters 4 and 5, it was shown that the effective erbium excitation cross section increases monotonically with ytterbium concentration, suggesting that for a low-threshold EDWA the ytterbium concentration should be as high as possible. However, concentration quenching in Yb^{3+} and backtransfer from Er^{3+} to Yb^{3+} will reduce the quantum efficiency for sensitization at high ytterbium concentrations. This is discussed in sections 7.6.1 and 7.6.2.

Furthermore, high ytterbium concentrations will cause very strong absorption of the 980nm pump light along the length of the amplifier, until the 980nm pump intensity eventually falls below the erbium inversion threshold. Indeed, the high absorption cross section at $\lambda = 980nm$ that makes Yb^{3+} such a good sensitizer for Er^{3+} will at the same time cause very short absorption lengths for the pump power. Given that the low Er^{3+} concentrations required to achieve low Er^{3+} concentration quenching can only provide a moderate gain coefficient, the pump power at high ytterbium concentrations might be completely absorbed before a reasonable gain can be attained.

In other words, for increasing Yb^{3+} concentrations, there will be a trade-off be-

tween sensitization of Er^{3+} on the one hand and decreasing pump efficiency and increased pump absorption on the other hand. It is therefore necessary to dilute both the Er^{3+} and the Yb^{3+} concentrations independently with Y^{3+} ions. The optimal $Er_xYb_yY_{2-x-y}Si_2O_7$ composition and the maximum gain that can be achieved are determined in section 7.6.4 using the full rate equation model developed above.

7.6.1 Branching ratio of the $Yb^{3+}\rightarrow Er^{3+}$ energy transfer

The first excited state $^2F_{5/2}$ in Yb^{3+} can decay in two different ways: the energy can be transferred resonantly to Er^{3+} or, alternatively, Yb^{3+} can lose its excitation without energy transfer to Er^{3+}, for example via spontaneous emission or via energy migration to a quenching center. With the rate for the latter process equal to W_b and the rate for energy transfer to Er^{3+} equal to $C_{b0}N_0$ (see Eq. 7.7), we can define a quantum efficiency η_{YbEr} for the $Yb^{3+}\rightarrow Er^{3+}$ energy transfer

$$\eta_{YbEr} \approx \frac{C_{b0}N_{Er}}{C_{b0}N_{Er} + W_b} \tag{7.27}$$

where we assume that all Er is in the ground state and therefore $N_0 \approx N_{Er}$ (this assumption will overestimate the quantum efficiency at higher pump powers). A quantum efficiency $\eta_{YbEr} = 1$ implies that all excited Yb^{3+} transfers its energy to Er^{3+}; $\eta_{YbEr} = 0$ implies that no energy is transferred from Yb^{3+} to Er^{3+}.

Figure 7-6 shows the two competing decay rates W_b (blue) and $C_{b0}N_{Er}$ (red) for the case of $Er_{0.10}Yb_yY_{1.90-y}Si_2O_7$. Note that the erbium concentration is constant (xEr = 0.10) in this alloy system and Yb^{3+} ions subsitute Y^{3+} ions as we go from left to right on the x-axis.

The figure shows that both decay rates increase with increasing ytterbium concentration, but the rate for energy migration increases faster than the rate for energy transfer to erbium. As a consequence, the quantum efficiency η_{YbEr} decreases from 48.36% at $N_{Yb} = 4.2 \times 10^{21}cm^{-3}$ to 20.67% at $N_{Yb} = 1.4 \times 10^{22}cm^{-3}$.

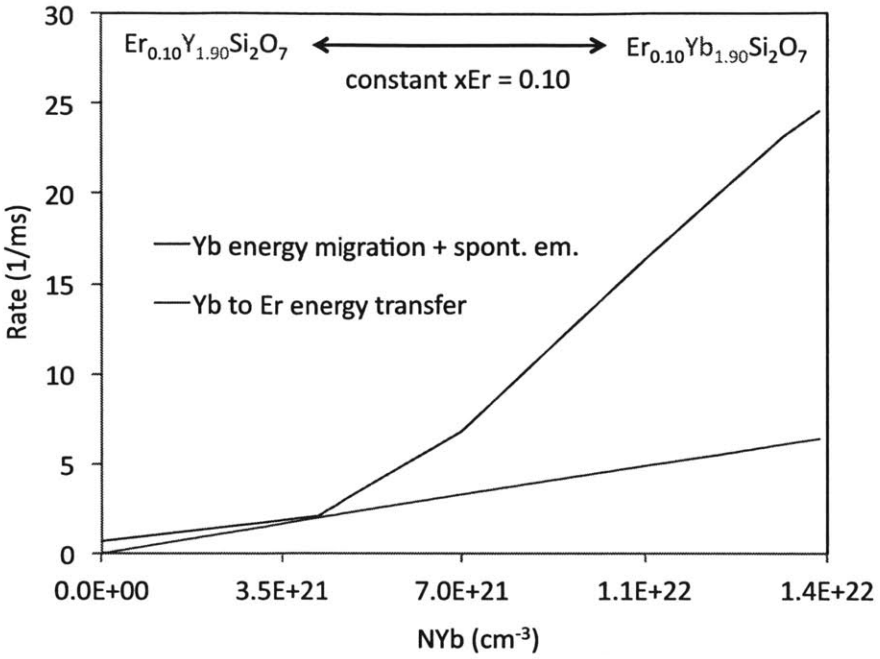

Figure 7-6: Rate of energy transfer from Yb^{3+} to Er^{3+} (red line) vs. rate of Yb^{3+} decay through energy migration or spontaneous emission (blue line) for $Er_{0.10}Yb_yY_{1.90-y}Si_2O_7$.

7.6.2 Branching ratio of the $^4I_{11/2} \rightarrow {}^4I_{13/2}$ transition

After energy transfer from Yb^{3+} to Er^{3+}, the erbium $^4I_{11/2}$ level at 980nm decays very fast ($W_{21} = 10^5 s^{-1}$, see Fig. 2-7) to the $^4I_{13/2}$ level at 1550nm. This decay is so fast that in most Er^{3+}-Yb^{3+}-doped materials, energy backtransfer from Er^{3+} to Yb^{3+} is completely ignored. Indeed, at low erbium and ytterbium concentrations, the rate of backtransfer is negligible compared to $W_{21} = 10^5$ s^{-1}. However, as discussed in section 7.2 and shown in Figure 7-3, we observe significant backtransfer at the erbium and ytterbium concentrations in erbium-ytterbium silicates.

Again, we can define a quantum efficiency η_{21}

$$\eta_{21} = \frac{W_{21}}{W_{21} + C_{2a}N_{Yb}} \tag{7.28}$$

where $\eta_{21} \rightarrow 1$ if there is no backtransfer and $\eta_{21} \rightarrow 0$ is all energy is transferred back

from Er^{3+} to Yb^{3+}. The rate W_{21} and the rate for energy backtransfer as a function of ytterbium concentration in $Er_{0.10}Yb_yY_{1.90-y}Si_2O_7$ (fixed erbium concentration) are shown in Figure 7-7.

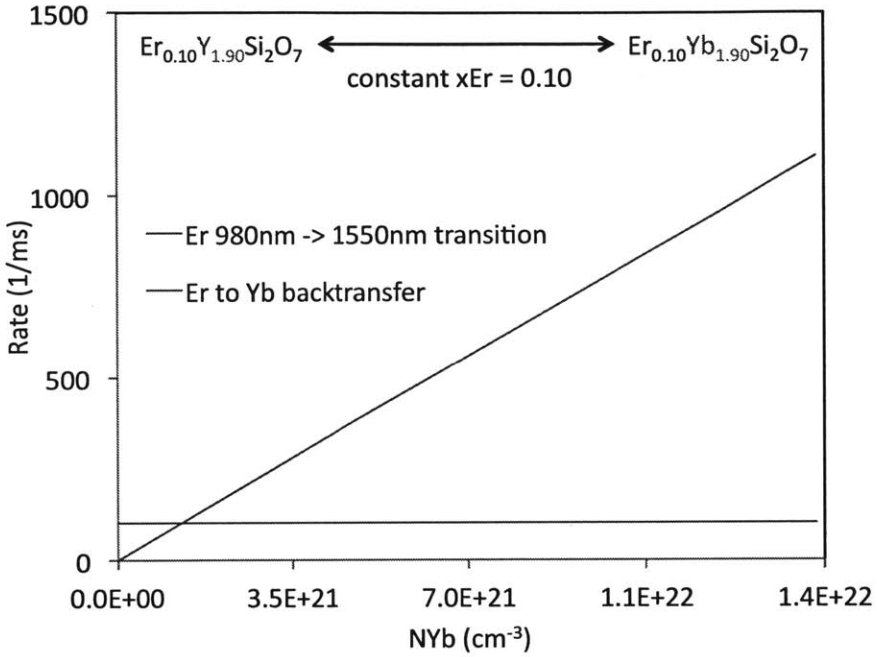

Figure 7-7: Rate of energy backtransfer from Er^{3+} to Yb^{3+} (red line) vs. rate W_{21} of $^4I_{11/2} \rightarrow {}^4I_{13/2}$ transition in Er^{3+} (blue line) for $Er_{0.10}Yb_yY_{1.90-y}Si_2O_7$.

In this case, the rate of energy backtransfer increases with increasing ytterbium concentration (as expected), whereas the rate W_{21} stays constant. As a consequence, the quantum efficiency η_{21} decreases from 100% at low N_{Yb} to only 8.28% at $N_{Yb} = 1.4 \times 10^{22} cm^{-3}$.

7.6.3 Inversion threshold of $Er_xYb_yY_{2-x-y}Si_2O_7$

Figures 7-8 and 7-9 show the population inversion $N_1 - N_0$ (in cm^{-3}) vs. 980nm pump flux (in $mW/\mu m^2$) for different compositions (i.e. yYb) of $Er_{0.05}Yb_yY_{1.95-y}Si_2O_7$ and $Er_{0.10}Yb_yY_{1.90-y}Si_2O_7$, respectively. The results are calculated using the rate equation model from section 7.1 using the parameters described in section 7.2. Any silicates with xEr > 0.10 could not be pumped to inversion.

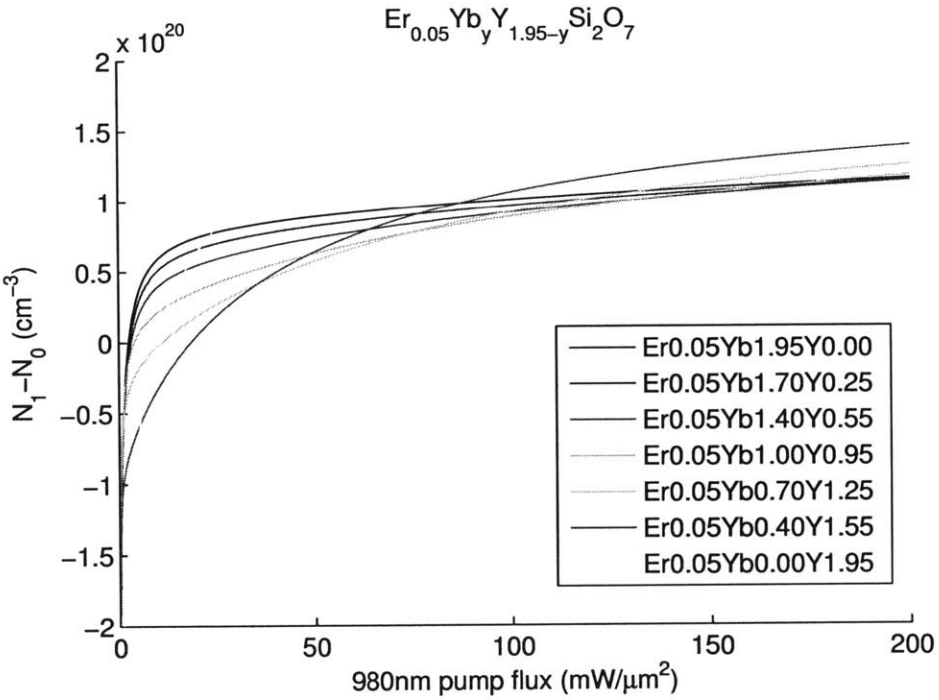

Figure 7-8: Population inversion vs. 980nm pump flux for xEr $= 0.05$ with $C'_{b0} = 3 \times 10^{-39} cm^6.s^{-1}$ and $C'_{2a} = 8.89 \times 10^{-38} cm^6.s^{-1}$.

It is seen that for the case xEr $= 0.05$ (Fig. 7-8), the inversion threshold (pump flux at which $\Delta N = 0$) generally decreases with increasing ytterbium concentration. This is consistent with the idea that sensitization by ytterbium lowers the erbium inversion threshold. However, unexpectedly, the inversion threshold for pure erbium-yttrium disilicate $Er_{0.05}Y_{1.95}Si_2O_7$ lies between the inversion thresholds of $Er_{0.05}Yb_{1.00}Y_{0.95}Si_2O_7$ and $Er_{0.05}Yb_{0.70}Y_{1.25}Si_2O_7$. In addition, for the case xEr $= 0.10$ (Fig. 7-9), the inversion threshold for pure erbium-yttrium disilicate $Er_{0.05}Y_{1.95}Si_2O_7$ is lower than any disilicate containing ytterbium.

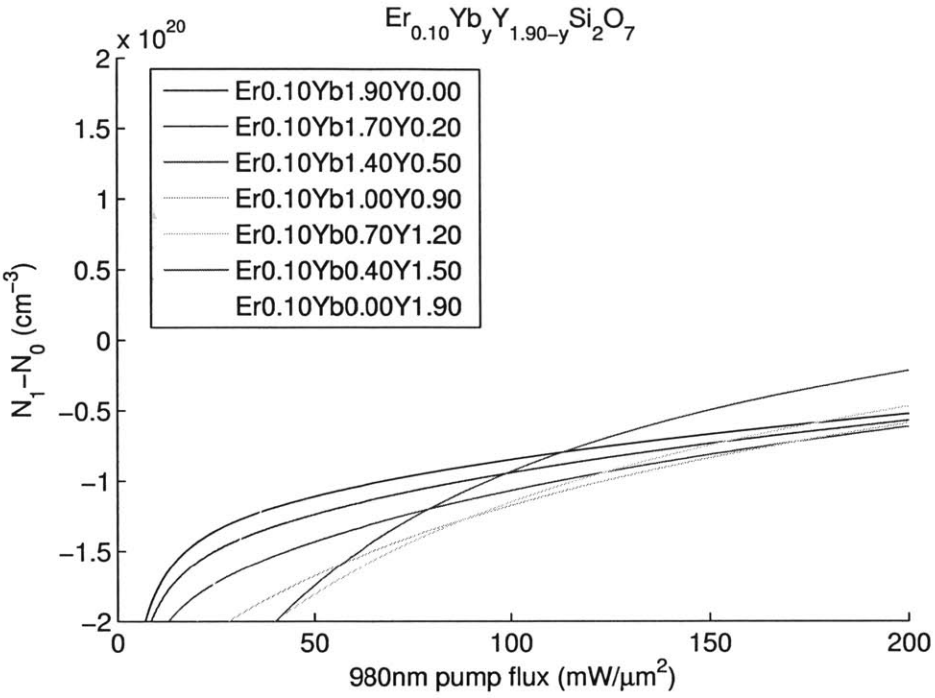

Figure 7-9: Population inversion vs. 980nm pump flux for xEr = 0.10 with $C'_{b0} = 3 \times 10^{-39}\text{cm}^6.\text{s}^{-1}$ and $C'_{2a} = 8.89 \times 10^{-38}\text{cm}^6.\text{s}^{-1}$.

These observations suggest that the magnitude of the backtransfer coefficient $C'_{2a} = 8.89 \times 10^{-38}\text{cm}^6.\text{s}^{-1}$ used in our model, which is almost 30 times larger than the forward energy transfer coefficient $C'_{b0} = 3 \times 10^{-39}\text{cm}^6.\text{s}^{-1}$, causes ytterbium to have a detrimental effect on amplifier performance. The reason for this unrealistic behavior is that the values for forward energy transfer reported in literature are obtained assuming that backtransfer can be neglected. However, as discussed above, at high erbium and ytterbium concentrations, backtransfer can significantly reduce sensitization quantum efficiency. As a consequence, the values for forward energy transfer reported in literature are really *net* energy transfer coefficients.

To test this hypothesis, we repeated the calculations with the same values for forward and backward energy transfer: $C'_{b0} = C'_{2a} = 8.89 \times 10^{-38}\text{cm}^6.\text{s}^{-1}$. The results are shown in Figures 7-10 and 7-11. In this case, we clearly see a monotonic decrease in inversion threshold with increasing ytterbium concentration. In what follows, we will use $C'_{b0} = C'_{2a} = 8.89 \times 10^{-38}\text{cm}^6.\text{s}^{-1}$ for the amplifier gain medium design.

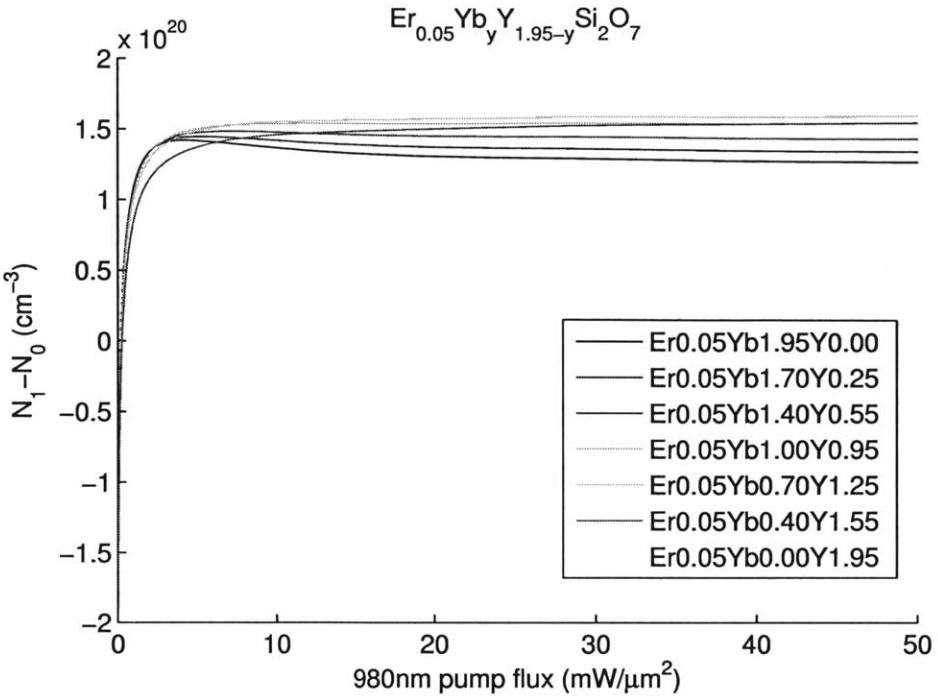

Figure 7-10: Population inversion vs. 980nm pump flux for x(Er) = 0.05 with $C'_{b0} = C'_{2a} = 8.89 \times 10^{-38}\text{cm}^6.\text{s}^{-1}$.

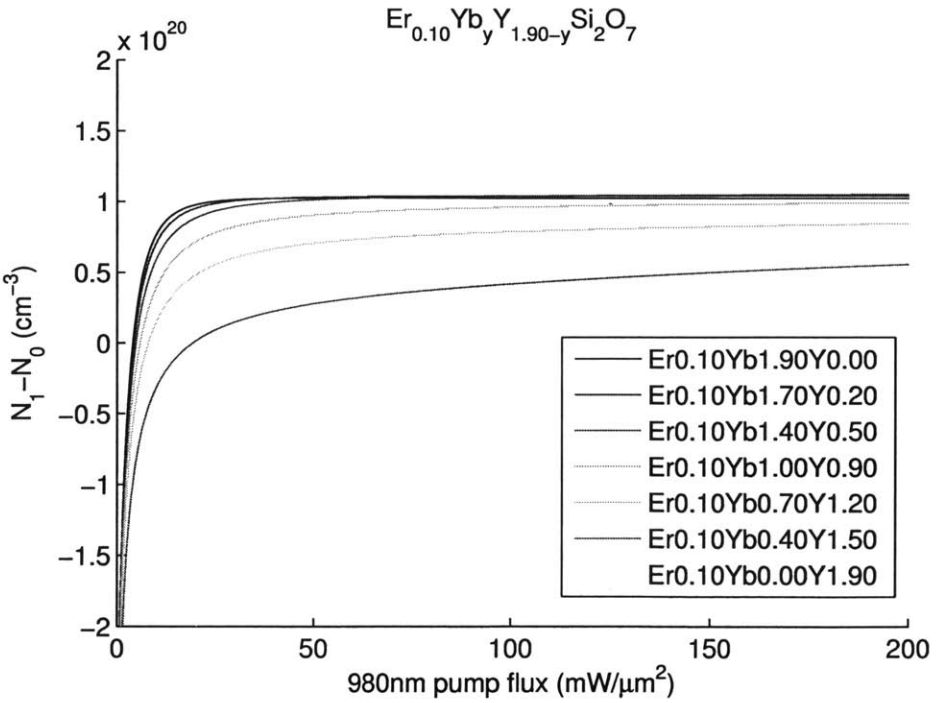

Figure 7-11: Population inversion vs. 980nm pump flux for x(Er) = 0.10 with $C'_{b0} = C'_{2a} = 8.89 \times 10^{-38}\text{cm}^6.\text{s}^{-1}$.

7.6.4 3dB $Er_xYb_yY_{2-x-y}Si_2O_7$ waveguide amplifier

Using the rate and propagation equation model discussed in sections 7.1-7.3, we can now model the gain in a $Er_xYb_yY_{2-x-y}Si_2O_7$ waveguide amplifier. As a case study, we design a 3dB waveguide amplifier, which is used in a photonic circuit to amplify a signal back to its original strength after a 50/50 split. For the design we optimize the figure of merit

$$\text{FOM} = \frac{\text{3dB}}{A \cdot P_{p0}} \tag{7.29}$$

where A is the total amplifier areal footprint in mm^2 and P_{p0} is the input 980nm pump power in mW.

The highest FOM is obtained for a $Er_{0.025}Yb_{0.200}Y_{1.775}Si_2O_7$ gain medium pumped at $\lambda = 980$nm with a pump flux of $5mW/\mu m^2$, corresponding to a pump power of 2.95mW for our 700×700 nm^2 waveguide cross section and confinement factor of 83.11%. A gain coefficient of 1.5dB/cm is achieved. Assuming a propagation loss of 0.5dB/cm, this implies a net gain coefficient of 1.0dB/cm or a 3dB amplifier length of 3cm. According to Saini et al. [71], using a coil design for the EDWA, the disilicate refractive index of $n = 1.73$ allows to fit a 3cm length into an area $3.6mm^2$ area, resulting in a figure of merit

$$\text{FOM} = \frac{\text{3dB}}{2.95\text{mW} \cdot 3.6\text{mm}^2} \tag{7.30}$$

A considerably higher figure of merit can be achieved if the upconversion coefficient can be reduced by an improved fabrication process. Assuming a reduction by a factor of 10, the optimum composition becomes $Er_{0.075}Yb_{0.200}Y_{1.725}Si_2O_7$, providing a net gain coefficient of 3.5dB/cm for a pump power of 2.95mW. This corresponds to a 12.2-fold increase in figure of merit compared to the case with high upconversion. A comparison with FOMs calculated from different literature reports is shown in Table 7.2. It is seen that even without further optimization of the upconversion coefficient, the $Er_{0.025}Yb_{0.200}Y_{1.775}Si_2O_7$ gain medium already outperforms other EDWA materials reported in literature by 35%.

Table 7.2: EDWA figure of merit for $Er_{0.025}Yb_{0.2}Y_{1.775}Si_2O_7$ compared to other EDWA materials reported in literature.

Material	Net gain coefficient (dB/cm)	3dB length (cm)	refractive index n	3dB area (mm^2)	Pump power (mW)	FOM $(\frac{1}{mm^2 \cdot mW})$
$Er_{0.075}Yb_{0.2}Y_{1.725}Si_2O_7$ ($C_{up} \times 1/10$)	3.5	0.857	1.74	0.225	2.95	1.15
$Er_{0.025}Yb_{0.2}Y_{1.775}Si_2O_7$ (measured C_{up})	1.0	3.000	1.74	3.6	2.95	9.40e-2
Phosphate glass	13.7	0.219	1.55	0.096	150	6.95e-2
Phosphate glass	4.1	0.732	1.55	1.07	21	4.45e-2
Soda-lime silicate glass	4.2	0.714	1.52	1.02	120	8.17e-3
Bi_2O_3	2.38	1.304	2.03	0.17	1050	5.60e-3
Al_2O_3	0.58	5.172	1.65	21.4	9	5.20e-3
Al_2O_3	2.0	1.500	1.65	1.80	80	2.78e-3

7.7 Conclusion

In this chapter, we developed a rate equation and propagation equation model that allows to optimize a $Er_xYb_yY_{2-x-y}Si_2O_7$ gain medium.

By matching the results of the rate equation model to our sensitization data from Chapter 5, we found that energy backtransfer from Er^{3+} to Yb^{3+} plays an important role. The backtransfer rate coefficient was determined to be $8.89 \times 10^{-38} cm^6.s^{-1}$. This is a factor 30 larger than the forward energy transfer rate coefficients reported in literature [153]. However, these literature values may underestimate the real forward energy transfer coefficient, since they are obtained from measurements of the *net* energy transfer rate (i.e. forward minus backward).

At high Yb^{3+} concentrations, there is be a trade-off between sensitization of Er^{3+} on the one hand and decreasing pump efficiency and increased pump absorption on the other hand. Therefore, we need to be able to dilute both the Er^{3+} and Yb^{3+} concentrations simultaneously by diluting with Y^{3+}. In order to determine the optimal $Er_xYb_yY_{2-x-y}Si_2O_7$ composition and the maximum gain of a real amplifier, we use the full rate and propagation equation model developed.

We conclude that $Er_{0.025}Yb_{0.200}Y_{1.775}Si_2O_7$ is the best candidate for a 3dB waveguide amplifier, providing a gain coefficient of 1.5dB/cm pumped at 2.95mW. This corresponds to a record EDWA figure of merit 3dB gain/(device area · pump power) compared to literature reports of other materials for EDWAs. Assuming a further reduction of the upconversion coefficient by an order of magnitude due to improved fabrication techniques, this figure of merit can increase by a factor 12.2.

Chapter 8

Summary and future work

8.1 Summary

In this thesis, erbium-ytterbium oxides ($Er_xYb_{2-x}O_3$) and silicates ($Er_xYb_{2-x}SiO_5$ and $Er_xYb_{2-x}Si_2O_7$) were investigated as novel materials systems for compact, high-gain and low-threshold erbium-doped waveguide amplifiers. The high refractive index and high erbium solubility make these materials great candidates for EDWA core materials.

Intense and broadband photoluminescence around 1.54μm was measured both in rare earth oxides and silicates. A dramatic increase in both PL intensity and lifetime was observed with annealing temperature in both $Er_xYb_{2-x}O_3$ and $Er_xYb_{2-x}Si_2O_7$ alloys, related to a reduction of the non-radiative decay to lattice defects.

The role of ytterbium in $Er_xYb_{2-x}O_3$ and $Er_xYb_{2-x}Si_2O_7$ is twofold. Firstly, just like yttrium in erbium-yttrium compounds, ytterbium increases the luminescence quantum efficiency by decreasing parasitic concentration quenching effects. In fact, the behavior of Yb^{3+} as a dilutant observed in $Er_xYb_{2-x}O_3$ is very similar to the results reported in literature on $Er_xY_{2-x}O_3$. Secondly, Yb^{3+} acts as a sensitizer for Er^{3+} for optical pumping at $\lambda = 980$nm, absorbing the pump photons very efficiently and transferring the absorbed energy resonantly to erbium.

In Chapter 4, we demonstrated that because of their nearly identical ionic radii, Er^{3+} and Yb^{3+} ions can substitute each other in the $Er_xYb_{2-x}O_3$ crystal lattice, allowing solid solutions across the entire concentration spectrum between pure erbium oxide and pure ytterbium oxide.

$Er_xYb_{2-x}O_3$ thin films show an onset of crystallinity after deposition and exhibit grain growth during annealing. At temperatures above 1000°C, rare earth silicates crystallize due to interfacial reactions between the sputtered $Er_xYb_{2-x}O_3$ films and the SiO_2 substrate. However, we found that the PL emission cross section for the rare earth silicates does not differ significantly from the emission cross section for rare earth oxides.

In Chapter 5, we found that as deposited $Er_xYb_{2-x}Si_2O_7$ thin films are amorphous. The crystallization temperature of the silicate thin films lies between 1000°C and 1100°C and we identified the different silicate phases that crystallize for different erbium-ytterbium concentrations and at different annealing temperatures. At low erbium concentrations, the α-disilicate phase crystallizes at 1100°C and the β-disilicate phase crystallizes at 1200°C. At high erbium concentrations, the α-disilicate crystallizes at both temperatures. These findings are consistent with the literature on bulk rare earth silicates.

We were able to correlate the photoluminescence spectra of the different films to the phases identified during XRD. The β-disilicate corresponds to a narrow PL spectrum (FWHW = 28nm) with several peaks apparent even at room temperature. The α-disilicate and the oxyapatite, like the amorphous silicates, have a broad spectrum (FWHW $\approx$ 45nm). This difference can be explained by the fact that there are several non-equivalent rare earth sites in the α-disilicate and the oxyapatite, whereas the β-disilicate has only one type of rare earth site. The rare earth ions in different sites each cause a different spectrum, giving rise to a bandwidth similar to the one for amorphous materials.

The upconversion coefficient C_{up} of $Er_xYb_{2-x}Si_2O_7$ was determined by fitting the PL saturation curves as a function of photon flux. C_{up} increases from 6.00×10^{-17} cm^3s^{-1}

at $N_{Er} = 1.54 \times 10^{20} cm^{-3}$ to 1.70×10^{-15} $cm^3 s^{-1}$ at $N_{Er} = 3.50 \times 10^{21} cm^{-3}$, consistent with the upconversion coefficients predicted by the Er:SiO_2 dipole-dipole model and literature values measured for $Er_xY_{2-x}Si_2O_7$.

In Chapter 6, we investigated a potential role of Yb^{3+} as an intermediate for energy transfer between Si and Er^{3+} for electrical excitation. The possibility of energy transfer from polycrystalline silicon to Yb^{3+} across an interface was studied in Yb_2O_3/Si and Yb−Si−O/Si multilayers with varying layer thicknesses and number of interfaces. It was found that the interfaces drive crystallization by increasing nucleation sites, but no Yb^{3+} PL caused by energy transfer from Si was observed. As a second experiment, $Yb_yY_{2-y}Si_2O_7$ thin films were deposited on quartz, silicon and thermal SiO_2 in order to compare the influence of possible energy transfer from the crystalline silicon substrate. Similar Yb^{3+} PL intensities around 980nm were observed on silicon and on quartz, indicating photoluminescence of ytterbium excited by an unidentified mechanism, but showing no additional energy transfer from crystalline silicon to the $Yb_yY_{2-y}Si_2O_7$ thin film across the interface. These findings are in line with the observations of Er^{3+}:Si and Yb^{3+}:InP, where any energy transfer from the semiconductor to the rare earth ions suffers from strong thermal quenching at room temperature.

Finally, in Chapter 7 we developed a rate equation and propagation equation model that allows to optimize an $Er_xYb_yY_{2-x-y}Si_2O_7$ gain medium. By matching the results of the rate equation model to our sensitization data from Chapter 5, we found that energy backtransfer from Er^{3+} to Yb^{3+} plays an important role. The backtransfer rate coefficient was determined to be $8.89 \times 10^{-38} cm^6.s^{-1}$. To our knowledge, this is the first description of energy backtransfer from Er^{3+} to Yb^{3+}, an effect that is negligible at lower concentrations and is therefore often ignored in literature.

We conclude that $Er_{0.025}Yb_{0.200}Y_{1.775}Si_2O_7$ is the best candidate for a 3dB waveguide amplifier, providing a gain coefficient of 1.5dB/cm pumped at $P_{p0} = 2.95$mW. This corresponds to a record EDWA figure of merit 3dB gain/(device area · pump power) compared to literature reports of other materials for EDWAs. Assuming a further reduction of the upconversion coefficient by an order of magnitude due to improved

fabrication techniques, this figure of merit can increase by a factor 12.2.

8.2 Future work

Several remaining challenges need to be overcome before erbium-ytterbium-yttrium compounds can become a competitive candidate for EDWA gain materials.

Firstly, cooperative upconversion remains the most important effect that limits the maximum erbium concentration and therefore the gain coefficient of the EDWA core material. Even when clustering can be prevented in a crystalline lattice, the upconversion coefficients determined in this thesis remain prohibitively high. However, as discussed in section 2.4.2, the upconversion coefficient is not merely a material parameter but also depends on the fabrication process. Upconversion coefficients over two orders of magnitude lower than in RF sputtered thin films have already been demonstrated for $Er_xY_{2-x}SiO_5$ nanocrystal aggregates, but this deposition technique is hardly CMOS compatible [53]. However, this does suggest that low upconversion coefficients in rare earth silicates are possible given a deposition technique that provides very uniform distribution of erbium in the lattice.

Secondly, this research has shown the importance of high temperature annealing to anneal out materials defects in order to increase luminescence lifetime and quantum efficiency. However, in processing of electronic-photonic integrated circuits, a so-called *thermal budget* limits the highest temperature that can be used in a certain fabrication step. Typically, interconnect-level processing is performed at temperatures under 450°C [155]. Therefore, it is important to develop a method to increase luminescence quantum efficiency that does not require long, high temperature anneals. Some recent publications have used substrate heating up to 400°C during RF sputter deposition, followed by a rapid thermal annealing step of 30s to reduce parasitic non-radiative decay [52, 153, 156]. Still, temperatures up to 1200°C are required to achieve an acceptable PL quantum efficiency.

Thirdly, an effective patterning method (either etching or lift-off) for rare earth oxides and silicates is required for the eventual fabrication of an EDWA device. As long as rare earth compounds can not be patterned effectively, silicate based EDWAs will have to rely on hybrid SiO_2/silicate or Si_3N_4/silicate waveguides. However, these designs cannot benefit from the high refractive index of silicates, which is required for energy efficient and compact devices.

Appendix A

Surface roughness

Surface roughness was characterized by means of Atomic Force Microscopy (AFM), using a Nanoscope IV Dimension 3100 Scanning Probe Microscope (SPM) operating in tapping mode. The surface roughness is calculated as the root mean square average R_q of the vertical distance between each data point and the mean

$$R_q = \sqrt{\frac{1}{n}\sum_{i=1}^{n}(z_i - \overline{z})^2} \tag{A.1}$$

where n is the number of data points collected.

The range ΔR is defined as the height difference between the highest and the lowest data point

$$\Delta R = \max(z_i) - \min(z_i) \tag{A.2}$$

A.1 Erbium-ytterbium oxides

Figure A-1 shows the AFM profiles of the $Er_{1.0}Yb_{1.0}O_3$ film for different annealing temperatures, measured over a $1 \times 1\mu m^2$ square area with a resolution of 256×256 datapoints. The roughness R_q and range ΔR derived from these AFM measurements are summarized in Table A.1.

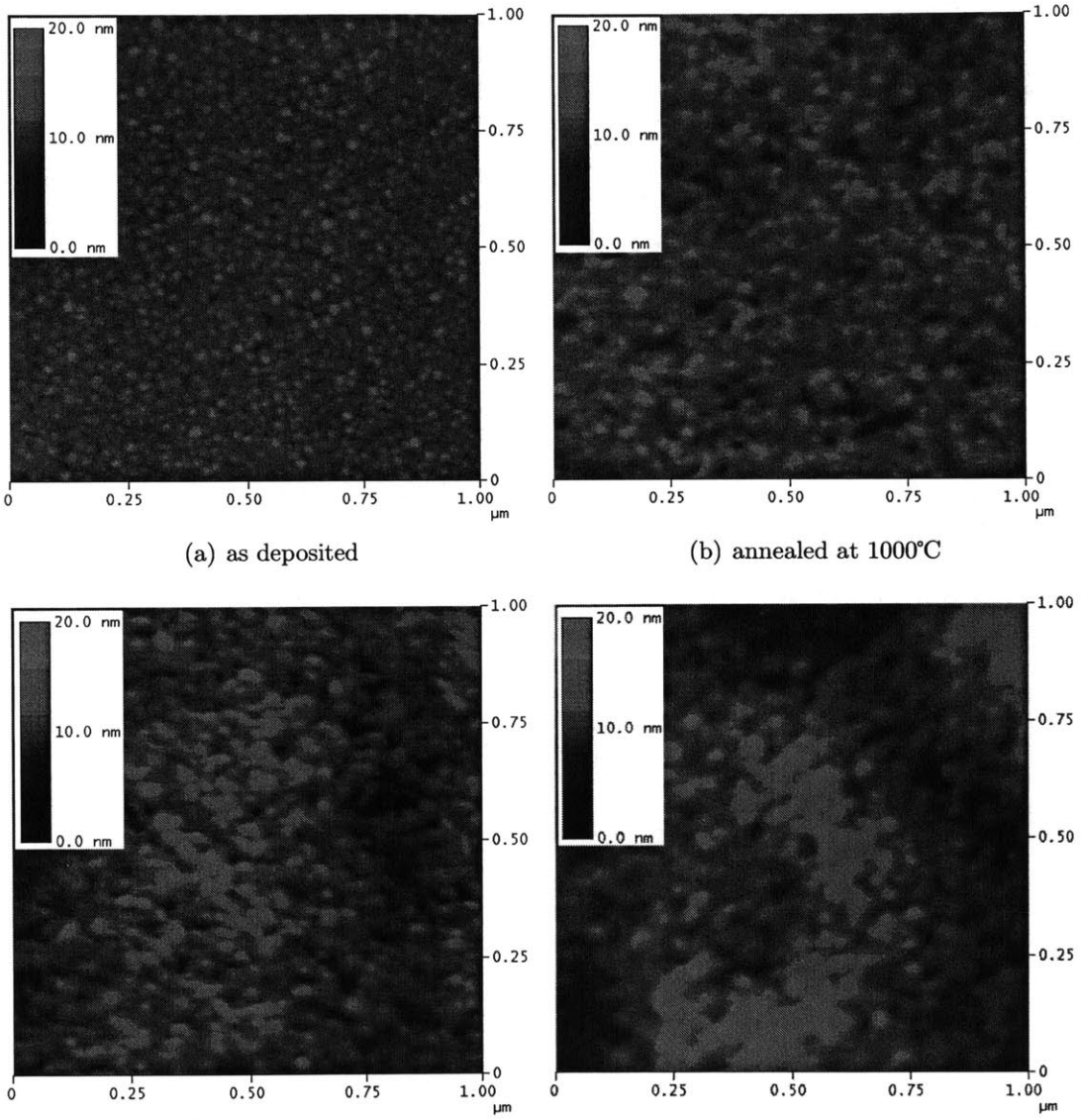

(a) as deposited

(b) annealed at 1000°C

(c) annealed at 1100°C

(d) annealed at 1200°C

Figure A-1: $1 \times 1\mu m^2$ AFM profile of $Er_{1.0}Yb_{1.0}O_3$ annealed at different temperatures. The color scale (0-20nm) is the same for each picture.

Table A.1: RMS roughness R_q and range ΔR measured by AFM over a $1 \times 1\mu m^2$ square area of film surface for $Er_{1.0}Yb_{1.0}O_3$.

annealing T	R_q (nm)	ΔR (nm)
as dep.	0.784	6.333
1000°C	1.206	10.533
1100°C	1.467	12.458
1200°C	2.227	15.779

The granular surface structure observed in Figure A-1 suggests that the as-deposited $Er_{1.0}Yb_{1.0}O_3$ film is crystalline with an estimated grain size of ~20nm and that the grain size increases with annealing temperature until it reaches ~50nm for the films annealed at 1100 and 1200°C. These results are consistent with the grain size analysis from XRD peak broadening discussed in Chapter 4. The increase in surface roughness with annealing temperature can be attributed to grain growth during annealing and crystallization of silicate phases at 1100 and 1200°C.

These results are also consistent with literature reports on Er_2O_3 thin films deposited on Si and SiO_2. AFM measurements by Mikhelashvili et al. [143] on Er_2O_3 thin films deposited on (100) Si by e-beam evaporation revealed a roughness $R_q = 1.1$nm and range $\Delta R = 7.3$nm for the as deposited film and $R_q = 1.2$ and $\Delta R = 8$ nm after a 1h anneal at 750°C in O_2.

Singh et al. [144] deposited Er_2O_3 thin films on (100) Si by MOCVD and reported an increase in film roughness with substrate temperature during growth from $R_q = 2.1$nm at 525°C to $R_q = 2.6$nm at 600°C. This increase in surface roughness is explained on the basis of grain growth during annealing.

A.2 Erbium-ytterbium silicates

Figure A-2 shows the AFM profiles of the $Er_{1.0}Yb_{1.0}Si_2O_7$ film for different annealing temperature. The roughness R_q and range ΔR derived from these AFM measurements are summarized in Table A.2.

Table A.2: RMS roughness and z-range measured by over a $1 \times 1\mu m^2$ square area of film surface for $Er_{1.0}Yb_{1.0}Si_2O_7$.

film	annealing T	R_q (nm)	ΔR (nm)
$Er_{1.0}Yb_{1.0}Si_2O_7$	as dep.	0.257	2.601
	1000°C	0.425	4.721
	1100°C	0.868	8.603
	1200°C	0.634	5.003

The surface roughness for the as deposited silicate film is seen to be about a factor 3 smaller than for the as deposited oxide film discussed in section A.1. In contrast to the oxide film, the as deposited silicate film does not exhibit a granular surface structure. This is in line with the observation in Chapter 5 that the as deposited silicate films are amorphous. Annealing at T = 1000°C introduces some surface roughness, even though the XRD analysis shows that this film is still amorphous.

The AFM data for the films annealed at 1100°C and 1200°C reveal that their surfaces are much smoother than the oxide films discussed in section A.1. The major contribution to surface roughness comes from cracks due to macroscopic stress, as observed in the AFM picture for the film annealed at 1100°C.

The low value for surface roughness may be unexpected, given that XRD analysis showed that these films are crystalline with a grain size of ~50nm. A possible explanation for the difference between oxide and silicate surface roughness may lie in the different crystallization process of the oxide and silicate films. The oxides are crystalline after deposition and exhibit grain growth during annealing. At 1100°C and 1200°C, silicate phases are formed due to interaction with the SiO_2 substrate, which requires significant mass transport between the film and the substrate. The disilicates, on the other hand, are amorphous after deposition. Crystallization of silicates from the amorphous phase can occur by short-range displacement of atoms into their crystal sites and does not require long-range mass transport. This process can occur without significant surface roughening.

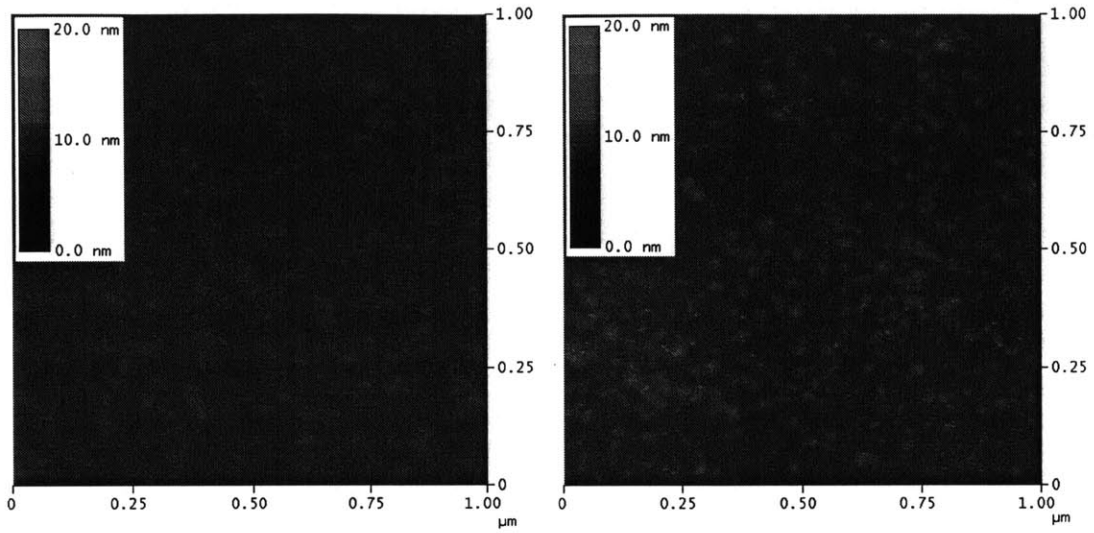

(a) as deposited

(b) annealed at 1000°C

(c) annealed at 1100°C

(d) annealed at 1200°C

Figure A-2: $1 \times 1\mu m^2$ AFM profile of $Er_{1.0}Yb_{1.0}Si_2O_7$ annealed at different temperatures. The color scale (0-20nm) is the same for each picture.

Appendix B

Etching erbium-ytterbium oxides and silicates

The development of an effective etching method for $Er_xYb_{2-x}O_3$ and $Er_xYb_{2-x}Si_2O_7$ is necessary to eventually be able to fabricate waveguide structures. To our knowledge, there is currently no known wet or dry etching method for $Er_xYb_{2-x}O_3$ or $Er_xYb_{2-x}Si_2O_7$ that provides good etch selectivity over Si or SiO_2. In fact, all papers reporting waveguides based on $Er_xY_{2-x}Si_2O_7$ or $Er_xYb_{2-x}Si_2O_7$ use hybrid waveguide designs where a SiO_2 or Si_3N_4 strip or ridge waveguide is patterned on top of or underneath a blanket silicate film [54, 135, 137, 138].

Three different dry etch recipes were tested on blanket thin films of Yb_2O_3 and $Yb_2Si_2O_7$ deposited on silicon and the etch rates were compared with the etch rates for Si (substrate) and thermal SiO_2 as a reference. The details of each recipe are shown in Table B.1. All recipes combine sputtering in Ar and chemical etching using either a chlorine based (BCl_3) or a fluorine based (SF_6) based etchant. BCl_3 is mainly known as an etchant for metals, while SF_6 is typically used to etch Si. The difference between recipes 2 and 3 is the sputtering power and etch gas pressure. Chemical etching favors etching of one species to another, whereas sputtering in Ar etches all species indiscriminately.

Table B.1: Different dry etch recipes tried.

recipe	etch gas mixture	pressure (mTorr)	RF sputtering power (W)
1	BCl_3:Ar (1:1)	30	200
2	SF_6:Ar (1:1)	30	300
3	SF_6:Ar (1:1)	20	500

Each recipe was applied for 5 min and the etch depth was measured using profilometry. The results are shown in Table B.2. For all three recipes the etch rates of Yb_2O_3 or $Yb_2Si_2O_7$ are very low. Even though the etch selectivity in recipe 3 is improved compared to recipe 2, there is not a single recipe where the etch selectivity of Yb_2O_3 or $Yb_2Si_2O_7$ over Si or SiO_2 reaches over 1:20.

Table B.2: Etch rates for Si, SiO_2, Yb_2O_3 and $Yb_2Si_2O_7$ for different dry etch recipes.

recipe	Si (Å/min)	SiO_2 (Å/min)	Yb_2O_3 (Å/min)	$Yb_2Si_2O_7$ (Å/min)
1	2460	no sample	20	40
2	7200	1152	50	32
3	2802	1666	74	76

Bibliography

[1] "International technology roadmap for semiconductors." `http://www.itrs.net`, 2011.

[2] K. Wada, H. S. Luan, K. K. Lee, S. Akiyama, J. Michel, and H. H. Kimerling, L.C. M. Popovic, "Silicon and silica platform for on-chip optical interconnection," *Proceedings of the LEOS Annual Meeting*, 2002.

[3] L. Kimerling, "Silicon microphotonics," *Applied Surface Science*, vol. 159, pp. 8–13, JUN 2000.

[4] L. Kimerling, L. Dal Negro, S. Saini, Y. Yi, D. Ahn, S. Akiyama, D. Cannon, J. Liu, J. Sandland, D. Sparacin, J. Michel, K. Wada, and M. Watts, "Monolithic Silicon Microphotonics," in *Silicon photonics*, vol. 94 of *Topics in Applied Physics*, pp. 89–119, Springer-Verlag Berlin, 2004.

[5] L. C. Kimerling, "The economics of science: from photons to products," *Optics and Photonics News*, vol. 9, p. 19, Oct 1998.

[6] A. Kenyon, "Recent developments in rare-earth doped materials for optoelectronics," *Progress in Quantum Electronics*, vol. 26, no. 4-5, pp. 225–284, 2002.

[7] S. Tewksbury and L. Hornak, "Optical clock distribution in electronic systems," *Journal of VLSI Signal Processing Systems for Signal, Image and Video Technology*, vol. 16, pp. 225–246, JUN-JUL 1997.

[8] E. Fitzgerald and L. Kimerling, "Silicon-based microphotonics and integrated optoelectronics," *MRS Bulletin*, vol. 23, pp. 39–47, APR 1998.

[9] S. Saini, *Gain Efficient Waveguide Optical Amplifiers for Si Microphotonics.* PhD thesis, Massachusetts Institute of Technology, 2004.

[10] K. Lee, D. Lim, L. Kimerling, J. Shin, and F. Cerrina, "Fabrication of ultralow-loss Si/SiO_2 waveguides by roughness reduction," *Optics Letters*, vol. 26, pp. 1888–1890, DEC 1 2001.

[11] D. Ahn, C.-Y. Hong, J. Liu, W. Giziewicz, M. Beals, L. C. Kimerling, J. Michel, J. Chen, and F. X. Kärtner, "High performance, waveguide integrated Ge photodetectors," *Optics Express*, vol. 15, pp. 3916–3921, APR 2 2007.

[12] H. Takahashi, S. Suzuki, K. Kato, and I. Nishi, "Arrayed-waveguide grating for wavelength division multi/demultiplexer with nanometre resolution," *Electronics Letters*, vol. 26, pp. 87–88, jan. 1990.

[13] J. Liu, M. Beals, A. Pomerene, S. Bernardis, R. Sun, J. Cheng, L. C. Kimerling, and J. Michel, "Waveguide-integrated, ultralow-energy GeSi electro-absorption modulators," *Nature Photonics*, vol. 2, pp. 433–437, JUL 2008.

[14] J. Michel, J. Liu, and L. C. Kimerling, "High-performance Ge-on-Si photodetectors," *Nature Photonics*, vol. 4, pp. 527–534, AUG 2010.

[15] J. Liu, X. Sun, R. Camacho-Aguilera, L. C. Kimerling, and J. Michel, "Ge-on-Si laser operating at room temperature," *Optics Letters*, vol. 35, pp. 679–681, MAR 1 2010.

[16] D. Zimmerman and L. Spiekman, "Amplifiers for the masses: EDFA, EDWA, and SOA amplets for metro and access applications," *Journal of Lightwave Technology*, vol. 22, pp. 63–70, JAN 2004.

[17] C. Giles, E. Desurvire, and J. Simpson, "Transient gain and cross talk in erbium-doped fiber amplifiers," *Optics Letters*, vol. 14, pp. 880–882, AUG 15 1989.

[18] E. Desurvire, C. Giles, and J. Simpson, "Gain dynamics of erbium-doped fiber amplifiers," *Proceedings of the Society of Photo-optical Instrumentation Engineers (SPIE)*, vol. 1171, pp. 103–117, 1990.

[19] Barbier, Denis, "Erbium-doped waveguide amplifiers promote optical-networking evolution.," *Lightwave*, vol. 17, no. 12, pp. 144–146, 2000.

[20] M. J. Digonnet, *Rare Earth Doped Fiber Lasers and Amplifiers*. CRC Press, 2nd ed., 2001.

[21] J. Felsche, "The crystal chemistry of the rare-earth silicates," in *Rare Earths*, vol. 13 of *Structure and Bonding*, pp. 99–197, Springer Berlin Heidelberg, 1973.

[22] R. Shannon, "Revised effective ionic-radii and systematic studies of interatomic distances in halides and chalcogenides," *Acta Crystallographica Section A*, vol. 32, no. SEP1, pp. 751–767, 1976.

[23] I. A. Bondar, "Rare-earth silicates," *Ceramics International*, vol. 8, no. 3, pp. 83 – 89, 1982.

[24] M. Bass, C. DeCusatis, J. Enoch, V. Lakshminarayanan, G. Li, C. MacDonald, V. Mahajan, and E. Van Stryland, *Handbook of Optics, Third Edition Volume IV: Optical Properties of Materials, Nonlinear Optics, Quantum Optics (set)*. Handbook of Optics, McGraw-Hill Companies, Inc., 2009.

[25] O. Medenbach, D. Dettmar, R. Shannon, R. Fischer, and W. Yen, "Refractive index and optical dispersion of rare earth oxides using a small-prism technique," *Journal of Optics A - Pure and Applied Optics*, vol. 3, pp. 174–177, MAY 2001.

[26] A. Kenyon, "Erbium in silicon," *Semiconductor Science and Technology*, vol. 20, pp. R65–R84, DEC 2005.

[27] N. A. Toropov and I. A. Bondar, "Silicates of the rare earth elements: phase diagram of the binary systems Sm_2O_3-SiO_2 and Yb_2O_3-SiO_2," *Russian Chemical Bulletin*, vol. 10, pp. 1278–1285, 08 1961.

[28] J. Wang, S. Tian, G. Li, F. Liao, and X. Jing, "Preparation and X-ray characterization of low-temperature phases of R_2SiO_5 (R = rare earth elements)," *Materials Research Bulletin*, vol. 36, pp. 1855–1861, SEP 1 2001.

[29] J. Felsche, "Crystal data on polymorphic disilicate $Y_2Si_2O_7$," *Naturwissenschaften*, vol. 57, no. 3, pp. 127–128, 1970.

[30] K. Liddell and D. Thompson, "X-ray diffraction data for yttrium silicates," *British Ceramic Transactions and Journal*, vol. 85, pp. 17–22, JAN-FEB 1986.

[31] A. Becerro, A. Escudero, P. Florian, D. Massiot, and M. Alba, "Revisiting $Y_2Si_2O_7$ and Y_2SiO_5 polymorphic structures by ^{89}Y MAS-NMR spectroscopy," *Journal of Solid State Chemistry*, vol. 177, no. 8, pp. 2783–2789, 2004.

[32] A. Escudero and A. I. Becerro, "Stability of the low temperature polymorphs (y and α) of Lu-doped $Y_2Si_2O_7$," *Journal of Physics and Chemistry of Solids*, vol. 68, no. 7, pp. 1348–1353, 2007.

[33] I. Hartenbach, S. Meier, and T. Schleid, "ζ-$Y_2Si_2O_7$: A new structure type within the yttrialite series," *Zeitschrift für Naturforschung - Section B Journal of Chemical Sciences*, vol. 61, no. 9, pp. 1054–1060, 2006.

[34] V. Kahlenberg, R. Kaindl, and J. Konzett, "η-$Y_2Si_2O_7$ - Structural investigations on a quenchable high-pressure mixed anion silicate," *Solid State Sciences*, vol. 9, pp. 542–550, JUN 2007.

[35] G. H. Dieke and H. M. Crosswhite, "The spectra of the doubly and triply ionized rare earths," *Applied Optics*, vol. 2, pp. 675–686, Jul 1963.

[36] J. D. B. Bradley and M. Pollnau, "Erbium-doped integrated waveguide amplifiers and lasers," *Laser & Photonics Reviews*, vol. 5, pp. 368–403, MAY 2011.

[37] W. Miniscalco, "Erbium-doped glasses for fiber amplifiers at 1500nm," *Journal of Lightwave Technology*, vol. 9, pp. 234–250, FEB 1991.

[38] W. Barnes, R. Laming, E. Tarbox, and P. Morkel, "Absorption and emission cross-section of Er^{3+} doped silica fibers," *IEEE Journal Of Quantum Electronics*, vol. 27, pp. 1004–1010, APR 1991.

[39] Y. Yan, A. Faber, H. deWaal, P. Kik, and A. Polman, "Erbium-doped phosphate glass waveguide on silicon with 4.1 dB/cm gain at 1.535 µm," *Applied Physics Letters*, vol. 71, pp. 2922–2924, NOV 17 1997.

[40] C. Strohhöfer and A. Polman, "Absorption and emission spectroscopy in Er^{3+}-Yb^{3+} doped aluminum oxide waveguides," *Optical Materials*, vol. 21, pp. 705–712, FEB 2003.

[41] T. Hoekstra, P. Lambeck, H. Albers, and T. Popma, "Sputter-deposited erbium-doped Y_2O_3 active optical waveguides," *Electronics Letters*, vol. 29, pp. 581–583, APR 1 1993.

[42] M. Dinand and W. Sohler, "Theoretical modeling of optical amplification in er-doped ti-linbo$_3$ waveguides," *IEEE Journal Of Quantum Electronics*, vol. 30, pp. 1267–1276, MAY 1994.

[43] A. Kahn, H. Kuehn, S. Heinrich, K. Petermann, J. D. B. Bradley, K. Worhoff, M. Pollnau, Y. Kuzminykh, and G. Huber, "Amplification in epitaxially grown Er:$(Gd,Lu)_2O_3$ waveguides for active integrated optical devices," *Journal of the Optical Society Of America B: Optical Physics*, vol. 25, pp. 1850–1853, NOV 2008.

[44] A. Polman, D. Jacobson, D. Eaglesham, R. Kistler, and J. Poate, "Optical doping of waveguide materials by MeV Er implantation," *Journal of Applied Physics*, vol. 70, pp. 3778–3784, OCT 1 1991.

[45] M. Sckerl, S. Guldberg-Kjaer, M. Poulsen, P. Shi, and J. Chevallier, "Precipitate coarsening and self organization in erbium-doped silica," *Physical Review B*, vol. 59, pp. 13494–13497, JUN 1 1999.

[46] H. Isshiki and T. Kimura, "Toward small size waveguide amplifiers based on erbium silicate for silicon photonics," *IEICE Transactions on Electronics*, vol. E91C, pp. 138–144, FEB 2008.

[47] A. Polman, "Erbium implanted thin film photonic materials," *Journal of Applied Physics*, vol. 82, pp. 1–39, JUL 1 1997.

[48] E. Snoeks, P. Kik, and A. Polman, "Concentration quenching in erbium implanted alkali silicate glasses," *Optical Materials*, vol. 5, pp. 159–167, MAR 1996.

[49] P. Becker, N. Olsson, and J. Simpson, *Erbium-Doped Fiber Amplifiers: Fundamentals and Technology.* Academic Press, 1999.

[50] M. Hehlen, N. Cockroft, T. Gosnell, A. Bruce, G. Nykolak, and J. Shmulovich, "Uniform upconversion in high-concentration Er^{3+}-doped soda lime silicate and aluminosilicate glasses," *Optics Letters*, vol. 22, pp. 772–774, JUN 1 1997.

[51] E. Snoeks, G. van den Hoven, A. Polman, B. Hendriksen, M. Diemeer, and F. Priolo, "Cooperative upconversion in erbium-implanted soda-lime silicate glass optical waveguides," *Journal of the Optical Society Of America B: Optical Physics*, vol. 12, pp. 1468–1474, AUG 1995.

[52] M. Miritello, R. Lo Savio, P. Cardile, and F. Priolo, "Enhanced down conversion of photons emitted by photoexcited $Er_xY_{2-x}Si_2O_7$ films grown on silicon," *Physical Review B*, vol. 81, JAN 2010.

[53] K. Suh, J. Shin, S. Seo, and B. Bae, "Er^{3+} luminescence and cooperative upconversion in $Er_xY_{2-x}SiO_5$ nanocrystal aggregates fabricated using Si nanowires," *Applied Physics Letters*, vol. 92, MAR 24 2008.

[54] K. Suh, M. Lee, J. S. Chang, H. Lee, N. Park, G. Y. Sung, and J. H. Shin, "Cooperative upconversion and optical gain in ion-beam sputter-deposited $Er_xY_{2-x}SiO_5$ waveguides," *Optics Express*, vol. 18, pp. 7724–7731, APR 12 2010.

[55] M. Federighi and F. Di Pasquale, "The effect of pair-induced energy-transfer on the performance of silica waveguide amplifiers with high Er^{3+}/Yb^{3+} concentrations," *IEEE Photonics Technology Letters*, vol. 7, pp. 303–305, MAR 1995.

[56] F. Di Pasquale and M. Federighi, "Improved gain characteristics in high-concentration Er^{3+}/Yb^{3+} codoped glass waveguide amplifiers," *IEEE Journal Of Quantum Electronics*, vol. 30, pp. 2127–2131, SEP 1994.

[57] F. Di Pasquale and M. Federighi, "Modeling of uniform and pair-induced upconversion mechanisms in high-concentration erbium-doped silica waveguides," *Journal of Lightwave Technology*, vol. 13, pp. 1858–1864, SEP 1995.

[58] V. Donzella, V. Toccafondo, S. Faralli, F. Di Pasquale, C. Cassagnettes, D. Barbier, and H. Hernandez Figueroa, "Ion-exchanged Er^{3+}/Yb^{3+} co-doped waveguide amplifiers longitudinally pumped by broad area lasers," *Optics Express*, vol. 18, pp. 12690–12701, JUN 7 2010.

[59] G. van den Hoven, E. Snoeks, A. Polman, C. van Dam, J. van Uffelen, and M. Smit, "Upconversion in Er-implanted Al_2O_3 waveguides," *Journal of Applied Physics*, vol. 79, pp. 1258–1266, FEB 1 1996.

[60] L. Agazzi, E. H. Bernhardi, K. Worhoff, and M. Pollnau, "Impact of luminescence quenching on relaxation-oscillation frequency in solid-state lasers," *Applied Physics Letters*, vol. 100, JAN 2 2012.

[61] T. Ohtsuki, S. Honkanen, S. Najafi, and N. Peyghambarian, "Cooperative upconversion effects on the performance of Er^{3+}-doped phosphate glass waveguide amplifiers," *Journal of the Optical Society Of America B: Optical Physics*, vol. 14, pp. 1838–1845, JUL 1997.

[62] S. Taccheo, G. Sorbello, S. Longhi, and P. Laporta, "Measurement of the energy transfer and upconversion constants in Er-Yb-doped phosphate glass," *Optical and Quantum Electronics*, vol. 31, pp. 249–262, MAR 1999.

[63] B. Hwang, S. Jiang, T. Luo, J. Watson, G. Sorbello, and N. Peyghambarian, "Cooperative upconversion and energy transfer of new high Er^{3+}- and Yb^{3+}-

Er^{3+}-doped phosphate glasses," *Journal of the Optical Society Of America B: Optical Physics*, vol. 17, pp. 833–839, MAY 2000.

[64] P. Golding, S. Jackson, T. King, and M. Pollnau, "Energy transfer processes in Er^{3+}-doped and Er^{3+}-Pr^{3+}-codoped ZBLAN glasses," *Physical Review B*, vol. 62, pp. 856–864, JUL 1 2000.

[65] E. Snoeks, A. Lagendijk, and A. Polman, "Measuring and modifying the spontaneous emission rate of erbium near an interface," *Physical Review Letters*, vol. 74, pp. 2459–2462, MAR 27 1995.

[66] D. Veasey, D. Funk, P. Peters, N. Sanford, G. Obarski, N. Fontaine, M. Young, A. Peskin, W. Liu, S. Houde-Walter, and J. Hayden, "Yb/Er-codoped and Yb-doped waveguide lasers in phosphate glass," *Journal of Non-Crystalline Solids*, vol. 263, pp. 369–381, MAR 2000.

[67] C. Strohhöfer and A. Polman, "Relationship between gain and Yb^{3+} concentration in Er^{3+}-Yb^{3+} doped waveguide amplifiers," *Journal of Applied Physics*, vol. 90, pp. 4314–4320, NOV 1 2001.

[68] M. Pollnau and S. Jackson, "Mid-infrared fiber lasers," in *Solid-State Mid-Infrared Laser Sources*, vol. 89 of *Topics in Applied Physics*, pp. 219–253, Springer-Verlag Berlin, 2003.

[69] W. Krupke, "Optical absorption and fluorescence intensities in several rare-earth-doped Y_2O_3 and LAF_3 single crystals," *Physical Review*, vol. 145, no. 1, pp. 325–337, 1966.

[70] H. Schober, D. Strauch, and B. Dorner, "Lattice-dynamics of sapphire Al_2O_3," *Zeitschrift für Physik B - Condensed Matter*, vol. 92, pp. 273–283, NOV 1993.

[71] S. Saini, J. Michel, and L. Kimerling, "Index contrast scaling for optical amplifiers," *Journal of Lightwave Technology*, vol. 21, pp. 2368–2376, OCT 2003.

[72] K. Hattori, T. Kitagawa, M. Oguma, H. Okazaki, and Y. Ohmori, "Optical amplification in Er^{3+}-doped P_2O_5-SiO_2 planar waveguides," *Journal of Applied Physics*, vol. 80, pp. 5301–5308, NOV 1 1996.

[73] F. Di Pasquale, S. Faralli, and V. Toccafondo, "Er^{3+}-Yb^{3+} codoped silica waveguide amplifiers longitudinally pumped by broad-area lasers," *IEEE Photonics Technology Letters*, vol. 19, pp. 1967–1969, NOV-DEC 2007.

[74] C. Faick and A. Finn, "The index of refraction of some soda-lime-silica glasses as a function of the composition," *Journal of the American Ceramic Society*, vol. 14, pp. 518–528, JUL 1931.

[75] J. Shmulovich, D. Muehlner, A. Bruce, J. Delavaux, G. Lenz, C. McIntosh, L. Gomez, E. Laskowski, A. Paunescu, R. Pafchek, I. Ryazansky, S. Kosinski, and A. White, "Recent progress in Erbium-doped waveguide amplifiers," in *Integrated Photonics Research, Technical Digest*, vol. 45 of *OSA Trends in Optics and Photonics*, pp. 35–37, Opt Soc Amer, 2000.

[76] J. D. B. Bradley, L. Agazzi, D. Geskus, F. Ay, K. Worhoff, and M. Pollnau, "Gain bandwidth of 80 nm and 2 dB/cm peak gain in Al_2O_3:Er^{3+} optical amplifiers on silicon," *Journal of the Optical Society Of America B: Optical Physics*, vol. 27, pp. 187–196, FEB 2010.

[77] T. Bååk, "Silicon oxynitride; a material for grin optics," *Applied Optics*, vol. 21, pp. 1069–1072, Mar 1982.

[78] R. R. Thomson, N. D. Psaila, S. J. Beecher, and A. K. Kar, "Ultrafast laser inscription of a high-gain Er-doped bismuthate glass waveguide amplifier," *Optics Express*, vol. 18, pp. 13212–13219, JUN 7 2010.

[79] R. Nayak, V. Gupta, A. Dawar, and K. Sreenivas, "Optical waveguiding in amorphous tellurium oxide thin films," *Thin Solid Films*, vol. 445, pp. 118–126, NOV 24 2003.

[80] E. Desurvire, J. Simpson, and P. Becker, "High-gain erbium-doped traveling-wave fiber amplifier," *Optics Letters*, vol. 12, pp. 888–890, NOV 1987.

[81] R. Mears, L. Reekie, I. Jauncey, and D. Payne, "Low-noise erbium-doped fiber amplifier operating at 1.54μm," *Electronics Letters*, vol. 23, pp. 1026–1028, SEP 10 1987.

[82] J. Palm, F. Gan, B. Zheng, J. Michel, and L. C. Kimerling, "Electroluminescence of erbium-doped silicon," *Physical Review B*, vol. 54, pp. 17603–17615, Dec 1996.

[83] B. Zheng, J. Michel, F. Ren, L. Kimerling, D. Jacobson, and J. Poate, "Room-temperature sharp line electroluminescence at λ=1.54μm from an erbium-doped, silicon light-emitting diode," *Applied Physics Letters*, vol. 64, pp. 2842–2844, MAY 23 1994.

[84] G. van den Hoven, J. van der Elsken, A. Polman, C. van Dam, K. van Uffelen, and M. Smit, "Absorption and emission cross sections of Er^{3+} in Al_2O_3 waveguides," *Applied Optics*, vol. 36, pp. 3338–3341, MAY 20 1997.

[85] C. Chryssou, F. Di Pasquale, and C. Pitt, "Improved gain performance in Yb^{3+}-sensitized Er^{3+}-doped alumina (Al_2O_3) channel optical waveguide amplifiers," *Journal of Lightwave Technology*, vol. 19, pp. 345–349, MAR 2001.

[86] P. Kik and A. Polman, "Cooperative upconversion as the gain-limiting factor in Er doped miniature Al2O3 optical waveguide amplifiers," *Journal of Applied Physics*, vol. 93, pp. 5008–5012, MAY 1 2003.

[87] G. van den Hoven, R. Koper, A. Polman, C. vanDam, J. vanUffelen, and M. Smit, "Net optical gain at 1.53 μm in Er-doped Al_2O_3 waveguides on silicon," *Applied Physics Letters*, vol. 68, pp. 1886–1888, APR 1 1996.

[88] A. Kenyon, C. Chryssou, C. Pitt, T. Shimizu-Iwayama, D. Hole, N. Sharma, and C. Humphreys, "Luminescence from erbium-doped silicon nanocrystals in

silica: excitation mechanisms," *Journal of Applied Physics*, vol. 91, pp. 367–374, JAN 1 2002.

[89] A. Polman and F. van Veggel, "Broadband sensitizers for erbium-doped planar optical amplifiers: review," *Journal of the Optical Society Of America B: Optical Physics*, vol. 21, pp. 871–892, MAY 2004.

[90] A. Kenyon, P. Trwoga, M. Federighi, and C. Pitt, "Optical properties of PECVD erbium-doped silicon-rich silica: evidence for energy transfer between silicon microclusters and erbium ions," *Journal of Physics: Condensed Matter*, vol. 6, pp. L319–L324, MAY 23 1994.

[91] M. Fujii, M. Yoshida, Y. Kanzawa, S. Hayashi, and K. Yamamoto, "1.54 μm photoluminescence of Er^{3+} doped into SiO_2 films containing Si nanocrystals: evidence for energy transfer from Si nanocrystals to Er^{3+}," *Applied Physics Letters*, vol. 71, pp. 1198–1200, SEP 1 1997.

[92] M. Fujii, M. Yoshida, S. Hayashi, and K. Yamamoto, "Photoluminescence from SiO_2 films containing Si nanocrystals and Er: effects of nanocrystalline size on the photoluminescence efficiency of Er^{3+}," *Journal of Applied Physics*, vol. 84, pp. 4525–4531, OCT 15 1998.

[93] M. Fujii, S. Hayashi, and K. Yamamoto, "Excitation of intra-4f shell luminescence of Yb^{3+} by energy transfer from Si nanocrystals," *Applied Physics Letters*, vol. 73, pp. 3108–3110, NOV 23 1998.

[94] X. Zhao and S. Komuro, "Time-resolved photoluminescence of ytterbium-doped nanocrystalline Si thin films," *Applied Physics Letters*, vol. 79, pp. 2151–2153, OCT 1 2001.

[95] S. Yerci, R. Li, and L. Dal Negro, "Electroluminescence from Er-doped Si-rich silicon nitride light emitting diodes," *Applied Physics Letters*, vol. 97, AUG 23 2010.

[96] M. Wojdak, M. Klik, M. Forcales, O. Gusev, T. Gregorkiewicz, D. Pacifici, G. Franzo, F. Priolo, and F. Iacona, "Sensitization of Er luminescence by Si nanoclusters," *Physical Review B*, vol. 69, JUN 2004.

[97] J. S. Chang, K. Suh, M.-S. Yang, and J. H. Shin, "Development and Application of Er-Doped Silicon-Rich Silicon Nitrides and Er Silicates for On-Chip Light Sources," in *Silicon Photonics II: Components and Integration* (Lockwood, DJ and Pavesi, L, ed.), vol. 119 of *Topics in Applied Physics*, pp. 95–130, Springer-Verlag Berlin, 2011.

[98] M. Suezawa and K. Sumino, "Strong photoluminescence from the reaction-product of erbium and oxygen on silicon crystal," *Japanese Journal of Applied Physics Part 2 - Letters*, vol. 33, pp. L1782–L1784, DEC 15 1994.

[99] A. Kasuya and M. Suezawa, "Resonant excitation of visible photoluminescence from an erbium-oxide overlayer on Si," *Applied Physics Letters*, vol. 71, pp. 2728–2730, NOV 10 1997.

[100] S. Saini, K. Chen, X. Duan, J. Michel, L. Kimerling, and M. Lipson, "Er_2O_3 for high-gain waveguide amplifiers," *Journal of Electronic Materials*, vol. 33, pp. 809–814, JUL 2004.

[101] M. Miritello, R. Lo Savio, F. Iacona, G. Franzo, C. Bongiorno, A. Irrera, and F. Priolo, "The influence of substrate on the properties of Er_2O_3 films grown by magnetron sputtering," *Journal of Luminescence*, vol. 121, pp. 233–237, DEC 2006.

[102] M. Miritello, R. Lo Savio, A. M. Piro, G. Franzo, F. Priolo, F. Iacona, and C. Bongiorno, "Optical and structural properties of Er_2O_3 films grown by magnetron sputtering," *Journal of Applied Physics*, vol. 100, JUL 1 2006.

[103] H. Ono and T. Katsumata, "Interfacial reactions between thin rare-earth-metal oxide films and Si substrates," *Applied Physics Letters*, vol. 78, pp. 1832–1834, MAR 26 2001.

[104] M. Miritello, R. Lo Savio, F. Iacona, G. Franzo, C. Bongiorno, and F. Priolo, "Synthesis and luminescence properties of erbium silicate thin films," *Materials Science and Engineering B: Solid State Materials for Advanced Technology*, vol. 146, pp. 29–34, JAN 15 2008.

[105] H. Isshiki, A. Polman, and T. Kimura, "Fine structure in the Er-related emission spectrum from Er-Si-O matrices at room temperature under carrier mediated excitation," *Journal of Luminescence*, vol. 102, pp. 819–824, MAY 2003.

[106] H. Isshiki, M. de Dood, A. Polman, and T. Kimura, "Self-assembled infrared-luminescent Er-Si-O crystallites on silicon," *Applied Physics Letters*, vol. 85, pp. 4343–4345, NOV 8 2004.

[107] X. J. Wang, T. Nakajima, H. Isshiki, and T. Kimura, "Fabrication and characterization of Er silicates on SiO_2/Si substrates," *Applied Physics Letters*, vol. 95, JUL 27 2009.

[108] K. Masaki, H. Isshiki, and T. Kimura, "Erbium-Silicon-Oxide crystalline films prepared by MOMBE," *Optical Materials*, vol. 27, pp. 876–879, FEB 2005. Symposium of the European-Materials-Research-Society on Si-Based Photonics - Towards True Monolithic Integration, Strasbourg, FRANCE, MAY 25-28, 2004.

[109] H. Isshiki, K. Masaki, K. Ueda, K. Tateishi, and T. Kimura, "Towards epitaxial growth of ErSiO nanostructured crystalline films on Si substrates," *Optical Materials*, vol. 28, pp. 855–858, MAY 2006. Meeting of the European-Materials-Research-Society, Strasbourg, FRANCE, MAY 30-JUN 03, 2005.

[110] T. Kimura, K. Masaki, and H. Isshiki, "Study on crystalline properties of Er-Si-O compounds in relation to Er-related 1.54 μm photoluminescence and electrical properties," *Journal of Luminescence*, vol. 121, pp. 226–229, DEC 2006.

[111] T. Kimura, Y. Tanaka, H. Ueda, and H. Isshiki, "Formation of highly oriented layer-structured Er_2SiO_5 films by pulsed laser deposition," *Physica E: Low-Dimensional Systems & Nanostructures*, vol. 41, pp. 1063–1066, MAY 8 2009. Spring Meeting of the European-Materials-Research-Society on Frontiers in Silicon-Based Photonics, Strasbourg, FRANCE, MAY 26-29, 2008.

[112] M. Miritello, R. Lo Savio, F. Iacona, G. Franzo, A. Irrera, A. M. Piro, C. Bongiorno, and F. Priolo, "Efficient luminescence and energy transfer in erbium silicate thin films," *Advanced Materials*, vol. 19, pp. 1582–1588, JUN 18 2007.

[113] R. Lo Savio, M. Miritello, F. Iacona, A. M. Piro, M. G. Grimaldi, and F. Priolo, "Thermal evolution of Er silicate thin films grown by rf magnetron sputtering," *Journal of Physics: Condensed Matter*, vol. 20, NOV 12 2008.

[114] R. Lo Savio, M. Miritello, A. M. Piro, F. Priolo, and F. Iacona, "The influence of stoichiometry on the structural stability and on the optical emission of erbium silicate thin films," *Applied Physics Letters*, vol. 93, JUL 14 2008.

[115] Kiss, Z.J. and Pressley, R.J., "Crystalline solid lasers," *Proceedings of the IEEE*, vol. 54, pp. 1236–1248, Oct 1966.

[116] R. Lo Savio, M. Miritello, P. Cardile, and F. Priolo, "Concentration dependence of the Er^{3+} visible and infrared luminescence in $Y_{2-x}Er_xO_3$ thin films on Si," *Journal of Applied Physics*, vol. 106, AUG 15 2009.

[117] L. A. Coldren and S. W. Corzine, *Diode Lasers and Photonic Integrated Circuits*. John Wiley & Sons, Incorporated, 1995.

[118] F. Patel, S. DiCarolis, P. Lum, S. Venkatesh, and J. Miller, "A compact high-performance optical waveguide amplifier," *IEEE Photonics Technology Letters*, vol. 16, pp. 2607–2609, DEC 2004.

[119] G. Della Valle, S. Taccheo, G. Sorbello, E. Cianci, V. Foglietti, and R. Laporta, "Compact high gain erbium-ytterbium doped waveguide amplifier fabricated by Ag-Na ion exchange," *Electronics Letters*, vol. 42, pp. 632–633, MAY 25 2006.

[120] J. Shmulovich, "Er-doped glass waveguide amplifiers on silicon," *Proceedings of the Society of Photo-optical Instrumentation Engineers (SPIE)*, vol. 2996, pp. 143–153, 1997.

[121] R. Ghosh, J. Shmulovich, C. Kane, M. deBarros, G. Nykolak, A. Bruce, and P. Becker, "8-mW threshold Er^{3+}-doped planar waveguide amplifier," *IEEE Photonics Technology Letters*, vol. 8, pp. 518–520, APR 1996.

[122] G. Nykolak, M. Haner, P. Becker, J. Shmulovich, and Y. Wong, "Systems evaluation of an Er^{3+}-doped planar waveguide amplifier," *IEEE Photonics Technology Letters*, vol. 5, pp. 1185–1187, OCT 1993.

[123] P. Camy, J. Roman, F. Willems, M. Hempstead, J. vanderPlaats, C. Prel, A. Beguin, A. Koonen, J. Wilkinson, and C. Lerminiaux, "Ion-exchanged planar lossless splitter at 1.5 μm," *Electronics Letters*, vol. 32, pp. 321–323, FEB 15 1996.

[124] R. Brinkmann, I. Baumann, M. Dinand, W. Sohler, and H. Suche, "Erbium-doped single-pass and double-pass Ti:$LiNbO_3$ waveguide amplifiers," *IEEE Journal Of Quantum Electronics*, vol. 30, pp. 2356–2360, OCT 1994.

[125] N. D. Psaila, R. R. Thomson, H. T. Bookey, A. K. Kar, N. Chiodo, R. Osellame, G. Cerullo, A. Jha, and S. Shen, "Er : Yb-doped oxyfluoride silicate glass waveguide amplifier fabricated using femtosecond laser inscription," *Applied Physics Letters*, vol. 90, MAR 26 2007.

[126] F. Horst, T. Hoekstra, P. Lambeck, and T. Popma, "Design of 1480nm diode-pumped Er^{3+}-doped integrated optical amplifiers," *Optical and Quantum Electronics*, vol. 26, pp. S285–S299, MAR 1994.

[127] I. Vasilief, S. Guy, B. Jacquier, B. Boulard, Y. Gao, C. Duverger, H. Haquin, V. Nazabal, J. Adam, M. Couchaud, L. Fulbert, C. Cassagnettes, F. Rooms, and D. Barbier, "Propagation losses and gain measurements in erbium-doped fluoride glass channel waveguides by use of a double-pass technique," *Applied Optics*, vol. 44, pp. 4678–4683, AUG 1 2005.

[128] W. Huang, R. Syms, E. Yeatman, M. Ahmad, T. Clapp, and S. Ojha, "Fiber-device-fiber gain from a sol-gel erbium-doped waveguide amplifier," *IEEE Photonics Technology Letters*, vol. 14, pp. 959–961, JUL 2002.

[129] A. Q. Le Quang, R. Hierle, J. Zyss, I. Ledoux, G. Cusmai, R. Costa, A. Barberis, and S. M. Pietralunga, "Demonstration of net gain at 1550 nm in an erbium-doped polymer single mode rib waveguide," *Applied Physics Letters*, vol. 89, OCT 2 2006.

[130] K. Shuto, K. Hattori, T. Kitagawa, Y. Ohmori, and M. Horiguchi, "Erbium-doped phosphosilicate glass waveguide amplifier fabricated by PECVD," *Electronics Letters*, vol. 29, pp. 139–141, JAN 21 1993.

[131] T. T. Fernandez, G. Della Valle, R. Osellame, G. Jose, N. Chiodo, A. Jha, and P. Laporta, "Active waveguides written by femtosecond laser irradiation in an erbium-doped phospho-tellurite glass," *Optics Express*, vol. 16, pp. 15198–15205, SEP 15 2008.

[132] T. Kitagawa, K. Hattori, K. Shuto, M. Yasu, M. Kobayashi, and M. Horiguchi, "Amplification in erbium-doped silica-based planar lightwave circuits," *Electronics Letters*, vol. 28, pp. 1818–1819, SEP 10 1992.

[133] K. Hattori, T. Kitagawa, M. Oguma, M. Wada, J. Temmyo, and M. Horiguchi, "Erbium-doped silica-based planar wave-guide amplifier pumped by 0.98 μm laser-diodes," *Electronics Letters*, vol. 29, pp. 357–359, FEB 18 1993.

[134] R. Schermer, W. Berglund, C. Ford, R. Ramberg, and A. Gopinath, "Optical amplification at 1534 nm in erbium-doped zirconia waveguides," *IEEE Journal Of Quantum Electronics*, vol. 39, pp. 154–159, JAN 2003.

[135] R. Guo, X. Wang, K. Zang, B. Wang, L. Wang, L. Gao, and Z. Zhou, "Optical amplification in Er/Yb silicate strip loaded waveguide," *Applied Physics Letters*, vol. 99, OCT 17 2011.

[136] R. Guo, B. Wang, X. Wang, L. Wang, L. Jiang, and Z. Zhou, "Optical amplification in Er/Yb silicate slot waveguide," *Optics Letters*, vol. 37, pp. 1427–1429, MAY 1 2012.

[137] L. Wang, R. Guo, B. Wang, X. Wang, and Z. Zhou, "Hybrid Si_3N_4-Er/Yb silicate waveguides for amplifier application," *IEEE Photonics Technology Letters*, vol. 24, pp. 900–902, JUN 1 2012.

[138] L. Wang, R. Guo, B. Wang, X. Wang, and Z. Zhou, "Hybrid Si_3N_4-Er/Yb/Y silicate waveguide amplifier with 1.25dB/cm internal gain," in *9th IEEE International Conference on Group IV Photonics*, pp. 249–251, 2012.

[139] H. P. Klug and L. E. Alexander, *X-Ray Diffraction Procedures for Polycrystalline and Amorphous Materials.* Wiley-Interscience, 2nd ed., 1974.

[140] J. Langford and A. Wilson, "Scherrer after 60 years - survey and some new results in determination of crystallite size," *Journal of Applied Crystallography*, vol. 11, no. APR, pp. 102–113, 1978.

[141] B. Warren, *X-Ray Diffraction.* Dover Publications, 1990.

[142] *ISO Standard 11146 "Lasers and laser-related equipment – Test methods for laser beam widths, divergence angles and beam propagation ratios".* 2005.

[143] V. Mikhelashvili, G. Eisenstein, and F. Edelmann, "Structural properties and electrical characteristics of electron-beam gun evaporated erbium oxide films," *Applied Physics Letters*, vol. 80, pp. 2156–2158, MAR 25 2002.

[144] M. Singh, C. Thakur, K. Shalini, N. Bhat, and S. Shivashankar, "Structural and electrical characterization of erbium oxide films grown on Si(100) by low-pressure metalorganic chemical vapor deposition," *Applied Physics Letters*, vol. 83, pp. 2889–2891, OCT 6 2003.

[145] J. Felsche, "Polymorphism and crystal data of rare-earth disilicates $RE_2Si_2O_7$," *Journal of the Less Common Metals*, vol. 21, no. 1, pp. 1–14, 1970.

[146] H. Ennen, J. Schneider, G. Pomrenke, and A. Axmann, "1.54-μm luminescence of erbium-implanted III-V semiconductors and silicon," *Applied Physics Letters*, vol. 43, no. 10, pp. 943–945, 1983.

[147] H. Ennen, G. Pomrenke, A. Axmann, K. Eisele, W. Haydl, and J. Schneider, "1.54 μm electroluminescence of erbium-doped silicon grown by molecular-beam epitaxy," *Applied Physics Letters*, vol. 46, no. 4, pp. 381–383, 1985.

[148] W. Haydl, H. Müller, H. Ennen, W. Körber, and K. Benz, "Ytterbium-doped InP light-emitting diode at 1.0 μm," *Applied Physics Letters*, vol. 46, no. 9, pp. 870–872, 1985.

[149] H. Krzyzanowska, K. S. Ni, Y. Fu, and P. M. Fauchet, "Electroluminescence from Er-doped SiO_2/nc-Si multilayers under lateral carrier injection," *Materials Science and Engineering B*, vol. 177, pp. 1547–1550, OCT 1 2012.

[150] R. Sun, P. Dong, N. ning Feng, C. yin Hong, J. Michel, M. Lipson, and L. Kimerling, "Horizontal single and multiple slot waveguides: optical transmission at λ = 1550 nm," *Optics Express*, vol. 15, no. 26, pp. 17967–17972, 2007.

[151] G. Valley, "Modeling cladding-pumped Er/Yb fiber amplifiers," *Optical Fiber Technology*, vol. 7, pp. 21–44, JAN 2001.

[152] A. Shooshtari, T. Touam, and S. Najafi, "Yb^{3+} sensitized Er^{3+}-doped waveguide amplifiers: a theoretical approach," *Optical and Quantum Electronics*, vol. 30, pp. 249–264, APR 1998.

[153] P. Cardile, M. Miritello, and F. Priolo, "Energy transfer mechanisms in Er-Yb-Y disilicate thin films," *Applied Physics Letters*, vol. 100, JUN 18 2012.

[154] E. Desurvire, *Erbium-Doped Fiber Amplifiers: Principles and Applications.* Wiley-Interscience, 1994.

[155] K. A. McComber, *Single-crystal Germanium Growth on Amorphous Silicon.* PhD thesis, Massachusetts Institute of Technology, 2011.

[156] M. Miritello, P. Cardile, R. Lo Savio, and F. Priolo, "Energy transfer and enhanced 1.54 μm emission in Erbium-Ytterbium disilicate thin films," *Optics Express*, vol. 19, pp. 20761–20772, OCT 10 2011.

[157] B. Saleh and M. Teich, *Fundamentals of Photonics.* Wiley-Interscience, 2nd ed., 2007.

[158] G. Reed, *Silicon Photonics: the State of the Art.* Wiley, 2008.

[159] A. Yariv and P. Yeh, *Photonics: Optical Electronics in Modern Communications.* Oxford University Press, 6th ed., 2007.